
**AFRL-AFOSR-VA-TR-2023-0260**

# Reconfigurable Matter from Programmable Atom Equivalents

**Mirkin, Chad**
**NORTHWESTERN UNIVERSITY**
**633 CLARK**
**EVANSTON, IL, 60208**
**USA**

**01/20/2023**
**Final Technical Report**



Air Force Research Laboratory
Air Force Office of Scientific Research
Arlington, Virginia 22203
Air Force Materiel Command

# REPORT DOCUMENTATION PAGE

**PLEASE DO NOT RETURN YOUR FORM TO THE ABOVE ORGANIZATION.**

| **1. REPORT DATE** | **2. REPORT TYPE** | **3. DATES COVERED** | |
|---|---|---|---|
| 20230120 | Final | **START DATE** 20170815 | **END DATE** 20220814 |

**4. TITLE AND SUBTITLE**
Reconfigurable Matter from Programmable Atom Equivalents

| **5a. CONTRACT NUMBER** | **5b. GRANT NUMBER** | **5c. PROGRAM ELEMENT NUMBER** |
|---|---|---|
| | FA9550-17-1-0348 | 61102F |
| **5d. PROJECT NUMBER** | **5e. TASK NUMBER** | **5f. WORK UNIT NUMBER** |
| | | |

**6. AUTHOR(S)**
Chad Mirkin

**7. PERFORMING ORGANIZATION NAME(S) AND ADDRESS(ES)**
NORTHWESTERN UNIVERSITY
633 CLARK
EVANSTON, IL 60208
USA

**8. PERFORMING ORGANIZATION REPORT NUMBER**

| **9. SPONSORING/MONITORING AGENCY NAME(S) AND ADDRESS(ES)** | **10. SPONSOR/MONITOR'S ACRONYM(S)** | **11. SPONSOR/MONITOR'S REPORT NUMBER(S)** |
|---|---|---|
| Air Force Office of Scientific Research<br>875 N. Randolph St. Room 3112<br>Arlington, VA 22203 | AFRL/AFOSR RTB2 | AFRL-AFOSR-VA-TR-2023-0260 |

**12. DISTRIBUTION/AVAILABILITY STATEMENT**
A Distribution Unlimited: PB Public Release

**13. SUPPLEMENTARY NOTES**

**14. ABSTRACT**
In Year 5, we continued to enhance our understanding of reconfigurable matter using programmable atom equivalents (PAEs) as building blocks. For example, nanoparticles from earth-abundant metals, such as aluminum, have been explored as highly plasmonic PAE feedstocks, and noncentrosymmetric Au bipyramids were introduced as feedstocks (Objective 1). PAE superlattices have been advanced to demonstrate a property known as hypereleasticity, where the crystals contain a shape memory capable of restoring their shape upon dehydration and rehydration (Objective 2). Superlattices with narrow size distributions have been synthesized by separating nucleation and growth during crystallization through the use of designed base mismatches in the DNA sticky ends (Objective 3). Finally, hollow nanoframe particles have been shown to be excellent broadband absorbers when ultrathin monolayers are dried on a substrate (Objective 4). Together, the progress made in Year 5 has substantially improved our ability to realize structurally sophisticated and complex programmable and reconfigurable superlattices and has enabled our exploration of their emergent functional properties.

**15. SUBJECT TERMS**

| **16. SECURITY CLASSIFICATION OF:** | | | **17. LIMITATION OF ABSTRACT** | **18. NUMBER OF PAGES** |
|---|---|---|---|---|
| **a. REPORT** | **b. ABSTRACT** | **c. THIS PAGE** | | |
| U | U | U | UU | 158 |

| **19a. NAME OF RESPONSIBLE PERSON** | **19b. PHONE NUMBER** *(Include area code)* |
|---|---|
| BENNETT IBEY | 000-0000 |

**Cover Page**
**Subject:** Final Report
**To**: Dr. Bennett Ibey, bennett.ibey@us.af.mil
**Contract/Grant Title:** Reconfigurable Matter from Programmable Atom Equivalents
**Contract/Grant #:** FA9550-17-1-0348
**Reporting Period:** August 15, 2017–August 14, 2022

Contents

**YEAR 1**
**Cover Page**
**To:** Dr. Sofi Bin-Salamon, sofi.bin-salamon@us.af.mil
**Subject:** Annual Report
**Contract/Grant Title:** Reconfigurable Matter from Programmable Atom Equivalents
**Contract/Grant #:** FA9550-17-1-0348
**Reporting Period:** August 15, 2017-August 14, 2018

## I. ABSTRACT

We are using DNA as a programmable ligand to design and study sophisticated, reconfigurable colloidal crystals composed of a diverse set of functional nanoparticle building blocks, referred to as programmable atom equivalents or PAEs. We assembled a team that is uniquely qualified to carry out this research. Mirkin is an expert in nanomaterials synthesis and assembly, nanoscale patterning, and assembly characterization. Dravid provides advanced characterization techniques of nanomaterials and assemblies. Aydin is an expert on metamaterials and has extensive experience in modeling and encoding information into such nanoscale structures. Harris is an emerging leader in metal-organic framework synthesis and characterization. Together, we are synthesizing and investigating new types of structurally complex architectures with dynamic interactions that would not be possible to prepare through any other techniques.

Over the past year, we have made significant progress that advances the aims of this grant and have reported these important results to the scientific community through publications in high impact journals and invited presentations. Specifically, we have developed approaches for synthesizing a new library of nanomaterials as building blocks for colloidal crystal engineering. Examples include low-symmetry plasmonic nanoparticles, multicomponent nanoparticles with catalytic and plasmonic relevance, monocrystalline 2D MOFs, as well as MOF nanoparticles.

To gain insight into the synthesis of functional nanoparticles as well as their assembly, we have utilized high-resolution electron microscopy. For example, we have systematically studied the formation of Au-Cu nanoparticles in the intermetallic and solid solution forms by combining scanning probe-directed synthesis and correlative electron microscopy. Additionally, we have made substantial advances in the characterization of soft materials and fluidic systems with electron microscopy. Characterization of soft materials suffers from two major challenges: low contrast and beam damage. We have developed protocols for selectively staining the DNA shell in PAEs that have a soft material core as well as achieved atomic resolution imaging of MOF nanoparticles.

Using PAE building blocks, we have shown that colloidal crystals can be engineered using DNA as a connecting ligand. Furthermore, we have developed strategies to manipulate the habit and size of these crystals and to post-synthetically modify them through the incorporation of stimuli-responsive moieties. Importantly, we have already begun to identify the diverse and tunable optical properties that arise from the ability to use DNA to program the arrangement of building blocks into crystals with a high degree of structural control.

Towards the ultimate goal of making functional devices composed of PAE assemblies, we have investigated the assembly of PAEs onto surfaces. We have demonstrated that single crystalline, multilayer thin films can be synthesized over sub-centimeter scale areas on lithographically patterned templates containing well-defined DNA binding sites. Importantly, we have shown that template mediated surface assembly is promising for developing tunable metamaterials for light guiding as well as multiplexed-surface encoding. Taken together, this year represents a major step forward towards the development of reconfigurable, structurally sophisticated, and highly functional colloidal crystals.

## II. OBJECTIVES

### Year 1

Objective 1: Develop a new feedstock of functional PAE building blocks

- *Synthesis of three-dimensional anisotropic plasmonic nanoparticles*
- *Synthesis of MOF nanoparticles with control over their physical properties*

Objective 2. Synthesize and investigate dynamically reconfigurable superlattices

- *Transmutable nanoparticle superlattices.*
- *High resolution and contrast imaging of soft materials by electron microscopy.*

Objective 3. Synthesize and investigate structurally sophisticated and functional superlattices.

- *Superlattices with controlled crystal habit.*
- *Explore emergent optical phenomena in nanoparticle superlattices.*

Objective 4. Assemble reconfigurable, sophisticated, and functional superlattices on surfaces

- *Fabricate surface templates with well-defined DNA binding sites.*

**Year 2**

Objective 1. Develop a new feedstock of functional PAE building blocks

- *Synthesis of two-dimensional anisotropic plasmonic nanoparticles.*
- *Algorithmic characterization of nanoparticle yield and dispersion.*
- *Synthesis of MOFs nanoparticles with control over their physical properties*

Objective 2. Synthesize and investigate dynamically reconfigurable superlattices

- *Transmutable nanoparticle superlattices.*
- *Sparse imaging for soft materials characterization.*
- *High resolution and contrast imaging of soft materials by electron microscopy.*

Objective 3. Synthesize and investigate structurally sophisticated and functional superlattices.

- *Co-crystallization of multiple building blocks with chemically, physically, and structurally distinct properties.*
- *Superlattices with controlled crystal habit.*
- *Explore emergent optical phenomena in nanoparticle superlattices.*

Objective 4. Assemble reconfigurable, sophisticated, and functional superlattices on surfaces

- *Layer-by-layer growth of single-crystal superlattices with defined crystal shape and size.*

**Year 3**

Objective 1. Develop a new feedstock of functional PAE building blocks

- *Synthesis of two-dimensional anisotropic plasmonic nanoparticles.*
- *High-throughput screening of anisotropic nanoparticle synthesis conditions*

Objective 2. Synthesize and investigate dynamically reconfigurable superlattices

- *Transmutable nanoparticle superlattices.*
- *In situ characterization of reconfigurable superlattices via fluidic-cell S/TEM.*

Objective 3. Synthesize and investigate structurally sophisticated and functional superlattices.

- *Co-crystallization of multiple building blocks with chemically, physically, and structurally distinct properties.*
- *Unique low-symmetry and quasicrystalline structures.*
- *Explore emergent optical phenomena in nanoparticle superlattices.*

Objective 4. Assemble reconfigurable, sophisticated, and functional superlattices on surfaces

- *Layer-by-layer growth of single-crystal superlattices with defined crystal shape and size.*

**Year 4**

Objective 1. Develop a new feedstock of functional PAE building blocks

- *High-throughput screening of anisotropic nanoparticle synthesis conditions*

Objective 2. Synthesize and investigate dynamically reconfigurable superlattices

- *Transmutable nanoparticle superlattices.*
- *In situ characterization of reconfigurable superlattices via fluidic-cell S/TEM.*

Objective 3. Synthesize and investigate structurally sophisticated and functional superlattices.

- *Co-crystallization of multiple building blocks with chemically, physically, and structurally distinct properties.*
- *Unique low-symmetry and quasicrystalline structures.*
- *Explore emergent optical phenomena in nanoparticle superlattices.*

Objective 4. Assemble reconfigurable, sophisticated, and functional superlattices on surfaces

- *Superlattice assembly on flexible and porous supports.*
- *Emergent properties of surface-bound superlattices.*

**Year 5**

Objective 1. Develop a new feedstock of functional PAE building blocks

- *High-throughput screening of anisotropic nanoparticle synthesis conditions*

Objective 2. Synthesize and investigate dynamically reconfigurable superlattices

- *Synthesis of dynamically responsive superlattices from MOF building blocks.*
- *Develop new strategies for transferring DNA-assembled superlattices to the solid state.*

Objective 3. Synthesize and investigate structurally sophisticated and functional superlattices.

- *Unique low-symmetry and quasicrystalline structures.*
- *Explore emergent optical phenomena in nanoparticle superlattices.*

Objective 4. Assemble reconfigurable, sophisticated, and functional superlattices on surfaces

- *Emergent properties of surface-bound superlattices.*

## III. FINDINGS

### A. Development of a New Feedstock of Functional PAE Building Blocks

This year we have developed: i) strategies for the synthesis of various PAE building blocks, including three-dimensional anisotropic plasmonic nanoparticles (section 1), chemically ordered or disordered Au-Cu alloy nanoparticles (section 2), and MOF nanoparticles (sections 3-6), ii) a foundational platform for future efforts towards the synthesis of 2D MOF-based PAEs and superlattices (sections 4 and 6) and iii) the chemistry to control intrinsic physical properties of MOF-based PAEs (section 5).

#### 1. Synthesis of three-dimensional anisotropic plasmonic nanoparticles

Over the last decade, AFOSR-funded research in the Mirkin group has enabled the establishment of a vast new phase space of previously inaccessible nanoparticle-based lattices. Nanoparticles (NPs) with many DNA strands attached to their surface (*i.e.* densely functionalized) can act as Programmable Atom Equivalents (PAEs), building blocks where the identity of the NP "atom" can be decoupled from its "bonding" behavior. Short, unpaired "sticky ends" at the termini of DNA ligands create collective, programmable "bonds" between building blocks via Watson-Crick base pairing. The ability to tune the sequence of the "sticky end" and the arrangement of DNA on the NP surface has enabled the creation of structurally diverse architectures with unique, functional behaviors. However, the complexity of the achievable lattices, and likely the resultant properties, depends on the size, shape, and uniformity of the NP building blocks. Simulations, supported by recent experimental work, suggest that one strategy to encode building blocks with more complex crystallization information would be to use anisotropic particles. With this approach, the particle core acts as a template to arrange the DNA into a conformant shell. Anisotropic shapes can thus encode spatially discrete, collective DNA interactions localized along each facet or spatial region of the particle. The number, geometry, and relative strength (*i.e.* the number of DNA molecules within each collective interaction) of these "bonds" can be tuned to

produce different crystal symmetries.

Realization of low-symmetry lattices via this approach is dependent on the availability of suitable chemical syntheses that yield the desired shapes with sufficient uniformity and yield. This remains a challenge even for some of the most studied nanomaterial systems (*e.g.* noble metals), due to the thermodynamic preference for highly symmetric products and the poor understanding of symmetry breaking events. Successful examples often result from trial-and-error, where kinetic processes trap structures in local energetic minima that are prone to fluctuations in reaction conditions. The lack of synthetic approaches to produce libraries of systematically varied anisotropic particles limits understanding of symmetry breaking processes in colloidal crystallization and access to low-symmetry colloidal crystals. Herein, we report a generalizable approach to access a new library of highly anisotropic NPs with tunable size and aspect ratio (*AR*). As a case study, a base shape of a rhombic dodecahedron was systematically tuned.

Robust syntheses for NPs require precise control over the placement of tens of millions of atoms. One strategy to achieve this control is to spatiotemporally separate homogeneous particle nucleation from heterogeneous growth onto existing particles, and thereby improve control over each step. In this "seed-mediated" approach, a pre-formed particle (*i.e.* "seed") is separately nucleated and added to mildly reducing growth solutions, such that the seed acts as a preferential site for heterogeneous nucleation. In many cases, this approach enables one to guide particles toward a single product with high uniformity and yield. Furthermore, the structure of the NP seed can direct the growth of the NP product.

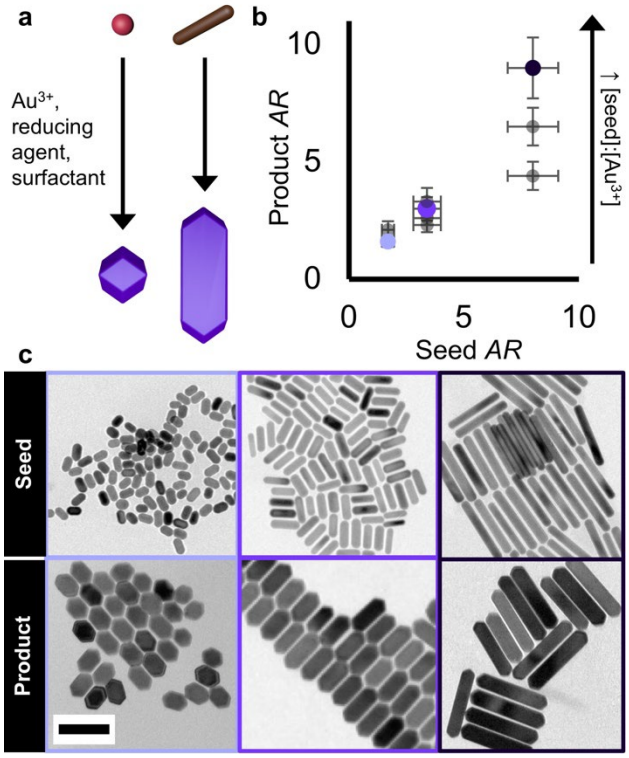


**Figure 1.** Seed-mediated synthesis of elongated rhombic dodecahedra with tunable ARs. **a** Schematic of seed-mediated synthesis with traditional spherical or rod seed and their resultant products. **b** Based on algorithmic analysis of TEM images , the seed aspect ratio and [seed]:[$Au^{3+}$] ratio can tune product AR. Error bars represent one standard deviation in each direction. **c** Representative TEM images of seed and product NPs that correspond to the colors in the plot in **b**. Scale bar = 100 nm.

An ideal low-symmetry particle seed would be accessible in high yield with broadly tunable anisotropy (**Figure 1a**). For this purpose, we chose the well-studied syntheses for single crystalline Au rods, a NP in which symmetry is broken in a single direction. The anisotropy of these particles is defined by the ratio of the rod length divided by the rod diameter (*i.e. AR*), and directly measured via transmission electron microscopy (TEM). The shape and size of the particles (seeds and products) can be analytically determined via algorithmic analysis of TEM images of 100s of NPs to approximate population-level statistics. The electronic structure of these particles enables structural changes to be measured via UV-Vis spectroscopy, where the broken symmetry manifests in two, spectrally separated localized surface plasmon resonances (LSPRs).

Several syntheses exist to control the *AR* of single crystalline Au rods through the inclusion of

different amounts of shape-directing additives (*e.g.* $Ag^{+}$). However, these syntheses simultaneously change both particle length and width to produce particles with a similar volume. An ideal platform to control seed *AR* would permit control over length, while holding the diameter constant (or vice versa). One strategy to achieve such control is to begin with high *AR* rods and selectively remove material from their tips; an approach previously demonstrated via the addition of an oxidizing agent (*i.e.* $Au^{3+}$ salt). Importantly, TEM of *AR*=8 rods etched to different extents revealed access to rods of *ARs* down to 4.4, while maintaining the uniformity and diameter of the original particles (**Figure 1b, 1c**). Starting the etching process with a lower *AR* rod (~3.4) afforded access to a range of low *ARs* down to 1.7 (**Figure 1b, 1c**).

To study the impact of seed anisotropy on product anisotropy, Au rods with the same diameter, but different *ARs* (1.7, 3.4, 4.4, 5.2, and 8) were added to a seed-mediated synthesis that conventionally produces Au rhombic dodecahedra, a particle with twelve equal rhombus faces. While this synthesis primarily produces a single product from single crystalline, spherical Au NP seeds, it was uncertain whether the trace amount of silver present or the different faceting/surface curvature of the rod seeds would result in multiple products or impact the resultant shape. TEM and UV-Vis revealed the formation of unique, anisotropic products that resembled elongated rhombic dodecahedra. More specifically, facets adjacent to the axis of four-fold symmetry remained fixed in surface area and formed the "tips", while the four remaining facets at 90 degrees to this axis elongated and increased in surface area (**Figure 1b, 1c**). Algorithmic image analysis of hundreds of particles confirmed the formation of this single product, fit to a hexagonal cross-section in TEM images, in >95% yield (**Figure 1b, 1c**). The *AR* of the elongated rhombic dodecahedra directly correlate with the *AR* of the seeds (**Figure 1b, 1c**) and an TEM image tilt series of products grown from the highest *AR* seeds revealed a consistent elongated rhombic dodecahedron shape, with the preservation of a square cross-section along the four-fold symmetry axis. Importantly, the introduction of rod seeds into several other syntheses for low anisotropy shapes (*e.g.* concave cubes, ditetragonal prisms) yielded similarly shifted LSPRs and similarly elongated products (**Figure 2**) as compared to products from spherical seeds.

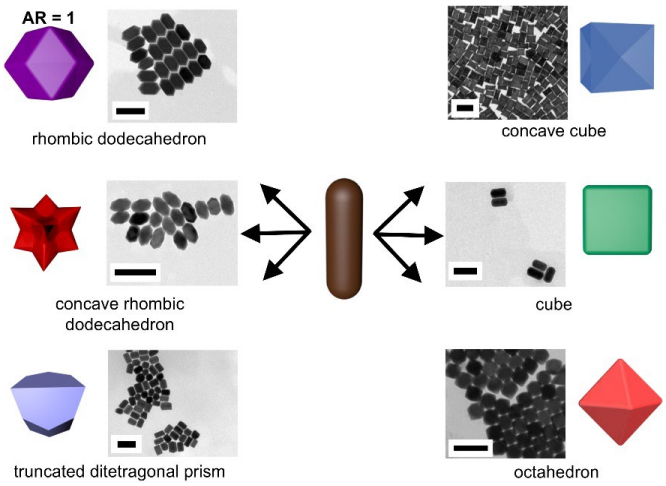


**Figure 2.** Au NPs grown from Au rod seeds. The center graphic represents the seed used to grow NPs in the TEM images. Elongated products were obtained in all cases, except for the octahedron particle. Rendered graphics represent the regular polyhedral that would be realized if a spherical seed were used. Scale bars represent 200 nm.

The anisotropy of the elongated particles could be further tuned by varying the ratio of rod concentration to Au concentration in the growth solution, with higher ratios leading to more anisotropic products (**Figure 1b**). With this approach, products from a single rod seed could be tuned by up to a factor of two in *AR* (here defined as the longest edge length divided by the shortest) and a factor of 3 in minor edge length. In totality, both approaches enabled realization of a library of elongated rhombic dodecahedron that spanned from a regular rhombic dodecahedron with an *AR*, by definition, of 1.15 to the most anisotropic with an *AR* = 9, with similar minor edge lengths. This expanded library of NP shapes affords new opportunities to push the boundaries of material structure using DNA to guide

crystallization.

## 2. Exploring the Synthetic Conditions for Chemically Ordered or Disordered Au-Cu Alloy Nanoparticles

The optical properties, especially the plasmonic properties, of metallic NPs can be tuned by creating alloys with multiple metal elements. Although alloy NPs are typically considered as homogeneous solid solutions, certain metal elements may form chemically ordered intermetallic compounds, and thereby may induce anisotropic plasmonic properties in the NP building blocks. Achieving controlled synthesis of chemically ordered and disordered alloy NPs has the potential to introduce a new level of plasmonic and photonic properties in crystals engineered with DNA through control over the atomic layer stacking along certain crystal orientations. Therefore, such building blocks are interesting target PAEs.

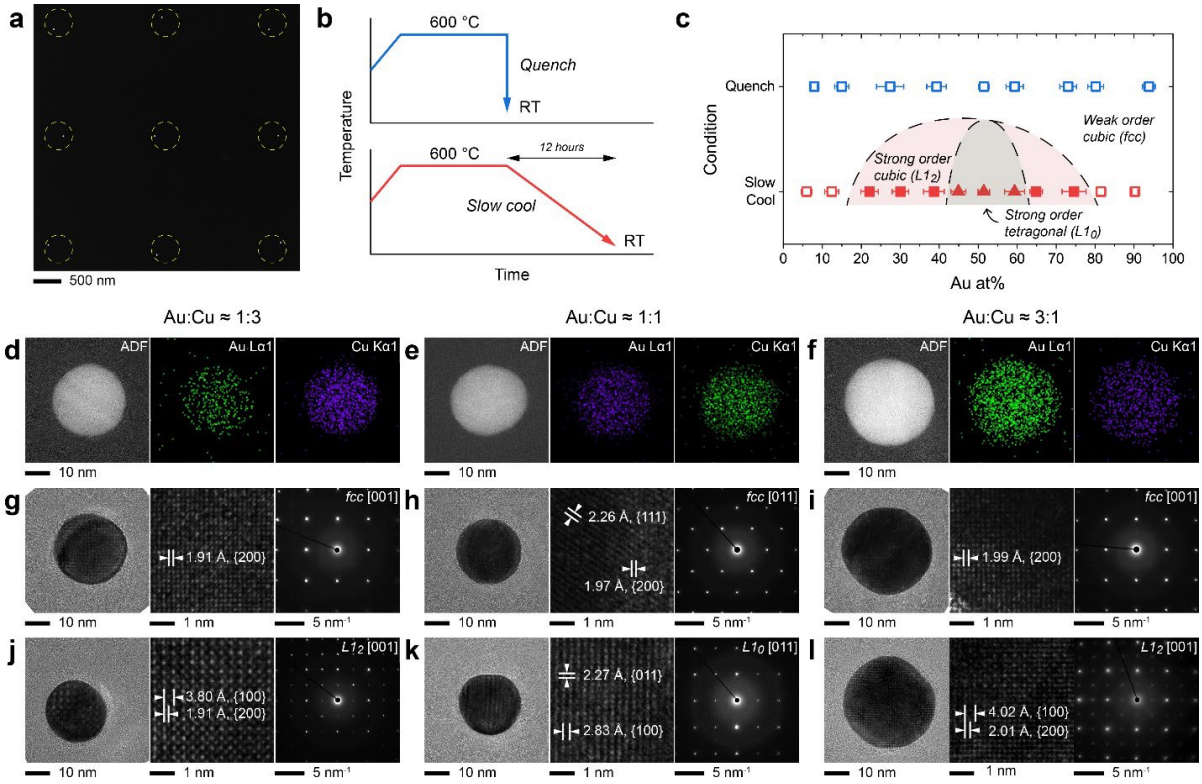


**Figure 3.** Au-Cu NPs with controlled composition and chemical ordering. (a) Annular dark field (ADF) scanning transmission electron microscopy (STEM) image of a Au-Cu bimetallic NP array. (b) Schematic of the heat treatment processes for synthesizing chemically ordered (bottom) or disordered (top) NPs. (c) Diagram showing the relationship between composition, processing condition, and structure of Au-Cu NPs. (d-f) Representative ADF images and energy-dispersive X-ray spectroscopy (EDS) elemental maps of Au-Cu NPs. Representative high-resolution transmission electron microscopy (HRTEM) images and electron diffraction patterns of Au-Cu NPs in (g-i) the chemically disordered and (j-l) ordered states.

Here, we used scanning probe block copolymer lithography (SPBCL) to generate Au-Cu NPs with arbitrarily controlled compositions and study their structures depending on synthetic conditions. Briefly, polymer inks composed of poly(ethylene oxide)-*b*-poly(2-vinyl-pyridine) (PEO-*b*-P2VP) and metal precursor ions (for Au and Cu) were coated onto AFM scanning probes. These inks were deposited onto a silicon nitride membrane in the form of dome-shaped nanoreactors. After a series of heat treatments in a hydrogen atmosphere, the metal precursor ions

were reduced resulting in the formation of individual, bimetallic NPs in each nanoreactor (**Error! Reference source not found.a**). We introduced a kinetically-controlled thermal treatment process to SPBCL-synthesized NPs to influence the chemical ordering of the atoms. NPs with different Au:Cu ratios can be synthesized in either the chemically disordered solid solution form, or chemically ordered intermetallic compound form, depending on the cooling rate (**Error! Reference source not found.b**, **c**). These NPs show a uniform distribution for both Au and Cu elements (**Error! Reference source not found.d-f**). When quenched from 600 °C, Au-Cu NPs of all compositions show a chemically disordered face-centered cubic (*fcc*) structure, in which all *fcc* lattice sites are randomly occupied by either Au or Cu atoms and show weak long-range ordering (**Error! Reference source not found.g-i**). In contrast, NPs synthesized by slow cooling show different crystal structures according to correlative electron microscopy imaging and electron diffraction (**Error! Reference source not found.j-l**). Both the $AuCu_3$- and $Au_3Cu$-type NPs have a cubic crystal structure, but the Au and Cu atoms occupy specific lattice sites resulting in an $L1_2$ structure. The AuCu-type NPs show a tetragonal $L1_0$ structure, and therefore, have a completely different lattice symmetry.

The unique composition- and chemical ordering-controlled synthesis also allowed us to study atom-stacking hierarchy in anisotropic NPs. Specifically, triangluar nanoprisms, a highly anisotropic NP building block for PAE-superlattices, have a highly defined relationship between their geometric shape and crystal orientation. The chemically-disordered single crystalline $Au_3Cu$ NPs along the [111] zone axis show only electron diffraction spots from the *fcc* framework (**Error! Reference source not found.a**). On the other hand, chemically-disordered nanoprisms show additional ⅓{422} reflections (**Error! Reference source not found.b**), originating from horizontal

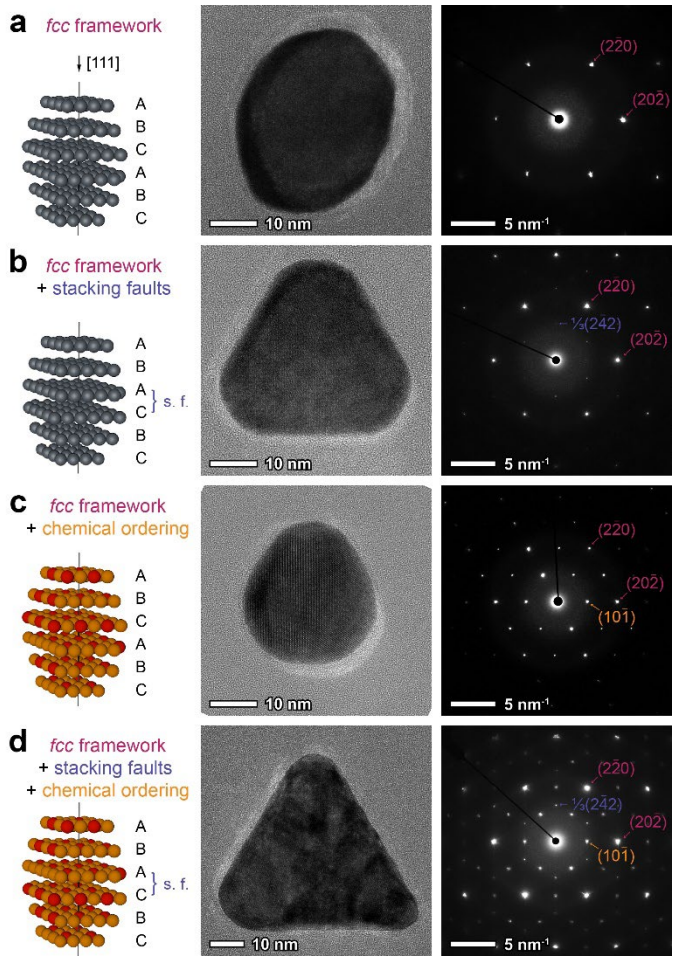


**Figure 4.** Development of electron diffraction spots based on atom stacking hierarchy along the [111] zone axis in cubic Au-Cu bimetallic nanostructures. The atomic ratio Au:Cu is near 3:1. (a) A single crystalline, chemically disordered NP. (b) A stacking fault-bearing, chemically disordered nanoprism. (c) A single crystalline, chemically ordered NP. (d) A stacking fault-bearing, chemically ordered ($L1_2$) nanoprism, showing a combination of electron diffraction spots from the fcc framework (red), stacking faults (blue), and chemical ordering (yellow). Left column: schematic illustration of the atomic stacking structure. Gray balls: randomly ordered Au or Cu atoms; yellow balls: Au atoms; red balls: Cu atoms. Atomic layers perpendicular to the [111] axis (black line) has been separated for clarity. s. f.: stacking faults. Middle column: HRTEM images. Right column: electron diffraction patterns.

stacking faults, as expected from previous research on Au and Ag nanoprisms. For single crystal, chemically-ordered $Au_3Cu$ NPs, the ordering between Au and Cu atoms induces strong reflection of the {110} lattices, which are forbidden in *fcc* crystals (**Error! Reference source not found.c**). In comparison, the $Au_3Cu$ intermetallic triangular nanoprism shows reflections from all three levels of atomic stacking hierarchy: the *fcc* framework, horizontal stacking faults, and chemical ordering (**Error! Reference source not found.d**). Taken together, these results offer important insights into how the elemental stacking can be controlled and results in the formation of well-defined hierarchical anisotropic NP building blocks. This knowledge may help design of superstructures from these building blocks that have exotic optical or catalytic properties.

### 3. Synthesis of Metal-Organic Framework (MOF) NPs, a novel class of PAEs

The range of building blocks for colloidal crystal engineering with DNA has typically been limited to a small number of well-studied NPs (e.g. Au, Ag), largely due to their ease of synthesis and the robust chemistries to attach DNA to their surface. However, crystal functionality could be dramatically expanded with the introduction of new classes of NP cores, provided that they may be similarly functionalized with DNA. Here, we show that functional molecular motifs on the surface of metal-organic framework (MOF) NPs can be leveraged as a functionalization site for DNA ligands to produce a novel class of PAEs. We hypothesized that the following design parameters should be met: 1) the relative uniformity of the MOF PAEs dictates the crystallinity of the resulting colloidal crystals; 2) colloidally stable MOF PAEs with high DNA surface coverage are necessary to ensure interparticle DNA bonds are dynamic and reversible upon thermal annealing; 3) chemical bonding interactions between the constituents of the lattices should be orthogonal, such that the MOF PAE architectures are stable all the time and ordering at different length scales are preserved. With these parameters in mind, as a proof-of-concept, uniform UiO-66 MOF NPs ($37 \pm 4$ nm sphere) were selected as a representative PAE core, featuring Zr clusters (inorganic secondary building units; SBUs) and terephthalic acid organic linkers (Error! Reference source not found.**b**). MOF NPs were first functionalized with hetero-bifunctional polyethylene glycol (phosphate-$PEG_{5k}$-$N_3$) spacers, composed of a phosphate head group which coordinates to surface SBUs and an azide modified tail capable of coupling with DNA (Error! Reference source not found.**c**). Next, these PEG spacer stabilized MOF NPs were coupled with DNA strands bearing a modified 5' pendent-strained octyne ring (DBCO-TEG modifier) to yield MOF PAEs with dense

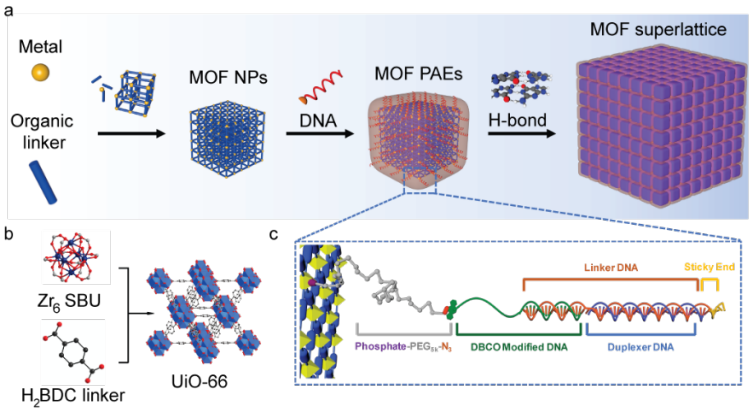


**Figure 5**. (a) Schematic of the synthesis of MOF NP-based PAEs and their DNA-programmed assembly. Metal ions and organic linkers were combined to synthesize MOF NPs. These MOF NPs were functionalized with DNA to produce MOF PAEs and subsequently crystallized into superlattices via DNA hybridization. (b) Schematic of a UiO-66 MOF composed of $Zr_6$ SBU and terephthalic acid. (c) Heterobifunctional linkers and DNA strands used to assemble MOF NP superlattices consist of (i) phosphate-$PEG_{5k}$-azide linker, (ii) a DBCO moiety with an 18 base recognition sequence that binds to a DNA linker, (iii) a linker hybridized with a duplexer sequence of programmable length to control interparticle distances, and (iv) a "sticky end" sequence that drives MOF PAE assembly.

shells of oligonucleotides. It should be noted that depending on the synthetic conditions and choice of precursors, the intrinsic crystal symmetries of MOFs could be leveraged to achieve diverse anisotropic particle shapes, significantly enriching the structural programmability of the resulting colloidal crystals. In this vein, we have shown that rod-shape PCN-222 NPs with a diameter of 37 ± 8 nm, and length of 159 ± 25 nm can be functionalized with DNA, resulting in anisotropic MOF-based PAEs.

## 4. Monocrystalline 2D MOF Thin Films

The Harris Group recently discovered an emerging class of 2D MOFs featuring redox active benzoquinoid ligands. These materials have shown rich chemical and physical properties associated with the redox state of both the metal and ligand. In order for these MOFs to act as functional particle cores for PAEs, tight control over their structure is needed, a challenge that would require controlling crystal growth along both the *ab* plane and *c* axis. Further, to maximize the physical properties of MOFs (*e.g.* electronic conductivity, magnetism) single crystalline NPs are desirable. To overcome this challenge, we implemented a top-down lithographic fabrication route to synthesize PAEs on a surface.

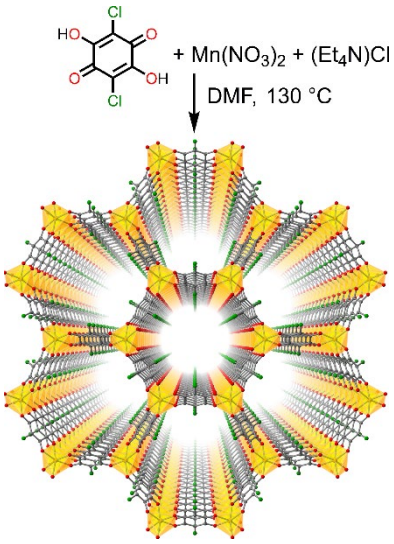


**Figure 6.** Scheme showing the synthesis and the structure of $(Et_4N)_2[Mn_2L_3]$, viewed down the crystallographic c axis.

The MOF was synthesized by reacting equimolar $Mn^{2+}$ and chloranilic acid ($H_2L$) with five equivalents of $Et_4N^+$ under solvothermal conditions afforded brown crystals of $(Et_4N)_2[Mn_2L_3]$ (**Figure 6**). Structural analysis using single crystal X-ray diffraction (XRD) revealed that this MOF features eclipsed stacked anionic 2D sheets of $[Mn_2L_3]^{2-}$ that are charge balanced with two $Et_4N^+$ located at the center of the two nearest Mn atoms from adjacent layers. According to optical and electron microscopy images, these crystals are ~ 200-300 µm wide and 100-150 µm thick. Although preliminary attempts to transfer exfoliated thin films to a silicon substrate resulted in fragmentation (Error! Reference source not found.), PMMA coating and electron-beam lithography on this thin film fragment was successful. Therefore, with appropriate synthetic conditions to create a single crystalline thin film over a large area, lithography may transform these MOFs into functional NPs.

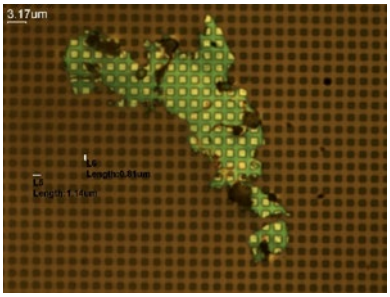


**Figure 8.** Optical microscopy image of a $(Et_4N)_2[Mn_2L_3]$ thin film fragment that is spin-coated with PMMA followed by EBL.

To create such a monocrystalline thin film, we controlled the reaction conditions such that the crystal grows preferentially along the *ab* plane. This was achieved by lowering the $Et_4N^+$ : $Mn^{2+}$ ratio. The lower concentration of $Et_4N^+$ weakens the electrostatic interactions between the layers, resulting in a lower crystal growth rate along the *c*

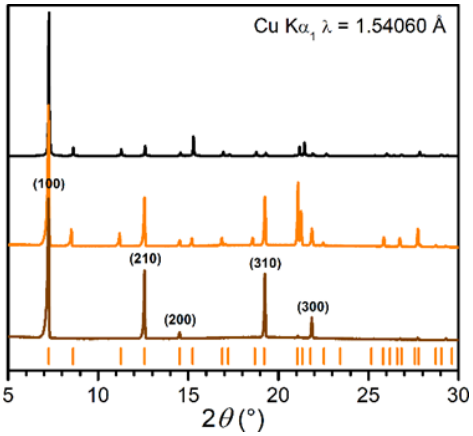


**Figure 7.** Simulated (black) and experimental powder XRD patterns of polycrystalline samples of $(Et_4N)_2[Mn_2L_3]$ synthesized using original (orange) and thin film (dark gold) methods.

axis. As shown in Error! Reference source not found., the bulk powder XRD pattern of the thin crystals exhibits peaks that only belongs to (*hk*0) reflections that are independent of the crystal thickness. The fact that intensities for (*hkl*, $l \neq 0$) reflections are negligible suggest these crystals have an extremely large aspect ratio between *ab* and *c* directions. The aspect ratio is quantified by profilometry to be ~ 1000:1. Finally, these thin crystals can be easily drop-casted on a silicon substrate. With the ability to incorporate lithography and synthetic approaches to form uniform MOF crystals, we aim to generate monocrystalline PAEs on a surface.

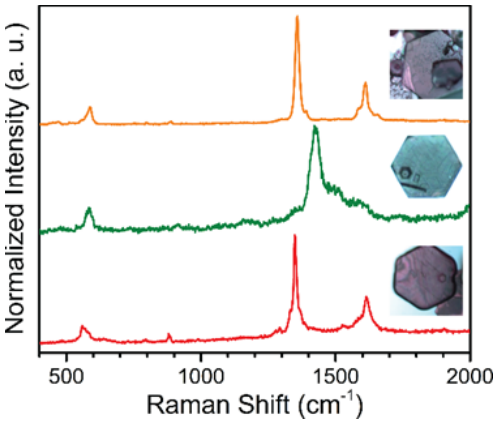


**Figure 9.** Raman spectra of $(Me_4N)_2[Mn_2L_3]$ (orange), $Na_3(Me_4N)_2[Mn_2L_3]$ (green) and reoxidized material (red). Optical microscopy images of their crystals are shown as insets above each spectrum.

## 5. Redox Switch of Conductivity and Magnetism in MOFs

The above results inspired the development of additional MOF NPs for use as PAEs. Over the past five years, research into the electronic conductivity of MOFs has unleashed their potential as materials for electronic devices. However, research into their magnetic properties has made little progress. Recently, the Harris group discovered a 2D iron-semequinoid MOF that magnetically orders beyond liquid nitrogen temperature.[1] The magnetic properties and electronic conductivity can be simultaneously tuned *via* post-synthetic chemical reduction.[2] These discoveries encouraged us to design materials with specific physical properties that might find use in spintronics. Here, we report the first example of a 2D MOF, that upon reduction and re-oxidation, can switch between a paramagnetic insulator and a semiconducting soft magnet.

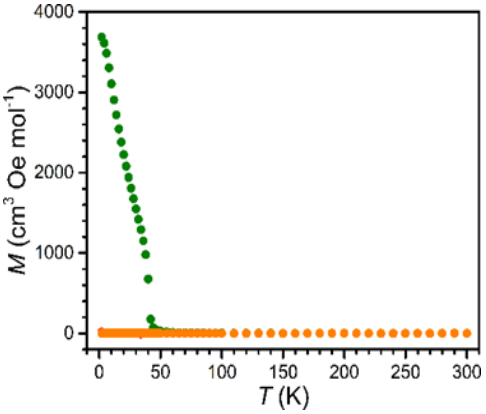


**Figure 10.** Variable-temperature field-cooled magnetization data for $(Me_4N)_2[Mn_2L_3]$ (orange), $Na_3(Me_4N)_2[Mn_2L_3]$ (green), and re-oxidized framework (red), collected under an applied dc field of 10 Oe.

Soaking $(Et_4N)_2[Mn_2L_3]$ (**Figure 6**) in a DMF solution of $(Me_4N)(BF_4)$ at 75 °C for 17 h produced crystals of $(Me_4N)_2[Mn_2L_3]$ *via* single-crystal-to-single-crystal conversion. X-ray crystallography indicates its structure is nearly identical compared to the parent MOF, except for the identity of the counterion. Chemical reduction using a mixture of sodium naphthalenide and sodium 1,2-dihydroacenaphthylenide in THF at −35 °C produced dark green crystals of reduced framework with a formula of $Na_3(Me_4N)_2[Mn_2L_3]$•3.9THF determined by ICP-OES, NMR spectroscopy and elemental analysis. The oxidation states for metal and ligand are determined to be $Mn^{2+}$ and $L^{3-\bullet}$ by Raman spectroscopy (Error! Reference source not found.). This reduced framework can be re-oxidized to the original phase, as confirmed by Raman spectroscopy and powder XRD.

As shown in Error! Reference source not found., the dc magnetization plot of the reduced framework indicates spontaneous magnetization below 50 K, whereas the magnetic susceptibility of the pristine and re-oxidized materials is negligible above 1.8 K. This suggests that the reduced material is a permanent magnet below 40 K, determined by ac magnetic susceptibility, whereas the pristine and re-oxidized materials are paramagnetic and do not become a permanent magnet at any temperature. Although there are several literature examples to show that post-synthetic

reduction of a 2D MOF can improve the magnetic ordering temperature, only one report showed a redox switch between a paramagnetic material and a permanent magnet in a $Ru_2$-TCNQ system.[3]

Notably, the two-point pressed-pellet electronic conductivity measured at 295 K for the reduced framework exhibit a conductivity of $1.76 \times 10^6$ S/m — the highest value among structurally-characterized manganese MOFs.

## 6. Vertically Processible Metal Exchange in MOFs

With the aim of eventual incorporation of crystals engineered with DNA and MOF NPs into device architectures, we developed new strategies to process MOF NPs. Recent efforts to measure and understand intrinsic physical properties of MOFs have accelerated the development of MOF-based devices. However, to create large-scale integrated devices, new fabrication methods are needed, due to the incompatibility of the MOFs with existing fabrication technology in semiconductor industries. Since most of the post-synthetic modification of MOFs are carried out in solution, a solution-based fabrication method would be ideal. This is achieved based on the diffusion of the dissolved reagents into the MOF pores to carry out chemical reactions. A key difference for this solution process compared to fabrication methods in the semiconductor industry is the directionality. Reagents diffuse along all directions within a porous material in the former method, while the latter methods (*e.g.* lithography, ion implantation, etching) operates only along the vertical direction. Therefore, a solution-based fabrication method that operates vertically and can prevent lateral diffusion would be advantageous. During this funding period, we investigated the detailed mechanism of post-synthetic metal exchange of a 2D manganese-benzoquinoid MOF. Herein, we report a foundational discovery of a vertically processible solution-based MOF fabrication for use in large-scale integrated MOF-based devices. Specifically, we show that solvated exogenous metal ions can only diffuse through the 1D channels along the crystallographic *c* aixs of this MOF.

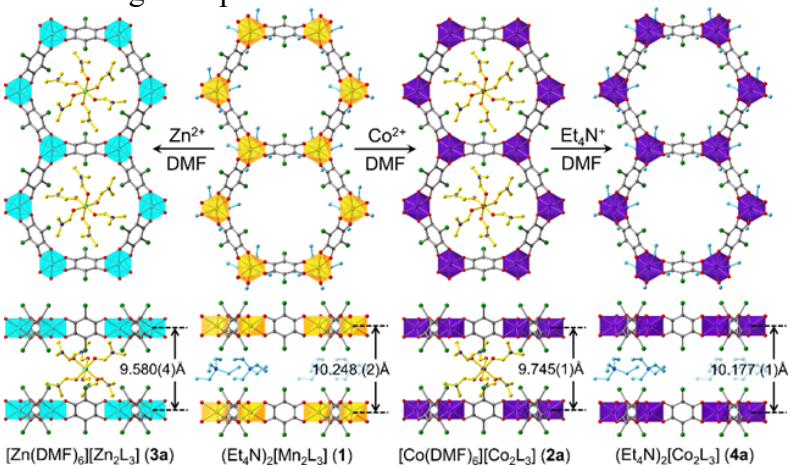


**Figure 11.** A scheme illustrating the metal exchange of $(Et_4N)_2[Mn_2L_3]$ with Zn and Co. Single crystal structure of each framework are shown.

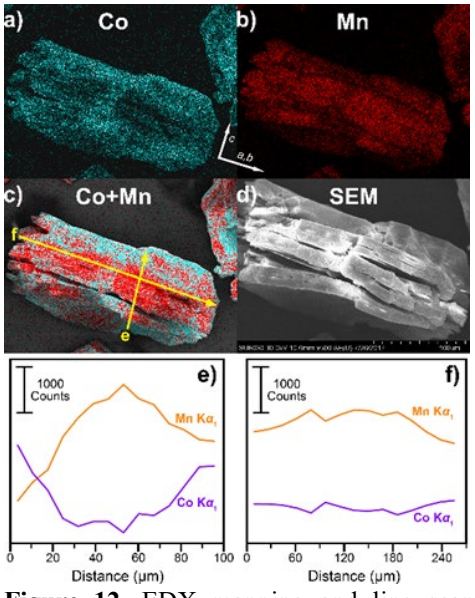


**Figure 12.** EDX mapping and line scan analysis of a partially cobalt exchanged MOF.

Error! Reference source not found. shows the single-crystal-to-single-crystal conversions of $(Et_4N)_2[Mn_2L_3]$ through metal exchange with Zn and Co. These processes are monitored by *ex situ* powder XRD and ICP-OES analysis: the complete conversion from the Mn to Co MOF takes 4 weeks. According to their crystal structures, we hypothesized that the diffusion of DMF-solvated exogenous metal ions might act as a major kinetic

barrier. This hypothesis is supported by EDX mapping of a partially Co exchanged MOF (Error! Reference source not found.). Co is concentrated at the top and bottom along the *c* axis, while Mn is between the Co; both Co and Mn concentrations are homogenous along the *ab* plane. This suggests that the exogenous metal ion only diffuses along the *c* axis without lateral diffusion in the *ab* direction. This diffusion-limited vertical process is supported by size-exclusion experiments, where the Mn MOF is subjected to Co exchange in different dialkylformamide solvents. Metal exchange does not occur when bulkier solvents diethylformamide and dibutyl formamide are used.

These findings encouraged us to explore this vertically processible metal exchange to create surface patterns of MOFs starting with a monocrystalline thin film, as detailed in above.

### B. Synthesis and investigation of dynamically reconfigurable superlattices

Under this objective, we first report new insight into the hybridization of DNA onto NPs surfaces, important for superlattice assembly (section 1). We then enumerate our progress towards improved, direct imaging of soft materials including NPs, PAEs, and PAE-based superlattices (sections 2-4). Finally, we describe the engineering of pH-responsive transmutable NP superlattices (section 5). These advances enable the thorough characterization of crystals directed by DNA and their post-synthetic manipulation.

#### 1. DNA Hybridization on PAEs

Crystal engineering with DNA involves the hybridization of complementary strands attached to particle cores to form specific base-pair interactions. Therefore, a fundamental understanding of the thermodynamics of this process can inform the design of such materials. It is known that DNA hybridization onto PAEs is enhanced compared to that of free DNA in solution. Using isothermal titration calorimetry, we revealed that the enhancement is enthalpically dominated, as opposed to being entropically favored. Coarse-grained molecular dynamics simulations show that surface confinement prevents the DNA on PAEs from adopting less enthalpically favored conformations like those observed in solution. Moreover, experiments and simulations confirm that by reducing the DNA density on the PAE surface or at increasing distance from the NP surface, the enthalpy approaches the less favorable duplexation enthalpy for free DNA in solution. This suggests new strategies to manipulate the behavior of crystals built from PAEs (*e.g.* melting temperature) as well as elucidates key design principles in the development of new PAEs.

#### 2. Selective staining of DNA for electron microscopy imaging of PAEs

To study the DNA-mediated interactions between PAEs using electron microscopy requires a technique that can visualize the DNA shell, or even, individual strands on the PAEs. In the past year, we developed a method to selectively stain the DNA shells on soft material-based PAEs (*i.e.* PAEs with a polymer particle core) through correlative fluorescence and electron microscopy known as click electron microscopy (click-EM).[4] This method tags the molecule of interest with a selective fluorescent molecule, and then bathes the sample in diaminobenzidine (DAB). Photobleaching induces the release of singlet oxygen, which catalyzes DAB polymerization localized to the fluorescent label. In the final step, the sample is stained with osmium tetroxide which binds strongly to DAB, resulting in strongly selective staining only in the labeled structures.

We demonstrate that the DNA shell on PAEs with polymer NP cores can be selectively stained using click-EM and sequentially visualized by TEM. Polymer-core PAEs were deposited directly onto grids for TEM, and the click-EM staining procedure was performed by the transfer of the grids into droplets of solution for the appropriate step. Four conditions were imaged in high angle annular dark field (HAADF) STEM mode to determine the effectiveness of the staining procedure:

1) pristine PAEs without a staining agent; 2) PAEs stained with $OsO_4$; 3) PAEs labeled with the fluorescent tag cyanine 5 (Cy5), washed in DAB, and stained with $OsO_4$; and 4) PAEs labeled with Cy5, washed in DAB, photobleached, and stained with $OsO_4$ (the entirety of the click-EM method). All preparations and microscopy were performed at room temperature. **Error! Reference source not found.a-d** shows HAADF STEM images of polymer-core PAEs under each treatment condition. While the PAEs are visible at all conditions, only the core material is visible if the PAEs were not treated or treated with conventional $OsO_4$ staining (**Error! Reference source not found.a** and **b**). On the contrary, a ring structure around the core appears in the two samples with the DAB wash (**Error! Reference source not found.c** and **d**). Interestingly, even without intentional photobleaching, the DNA shell structure is visible. This observation may suggest that even room lighting is sufficient to enable the release of singlet oxygen and induce the

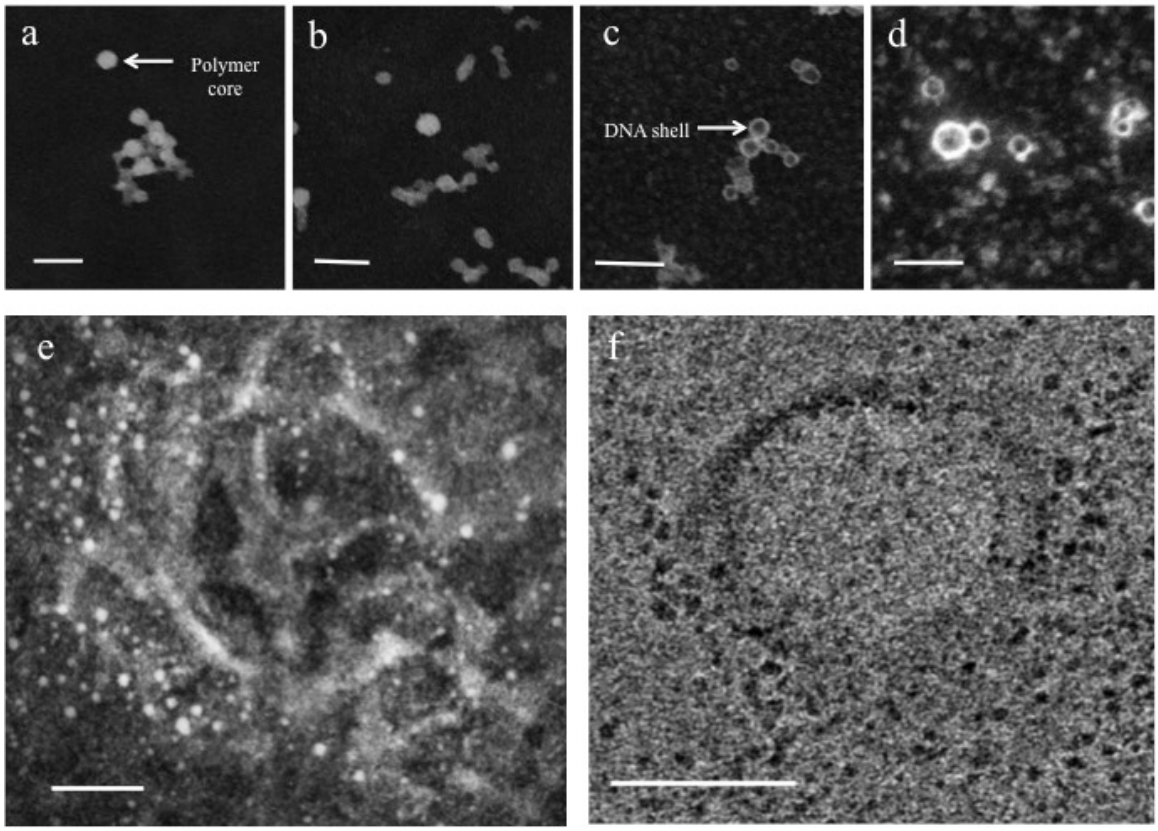


**Figure 13.** Selective staining of soft material PAEs for electron microscopy. (a-d) HAADF STEM images of Cy5-labeled polymer-core PAEs under various staining conditions: (a) no staining, (b) staining with $OsO_4$, (c) DAB wash and staining with $OsO_4$, and (d) DAB wash, photobleaching, and staining with $OsO_4$. Scale bars are 200 nm. (e, f) Magnified micrographs of individual polymer-core PAEs selectively stained using the click-EM method. Imaging conditions: (e) HAADF STEM, and (f) TEM. Scale bars are 30 nm.

polymerization of DAB on the DNA shells in the colloidal PAE samples. Taken together, these results suggest that Cy5 successfully polymerizes DAB localized to the fluorescent dye and leads to the selective staining on only DNA shells by the $OsO_4$ while the polymer core is largely intact.

Furthermore, this technique has the potential to visualize the distribution of DNA around individual PAEs, which is critical to understanding the direction-dependent interaction between anisotropic inorganic-core PAEs as well as soft material-core PAEs. **Error! Reference source not found.e** and **f** show a HAADF STEM image and a TEM image of individual polymer-core PAEs with the DNA shell selectively stained by the click-EM method. The core region has lower contrast

than the shell. Importantly, the distribution of DNA around the core can be directly mapped on single PAE level. We anticipate that the use of this imaging method will provide a fundamental understanding to the formation of DNA-assembled superlattice structures.

### 3. Beam-induced chemical reactions in liquid cell electron microscopy

Modern fluidic cell holders for (scanning) transmission electron microscopy ((S)TEM) allow for the observation of many materials in their native physiological environment. For both fluidic cell and atomic resolution imaging and characterization, electron dose and beam specimen interactions are of significant concern. Resolving such fine structures demands large current densities and high energy electrons that produce ionizing radiation leading to atomic rearrangements and bond breakage within the sample. However, studying highly beam-sensitive systems, such as DNA in aqueous solutions, is exceptionally challenging with (S)TEM fluidic cells, due to the limited diffusion length in the thin liquid layer, as well as the high acceleration voltage and high dose rate of the electron beam. (S)TEM inherently requires small volumes (on the order of femtoliters) and extremely confined geometries to enable electron transparency for fluidic cell imaging and characterization. These confined geometries and volumes restrict the uniformity within these experiments, as edge effects often dominate.

In working towards the goal of observing PAE interactions and assembly *in situ*, we designed and built a scanning electron microscopy (SEM) fluidic cell that is capable of allowing a much thicker liquid layer and operating under much lower beam voltage than in typical liquid cell (S)TEM experiments (**Error! Reference source not found.a** and **b**). The cell consists of a titanium cell substrate that is grounded to allow good electrical and thermal conductance. Fluids of interest are encapsulated between the titanium cell and a silicon nitride window and a rubber O-ring is used to seal the cell against the vacuum. To study electron beam-induced chemical reactions as a function of electron dosage, an aqueous palladium chloride was used as a model system. The reduction potential of palladium chloride to palladium in aqueous solution is +0.591 V. Under a low dose imaging condition typical for SEM imaging of soft materials (2.4E+10 $e^-/cm^2 \cdot s$), no reaction was observed. Then, we scanned an array of rectangular regions where the total dosage was varied. When the total dosage is above ~1E+14 $e^-/cm^2$, the deposited porous, palladium is distinguishable from the background in terms of the secondary electron signal (**Error! Reference source not found.c-e**). This confirms

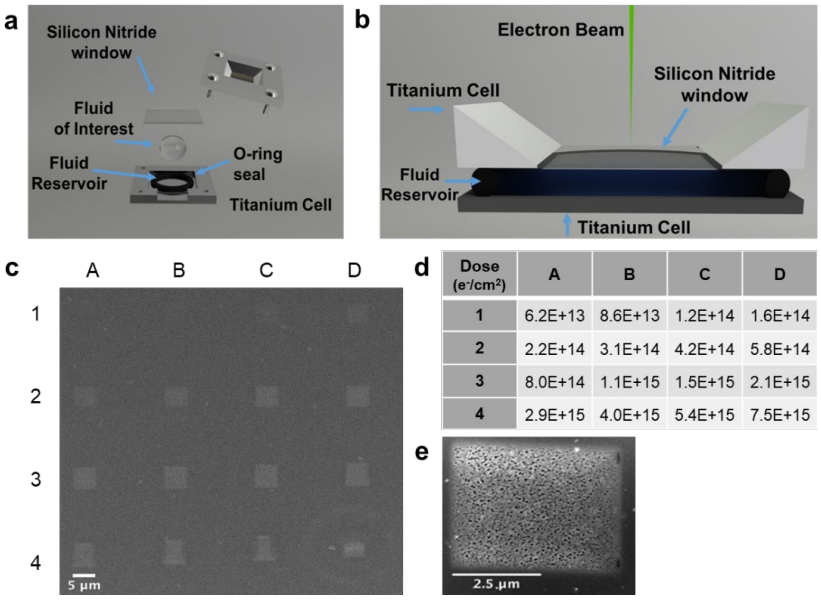


| Dose ($e^-/cm^2$) | A | B | C | D |
|---|---|---|---|---|
| 1 | 6.2E+13 | 8.6E+13 | 1.2E+14 | 1.6E+14 |
| 2 | 2.2E+14 | 3.1E+14 | 4.2E+14 | 5.8E+14 |
| 3 | 8.0E+14 | 1.1E+15 | 1.5E+15 | 2.1E+15 |
| 4 | 2.9E+15 | 4.0E+15 | 5.4E+15 | 7.5E+15 |

**Figure 14.** Beam-induced metal deposition in a custom SEM liquid cell. (a, b) Top (a) and side (b) views of the fluidic cell schematic. Fluid is deposited via pipette in the fluidic reservoir. The incident electron beam is depicted as a green arrow, electrons are transmitted through the electron transparent silicon-nitride window, and some secondary and backscatter electrons exit for imaging. (c) SEM image of $PdCl_2$ deposits at varied electron dose (provided in (d)). (e) STEM image of an individual Pd deposit.

that with the typical SEM imaging electron dose rate employed in this work, no significant reaction will be induced, therefore enabling characterization of nanostructures with minimum beam induced reaction, at least for this specific system. We coupled this fluidic cell system with a Peltier stage with precise temperature control to inspect how temperature may impact deposition. Environmental variables are being systematically explored in tandem with other properties such as electron dose level, electron dose rate, and membrane surface effects to fully characterize the deposition parameter space and understand the role dose and environmental variables may play in fluidic cell imaging and characterization of nanomaterials.

## 4. Atomic resolution imaging of MOF nanoparticles and their interfacial structures

Although the crystal structure of MOF NPs can be studied by ensemble-level characterization techniques (*e.g.* XRD) their atomic structure in real space, especially on surfaces, interfaces, and defects, is difficult to probe by local techniques that afford such information (*e.g.* electron microscopy) due to the low chemical stability and fast degradation of MOF NPs under a high energy electron beam. Direct, atomic resolution imaging of MOF NPs would not only reveal crucial structural information, but also offer insight into how their properties relate to their atomic scale imperfections which enables targeted development of MOF NPs as building blocks.

Here, aberration-corrected STEM, which can provide sub-angstrom resolution, is used to directly identify the atom columns in NU-1007 MOF nanorods[5] (**Error! Reference source not found.a**). In particular, a low dose imaging condition (~200 $e^-/Å^2$) was successfully used to investigate the interfacial structures in NU-1007 nanorods without causing significant beam damage. HAADF Z-contrast images of MOF crystals were obtained where it was possible to visualize the arrangement of pores and zirconium nodes (**Error! Reference source not found.b**). In the Z-contrast image, zirconium atom columns appear as bright dots. Fourier diffractogram analysis on a single crystalline nanorod reveal that these atom columns have orthogonal periodicities of 18 Å and 16 Å, respectively (**Error! Reference source not found.c**). These values correlate well with the zirconium node positions along the [110] zone axis.

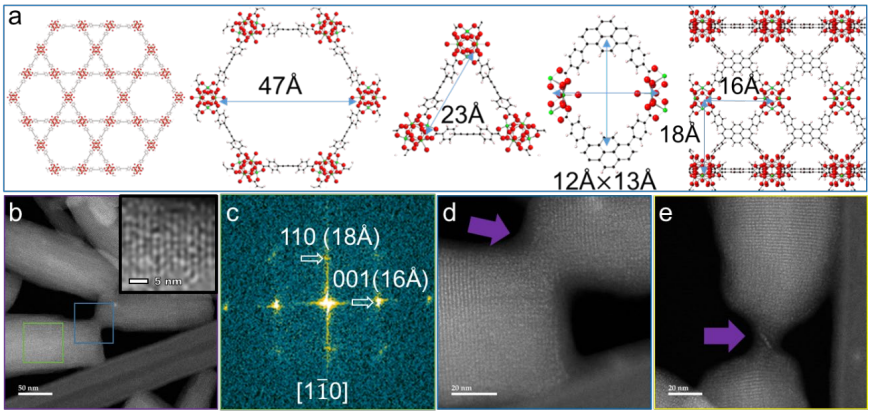


**Figure 15.** Atomic resolution imaging of crystal and interfacial structures in MOF NPs. (a) Crystal structure of the NU-1007 Zirconium MOF derived from X-ray diffraction. From left: atom packing along the [001] zone axis, hexagonal pores, triangular pores, windows between hexagonal and triangular pores, and atom packing along the [110] zone axis. (b) High-angle annular dark field (HAADF) scanning transmission electron microscopy (STEM) Z-contrast images of NU-1007 nanorods. Inset: Magnified image showing individual atom colomns. (c) Fourier diffractograms from the green box region in (b). (d, e) Two types of interfacial structures between two MOF nanorods.

Two types of interfaces between individual MOF nanorods were revealed in the Z-contrast imaging. In the first type, two nanorods whose crystal orientations are not aligned connect via a disordered region (**Error! Reference source not found.d**). Such a connection shows uniform Z-contrast, but the atom columns lose their periodicity near the interface, indicating the deformation

of the MOF lattice when two MOF NPs touch in the dried state. In the second type, significantly higher Z-contrast is observed at the interface, indicating the accumulation of zirconium atoms at the interface. Taken together, aberration-corrected HAADF STEM imaging can be configured under low dosage to reveal the atomic structure of crystalline MOF NPs and their interfacial structures despite of their high beam sensitivity.

### 5. Transmutable nanoparticle superlattices

The programmability of nucleic acids allows for the structural arrangement of inorganic NPs into complex and functional colloidal crystals with varying lattice constant, symmetry, and habit. More importantly, the DNA bonds can be dynamically tuned by applying external stimuli such as the addition of small molecules or changes in dielectric media that can lead to reconfiguration of the crystal structure or crystallization trajectories of PAEs.

However, most manipulation methods are time-consuming and create waste products that require repeated washing steps. pH (*i.e.* proton environment) is one of the most widely used stimulus to trigger structural changes in materials, but it has yet to be explored in the context of DNA-mediated crystal engineering strategies. We report the synthesis and characterization of pH-responsive NP superlattices with tunable lattice size or symmetry by incorporating i-motif structures into the DNA bonds (Error! Reference source not found.**a**). An i-motif is a cytosine-rich DNA strand that undergoes reversible conformational change between a quadruplex (acidic condition) and a single stranded state (basic condition) upon pH change. We demonstrate that the pH-driven molecular motion of an i-motif can be translated into a controllable change in the DNA bond length, inducing a lattice expansion or contraction (Error! Reference source not found.**b**). Alternatively, we construct pH-responsive NP superlattices where the folding and unfolding of an i-motif can be used to induce a change in crystal symmetry between fcc and bcc crystal structures via "bond breaking" and "bond forming" processes (Error! Reference source not found.**c**). As such, the synthesis of pH-responsive NP superlattices with tunable DNA bonds marks a significant step toward the preparation of "smart materials" that can be dynamically manipulated on-demand.

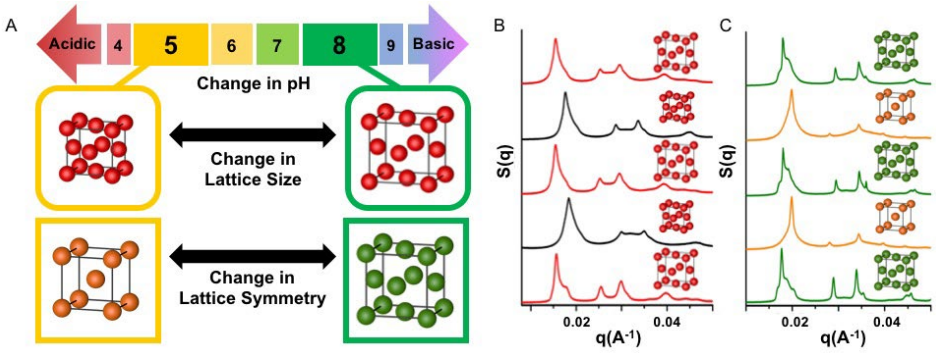


**Figure 16.** (A) Scheme showing pH-responsive NP superlattices with tunable lattice size or symmetry. (B) SAXS data show the formation of *fcc* crystals upon assembly of pH-responsive colloidal crystals, which can be reversibly toggled between contracted and expanded states upon pH change. (C) SAXS data show the crystal symmetry of NP superlattices can be switched between *fcc* and *bcc* crystal structures upon pH change.

### C. Synthesis and investigation of structurally sophisticated and functional superlattices

Under this objective, we report progress on developing structurally sophisticated superlattices, including those with controlled crystals habits (section 1) and structurally tunable MOF-based compositions (section 2). Subsequently, we show that the assembly of plasmonic NPs into superlattices leads to emergent optical properties (section 3), demonstrating the significance of this

approach.

## 6. Superlattices with controlled crystal habits

An ongoing effort in the Mirkin group has been to develop methods to better control the microscale forms of crystals engineered with DNA. In particular, contrary to the well-defined design rules for nanoscale lattice structures, few rules have been developed to control the size of and limit defect formation in single crystals built from PAEs. Such inconsistency in the microscale geometry is one of the biggest challenges that must be overcome for colloidal single crystals to be used for future applications in the fields of optics and optoelectronics.

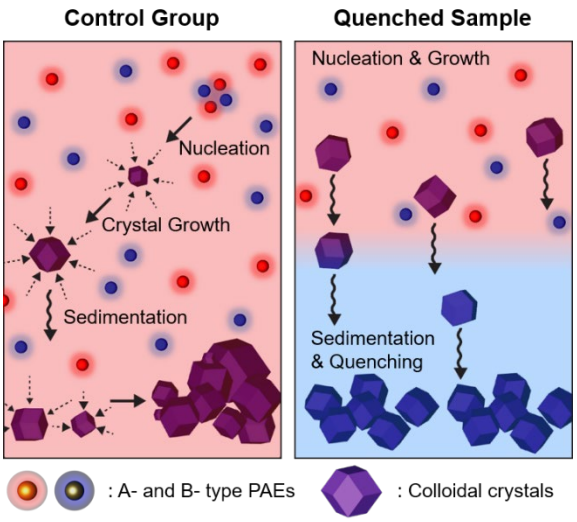


**Figure 17.** Schematics illustrating (left) the conventional PAE crystallization processes and (right) the quenching method.

To overcome this limitation, we were inspired by methods used in biology where layers of aqueous solutions with various density are prepared for separation purposes, and thus we designed a multi-layered crystallization bath for enhanced size and shape uniformity (Error! Reference source not found.). In this method, a sublayer of greater density and viscosity was placed underneath the crystal growth solution. This sublayer excludes the free particles from diffusing across the density barrier, whereas the microcrystals are able to sediment through and are collected at the bottom of the sublayer. With this system, two major contributors to size and shape dispersity, overgrowth and coalescence, are suppressed. As microcrystals enter the sublayer, their growth is quenched as they are separated from free PAEs. Additionally, the high viscosity of the sublayer retards the kinetic movement of the colloidal crystals minimizing inter-crystal aggregation, or coalescence, which result in discrete, well-shaped rhombic dodecahedra microcrystals.

During colloidal crystallization, the free PAEs are colloidally stable in the growth solution. Upon their nucleation and growth, there is a certain size of microcrystal, where the gravitational potential becomes greater than the stabilizing Brownian motion. Assuming spherical shapes, this competitive

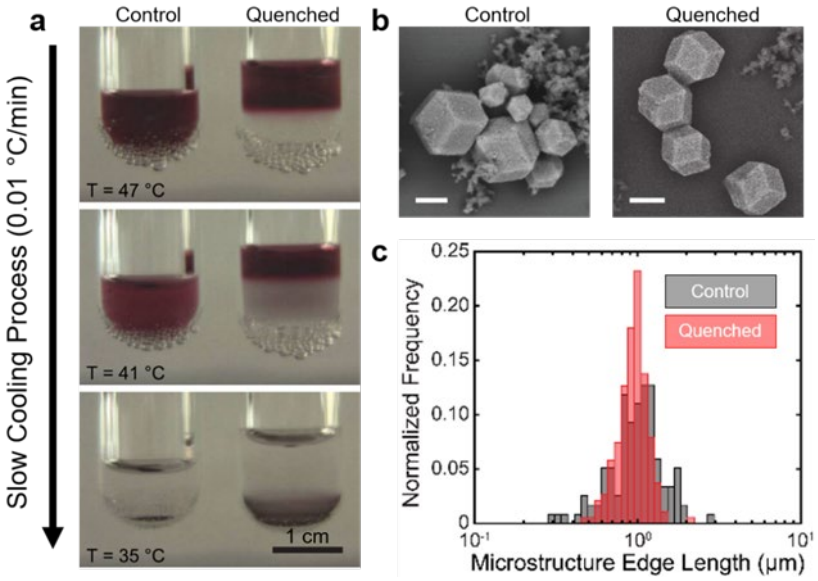


**Figure 18.** The optical images at different stages of the crystallization process for the control (left) and quenched samples (right). (b) Representative SEM images. Scale bar is 1 μm. (c) Plot of the size distribution shows the quenching layer improves the uniformity of the microcrystals.

effect between sedimentation and colloidal stability can be expressed as dimensionless Peclet number, by which the critical size of sedimentation is solved as a function of the temperature and density difference between the material and solvent. Since the crystallization temperature and the density of microcrystals are constant within a given PAE superlattice system (core particle and DNA linker), uniform sizes of microcrystals are expected.

Experiments were carried out to verify this hypothesis. An aqueous solution of sodium dextran sulfate (negatively charged polysaccharide) was found to be an effective sublayer. A test tube with sodium dextran sulfate solution was placed in a water bath equipped with a precise immersion circulator, and then the PAE growth solution was slowly layered on top of the solution. An identical growth solution without the sublayer was prepared as a control. In the layered system, the free PAEs, visibly identified as red, did not penetrate the density barrier throughout the crystallization process, while the microcrystals sedimented through the sublayer forming a dark grey suspension (Error! Reference source not found.**a**). The resulting crystals were collected and embedded in silica, and their size and shape were analyzed by SEM (Error! Reference source not found.**b**). While the mean edge lengths of the microcrystals did not change significantly, the polydispersity was greatly improved ($1.04 \pm 0.38$ μm (118 counts) → $0.95 \pm 0.20$ μm (189 counts), Error! Reference source not found.**c**). A significant enhancement in the shape uniformity (42% (114 counts) → 83% (181 counts) of well-formed rhombic dodecahedra crystals) was observed. This method is a simple and reproducible method for narrowing size distribution and improving shape uniformity and may be generalizable for many colloidal crystallization processes.

## 7. Assembly of 2D and 3D MOF superlattices

Following the synthetic advances discussed in Section A3-6, the ability of MOF PAEs to form crystalline, hybrid superlattices with metal core PAEs was evaluated. Previously established design rules predict that complementary DNA functionalized PAEs composed of different core NPs will assemble into CsCl-type ($Pm\bar{3}m$) lattices. However, because the scattering cross-sections of MOFs are negligible relative to Au NPs, MOF–Au binary lattices produce scattering patterns that are dependent solely on the arrangement of AuNPs within the lattice. Indeed, when 37 nm UiO-66 MOF PAEs were combined in a 1:1 ratio with complementary 20 nm Au PAEs, the resulting CsCl-type lattices (lattice constant = 79.6 nm) produced simple cubic (sc, $Pm\bar{3}m$) scattering patterns, with $AlB_2$-type impurities (sh, P6/mmm: lattice constant, a = b = 76.5 nm, c = 47.6 nm) which produced simple hexagonal scattering patterns (**Error! Reference source not found.a**). In a second example, 37 nm MOF PAEs were combined in a 1:1 ratio with complementary 40 nm Au PAEs and the resulting CsCl-type lattices (lattice constant = 88.2 nm) produced simple cubic scattering patterns (**Error! Reference source not found.b**). To directly probe crystal formation by polyvalent DNA hybridization, *in situ* SAXS measurements were performed by gradually heating disordered MOF-Au aggregates until crystalline order was observed (**Error! Reference source not found.c**). Crystal morphologies were investigated by STEM of silica-embedded crystals (binary 37 nm UiO-66 – 40 nm Au NP system) where uniform single crystals 1 - 2 μm in each dimension were observed (**Error! Reference source not found.d**). The binary MOF–Au PAE crystals displayed clear facets, consistent with rhombic dodecahedra shaped single crystals formed by other PAEs (**Figure 2e,f**).

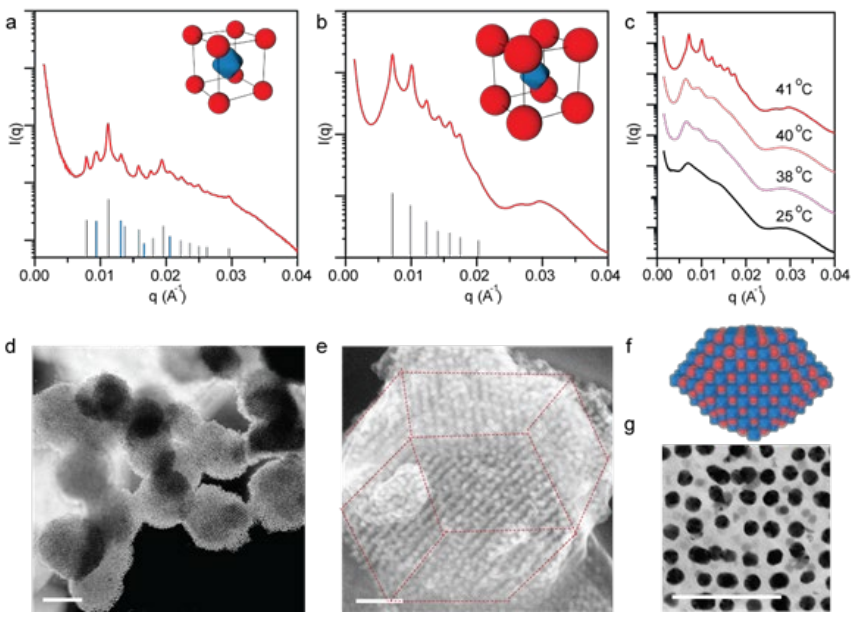


**Figure 19.** Binary superlattices assembled from MOF and Au PAEs. SAXS data for CsCl lattices formed by 37 nm UiO-66 with (a) 20 nm and (b) 40 nm AuNP. Experimental data are shown in red and predicted patterns are shown in grey (impurity phase shown in blue). (c) *in situ* SAXS data of annealing MOF-Au aggregates show a transition from the amorphous state into crystalline state. STEM characterization of single crystal superlattice: (d) low magnification HAADF, (e) high magnification secondary electron mode image, and (g) high magnification TEM of the UiO-66 and 40 nm AuNP superlattices showing the uniform formation of the expected rhombic dodecahedron crystal habit (f). Scale bars: 1 μm for (d) and 100 nm for (e) and (g).

Furthermore, an attractive property of MOF PAEs relies on their structural tunability. Depending on the synthetic conditions and choice of precursors, the intrinsic crystal symmetries of MOFs can be leveraged to synthesise anisotropic particle shapes, thus enriching the structural programmability of the colloidal crystals. Here, we used self-complementary DNA linkers to assemble rod-shape PCN-222 NPs with a diameter of 37 ± 8 nm, and length of 159 ± 25 nm (AR = 4.3, Error! Reference source not found.**a-c**). Upon annealing with self-complementary linkers, SAXS data suggest the resulting superlattices possessed hexagonal symmetry with an interparticle distance of ~ 52 nm (Error! Reference source not found.**d**). Cryo-TEM reveals that the PCN-222 PAEs align parallel to each other and form close-packed 2D sheets (including single and multiple layers; Error! Reference source not found.**e,f**), a favorable arrangement that maximizes DNA hybridization interactions.

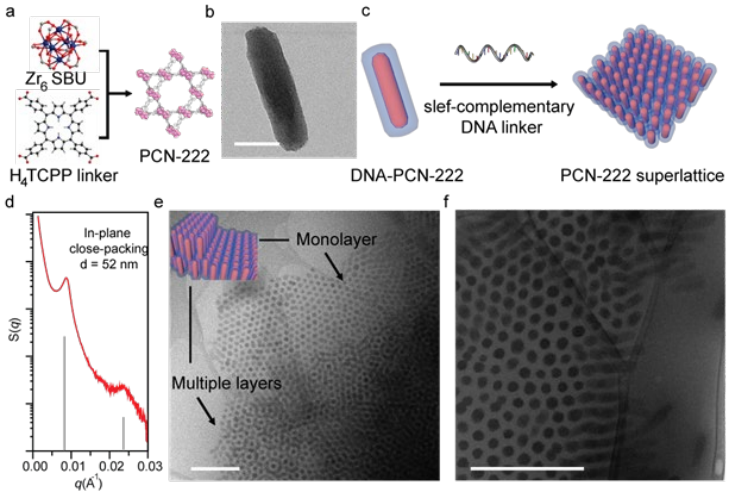


**Figure 20.** (a) Schematic of PCN-222 nanorod constructed from $Zr_6$ SBU and tetrakis(4-carboxyphenyl)porphyrin. (b) TEM image of a single PCN-222 nanorod. (c) Schematic of DNA mediated assembly of PCN-222 PAEs into 2D superlattice sheets. (d) SAXS data of PCN-222 superlattice showing in plane close packing behavior (interparticle spacing d = 52 nm) with no long range out-of-plane ordering. (e - f) Cryo-TEM images of PCN-222 superlattices. Scale bars: 100 nm for (b) and 500 nm for (e-f).

## 8. Emergent optical phenomena in nanoparticle superlattices

Crystal engineering with DNA affords the opportunity to design novel photonic crystals (PCs) and to study their emergent properties. PCs have been widely studied due to their broad technological applications in lasers, sensors, optical telecommunications, and display devices. Typically, PCs are periodic structures of *touching* dielectric materials with alternating high and low refractive indices, and to date, the variables of interest have focused primarily on crystal symmetry and the refractive indices of the constituent materials, primarily polymers and semiconductors. Using DNA-mediated crystallization, additional variables (*e.g.* interparticle distance) can act as design parameters to tune the properties of PCs.

Finite-difference time-domain (FDTD) simulations suggest that plasmonic NP superlattices offer a promising new route to PCs due to the controllable spacing of the NPs via spacer groups and the high refractive index of the lattices. Herein, we investigate the photonic properties of these lattices by fixing the light incidence to one direction and characterizing the features of the stopband in the reflectance spectra. Due to the use of spacer groups, we found that the 3D lattice, when viewed from any direction, can be considered as 1D stack of alternating layers of high- and low-refractive indices, where the high-index layer consists of NPs (the NP layer) and the low-index layer consists of only the dielectric medium (Error! Reference source not found.**a**). This simplification extends to the design process, where instead of considering a multitude of lattice parameters, the stopband features of 1D PCs are dictated by the periodicity, index contrast, and the total number of layers of the periodic structure. By investigating experimentally accessible lattice structures composed of spherical Au NPs (diameter 108 nm, unless otherwise specified) embedded in a silica matrix with a refractive index of 1.46, we derived a set of design rules. To minimize computational time and keep the simulations tractable, we found that 7 layers of NPs

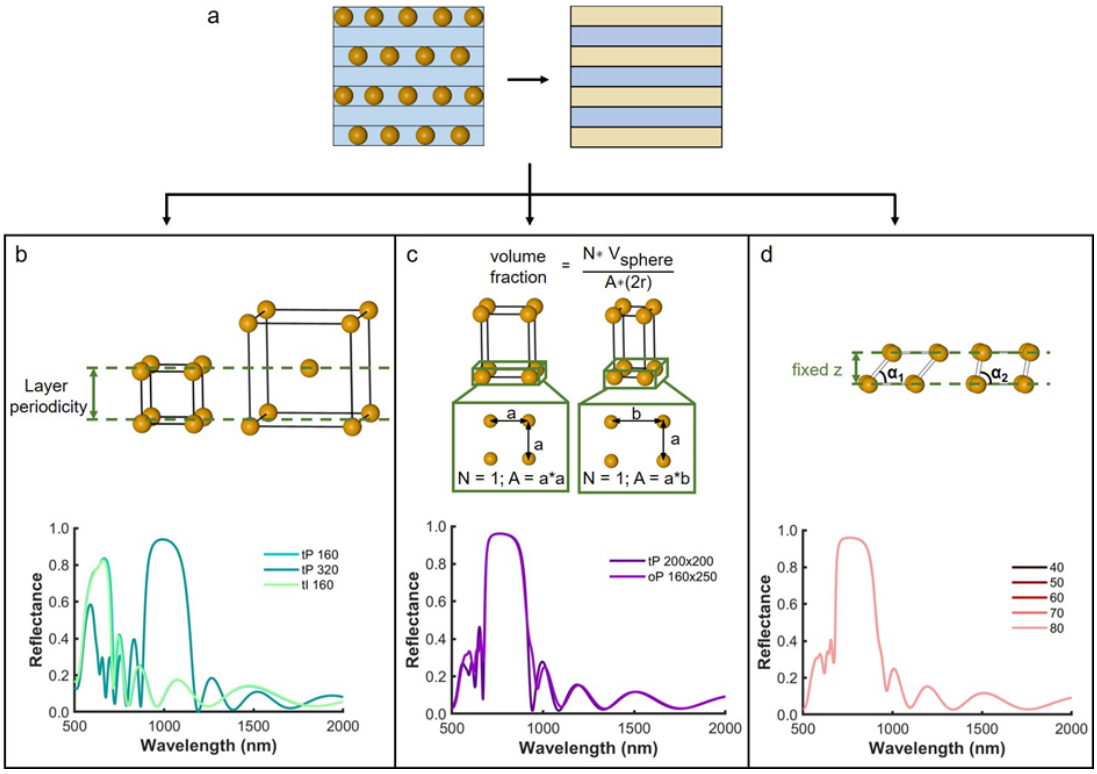


**Figure 21.** (a) Schematic showing that a 3D NP lattice can be considered a 1D structure with alternating high- and low-refractive indices along the light propagation direction. (b) Layer periodicity is defined by the distance between two adjacent layers that contain NPs (top). The spectra of tP (tP 160) and tI (tI 160) lattices with the same in-plane lattice constants (200 nm * 200 nm) and layer periodicity (160 nm) overlap as compared to spectrum with the same lattice constant c in the z direction (tP 320 and tI 160, c = 320 nm). (c) The volume fraction of each NP layer is defined by the equation. N indicates the number of NPs in each unit cell, 2r is the diameter of the NP and the thickness of the NP layer, $V_{sphere}$ is the volume of the NP, and A is the area of each unit cell (tP and oP on the left and right, respectively). The reflectance spectra of the tP and oP lattices overlap as they have the same layer periodicity and volume fraction. (d) The registry of NPs between different layers can be changed in a mP lattice by changing the lattice constant c and the angle α in such a way that the in-plane lattice constants (a and b) and the layer periodicity is not changed. The reflectance spectra of mP lattices with fixed in-plane lattice constants (a = 250 nm and b = 160 nm) and layer periodicity (240 nm), but varying α overlap completely.

are sufficient to represent thin plasmonic PCs films. Additionally, we used a normal incidence of light (z-direction) onto the (001) plane (x-y plane) of the lattice.

Investigating the stopband features of 13 of the 14 Bravais lattices, three design principles were discovered. First, layer periodicity, as compared to the lattice constant along the light propagation direction, dictates the location of the photonic stopband. In other words, a single body-centered or face-centered unit cell has three layers (top, middle, bottom), and the periodicity of each NP layer (layer periodicity) in the z-direction is half of the lattice constant (Error! Reference source not found.**b**). For example, Error! Reference source not found.**b** shows the reflectance spectrum of a body-centered-tetragonal (tI) lattice with 160 nm layer periodicity (lattice constant in the z-direction, $c$ = 320 nm) overlaps almost completely with that of the tetragonal (tP) lattice with 160 nm layer periodicity ($c$ = 160 nm) and is drastically different from a tP lattice with 320 nm layer periodicity ($c$ = 320 nm).

Second, the volume fraction of each NP layer dictates the bandwidth, regardless of the exact NP arrangement. The volume fraction of a NP layer is simply the volume of all the NPs in one unit cell divided by the total volume of the unit cell, where the thickness of the unit cell is considered the diameter of the NP (Error! Reference source not found.**c**). For example, for a tP and an orthorhombic (oP) lattice with the same layer periodicity but different lattice constants in the x-y plane (tP: $a$ = 200 nm, $b$ = 200 nm; oP: $a$ = 250 nm, $b$ = 160 nm) the spectra overlap almost perfectly since the volume fraction of the NP layer is the same.

Lastly, the registry between different NP layers does not affect the stopband properties. This was probed by studying monolithic (mP) lattices, where all three lattice constants and the angle can be independently controlled. When the $a$ and $b$ are fixed and $c$ is changed such that the layer periodicity remains constant when varying the angle, the reflectance spectra overlap completely (Error! Reference source not found.**d**). This proves the key concept that the stopband properties are governed by two structural parameters, the layer periodicity and volume fraction of each NP layer and are minimally affected by the exact arrangement of the NPs.

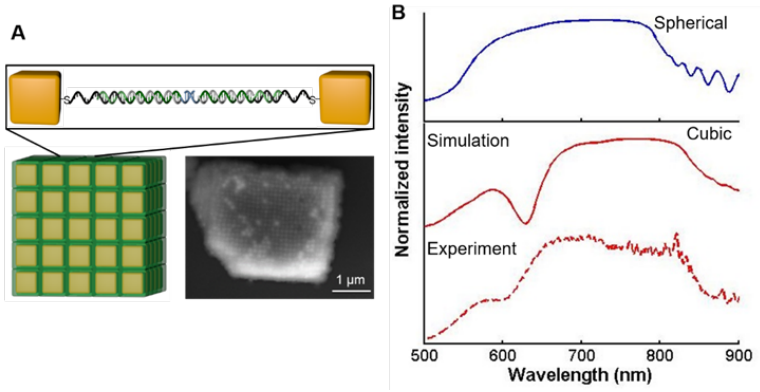


**Figure 22.** Experimental measurement and FDTD simulations of cubic NP superlattices. (A) Schematic (bottom-left) and SEM (bottom-right) image of a superlattice made through DNA-mediated assembly of nanocubes, after encasing in silica. The Au nanocubes have an 88 nm edge length and a 5 nm corner rounding. The lattice constant of the superlattice is 134 nm and defined by the duplex DNA interconnects An enlarged view of one hybridized DNA-pair between nearest neighbor nanocubes in a lattice is shown in the top image. (B) Top: simulation of a simple cubic superlattice with spherical NPs with the same lattice constant and volume fraction as the superlattice shown in the (A). Bottom: simulation and experimental data for the superlattice in (A).

The design rules found in 1D for PCs can be applied in any direction for a 3D PC. We used crystal engineering with DNA to prepared 3D PCs as this method provides sub-nm tunability over particle spacing. Moreover, interparticle spacing can be dynamically tuned after PC formation, enabling dynamic tuning of the stopband location. As a proof-of-concept, micron-sized simple cubic superlattices with well-faceted cubic crystal habits were made from DNA-functionalized cubic Ag NPs (88 ± 4 nm edge length and 5 ± 1 nm corner rounding, lattice constant: 134 nm, **Figure 22a**). The cubic crystal habit facilitates the

alignment of the microcrystal with its (001) facet facing up. Simulation results for a superlattice of spherical NPs with the same volume and lattice constants show the existence of a broad stopband (Error! Reference source not found.**b**, top), a property that is observed both experimentally and through simulation for the cubic NP superlattice (Error! Reference source not found.**b**, bottom). The experimentally observed stopband matches the simulation prediction, thus emphasizing that the design rules articulated above are not limited to spherical NPs. Although only a cP lattice was studied experimentally, other lattice structures have been made through DNA-programmable assembly. For lattices with symmetries that do not belong to the cubic lattice system, one can obtain different stopband properties using different crystal orientations of the same superlattice.

### D. Assembly of reconfigurable, sophisticated, and functional superlattices on surfaces

Under this objective, we report the progress on surface assembly of NPs through the use DNA ligands. In section 1, we report a comparative study of epitaxially grown films of NPs vs atoms. In section 2, we describe the rules to grow superlattices on a surface via template-confined DNA-mediated NP assembly which provide insight for the development of functional materials in sections 3 and 5. Section 3 reveals size-selective NP assembly can be used for multiplexed surface encoding. In section 4, we demonstrate that patterning of surface DNA-density, as opposed to confinement within a template, can act as an additional variable to direct surface-based assembly. Lastly, section 5 shows that dynamic modulation of the inter-NP and NP-substrate DNA-bond can be used to create tunable metasurfaces for light guiding.

### 9. Fabrication of surface templates with well-defined DNA binding sites

The synthesis of multilayer single crystals of defined size on a surface remained a challenge until recently.[6] In the cited work, single crystalline, multilayer thin films were synthesized over 500 × 500 $\mu m^2$ areas on lithographically patterned templates under equilibrium conditions. Importantly, these superlattices follow the same patterns of crystal growth demonstrated in atomic thin film deposition, allowing these processes to be understood in the context of well-studied atomic epitaxy and enabling a nanoscale model to study fundamental crystallization processes. In atomic thin films, however, lattice mismatch during heteroepitaxy leads to an accumulation of strain energy, generally causing the films to irreversibly deform and generate defects. In contrast, more elastically malleable building blocks, such as DNA-modified NPs should be better able to accommodate this mismatch and the resulting strain.

Herein, PAEs were used to grow heteroepitaxial colloidal thin films with intentional lattice mismatch. In particular, 20 nm spherical Au NPs were functionalized with one of two oligonucleotide sequences bound to linker strands with complementary “sticky ends”. This binary system was assembled into *bcc* crystals with an equilibrium lattice parameter of 65 nm. Arrays of gold dots commensurate in size with the PAEs were deposited on a silicon wafer in a pattern mimicking the (001) plane of the targeted *bcc* superlattice using electron beam lithography. Once the dots were functionalized with one of the DNA strands and linkers, PAEs functionalized with the complementary sequence could bind and form a monolayer on the patterned array. Previous studies found that PAEs bind to the dot array in the manner that maximizes the number of DNA linkages. In this case, the PAEs were driven to sit in the center of four dots, epitaxially continuing the patterned crystal plane (*i.e.*, formation of the (002) plane). This process was carried out in a layer-by-layer fashion to assemble multiple layers on each template.

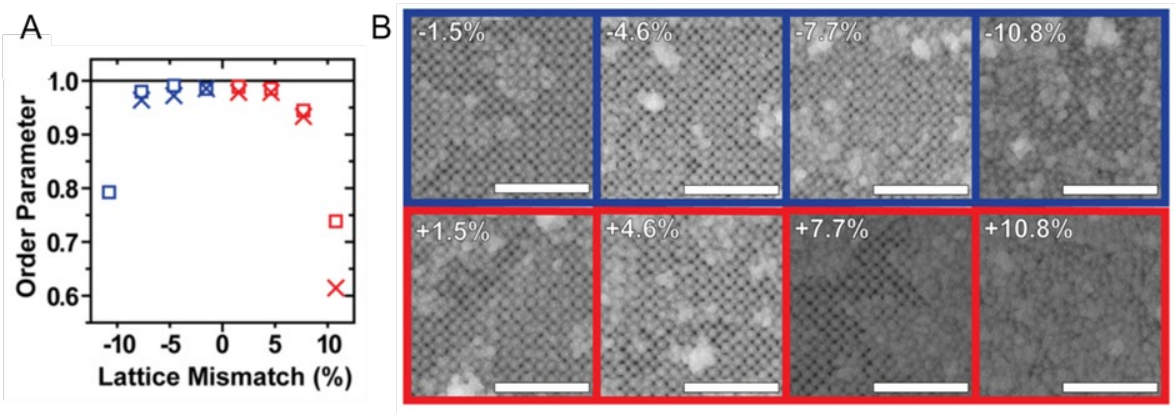


**Figure 24.** PAE thin films maintain coherency with the patterned crystallography up to ±7.7% lattice mismatch. (A) Order parameter, calculated by comparing the integrated intensity of the (110) spot to the intensity of the amorphous ring, as a function of lattice mismatch. (B) Representative SEM image of the thin film surface.

To study heteroepitaxy and the impact of lattice mismatch, arrays were fabricated with different lattice parameters other than the ideal bulk PAE superlattice (up to ±10.8% lattice mismatch). The thin films were embedded in silica and the structure of each was determined by SAXS, as well as focused ion beam (FIB) cross sectioning followed by SEM. The degree of ordering of the sample (i.e. order parameter) was measured by comparing the integrated SAXS intensity of a diffraction spot to the relative integrated intensity of the diffuse ring over the same q-range. **Error! Reference source not found.** shows the order parameter of lattices with compressive and tensile strain up to ±10.8% lattice mismatch. Consistent with both the hypotheses and the calculations of interaction potentials, all samples exhibit a reasonably high degree of order, even the cases of ±10.8% lattice mismatch. Within ±7.7%, the thin films exhibit near perfect ordering, matching the analytical model. This is in stark comparison to atomic thin film heteroepitaxy, which rarely remains epitaxial and coherent above ±1% lattice mismatch. Moreover, we show that the tensile samples have a much higher degree of translational freedom. The significant difference between translational freedom in the negative versus positive mismatch cases is visually apparent by observing the [001] vectors moving in the z-direction in the representative FIB cross sections for ±7.7% samples (**Error! Reference source not found.**). Similar to atomic materials under tensile strain, the PAE films under positive lattice mismatch show signs of "micro-tears" (gaps) where void space within the structure is a result of PAEs locally breaking bonds in the same direction. The fact that these gaps are not observed in the negative mismatch samples indicates that the PAEs' "soft" coronae can be compressed with the addition of strain but not as readily stretched. This work illustrates additional design considerations to enable the growth of single crystal lattices

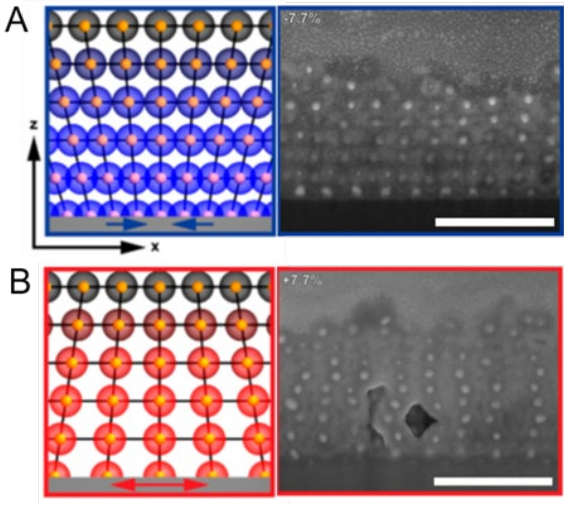


**Figure 23.** Plastic alleviation of strain in PAE thin films in the presence of high strain. The higher frequency of random, lateral deviations in x,y-planes under large negative mismatch (A) versus large positive mismatch (B) was verified visually from the FIB cross sections. Scale bars are 250 nm.

on surfaces for use within device architectures.

## 10. Design rules for template-confined DNA-mediated nanoparticle assembly

We recently showed that a wide variety of structures not attainable through conventional top-down lithographic methods could be made using a combination of top-down lithographic and bottom-up DNA-programmable assembly, thereby establishing a platform for the metamaterial community to consider a more diverse set of architectures to discover, design, and realize unusual NP-based materials with desirable properties.[7]

The design and synthesis of these new colloidal NP surface architectures will benefit from an improved understanding of the fundamental diffusion and adsorption behaviors of NPs on surfaces and in confined environments. The behavior of NPs is strongly governed by Brownian motion; hence tracking individual NP interactions with a surface covered by a porous template is experimentally challenging. Given the difficulty of studying such interactions *in-situ*, we used template-confined, DNA-mediated assembly technique to investigate NP adsorption thermodynamics and kinetics. This technique involves using Electron Beam Lithography (EBL) to fabricate 1D pore channels at fixed positions in a PMMA polymer thin film on a gold-coated silicon substrate with a specific DNA sequence covalently attached to the

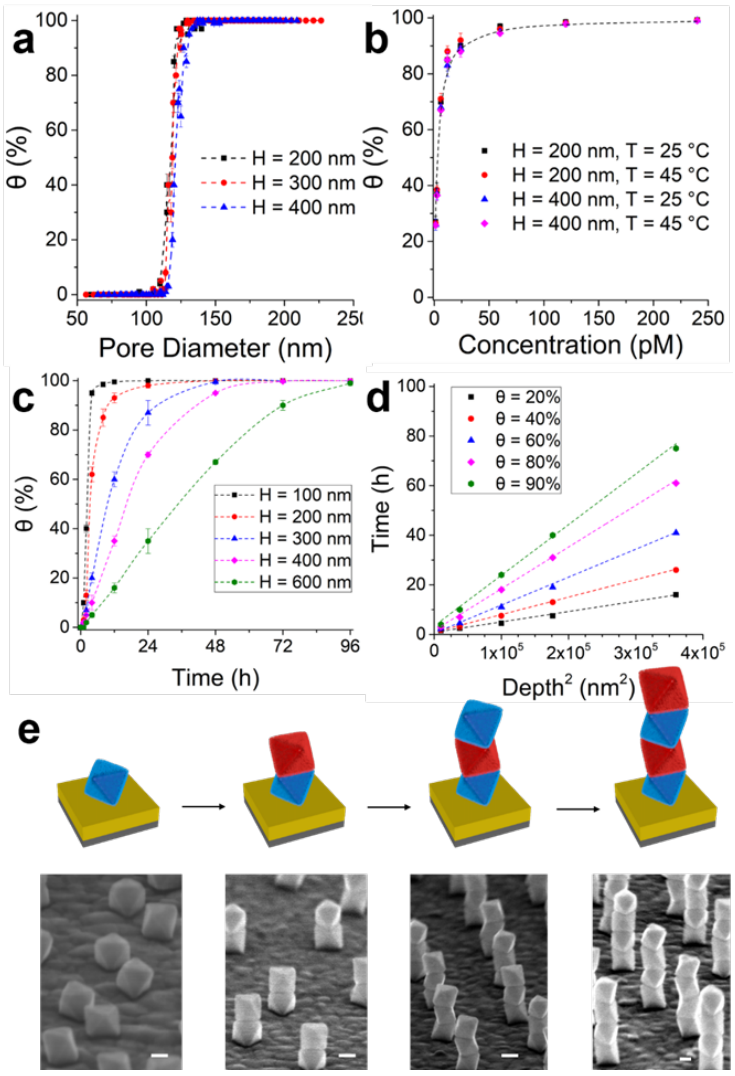


**Figure 25.** (a) Assembly yield as a function of pore size. Spherical NPs (diameter = 80 nm, concentration = 150 pM) were adsorbed in nanopores (depth = 200, 300, and 400 nm) at a temperature of 25 °C for > 96 h. (b) Assembly yield as a function of NP concentration. Spherical NPs (diameter = 80 nm) were adsorbed in nanopores (diameter = 140 nm, depth = 200 and 400 nm) at a temperature of 25 °C and 45°C for > 96 h. (c) Assembly yield as a function of assembly time. Spherical NPs (diameter = 80 nm, concentration = 150 pM) were adsorbed in nanopores (diameter = 140 nm, depth = 100, 200, 300, 400, and 600 nm) at 25 °C for varying time. (d) The time required to reach 20%, 40%, 60%, 80%, and 90% yields is plotted as a function of the square of pore depth. (e) Template-confined vertical assembly of one-, two-, three-, and four-layer architectures of octahedral NPs. Guided by PMMA nanopores (diameter = 165 nm, depth = 400 nm), octahedral NPs (edge length = 80 nm) are assembled layer-by-layer through DNA-mediated assembly. NP architectures show good facet registry, which leads to highly stable structures. Different colors represent octahedral NPs capped with different DNA sequences, where blue is complementary to red. Scale bars: 50 nm**.** Each data point represents an average of two independent experiments, with an error bar as the standard deviation.

exposed gold at the base of each pore.

Through a statistical investigation the relationships between adsorption yield and NP size, NP concentration, pore size, pore depth, temperature, and time, valuable insights into thermodynamic and kinetic considertations of colloidal NP assembly were elucidated as the following design rules:
***Rule 1*:** The relationship between adsorption yield in pores and NP concentration at equilibrium can be described by the Langmuir adsorption equation, where $\theta = \frac{K_L c}{1+K_L c}$ ($\theta$: adsorption yield; $K_L$: Langmuir constant; $c$: NP concentration).
***Rule 2*:** The relationship between assembly time and pore depth at fixed adsorption yield follows Fick's Law, where $t \propto H^2$ ($t$: assembly time; $H$: pore depth).
***Rule 3*:** To maximize NP adsorption, the pore radius should be ≥1.4 times the hydrodynamic radius of the adsornbing NPs.
***Rule 4*:** For pseudo-spherical anisotropic NPs (*e.g.* cubes and octahedra), the size can be approximated based upon the diameter of the smallest sphere required to circumscribe such NPs.
***Rule 5:*** Equilibrium adsorption yield is independent of pore depth.

As a proof-of-concept, we showed how the fundamental relationships elucidated in this work can be leveraged to synthesize sophisticated nanostructures with a high degree of structural control. Specifically, we targeted the assembly of four-layer NP architectures composed of gold octahedra (**Error! Reference source not found.**).

**11. DNA-mediated size-selective nanoparticle assembly for multiplexed surface encoding**

Due to their small size, nanomaterials provide a pathway to design high-resolution, high-density multiplexed platforms for high-security encoding. Realization of this vision, however, necessitates new synthetic techniques to enable multiple sizes, shapes, and/or compositions of colloidal NPs to be assembled on surfaces with individual particle control. The template-confined DNA-mediated NP assembly strategy provides an ideal platform for encoding patterned information using the specific absorption wavelength induced by the gap between the NP and substrate. To achieve such goal, we leverage template-confined, DNA-mediated NP assembly to position two different sizes of gold nanocubes on gold surfaces with precisely defined locations for each particle. (Error! Reference source not found.**a**) Importantly, since different size cubes give rise to different absorption spectra when positioned a fixed distance above a gold film, this size-selective assembly approach can be used for multiplexed surface encoding applications.

To experimentally evaluate the size-selective assembly of nanocubes, single crystalline Au cubes with an average edge length of 86 ± 3 and 63 ± 2 nm were synthesized and functionalized with thiolated DNA. The optimal pore diameters for each size of cube are 200 and 130 nm, respectively (Error! Reference source not found. **b,c**). For the encoded surfaces reported here, the presence of a nanocube at a specific position on the gold surface will determine whether or not significant light is absorbed at the gap mode resonance wavelength, effectively serving as a bit of information. Since the resonance wavelength depends on the edge length of the cube at a constant gap length of 10 nm (Error! Reference source not found.**d**), the assembly of multiple sizes of cubes on a substrate allows for multiplexed surface encoding at multiple resonance wavelengths.

To confirm that these pixels encode the surface at multiple wavelengths, FDTD simulations were performed to test the strength of coupling between two gap modes in close proximity to each other. Error! Reference source not found.**e,f** shows the simulated field profile of the sample along the cross-section plane within the gap at λ = 773 nm (Error! Reference source not found.**e**) and λ = 687 nm (Error! Reference source not found.**f**), when both 86 and 63 nm cubes are on the gold surface. The absorption at the two gap mode resonance wavelengths displays a large contrast

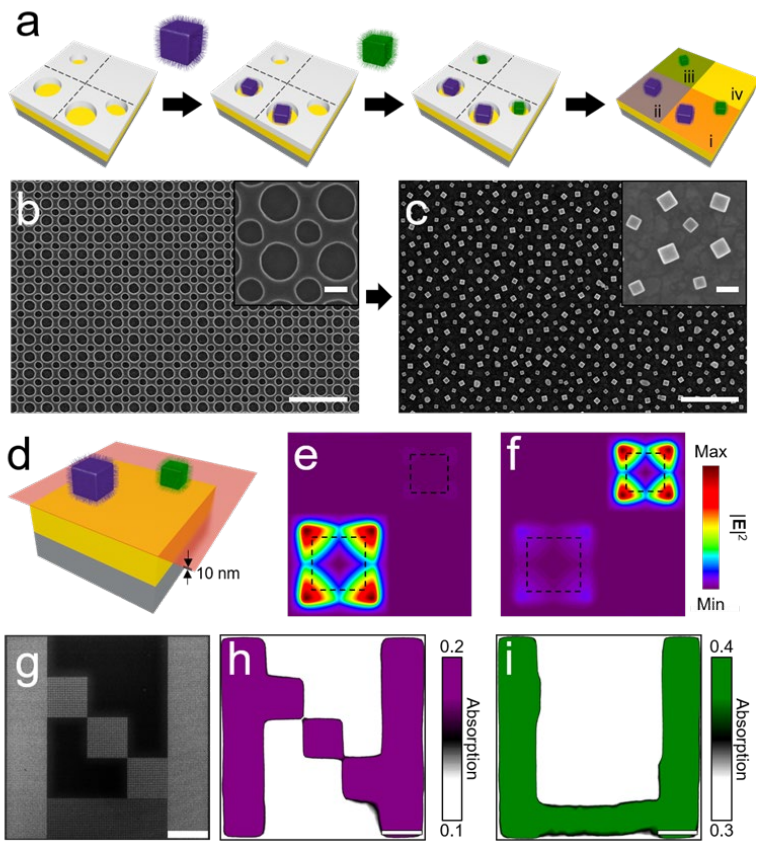


**Figure 26.** (a) Scheme showing the stepwise, DNA-mediated, size-selective NP assembly. Two different diameter polymer pores were used to assemble large (purple) and small (green) cubes into four types of encoding pixels on the surface. (b-c) SEM images of an array cubes with 63 and 86 nm edge lengths assembled in the polymer template shown in b. The scale bars are 1 μm for the large images and 100 nm for the insets. (d) Scheme of an encoding pixel that contains two different size cubes with a cross-section plane within the gap (gap plane with a thickness of 10 nm highlighted in red). (e-f) Simulated electric field profile of the sample along the cross-section plain at (g) $\lambda = 773$ nm and (h) $\lambda = 687$ nm. (g) SEM image showing a surface encoded with two sizes of cubes. (h-i) Absorption intensity maps of the surface at (h) $\lambda = 773$ nm showing the image of letter 'N' formed by cubes with 86 nm edge lengths and (i) $\lambda = 687$ nm showing the image of letter 'U' formed by cubes with 63 nm edge lengths. All arrays have a periodicity of 300 nm. Scale bars are 10 μm.

whether the cube is on or off the surface, making it possible to use absorption intensity to decode surface patterns.

As a proof-of-concept example, we designed a surface pattern with two images encrypted (Error! Reference source not found.**g**). Cubes with 86 nm in edge length were arranged to form the letter 'N', while cubes with 63 nm in edge length are arranged into the letter 'U'. SEM confirmed that NPs were assembled in high yield over all areas. Using a 2 by 2 $\mu m^2$ mapping pixel, the absorption spectrum of the surface was measured with an inverted optical microscope. Error! Reference source not found.**h** and **i** show that by comparing the absorption intensity of the surface at different wavelengths, both images in the pattern could be decoded.

### 12. High resolution DNA density patterning for reconfigurable assembly

The 2D assembly of NPs on DNA-functionalized landing sites has typically relied on lithographically defined posts or templates to achieve site-specific positioning. These surfaces enable control of NP assembly largely through geometric variations in the patterned structures. In this section, we demonstrated gray-scale patterning of surface DNA-density as an additional variable in the 2D DNA-based assembly process. This was achieved by direct electron beam irradiation of DNA monolayers (DNA-EBL) which enables the fabrication of surfaces with systematic control over particle-surface interactions and high spatial resolution by modulating both the landing-site size (**Error! Reference source not found.a**) as well as the relative DNA density (**Error! Reference source not found.b**). The primary limiting factor in achieving high spatial resolution in DNA-EBL is related to electron beam scattering in the substrate, resulting in significant proximity dose. Given the high sensitivity of the DNA monolayer to low levels of radiation damage, such proximity dose

precludes the patterning of small features with high density over large areas (tens of μm). To solve this problem, we created suspended silicon nitride membranes (50 nm thick) that were functionalized with DNA; the reduced thickness mitigates the impact of electron scattering on resolution. To demonstrate the high fidelity of the resulting patterns, high-dose binary exposures (*i.e.* DNA in exposed regions is rendered completely inactive for NP binding) were carried out followed by the assembly of Au nanorods with complementary DNA sequences (**Error! Reference source not found.c-e**). These patterns illustrate the ability to assemble individual nanorods with orientation control over large areas.

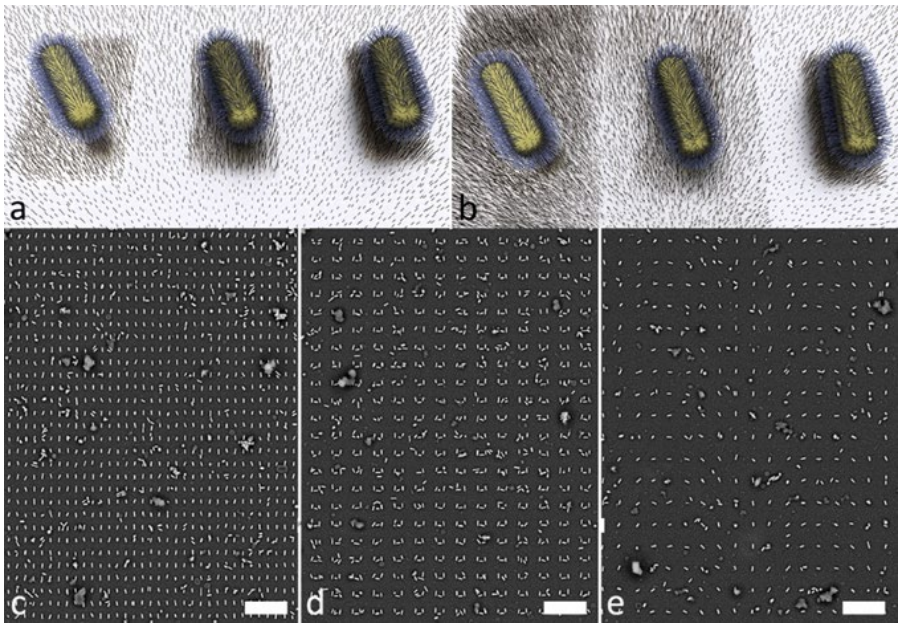


**Figure 27.** Electron beam patterning of DNA density for orientation-controlled Au nanorod assembly on surfaces. (a, b) DNA density patterning schemes showing variation in (a) landing site size and (b) relative DNA density. (c-e) SEM images showing Au nanorod assembly on patterned DNA on silicon nitride membranes. High-resolution patterning allows for the assembly of nanorods in multiple configurations, including in a (c) grid, (d) split ring, and (e) arbitrary orientation. Scale bars are 1 μm.

The lack of a physical template in these systems provides opportunities to explore methods for the in-plane reorganization of the 2D NP arrays. By carefully controlling both the geometry and the electron dose, surfaces with spatially varying DNA density were fabricated that enabled a temperature dependent arrangements of particles. This was only possible due to the gray-scale nature of the patterning process, which preserves a significant fraction of the DNA in the exposed regions. The patterns shown in **Error! Reference source not found.a-d** illustrate one example of the type of reorganization that is possible in these systems. Here, a rectangular grid pattern was exposed with a moderate electron dose, resulting in rectangular, high-DNA-density landing sites of similar size to the nanorods and lower-DNA-density interstitial regions. The distance between landing sites was small enough that particles were able to interact with multiple landing sites (unlike in the high-dose patterns in **Error! Reference source not found.**). At low temperature, the strength of each individual DNA "bond" is high, which results in a relatively disordered film. As the temperature increases, the lower interstitial DNA density becomes more important and particles assemble in highly ordered arrays. Gray-scale patterning in these systems is critical for reconfigurability as high-dose, binary patterns result in ordered patterns even at low temperature. Due to the high degree in ordering in these systems, the assembled 2D NP arrays exhibit strong polarization-dependent optical reflectance (**Error! Reference source not found.e-g**). Future work will involve the use of anisotropic NPs selected to improve optical properties by exploiting gap modes (*e.g.* cubes or rectangular solids with flat facets), exploration of reconfiguration dynamics

by liquid-cell SEM, and coupling of particle-particle interactions with the particle-substrate interactions.

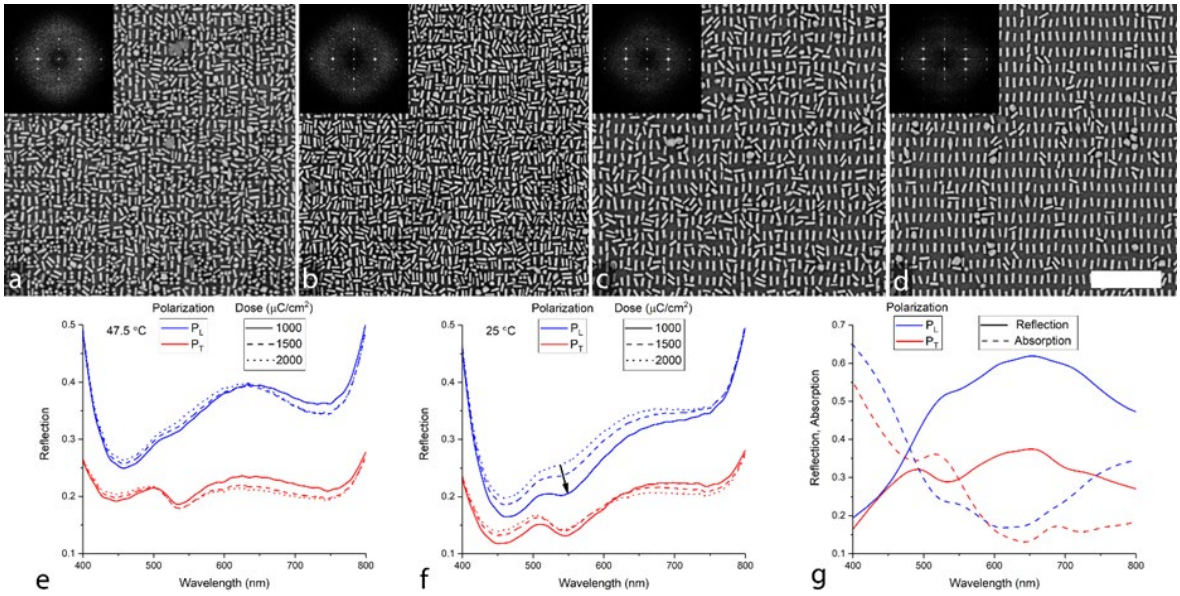


**Figure 28.** Temperature-controlled ordering in Au nanorods surface assemblies. (a-d) SEM images for Au nanorod assemblies on 2D rectangular grids showing a disorder-to-order transition with increasing temperature at (a) 25 °C, (b) 32.5 °C, (c) 40 °C, and (d) 47.5 °C. Scale bar is 1 μm. Insets: fast Fourier transform (FFT) of the SEM images. (e, f) Optical reflectance measurements at high (e, 47.5 °C) and low (f, 25 °C) temperature show polarization-dependent optical properties. The arrow in (f) indicates the need for moderate electron dose to achieve the largest change in nanorod configuration. (g) Optical simulations of an ordered assembly with the same geometry support the large change in reflectance.

## 13. Tunable nanoparticle metasurfaces for light guiding

One advantage of using DNA to assemble NPs on surfaces is that one could combine the reconfigurability of DNA with device architecture to create a highly tailorable system not possible through any other technique. Specifically, as shown in Error! Reference source not found.**a,b** there is a gap mode resonance created by the DNA bonds that can be excited separately from the lattice mode and localized mode. The gap mode is dependent on the distance between the nanocube and the substrate, which indicates that if one could control the length of the DNA, one could potentially control the gap mode resonance.

One way to control the DNA length is using ethanol (EtOH) to change dielectric

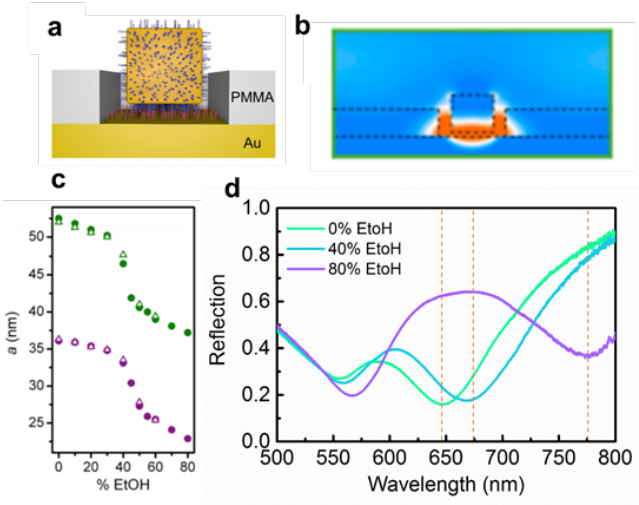


**Figure 29.** (a, b) Gap mode between a Au nanocube and substrate. (c) DNA length is dependent on the EtOH concentration. (d) Measured reflection spectra for Au cubes with different EtOH concentrations.

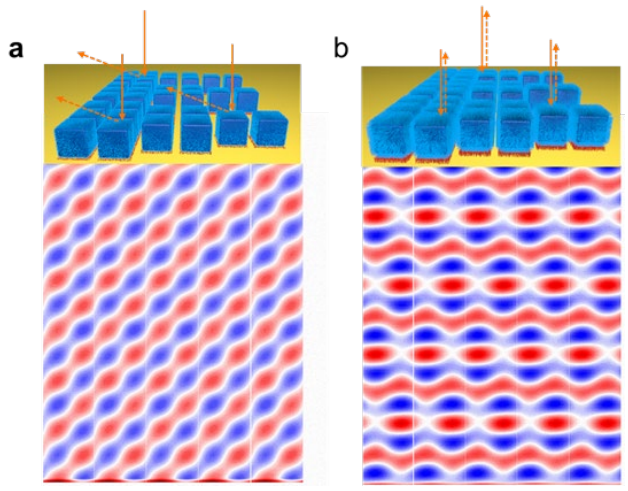


**Figure 30.** Calculated electric field power distribution around the pattern with gaps of (a) 3 and (b) 20 nm.

environment around the DNA. It has been shown that by changing the EtOH concentration, the length of the DNA can be modulated (Error! Reference source not found.**c**).[8] In this Au nanocube system, with 0% EtOH (PBS buffer solution), the length of the DNA is ~ 20 nm, while with 80% EtOH, the length of the DNA contracts to ~3 nm. As the gap mode is sensitive to the distance between the particles and the substrate, the resonance can be turned from 650 nm to 775 nm by changing the EtOH concentration (Error! Reference source not found.**d**).

The tunability of the gap mode can be leveraged to design metasurfaces for anomalous absorption (Error! Reference source not found.). Here, the structure is composed of three different elements: one-cube, two-cube, and three-cube arrays which when patterned in a gradient enable metasurface light guiding. The effect of the array was investigated by calculating the electric field distribution around the structure at 670 nm (Error! Reference source not found.) for different DNA lengths. For 3 nm DNA, the reflected power is guided to the anomalous angle, while for 20 nm DNA, the structure acts like a mirror and most of power is reflected.

To analyze the deflection, we calculated the far field power at various collection angles from -90° to 90° (Error! Reference source not found.). When the DNA length is 3 nm (Error! Reference source not found.**a**), we achieve anomalous reflection around -60° over a broad bandwidth from 610 nm to 690 nm, while for the DNA length of 20 nm (Error! Reference source not found.**b**), most reflected power is reflected at 0°. This is clearly seen by looking at the reflected power at at 670 nm (Error! Reference source not found.**c,d**). Taken together, these results show that DNA-mediated surface assembly is a powerful platform for the design of unprecedented metamaterials with dynamically tunable optical properties.

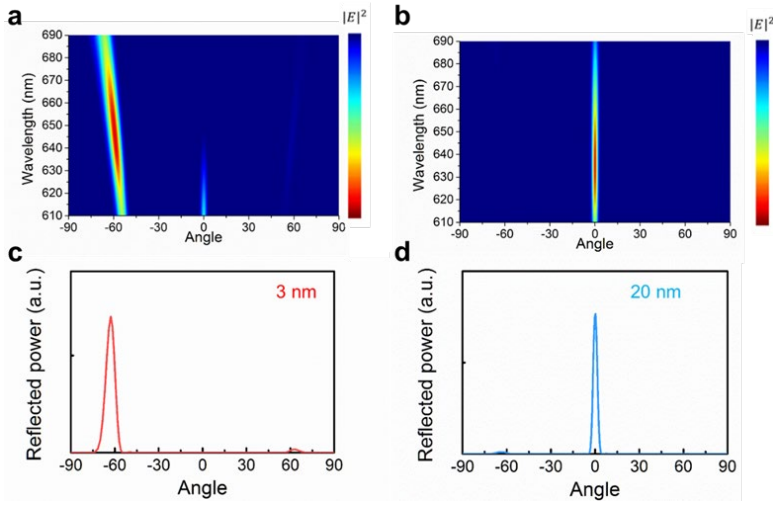


**Figure 31.** Calculated reflected power from 610 nm to 690 nm for a DNA length of (a) 3 and (b) 20 nm. Calculated reflected power at 670 nm for (c) 3 and (d) 20 nm DNA.

## References

1. Jeon, I.-R., *et al.*, *J. Am. Chem. Soc.* **2015,** *137*, 15699, 10.1021/jacs.5b10382.

2. DeGayner, J. A.*, et al.*, *J. Am. Chem. Soc* **2017,** *139*, 4175, 10.1021/jacs.7b00705.
3. Kouji, T.*, et al.*, *Angew. Chemie Int. Ed.* **2016,** *55*, 5238, doi:10.1002/anie.201601672.
4. Ngo, J. T.*, et al.*, *Nature Chemical Biology* **2016,** *12*, 459, 10.1038/nchembio.2076.
5. Li, P.*, et al.*, *Chem* **2018,** *4*, 1022, https://doi.org/10.1016/j.chempr.2018.03.001.
6. Wang, M. X.*, et al.*, *ACS Nano* **2017,** *11*, 180, 10.1021/acsnano.6b06584.
7. Lin, Q.-Y.*, et al.*, *Science* **2018**, 10.1126/science.aaq0591, 10.1126/science.aaq0591.
8. Mason, J. A.*, et al.*, *J. Am. Chem. Soc* **2016,** *138*, 8722, 10.1021/jacs.6b05430.

**CHANGES IN RESEARCH OBJECTIVES, if any:**

none

**SUPPORTED PERSONNEL**

The Mirkin Group

1. Chad Mirkin, PI
2. Anindita Das, postdoctoral fellow
3. Haixin Lin, postdoctoral fellow, (IIN fellowship)
4. Sarah Park, postdoctoral fellow, (IIN fellowship)
5. Devleena Samanta, postdoctoral fellow)
6. Jarad Mason, postdoctoral fellow, (IIN fellowship)
7. Lam-Kiu Fong, graduate student
8. Qingyuan Lin, graduate student
9. Taegon Oh, graduate student, (Kwanjeong fellowship)
10. So Young Seo, graduate student
11. Lin Sun, graduate student
12. Zachary Urbach, graduate student, (DSEG fellowship)
13. Mary Wang, graduate student
14. Wenjie Zhou, graduate student
15. Jinghan Zhu, graduate student

The Aydin Group

1. Koray Aydin, Co-PI
2. Zizhuo Liu, graduate student
3. Edgar Palacios, graduate student

The Dravid Group

1. Vinayak Dravid, Co-PI
2. Chamille Lescott, graduate student, funded partially on this grant, (Murphy Scholarship, Northwestern Materials Science and Engineering)
3. Jingshan Du, graduate student
4. Ben Myers, graduate student, (unfunded)
5. Karl Hujsak, graduate student, (unfunded)
6. Kelly Parker, graduate student, (Northwestern MRSEC fellowship, NSF-GRF)
7. Qingyuan Lin, graduate student, (unfunded)

8. Will Kellogg, graduate student, (unfunded)

The Harris Group

1. David Thomas Harris, Co-PI
2. Lujia Liu, postdoctoral associate
3. Jordan A. DeGayner, graduate student

**COLLABORATIONS**

1. Mirkin, Dravid, Aydin, and Harris performed electron micrscopy at the Electron Probe Instrumentation Center (EPIC)
2. Mirkin collaborated with Prof. Olvera de la Crus (Northwestern University) to simulate the DNA-mediated crystallization behavior of the new library of anisotropic particles that I have developed (elongated rhombic dodecahedron)
3. Mirkin performed grazing incidence small angle x-ray scattering (GISAXS) experiments Argonne National Laboratory where they worked with Dr. Byeongdu Lee to analyze data
4. Mirkin collaborated with Prof. Hersam (Northwestern University) on developing a density gradient method for uniform synthesis of PAE colloidal single crystals

**PUBLICATIONS:**

1. Lin, Q.-Y.; Mason, J. A.; Li, Z.; Zhou, W.; O'Brien, M. N.; Brown, K. A.; Jones, M. R.; Butun, S.; Lee, B.; Dravid, V. P.; Aydin, K.; Mirkin, C. A. "Building Superlattices from Individual NPs via Template-Confined DNA-mediated Assembly," *Science*, **2018**, *359*, 669-672, doi: 10.1126/science.aaq0591.
2. Gabrys, P. A.; Seo, S. E.; Wang, M. X.; Oh, E.; Macfarlane, R. J.; Mirkin, C. A. "Lattice Mismatch in Crystalline Nanoparticle Thin Films," *Nano Letters*, **2018**, 18, 579-585, 10.1021/acs.nanolett.7b04737.
3. Wang, S.; McGuirk, C. M.; d'Aquino, A. I.; Mason, J. A.; Mirkin, C. A. "Metal-Organic Framework NPs," *Advanced Materials*, **2018**, doi: 10.1002/adma.201800202.
4. Lin, Q.-Y.; Palacios, E.; Zhou, W.; Li, Z.; Mason, J. A.; Liu, Z.; Lin, H.; Chen, P.-C.; Dravid, V. P.; Aydin, K.; Mirkin, C. A. "DNA-Mediated Size-Selective Nanoparticle Assembly for Multiplexed Surface Encoding," *Nano Letters*, **2018**, *18*, 2645-2649, doi: 10.1021/acs.nanolett.8b00509.
5. Sun, L.; Lin, H.; Kohlstedt, K. L.; Schatz, G. C.; Mirkin, C. A. "Design Principles for Photonic Crystals Based upon Plasmonic Nanoparticle Superlattices," *PNAS*, **2018**, doi: 10.1073/pnas.1800106115.
6. Zhu, J.; Kim, Y.; Lin, H.; Wang, S.; Mirkin, C. A. "pH-Responsive Nanoparticle Superlattices with Tunable DNA Bonds," *J. Am. Chem. Soc*., 2018, 140, 5061-5064, doi: 10.1021/jacs.8b02793.
7. Fong L.-K.; Ziwei, W.; Schatz, G. C.; Luijten, E.; Mirkin, C. A. "The Role of Structural Enthalpy in Spherical Nucleic Acid Hybridization," *J. Am. Chem. Society*, **2018**, *140*, 6226-6230, doi: 10.1021/jacs.8b03459.
8. Oh. T.; Ku, J. C.; Lee, J.-H.; Hersam, M. C.; Mirkin, C. A. "Density-Gradient Control over Nanoparticle Supercrystal Formation," *Nano Letters*, **2018**, doi: 10.1021/acs.nanolett.8b02910.
9. Liu, L.; Li, L.; DeGayner, J. A.; Winegar, P. H.; Fang, Y.; Harris, T. D.; "Harnessing Structural Dynamics in a 2D Manganese-Benzoquinoid Framework to Dramatically

Accelerate Metal Transport in Diffusion-Limited Metal Exchange Reactions," *J. Am. Chem. Soc.,* **2018***,* doi*:* 10.1021/jacs.8b06774.

10. Zhou, W.; Lin, Q.-Y.; Mason, J. A.; Dravid, V. P.; Mirkin, C. A. "Design Rules for Template-confined DNA-mediated Nanoparticle Assembly," *Small*, **2018**, submitted.
11. Seo, S. E.; Girard, M.; Olvera de la Cruz, O.: Mirkin C. A. "Kinetically Controlled Anisotropic Colloidal Crystal Growth with DNA," *Nature Comm*., **2018**, submitted.
12. Laramy, C. R.; O'Brien, M. N.; Mirkin, C. A. "Crystal Engineering with DNA*," Nature Reviews Materials*, **2018**, submitted.

**PRESENTATIONS**

Chad A. Mirkin. ACS Fall Conference, Washington, DC, "Colloidal Crystal Engineering with DNA" (2017).

ACS Fall Conference, Washington, DC, "Unlocking the Materials Genome through Combinatoric Nanoscience" (2017).

Chad A. Mirkin. Beihang University Advanced Innovation Center Lecture, Beijing China, "Combinatorial Nanoscience" (2017).

Chad A. Mirkin. Sixth International Conference on DNA Nanotechnology, Beijing, China, "Crystal Engineering with DNA" (2017).

Chad A. Mirkin. ChinaNANO 2017, Beijing, China, "Crystal Engineering with DNA" (2017).

Chad A. Mirkin. Small Sciences Symposium, Beijing, China, "Next Generation Materials through Combinatorial Nanoscience" (2017).

Chad A. Mirkin. ACS Publications Forum, Beijing China, "Ushering in The Digital Drug Design Revolution with Spherical Nucleic Acids" (2017).

Chad A. Mirkin. Laird Lecture, University of British Columbia, Vancouver, British Columbia, "Next-Generation Materials through Combinatorial Nanoscience" (2017).

Chad A. Mirkin. Presidential Scholars Symposium, Brown University, Providence, Rhode Island, "Ushering in the Age of Digital Medicine and Drug Design" (2017).

Chad A. Mirkin. Korean Academy of Science and Technology Prestige Workshop, Seoul, Korea, "Spherical Nucleic Acids as a Powerful New Platform for Cancer Therapy" (2017).

Chad A. Mirkin. Yonsei University Chemistry Centennial Symposium, Seoul, Korea, "Next Generation Materials through Combinatorial Nanoscience" (2017).

Chad A. Mirkin. Frontiers of Chemical Biology and Nanomedicine Symposium, Hunan University, Changsha, China, "Ushering in the Age of Digital Medicine and Drug Design with Spherical Nucleic Acids" (2017).

Chad A. Mirkin. Hunan University, Changsha, China, "Colloidal Crystal Engineering with DNA" (2017).

Chad A. Mirkin. The Power of Collaboration Seminar Series, Feinberg School of Medicine, Northwestern University, Chicago, IL, "The Era of Digital Medicine: What It Means For You" (2017).

Chad A. Mirkin. 5$^{th}$ Nano Today Conference, Waikoloa Village, Hawaii, "Colloidal Crystal Engineering" (2017).

Chad A. Mirkin. 14th US-Japan Symposium on Drug Delivery Systems, Maui, HI "Structure-Function Relationships in the Development of Immunotherapeutic Agents" (2017).

Chad A. Mirkin. CEMSupra 2018 Symposium, Tokyo, Japan, "Colloidal Crystal Engineering with DNA" (2018).

Chad A. Mirkin. KAUST Research Conference: New Challenges in Heterogeneous Catalysis for the Activation of Small Molecules, Jeddah, Saudi Arabia, “Combinatorial Nanoscience: Expanding the Materials Genome” (2018).
Chad A. Mirkin. AAAS Annual Meeting, Synergistic Defense-Academic Collaborations: Moving Ideas From the Lab to Application Symposium, Austin, TX, (2018).
Chad A. Mirkin. The University of Austin Department of Chemistry, Austin, TX, “Combinatorial Nanoscience: Expanding the Materials Genome” (2018).
Chad A. Mirkin. Pittcon 2018, Orlando, FL, “Ushering in the Digital Drug Design Revolution with Spherical Nucleic Acids” (2018.)
Chad A. Mirkin. Northwestern Trustees Meeting, Scottsdale, AZ, “Digital Medicines: The Coming Revolution” (2018).
Chad A. Mirkin. ACS Spring Conference, New Orleans, LA, “Scanning Probe Block Copolymer Lithography as a Route to Combinatorial Nanoscience” (2018).
Chad A. Mirkin. ACS Spring Conference, New Orleans, LA, “Programmable Metamaterials” (2018).
Chad A. Mirkin. Materials Research Society Spring Conference, Phoenix, AZ, “Spherical Nucleic Acids as Immunotherapeutic Materials” (2018).
Chad A. Mirkin. Temple University Dean’s Distinguished Lecture Series, Philadelphia, PA, “Combinatorial Nanoscience: Expanding the Materials Genome” (2018).
Chad A. Mirkin. The University of Pennsylvania Hirschmann Visiting Professor, Philadelphia, PA, “Colloidal Crystal Engineering with DNA: Creating a Genetic Code for Materials Design” (2018).
Chad A. Mirkin. University of Washington State MSE Lecture, Seattle, WA, “Expanding the Materials Genome with Nanocombinatorics” (2018).
Chad A. Mirkin. Pacific Northwest National Laboratory Distinguished Lecture Series, Richland, WA, “Combinatorial Nanoscience: Expanding the Materials Genome” (2018).
Chad A. Mirkin. TIDES 2018 Conference, Boston, MA, “Rational Vaccinology: Structure-Function Relationships in the Development of Immunotherapeutic Agents” (2018).
Chad A. Mirkin. Frontiers in Macromolecular and Supramolecular Science Symposium, Bucharest, Romania, “Colloidal Crystal Engineering with DNA” (2018).
T. David Harris. Chongqing Normal University, Chongqing, China, "Spin-Modulated Magnetic Resonance Imaging Probes" (2018).
T. David Harris. Chongqing University, Chongqing, China, "Metal-Semiquinoid Magnets: From Molecules to Materials" (2018).
T. David Harris. University of Kent, Canterbury, United Kingdom, "Spin-Modulated Magnetic Resonance Imaging Probes" (2018).
T. David Harris. Stanford University, Stanford, CA, "Chemical Control of Spin in the Synthesis of Metal-Organic Magnets and MRI Probes" (2018).
T. David Harris. Apple, Inc., Cupertino, CA, "Spin-Modulated Magnetic Resonance Imaging Probes" (2018).
T. David Harris. University of Pennsylvania, Philadelphia, PA, "Chemical Control of Spin in the Synthesis of Metal-Organic Magnets and MRI Probes" (2018).
T. David Harris. University of Washington, Seattle, WA, "Chemical Control of Spin in the Synthesis of Metal-Organic Magnets and MRI Probes" (2018).
T. David Harris. ACS National Meeting, New Orleans, LA, " Metal-Semiquinoid Magnets: From Molecules to Materials " (2018).

T. David Harris. Texas A&M University, College Station, TX, "Chemical Control of Spin in the Synthesis of Metal-Organic Magnets and MRI Probes" (2018).
T. David Harris. North Carolina State University, Raleigh, NC, "Chemical Control of Spin in the Synthesis of Metal-Organic Magnets and MRI Probes" (2018).
T. David Harris. California Institute of Technology, Pasadena, CA, "Chemical Control of Spin in the Synthesis of Metal-Organic Magnets and MRI Probes" (2017).
T. David Harris. Illinois State University, Normal, IL, "Chemical Control of Spin in the Synthesis of Metal-Organic Magnets and MRI Probes" (2017).
T. David Harris. University of California, Santa Barbara, Santa Barbara, CA, "Chemical Control of Spin in the Synthesis of Metal-Organic Magnets and MRI Probes" (2017).
T. David Harris. University of California, Los Angeles, Los Angeles, CA, "Chemical Control of Spin in the Synthesis of Metal-Organic Magnets and MRI Probes" (2017).
T. David Harris. Japan Society of Coordination Chemistry Annual Meeting, Sapporo, Japan, "Spin-Modulated Magnetic Resonance Imaging Probes" (2017).
T. David Harris. 2nd Japan-US Bilateral Meeting on Coordination Chemistry, Sapporo, Japan, "Metal-Semiquinoid Magnets: From Molecules to Materials" (2017).
Vinayak P. Dravid. University of California, Santa Barbara, "Research Facilities/Infrastructure: Emerging Perspectives," (2018).
Vinayak P. Dravid. University of Lincoln-Nebraska, "Teaching 'Old' Materials 'New' Tricks: Nanopatterning & Microscopy of Multifunctional Materials," (2018).
Vinayak P. Dravid. Southern University of Science and Technology, Shenzhen, China, "Teaching 'Old' Materials 'New' Tricks: Nanopatterning & Microscopy of Multifunctional Materials," (2018).
Vinayak P. Dravid. Liquid Phase Electron Microcopy Meeting, Eindhoven, The Netherlands, "Towards Correlative, Multimodal and Adaptive Fluidic-Cell Electron Microscopy," (2017).
Vinayak P. Dravid. Frontiers in Biomagnetic Particles Meeting, Asheville, NC, "Theranostic Magnetic Nanostructures (MNS) in Biomedicine," (2017).
Koray Aydin. SPIE Optics and Photonics 2018, San Diego, CA, "Plasmonics meet 2D materials: enhanced light-matter interactions in the flatland" (2018)
Koray Aydin. Third Northwestern Univ. – Tel Aviv Univ. Workshop on Semiconductors, Electronic Materials, Thin Films and Photonic Materials, Evanston, IL," Nanophotonics in the flatland: Engineering Novel Photonic Platforms from 2D Materials to Metadevices and Metamaterials" (2018)
Koray Aydin. GRC Plasmonics and Nanophotonics, Newry, ME, "GRC Plasmonics and Nanophotonics" July 2018
Koray Aydin. 2018 APS/CNM Users Meeting, Lemont, IL, "Nanophotonics in the Flatland: Engineering Novel Photonic Platforms from 2D Materials to Metadevices and Metamaterials" (2018)
Koray Aydin. SPIE Optics and Photonics 2017, San Diego, CA, "Plasmon-enhanced photon emission and absorption in monolayer, two-dimensional semiconductors" (2017).
Koray Aydin. California Institute of Technology, Applied Physics Seminar, CA, "Nanophotonics in the Flatland: Controlling Light at the Nanoscale with Plasmonics and Metasurfaces" (2018).
Koray Aydin. Northrop Grumman NEXT, (2017)
Koray Aydin. Stanford University, Materials Science Seminar, (2017)
Koray Aydin. Lawrence Livermore National Laboratory, PLS Division Seminar, (2017)

Lujia Liu. Inorganic Chemistry GRC, Biddeford, ME, "Redox-Active 2D Metal-Benzoquinoid Magnetic Frameworks" (2018) poster.

Jingshan S. Du, Peng-Cheng Chen, Vinayak P. Dravid, Chad A. Mirkin. 2018 MRS Spring Meeting, Phoenix, AZ, "Site-Specific Polymer Nanoreactors for Studying Complex Nanoparticles Using Correlative Electron Microscopy," (2018).

Taegon Oh, J. Park, Jessie Ku, Tuncay Ozel, Chad A. Mirkin, ACS National Meeting, Spring, New Orleans, LA, "Orthogonal Chemical Modification of Template-Synthesized Nanostructures with Oligonucleotides." (2018).

Jinghan Zhu, Chad A. Mirkin, Hillard Symposium, Evanston, IL, "Responsive Nanoparticle Superlattices." (2018).

Lin Sun, Chad A. Mirkin, Center for Nanoscale Materials 10th Anniversary Symposium, Chicago, IL, "Design Principles for Photonic Crystals Based Upon Metallic Nanoparticle Superlattices." (2018) poster.

**AWARDS**

Chad A. Mirkin, Nano Research Award, China, (2018)

Chad A. Mirkin, Harrison How Award, Rochester, NY, (2018)

Chad A. Mirkin, Remsen Award, J Johns Hopkins and Maryland Section of the American Chemical Society (2018)

Chad A. Mirkin, 2018 Ralph N. Adams Award in Bioanalytical Chemistry (2018)

T. David Harris. Keith Fagnou Lectureship, University of Ottawa (2018).

T. David Harris. Chemistry of Life Processes Cornew Innovation Award (2017).

Vinayak P. Dravid. Fellow, Royal Microscopical Society (2018)

**INTERACTIONS/TRANSITIONS**

**Patent Applications**

"Photonic Crystals Comprising Nanoparticles and Spacer Groups" Chad A. Mirkin, George C. Schatz, Haixin Lin, Lin Sun, 62-624,328, Jan. 21, 2018.

**YEAR 2**
**Cover Page**
**To:** Dr. Aura Gimm, jung-hwa.gimm.1@us.af.mil
**Subject:** Annual Report
**Contract/Grant Title:** Reconfigurable Matter from Programmable Atom Equivalents
**Contract/Grant #:** FA9550-17-1-0348
**Reporting Period:** August 15, 2018-August 14, 2019

**ABSTRACT**

DNA-functionalized colloidal nanoparticles, termed programmable atom equivalents or PAEs, can be assembled into sophisticated architectures through their surface DNA ligands. The central theme of our ongoing work under this grant is to design, assemble, and study reconfigurable colloidal crystals composed of a diverse set of functional PAE building blocks.

In Year 2, we have made significant progress that advances the aims of this grant and reported these important results to the scientific community through publications in high-impact journals and invited presentations at a number of venues worldwide. Specifically, we have developed a strategy that allows for the synthesis of new libraries of PAE building blocks composed of multimetallic nanomaterials containing up to seven different metals. We have also shown that, when they are substantially reduced in size and DNA density, PAEs become electron equivalents (EEs) that can diffuse freely through a colloidal crystal as electrons diffuse through a metal lattice. Thus, EEs represent a new class of building blocks that can introduce further complexity and functionality into colloidal crystals, while deepening our fundamental understanding of such systems. We have utilized high-resolution electron microscopy to characterize new types of PAE building blocks and study their assembly. For example, we have developed a low-electron dose strategy that enables one to observe electron-beam sensitive materials like MOFs in their unaltered forms by TEM. As means to control structure, we also have developed methods that allow both the size and shape of a superlattice to be controlled, and we have explored the post-synthetic structural modification of superlattices using external stimuli. Importantly, we have begun to show that using functional PAE building blocks, such as photocatalytically active MOFs and magnetic nanoparticles, sophisticated and functional colloidal crystals can be obtained.

Towards the ultimate goal of making functional devices composed of PAE assemblies, we have investigated the assembly of PAEs onto surfaces and the properties of such systems as optical metamaterials. We have developed strategies to control the arrangement and orientation of PAEs onto substrates. Importantly, we have achieved the facet-directed anchoring of nanoparticles, which has led to the first dynamically tunable anomalous reflector. Taken together, significant advances were made in Year 2 towards the development of reconfigurable, structurally sophisticated, and highly functional colloidal crystals.

**OBJECTIVES**

**Year 1**

Objective 1: Develop a new feedstock of functional PAE building blocks

- *Synthesis of three-dimensional anisotropic plasmonic nanoparticles*
- *Synthesis of MOF nanoparticles with control over their physical properties*

Objective 2. Synthesize and investigate dynamically reconfigurable superlattices

- *Transmutable nanoparticle superlattices.*
- *High resolution and contrast imaging of soft materials by electron microscopy.*

Objective 3. Synthesize and investigate structurally sophisticated and functional superlattices.

- *Superlattices with controlled crystal habit.*
- *Explore emergent optical phenomena in nanoparticle superlattices.*

Objective 4. Assemble reconfigurable, sophisticated, and functional superlattices on surfaces

- *Fabricate surface templates with well-defined DNA binding sites.*

**Year 2**

Objective 1. Develop a new feedstock of functional PAE building blocks

- *Synthesis of two-dimensional anisotropic plasmonic nanoparticles.*
- *Algorithmic characterization of nanoparticle yield and dispersion.*
- *Synthesis of MOFs nanoparticles with control over their physical properties*

Objective 2. Synthesize and investigate dynamically reconfigurable superlattices

- *Transmutable nanoparticle superlattices.*
- *Sparse imaging for soft materials characterization.*
- *High resolution and contrast imaging of soft materials by electron microscopy.*

Objective 3. Synthesize and investigate structurally sophisticated and functional superlattices.

- *Co-crystallization of multiple building blocks with chemically, physically, and structurally distinct properties.*
- *Superlattices with controlled crystal habit.*
- *Explore emergent optical phenomena in nanoparticle superlattices.*

Objective 4. Assemble reconfigurable, sophisticated, and functional superlattices on surfaces

- *Layer-by-layer growth of single-crystal superlattices with defined crystal shape and size.*

**Year 3**

Objective 1. Develop a new feedstock of functional PAE building blocks

- *Synthesis of two-dimensional anisotropic plasmonic nanoparticles.*
- *High-throughput screening of anisotropic nanoparticle synthesis conditions*

Objective 2. Synthesize and investigate dynamically reconfigurable superlattices

- *Transmutable nanoparticle superlattices.*
- *In situ characterization of reconfigurable superlattices via fluidic-cell S/TEM.*

Objective 3. Synthesize and investigate structurally sophisticated and functional superlattices.

- *Co-crystallization of multiple building blocks with chemically, physically, and structurally distinct properties.*
- *Unique low-symmetry and quasicrystalline structures.*
- *Explore emergent optical phenomena in nanoparticle superlattices.*

Objective 4. Assemble reconfigurable, sophisticated, and functional superlattices on surfaces

- *Layer-by-layer growth of single-crystal superlattices with defined crystal shape and size.*

**Year 4**

Objective 1. Develop a new feedstock of functional PAE building blocks

- *High-throughput screening of anisotropic nanoparticle synthesis conditions*

Objective 2. Synthesize and investigate dynamically reconfigurable superlattices

- *Transmutable nanoparticle superlattices.*
- *In situ characterization of reconfigurable superlattices via fluidic-cell S/TEM.*

Objective 3. Synthesize and investigate structurally sophisticated and functional superlattices.

- *Co-crystallization of multiple building blocks with chemically, physically, and structurally distinct properties.*
- *Unique low-symmetry and quasicrystalline structures.*
- *Explore emergent optical phenomena in nanoparticle superlattices.*

Objective 4. Assemble reconfigurable, sophisticated, and functional superlattices on surfaces

- *Superlattice assembly on flexible and porous supports.*
- *Emergent properties of surface-bound superlattices.*

**Year 5**

Objective 1. Develop a new feedstock of functional PAE building blocks

- *High-throughput screening of anisotropic nanoparticle synthesis conditions*

Objective 2. Synthesize and investigate dynamically reconfigurable superlattices

- *Synthesis of dynamically responsive superlattices from MOF building blocks.*
- *Develop new strategies for transferring DNA-assembled superlattices to the solid state.*

Objective 3. Synthesize and investigate structurally sophisticated and functional superlattices.

- *Unique low-symmetry and quasicrystalline structures.*
- *Explore emergent optical phenomena in nanoparticle superlattices.*

Objective 4. Assemble reconfigurable, sophisticated, and functional superlattices on surfaces

- *Emergent properties of surface-bound superlattices.*

**FINDINGS**

**Development of a New Feedstock of Functional PAE Building Blocks**

In Year 1, we developed strategies for the synthesis of various PAE building blocks, including three-dimensional (3D) anisotropic plasmonic nanoparticles, chemically ordered or disordered Au-Cu alloy nanoparticles, and MOF nanoparticles. In Year 2, we have greatly expanded the library of PAE building blocks by developing significantly more complex multimetallic PAEs building blocks containing up to seven different metals. Moreover, we have uncovered design rules that allow one to engineer the interfaces between these metals (Section A1). In parallel, we have shown that when PAEs are sufficiently reduced in size and DNA grafting density, they give rise to a new class of building blocks called "electron equivalents", or EEs, that freely diffuse through a static superlattice defined by larger PAEs (analogous to how electrons diffuse through metallic lattices). These EEs allow one to engineer structurally sophisticated superlattices and are discussed in Section C3.

**Interface Engineering in Polyelemental Metal Nanoparticles**

Phase boundaries or interfaces are important structural features in functional polyelemental nanomaterials. For example, in the case of plasmonic and catalytic nanoparticles, the charge transfer occurring across an interface can be utilized to tune the properties of one material domain with a neighboring one. In addition, strain engineering provides a way to modulate the electronic structure of materials when the neighboring phases are epitaxial. As such, exploring the possible heterostructures and interfacial configurations in nanoparticles comprising multiple elements and grains, and further studying the thermodynamic conditions for their formation, is important for designing the next generation of nanoparticle building blocks that can assemble into larger synergistic structures.

Here, we utilize scanning probe block copolymer lithography (SPBCL) in combination with density functional theory (DFT) calculations to understand the principles of interface arrangement in multi-phase nanoparticles, and eventually realized the synthesis of an unprecedented tetra-phase nanoparticle made from Au, Co, Pd, Sn, and Ni with six phase boundaries. Briefly, a block-copolymer was mixed with metal precursor ions for Pd, Sn, and other metals - Au, Ag, Cu, Co, and Ni. This polymer mixture was delivered to silicon nitride thin films using an atomic force microscopy (AFM) probe in the form of attoliter-volume, dome-shaped polymer nanoreactors. After heat treatment in a hydrogen atmosphere, the metal precursors were reduced and converged to form an individual nanoparticle in each nanoreactor through nucleation, growth, and coarsening. Consequently, the nanoparticle composition directly reflects the ratios of the metal precursors

added into each nanoreactor.

We first identified bi-phase metallic combinations that have large miscibility gaps and yield phase-segregated Janus nanoparticles. For instance, in the Au-Co-PdSn and Ag-Cu-Co systems, all bi-phase combinations have a Janus structure (**Figure 1A and D**). When all elements are present in a tri-phase nanoparticle, the Au-Co-PdSn particles form a pie-shaped structure (**Figure 1B**), while the Ag-Cu-Co particles form a Janus structure with three stacking layers (**Figure 1E**). This distinct behavior is understood by density functional theory (DFT) calculations based on total surface and interfacial energy values of the possible structural configurations. For the Au-Cu-PdSn case, the pie-shaped structure results in the lowest energy, while the tri-layer structure in the stacking order of Ag/Cu/Co shows the lowest energy for the Ag-Cu-Co case, both consistent with the experimental observations.

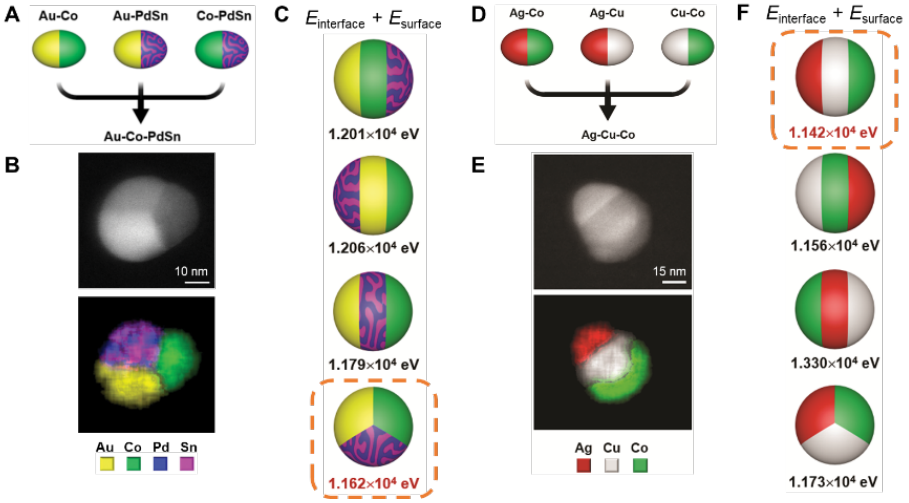


**Figure 1. Engineering the structural configuration of tri-phase metal nanoparticles based on interfacial and surface energetics**. (A−C) For a Au-Co-PdSn nanoparticle, a pie-shaped structure is obtained. (D−F) For a Ag-Cu-Co nanoparticle, a tri-layer Janus shape is obtained. Nanoparticle structures were identified by scanning transmission electron microscopy (STEM) and corresponding energy-dispersive X-ray spectroscopy (EDS) elemental mapping (B, E). The sum of interfacial and surface energy values of possible configurations are calculated by density functional theory (DFT), and the lowest ones (highlighted by orange dashed boxes) are considered as thermodynamically stable configurations (C, F).

Based on these findings, we realized the synthesis of a library of complicated multi-phase nanoparticles utilizing PdSn as the basic building block. Heterodimers can be synthesized by combining PdSn with any of the other five metals of Au, Ag, Cu, Co, or Ni, which lead to Au-PdSn, Ag-PdSn, $Cu_{0.92}Pd_{0.08}$-$Cu_{0.2}(PdSn)_{0.8}$, Co-PdSn, and $Ni_{0.6}$-$Sn_{0.4}$-$Ni_{0.08}(PdSn)_{0.92}$ (**Figure 2A**). For quaternary particles, AuAg-PdSn, AuCu-PdSn, CuNi-PdSn, and CoNi-PdSn forms a heterodimer structure, while Au-Co-PdSn, Au-NiSn-PdSn, Ag-Cu-PdSn, Ag-NiSn-PdSn, and Ag-Co-PdSn are heterotrimers with three interconnected interfaces and Co-Cu-PdSn is a heterotrimer with two disconnected interfaces (**Figure 2B**). Quinary particles AuAg-AuCu-PdSn, AuCu-CuNi-PdSn, AuAg-Co-PdSn, AuAg-NiSn-PdSn, AuCu-Co-PdSn, Au-CoNi-PdSn, Ag-CuNi-PdSn, Ag-CoNi-PdSn are heterotrimers with three interconnected interfaces, but CoNi-CuNi-PdSn is a heterotrimer with two disconnected interfaces and Ag-Cu-Co-PdSn is a heterotetramer with four interfaces (**Figure 2C**). For senary nanoparticles, AuAg-CoNi-PdSn and AuCu-CoNi-PdSn are heterotrimers with three interfaces, AuAg-AuCu-NiSn-PdSn and AuAg-AuCu-Co-PdSn are heterotetramers with five interfaces, and Ag-Cu-CoNi-PdSn is a heterotetramer with four interfaces (**Figure 2D**). Finally, when all seven elements are present in a nanoparticle, the AuAgCu-CoNi-PdSn combination shows a heterotrimer structure with three interfaces. Looking forward, the findings and guidelines from this work will be particularly useful in elucidating the

complex architectures of nanoparticles containing more than four phases, where the nanoparticles may have ten or more different interfaces. Interface engineering in polyelemental nanomaterials will be essential for optimizing their use in catalysis, plasmonics, nanoelectronics, and energy harvesting, and a goal moving forward is to establish high-throughput ways for characterizing their properties as a function of composition, size, phase, and architecture and to develop methods to scale up their syntheses.

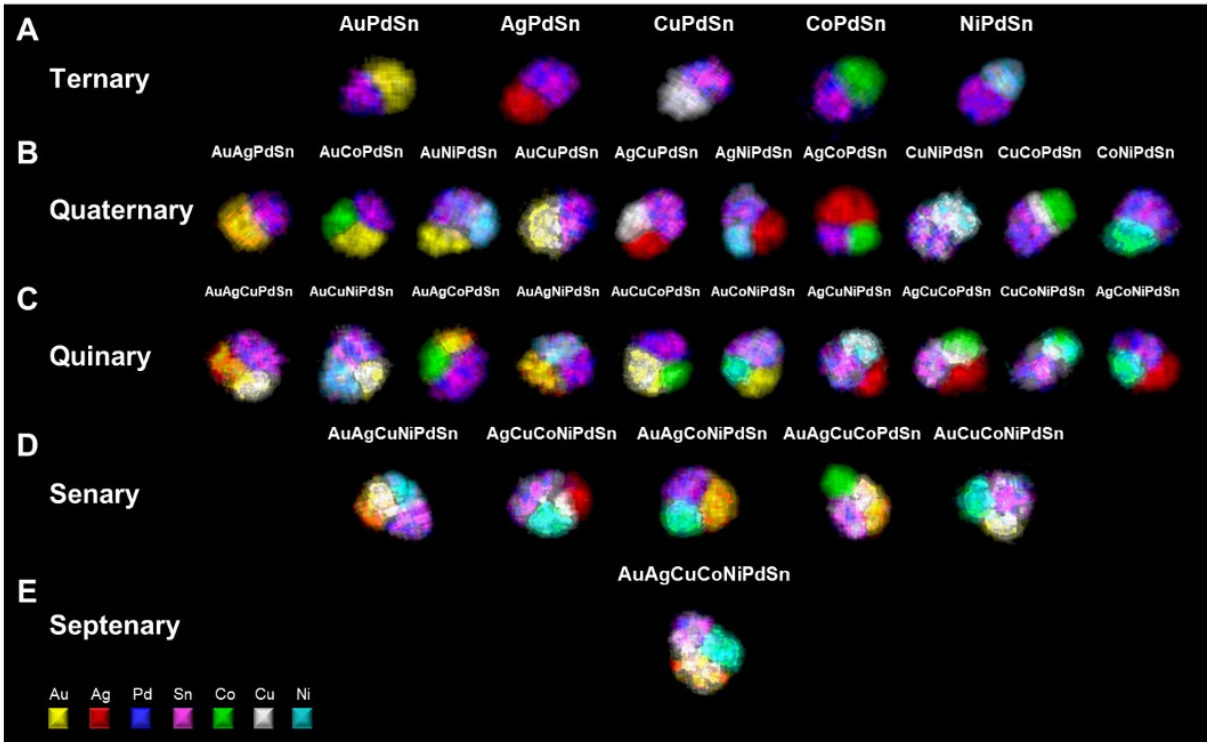


**Figure 2. A seven-element library of multi-phase heterostructured nanoparticles.** All particles shown here utilize PdSn as the basic building block. One specific composition for each combination of metals is shown.

**Synthesis and investigation of dynamically reconfigurable superlattices**

Under this objective, we first report progress on developing techniques that allow for the structural characterization of soft materials such as MOF-based PAEs through electron microscopy (Section B1). We then enumerate our progress towards engineering stimuli-responsive nanoparticle superlattices using light (Section B2). These advances enable the thorough characterization of PAE building blocks and their post-synthetic manipulation.

**1. High-resolution and contrast imaging of soft materials by electron microscopy**

The ability to perform a full structural characterization of MOFs on the local scale is key for the design of novel classes of MOF-based PAEs. The complete structural characterization of nanomaterials is generally accomplished using a combination of transmission electron microscopy (TEM) techniques, such as high resolution TEM, high-angle annular dark field scanning TEM (HAADF-STEM), annular bright field (ABF)-STEM, and electron diffraction (ED). However, the

pronounced instability of MOFs under the electron beam limits the application of conventional TEM techniques. Therefore, the use of low-electron dose conditions is necessary in order to image MOF structures in an unaltered form. To this end, direct electron detectors (DED), cameras with exceptionally high detective quantum efficiency, have enabled HRTEM at ultralow electron doses (**Figure 3**).

During this reporting period, we explored the use of a recently installed DED in the Northwestern Atomic and Nanoscale Characterization Experimental Center (NU*ANCE*) to obtain atomic resolution images of NU-1000 MOF crystals. **Figure 3b-d** shows a series of images collected using dose fractionation mode at different accumulated electron doses. This mode allows us to monitor electron beam damage while obtaining local structural information. In addition, we also explored the use of low-dose aberration corrected STEM techniques to image dopants located in the MOF pores (**Figure 4**). STEM imaging provides us with a more direct interpretation as the positions of bright/dark dots can be readily interpreted as atomic column positions in a well-oriented sample. ABF-STEM imaging is a robust and powerful method for directly visualizing both light and heavy atom columns simultaneously, with few contrast reversals over a large range of thickness. **Figure 4** shows an example of an ABF image acquired from a Zn-doped $Cu_3(HHTP)_2$ MOF sample. Although the low total electron beam dose applied (~100 e/Å$^2$) limits the resolution to ~6Å, the structure motif, pore size (2 nm), and presence of Zn atom dopants

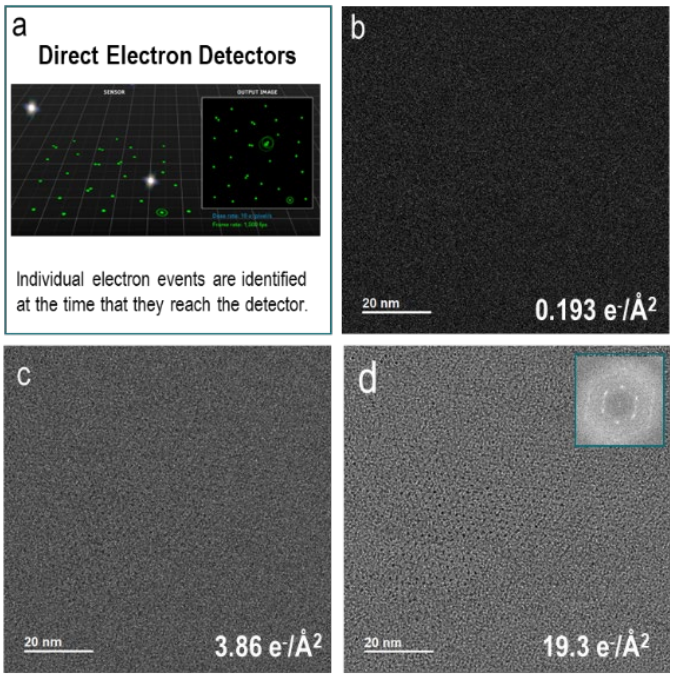


**Figure 3. Direct Electron Detectors (DED) for TEM.** A DED (a) was used to capture HRTEM images of a NU-1000 MOF crystal structure. Dose fractionation mode was used to acquire images at different electron total dose (b-d). Inset in (d) shows a fast Fourier transform (FFT) of the whole field of view.

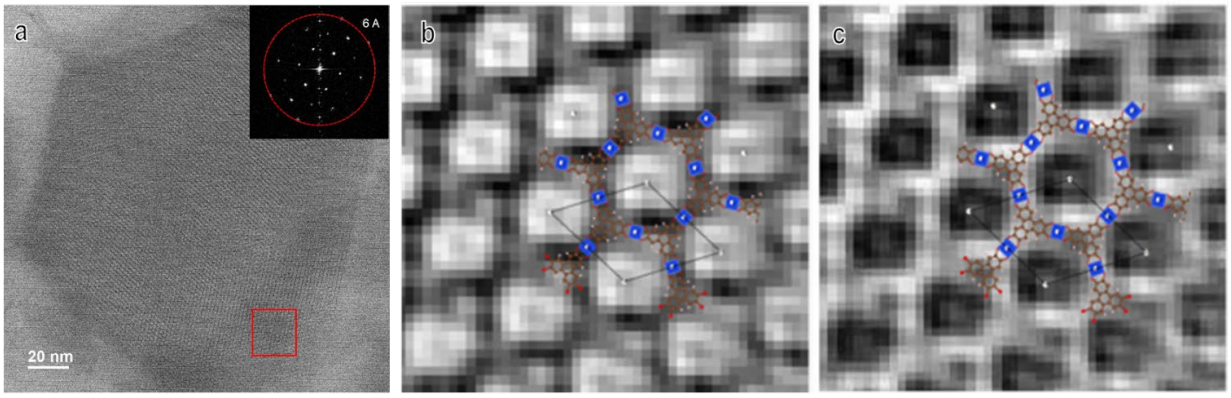


**Figure 4. TEM imaging of MOF colloidal crystals.** (a) Annular Bright Field (ABF) raw image of a Zn-doped $Cu_3(HHTP)_2$ MOF crystal. (b) Image of the area marked in (a) after denoising using Fourier filtering. (c) A contrast-reversed ABF image highlighting the insertion of atoms in the MOF pores. Sub-nm information transfer is possible, as indicated by the reflection circled in the inset in (a), which is sufficient to depict the structure motif, pore size (2 nm), and presence of Zn atom dopants.

are directly identified (**Figure 4b-c**). The ability to image MOFs will allow us to more fully characterize superlattice structures comprised of them; therefore, this work is foundational to achieving the specific aims of this grant.

**Light-responsive colloidal crystals engineered with DNA**

Colloidal nanoparticles are promising building blocks for the construction of 2D and 3D components for use in optical, electronic, magnetic, and therapeutic devices. Therefore, multiple assembly techniques (e.g., interface/template-assisted, field-induced, diffusion-controlled, ligand-directed) have been developed to engineer hard or soft nanoparticle-based crystalline materials. Colloidal crystal engineering with DNA, which uses DNA-grafted nanoparticles as "artificial atoms" to generate hierarchically ordered superlattices, has advantages over other assembly techniques because the size, shape, and composition of the core nanoparticle "atom" can be tuned independent of the length, sequence, and density of the DNA "bonds". Moreover, stimuli-responsive DNA "bonds" allow PAEs to respond to external cues, such as pH, enzymatic activity, dielectric media, and the presence of small molecules, and reconfigure their inter-particle binding. As a stimulus, light is widely used in chemical and biological systems to effect structural changes and regulate important processes. Indeed, light provides high spatial and temporal resolution, remote control, and wavelength tunability. The ability to photo-direct the generation and disassembly of colloidal crystals on surfaces may provide a general way to pattern and integrate such structures with surfaces and device components over large areas. In addition, by combining such capabilities with nanoparticle-based lattices engineered from DNA, one could affect such changes with nanoscale building blocks with almost unlimited access to

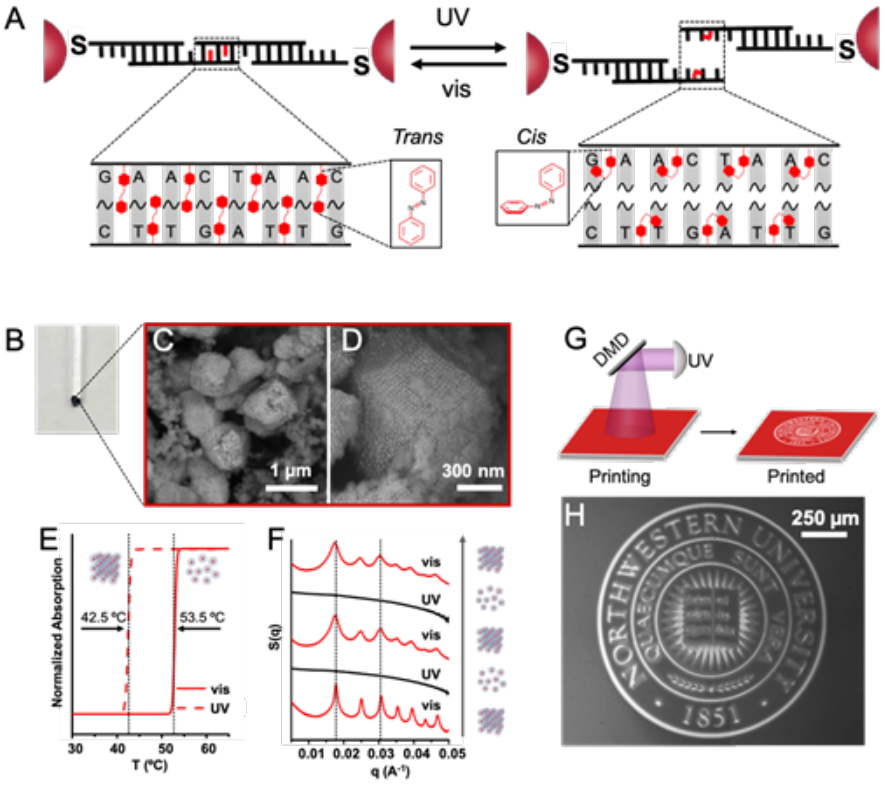


**Figure 5. Light-responsive colloidal crystals mediated by azoDNA.** (A) Scheme showing that light-responsive nanoparticle superlattices functionalized with azoDNA linkers can be toggled between assembled and disassembled states. (B) Aggregated PAEs were annealed via a slow-cool method, and (C, D) SEM images confirmed the formation of ordered colloidal crystals. (E) Melting curves of light-responsive PAEs show two different melting temperatures, one under visible and one under UV light. (F) Small-angle X-ray Scattering (SAXS) data confirm the formation of bcc crystals (red lines) and a dynamic and reversible change between assembled (visible light, red lines) and disassembled (UV light, black lines) states upon tuning the wavelength of light. (G) A cantilever-free scanning probe lithography instrument equipped with a digital micromirror device (DMD) is used to photo-pattern crystalline PAE thin-films. (H) Optical microscope images confirm successful photopatterning of a patterned image.

crystal symmetry and related parameters.

Here, we report the proof-of-concept synthesis of light-responsive DNA-interconnected colloidal crystals and describe two separate light-directed processes – (i) the light-directed assembly and disassembly of crystalline nanoparticle superlattices, respectively, and (ii) the light-directed patterning of colloidal crystals. Light-responsive PAEs were synthesized by integrating azobenzene-tethered DNA (azoDNA) in the DNA bonding elements such that the light-induced molecular change in the conformation of azoDNA (between trans- and cis-states) effects DNA hybridization or dehybridization causing the bonding or dissociation of neighboring PAEs (**Figure 5A**). Upon confirming that the incorporation of azoDNA does not affect the crystallinity of the PAE superlattices, we found that the assembly/disassembly of PAE crystals can be triggered using light under isothermal conditions (**Figure 5B-F**). We then tested the ability to pattern the nanoparticle films using the light-directed disassembly of PAEs to selectively remove nanoparticles located outside of a desired pattern (**Figure 5G**). As a result, centimeter-scale colloidal crystal thin films were patterned into predesigned shapes upon UV irradiation (**Figure 5H**). Our findings mark a significant step towards integrating colloidal crystals into advanced "smart materials" that can be dynamically manipulated on demand.

**Synthesis and investigation of structurally sophisticated and functional superlattices**

Under this objective, we report progress on the development of structurally sophisticated superlattices, including those with controlled crystal habits in terms of size (Section C1) and shape (Section C2). In addition, we report the discovery of a new class of "metallic" colloidal crystals (Section C3). Toward building functional superlattices, we show that MOF-based PAEs can be assembled into catalytically active colloidal crystals (Section C4) and iron oxide-based PAEs assemble into magnetic colloidal crystals (Section C5). Subsequently, we show that superlattices can be transferred to the solid-state (important for practical applications) using two different DNA-crosslinking approaches (Sections C6 and C7).

**2. The importance of salt-enhanced electrostatic repulsion in colloidal crystal engineering**

Realizing functional colloidal single crystals requires precise control over nanoparticles in three dimensions across multiple size regimes. In this regard, colloidal crystallization with PAEs composed of DNA-modified nanoparticles allows one to program, in a sequence-specific manner, crystal symmetry, lattice parameter, and, in certain cases, crystal habit. In addition, the size of colloidal crystals is an important design parameter for the preparation of device architectures, particularly those requiring control over the optical path length (i.e., the distance that light travels across the crystal in the orientation of interest); however, methods for realizing single crystals with tunable sizes have yet to be fully developed. The sizes of single crystals generated by the slow cooling of PAEs typically fall in the 2 μm or less range when synthesized in solutions with monovalent salt concentrations between 50 and 500 mM.

Here, we investigated how salt and the electrostatic properties of DNA can regulate the attachment kinetics between PAEs. Molecular dynamics (MD) simulations were used to calculate PAE interaction potential energies as a function of interparticle distances (i.e., core-to-core distance) ranging from 30 to 40 nm. These simulations used a PAE design consisting of two 15-nm spherical gold nanoparticles, each functionalized with one of two DNA sequences bound to linker strands with complementary "sticky ends". Counterintuitively, simulations and theory show that at high salt concentrations (1 M NaCl), the energy barrier for crystal growth increases by over an order of magnitude compared to low concentration (0.3 M), resulting in a transition from interface-limited to diffusion-limited crystal growth at larger crystal sizes.

To investigate whether PAE assembly at elevated salt concentrations leads to the growth of larger microcrystals, two sets of 15-nm spherical PAEs with complementary DNA sequences were prepared. Each sample was assembled in solution at three different salt concentrations (0.3, 0.5, and 1 M NaCl) and then slowly cooled. This process enables DNA-driven crystallization that favors the formation of single-crystalline rhombic dodecahedra with the gold nanoparticles in a bcc crystallographic symmetry (over a polycrystalline assembly). Remarkably, at elevated salt concentrations, well-formed rhombic dodecahedron-shaped microcrystals up to 21 μm in size grow, whereas at low salt concentration, the crystal size typically does not exceed 2 μm (**Figure 6**). Simulations show an increased barrier to hybridization between complementary PAEs at elevated salt concentrations. Therefore, although one might intuitively conclude that a higher salt concentration would lead to less electrostatic repulsion and faster PAE-to-PAE hybridization kinetics, the opposite is the case, especially at larger inter-PAE distances.

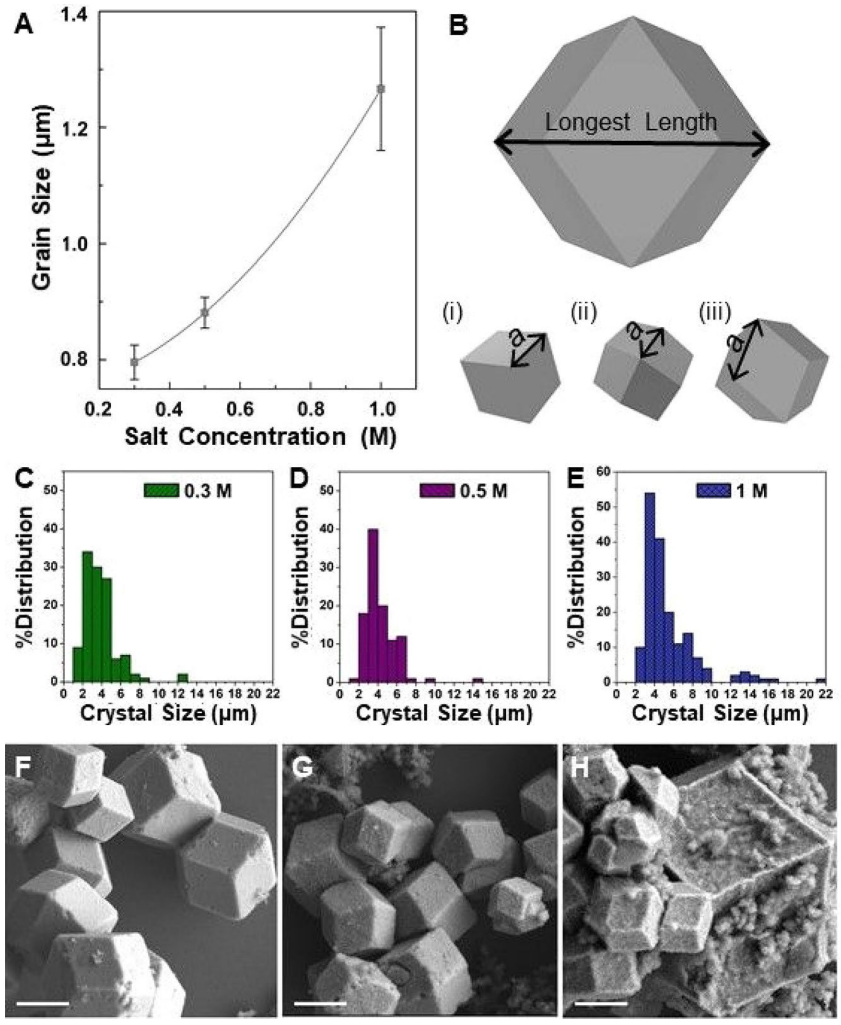


**Figure 6. Crystal size of bcc superlattices determined by salt concentration.** (A) Williamson-Hall analysis of SAXS data deconvolutes peak broadening arising from grain size (intercept) and microstrain (slope). (B) Scheme (top) showing the dimension that was measured for the statistical analysis of crystal size distribution using SEM images. (i), (ii), and (iii) are schematic representations of three different orientations of the microcrystals commonly observed on the substrate. The edge length "a" was measured and mathematically converted to convey the length shown in the top drawing. Size analyses of approximately 150 microcrystals, assembled at (C) 0.3, (D) 0.5, and (E) 1 M NaCl, show an increase in average crystal size with increasing salt concentration. SEM images of silica-encapsulated bcc gold nanoparticle microcrystals, interlinked with DNA and assembled at (F) 0.3, (G) 0.5, and (H) 1 M NaCl confirm faceted rhombic dodecahedra. For this set of data, nanoparticle assemblies were done using complementary seven-base pair sticky ends. Scale bars are 2 μm.

These observations reveal the properties of polyelectrolyte brushes of nanoparticle-based DNA bonds and provide powerful methods to alter the attachment kinetics of PAEs to control mesoscale crystal size. Importantly, PAE crystallization at elevated salt concentrations can be used to synthesize colloidal single crystals over a significantly

larger length scale. Furthermore, through post-synthetic salt exchange processes, the salt-induced transition is fully reversible. The extension of this work to different annealing conditions, multivalent cations, and DNA loadings should enhance our fundamental understanding of how kinetics can be tuned to control materials properties, leading to new possibilities for the realization of kinetically controlled superlattice structures. The high-level of structural control over colloidal single crystals will enable researchers to probe the effect of crystal size on the optoelectronic and mechanical properties of these materials.

**Non-equilibrium anisotropic colloidal single crystal growth with DNA**

The crystal shape (habit) of a system is an external expression of its internal structure. Experimental observations of colloidal single crystals have been restricted to PAEs with similar hydrodynamic radii (a combination of the nanoparticle radius and the DNA length) which form relatively isotropic habits. Here, we show that combining nanoparticles of different sizes can alter the interface kinetics in the system, leading to the formation of highly anisotropic single crystals (**Figure 7**). The $AB_2$ (isostructural with the aluminum diboride phase) structure yields elongated hexagonal prism microcrystals upon slow cooling. Importantly, these anisotropic microcrystals can be realized from the $AB_2$ structure with different lattice parameters. The experimental results are corroborated with theoretical studies and suggest that the formation of highly anisotropic single crystals is facilitated by anisotropy in the interface kinetics, where the fast-growing facets grow out and disappear, and the slow-growing facets, $AB_2$ $(10\bar{1}0)$ and $AB_2$ $(0001)$ (the facet normal to $AB_2$ $(10\bar{1}0)$), are present in the final shape. It is important to note that based on MD simulation results, the facets enclosing the crystals have the highest surface energies, in contrast with the usual equilibrium Wulff constructions. Such crystal growth behavior stems from the nucleation barrier between each termination of $AB_2$ $(10\bar{1}0)$, which significantly decelerates the growth rate due to the energetic penalty involved in nucleation of a layer with a high- surface energy atop a layer with a low surface energy. The results shown in this work present a solution to a synthetic and materials challenge in colloidal crystal engineering that had not been

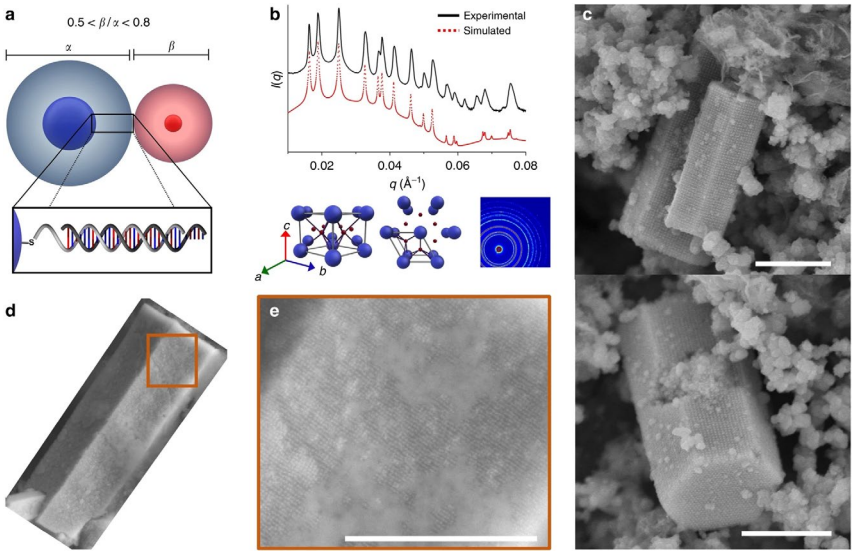


**Figure 7. Hexagonal prism microcrystals formed from DNA-functionalized nanoparticles. a** Scheme of a set of DNA-functionalized gold nanoparticles with a hydrodynamic radius ratio (β/α) between 0.5 and 0.8 used to produce superlattices with $AB_2$ crystallographic symmetry. α and β denote the hydrodynamic radii of particles A and B. **b** Representative one-dimensional (top) and two-dimensional (bottom, right) SAXS data for $AB_2$ superlattices assembled from the slow-cooling approach. Different views of the $AB_2$ unit cell (bottom, left) are shown for reference. SAXS data are shown as plots of the overall scattering intensity from a crystal domain (I(q), in arbitrary units) versus scattering vector (q, in units of $Å^{-1}$). **c** SEM images of hexagonal prism microcrystals in different orientations. **d**, **e** SEM images of a representative microcrystal with visible faceting (**d**) where the constituent nanoparticles can be seen (**e**). Scale bars are 1 μm.

addressed previously, where the deviation from minimal energy shapes and the broken bond model picture enables the synthesis of anisotropic colloidal crystals. This further suggests that external parameters, such as ionic strength, temperature, and stress, could be used to control colloidal crystallization. The ability to design and generate colloidal crystals with desired crystal shape is crucial for the fabrication of next-generation optoelectronic devices since optical modes are highly dependent on crystal shape.

**Synthesis of electron equivalents and metallic phase colloidal crystals**

AFOSR-funded research over the past decade has resulted in the development of design rules to engineer crystallization outcomes with PAE building blocks. This work shows, for the first time, that when PAEs are reduced in size and DNA grafting density, the PAEs behave as electron equivalents (EEs), roaming through and stabilizing the lattices defined by larger PAEs, as electrons do in metals in the classical picture. This discovery defines a new property of colloidal crystals, metallicity, that is characterized by the extent of EE delocalization and diffusion. As the number of strands increases or the temperature decreases, the EEs localize, which is structurally reminiscent of a metal−insulator

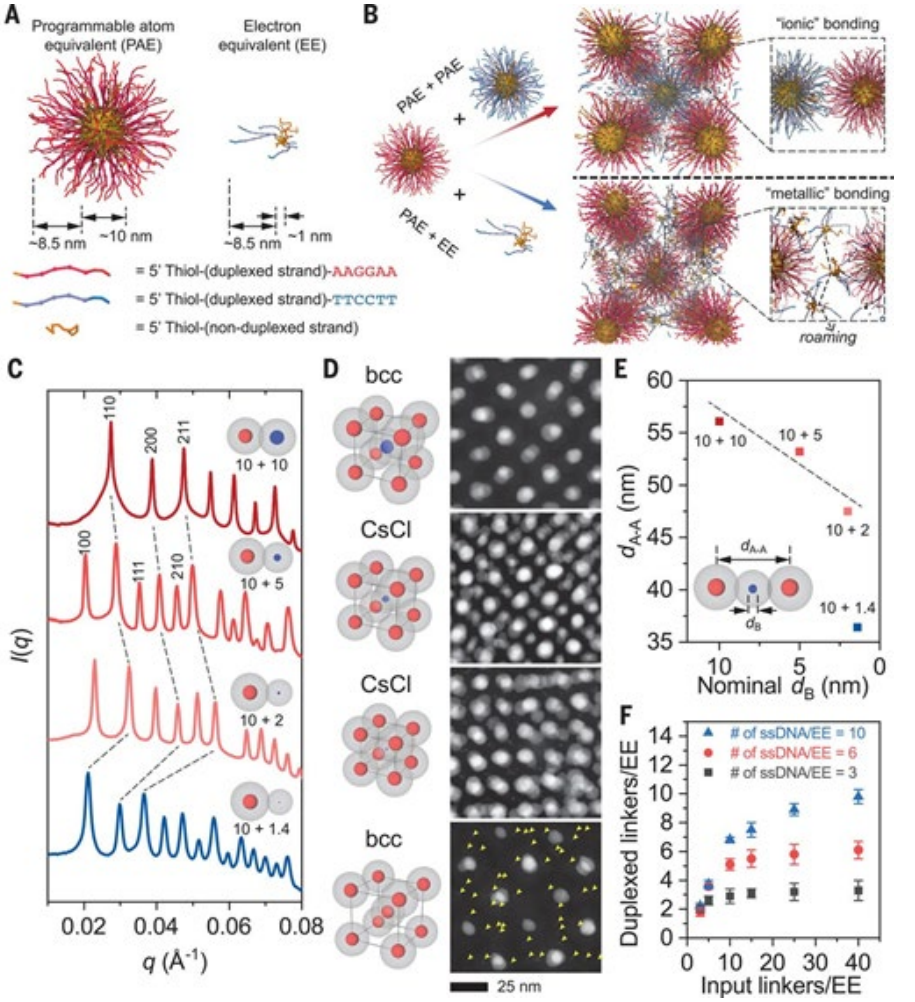


**Figure 8. Transition from PAE-PAE systems to PAE-EE systems.** (**A**) Illustrations of DNA-functionalized Au nanoparticles behaving as PAEs or EEs used in the MD simulation. (**B**) Snapshots from the MD simulation depicting "ionic" bonding behavior shown by PAE + PAE assemblies, and "metallic" bonding behavior shown by PAE + EE assemblies, where roaming EEs hold the crystal of repulsive PAEs together. (**C**, **D**) Four crystalline lattices assembled from 10-nm PAEs and complementary DNA–functionalized Au nanoparticles (nominal core diameters of 10, 5, 2, and 1.4 nm, respectively). Shown are (**C**) SAXS spectra, (**D**) models, and cross-sectional LAADF images of silica-encapsulated samples. Scale bar, 25 nm. The 1.4-nm Au nanoparticles in (D) (yellow arrows indicate visually identified ones) are dispersed randomly in the lattice and do not occupy specific lattice sites. (**E**) SAXS-determined distance between bonding 10-nm PAE pairs (same DNA type, defined in the inset according to CCM assumptions). (**F**) Quantification of linker DNA strands duplexed on 1.4-nm Au nanoparticles (EEs) as a function of the input number of linkers per EE in the solution.

transition. Colloidal crystal metallicity, therefore, provides new routes for the synthesis of metallic, intermetallic, and compound phases.

This electron–atom duality analog in colloidal crystal engineering with DNA results in colloidal assemblies that are better classified as "metallic" structures. In such structures, small DNA-functionalized nanoparticles become mobile and "electron-like" (EEs), and they are essential for maintaining the positions of the larger PAE "atom" components. Mixtures of complementary DNA-functionalized nanoparticles that vary in size and DNA surface density were assembled and characterized by electron microscopy, synchrotron small-angle X-ray scattering (SAXS), and MD simulations with explicit hybridization. Through a combination of theory, simulation, and experiment, we show that small particles grafted with low numbers of DNA strands (e.g., < 6), when mixed with complementary functionalized nanoparticles (**Figure 8**), form crystals, but that the EEs do not occupy specific lattice sites and diffuse through the crystal in a manner reminiscent of classical electrons in metals, as described by the original Drude model. The PAEs alone do not form crystals since they are almost solely repulsive. The delocalized EEs that move freely through the lattice are responsible

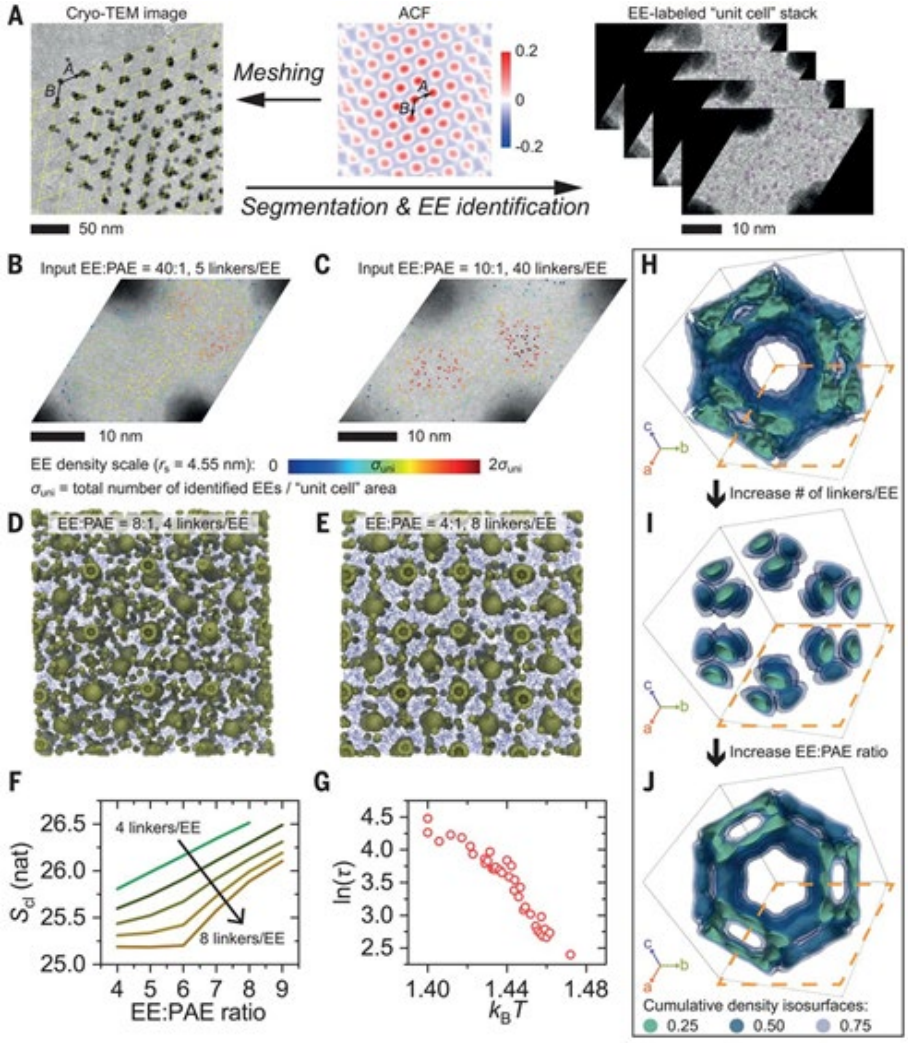


**Figure 9. Spatial probability distribution of EEs in PAE-EE assemblies in the bcc structure.** (A) Workflow for obtaining EE location-labeled "unit cell" images from cryo-TEM by using image segmentation. ACF, auto-correlation function. (B and C) Overlay of averaged-intensity TEM images and identified EE locations in "unit cells" along the [111] direction. The input parameters refer to the ratio of each substance added to the solution, not within a crystal. (D and E) MD simulation snapshots of PAE-EE assemblies. (F) Measure of clustering tendency ($S_{cl}$) of EEs in MD simulations. (G) Temperature-dependent trapping time (τ) of EEs in MD simulations. $k_B$, Boltzmann constant. (H to J) Simulated Boltzmann volumes of EEs viewed along the [111] direction with EE:PAE = 4:1 and (H) 4 or (I) 8 linkers per EE, or with (J) EE:PAE = 9:1 and 8 linkers per EE. Orange dashes approximate a repeating "unit cell" used in cryo-TEM image analysis.

for stabilizing it, a type of bonding more reminiscent of metals than ionic compounds (**Figure 9**). Furthermore, when the interactions are tailored by increasing the number of potential DNA bonds or lowering the temperature, these EEs condense into specific locations, yielding a transition akin to a metal–insulator transition. Finally, by taking advantage of this duality and the structural features of the DNA-modified particles that govern it, we realize three polymorphic crystal phases—body-centered cubic (bcc), face-centered cubic (fcc), and Frank-Kasper A15—and analyze the distribution and diffusion of the particles (EEs and PAEs) within them as a function of temperature and number of linkers/EE.

Taken together, this work makes the case for describing certain classes of colloidal crystals in a fundamentally new way, in which, in the case of mobile particles (EEs), the concept of metallicity becomes important. By understanding the factors that govern EE diffusion and delocalization, we have a better understanding of the structures and phases that can be accessed through colloidal crystals, potentially including metals, intermetallics, and complex metal alloys. It also challenges the colloid science community to identify exotic new properties that arise from the PAE-to-EE transition and structures that exhibit high degrees of metallicity, as well as to develop theoretical models that capture the effects that lead to metallicity.

**Synthesis of catalytically active colloidal crystals with MOF nanoparticles**

Previously, we have shown that metal-organic framework (MOF) nanoparticles densely functionalized with oligonucleotides can be programmed to crystallize into a diverse set of superlattices with well-defined crystal symmetries and compositions. Electron microscopy and small-angle X-ray scattering (SAXS) characterization confirm the formation of single-component MOF superlattices, binary MOF-Au rhombic dodecahedral single crystals, and two-dimensional MOF nanorod assemblies (**Figure 10**). The formation of these superstructures is programmed by

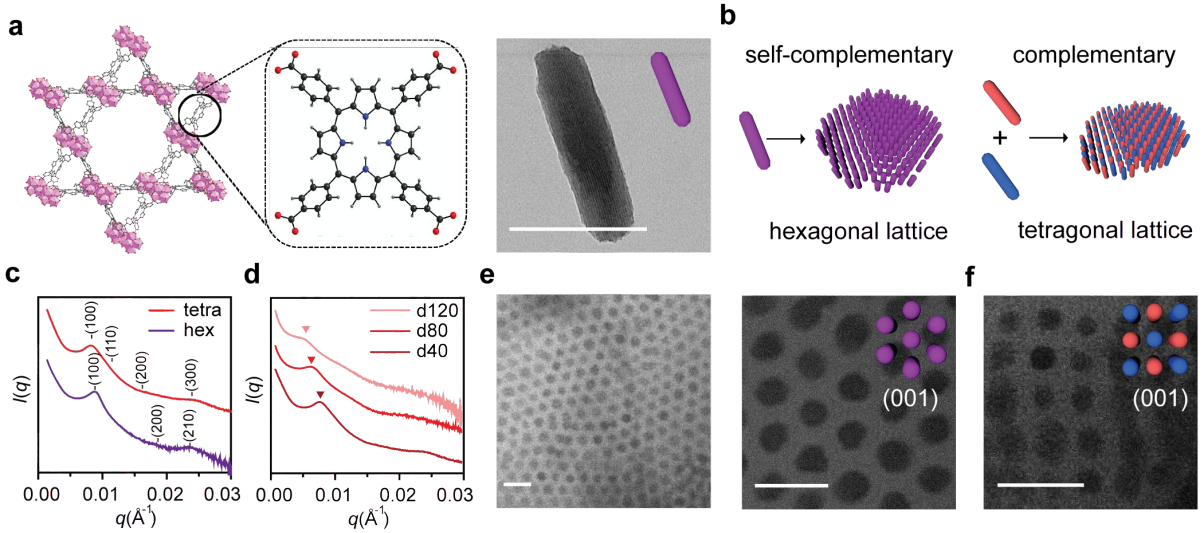


**Figure 10. Shape-dependent MOF superlattice assemblies**. (a) Crystal structure and TEM image of a single PCN-222 nanorod formed by the connection of $Zr_6$ SBUs and tetrakis(4-carboxyphenyl)porphyrin linkers (box). (b) Schematic representation of PCN-222 PAEs assembled into two different lattices depending on DNA linker design: self-complementary DNA linkers (left, 2D hexagonal superlattice) and complementary DNA linkers (right, 2D tetragonal superlattice). (c) 1D SAXS patterns of PCN-222 superlattice with in-plane hexagonal and tetragonal symmetries. (d) 1D SAXS patterns of PCN-222 tetragonal superlattice with tunable interparticle spacings by changing DNA linker lengths (d40: 77 nm, d80: 92 nm, d120: 109 nm). (e) Cryo-TEM images show PCN-222 PAEs with self-complementary DNA linkers close-pack into 2D hexagonal lattices. (f) Cryo-TEM image shows PCN-222 PAEs interconnected by complementary DNA linkers form a 2D tetragonal lattice. Scale bars, 100 nm.

colloidal crystal engineering rules defined by the complementary contact model and anisotropic MOF nanoparticle shape-induced bonding interactions.

From a utility standpoint, it is important to determine if MOF nanoparticle functionality is preserved post-DNA functionalization and incorporation in a superlattice. Therefore, the photocatalytic activity of a PCN-222 [$(Zr_6O_8(H_2O)_8(TCPP\text{-}H_2)_2$, TCPP = tetrakis(4-carboxyphenyl)porphyrin)] MOF nanorod 2D superlattice was investigated and evaluated as a photooxidation catalyst for 2-chloroethyl ethyl sulfide (CEES, a chemical warfare simulant of mustard gas). The selective partial oxidation of CEES was studied as a model reaction because of its implications for detoxification. The porphyrin moiety of the MOF ligand was expected to serve as a high-quantum yield photosensitizer for the generation of singlet oxygen, which can subsequently oxidize CEES to non-toxic 2-chloroethyl ethyl sulfoxide (CEESO). In a typical reaction, the samples (TCPP ligand loading of 0.01 mol %) were suspended in methanol and purged with $O_2$ before the addition of the internal standard and CEES, the reaction progress was monitored by gas chromatography, and the product selectivity was verified by $^1H$ NMR spectroscopy. To preserve superlattice structure and MOF porosity, the double-stranded DNA bonds of the PCN-222 superlattices were post-synthetically stabilized with $Ag^+$, a method developed to preserve colloidal crystal crystallinity under conditions where DNA bonds are typically denatured. Importantly, the PCN-222 nanoparticle superlattice shows selective conversion of CEES to CEESO and a higher catalytic conversion efficiency as compared to bulk PCN-222 crystals (**Figure 11**). This observation is attributed to faster substrate diffusion kinetics induced by the mesoporosity created by the DNA bonds and a higher photosensitization efficiency associated with the 2D superlattice, which supports a larger light absorption cross-section than 3D crystals.

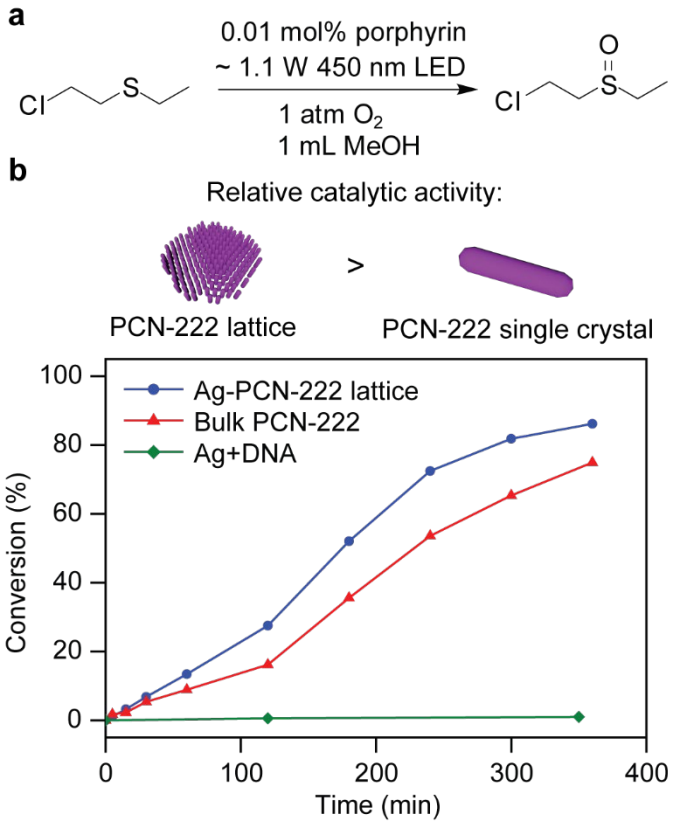


**Figure 11. Photocatalytic activity of the 2D PCN-222 nanorod superlattices**. (a) Reaction pathway for the oxidation of mustard gas simulant CEES, using oxygen and a porphyrin photosensitizer. (b) Reaction profiles for the oxidation of CEES using $Ag^+$-stabilized PCN-222 superlattice and a PCN-222 single crystal, respectively (same porphyrin loading). All samples were irradiated with blue LEDs ($wavelength_{max}$ = 450 nm) with equivalent power density. No appreciable catalytic activity was observed for the $Ag^+$ ion and single strand DNA control group.

These experiments show that the MOF building blocks are indeed catalytically active when incorporated into crystals, and that activity depends upon material dimensionality. Taken together, these new materials and methods provide access to a new set of colloidal crystals that

incorporate particles with the well-established designer properties of MOFs and, therefore, significantly increase the scope of possibilities for colloidal crystal engineering with DNA.

**DNA- and field-mediated assembly of magnetic nanoparticles**

In this work, we investigated the effect of magnetic fields on the structures resulting from the assembly of magnetic $Fe_3O_4$ programmable atom equivalents (PAEs). As shown in **Figure 12a**, two sets of PAEs with complementary DNA were assembled in the presence of a static magnetic field. Small angle X-ray scattering (SAXS) data (**Figure 12b**) show that the particles still assemble into body-centered cubic type particle packing. However, unlike the rhombic dodecahedron crystal habits obtained in the absence of a magnetic field, elongated rods are formed when the magnetic field is present. High-resolution electron microscopy studies and 3D tomographic tilt series were done to study the morphology of the crystals assembled under various strength magnetic fields. **Figures 12c** and **d** are snapshots of rods formed from 10-nm and 20-nm PAEs highlighting the ill-defined faceting or rounded surfaces and the many grains that exist within the crystals.

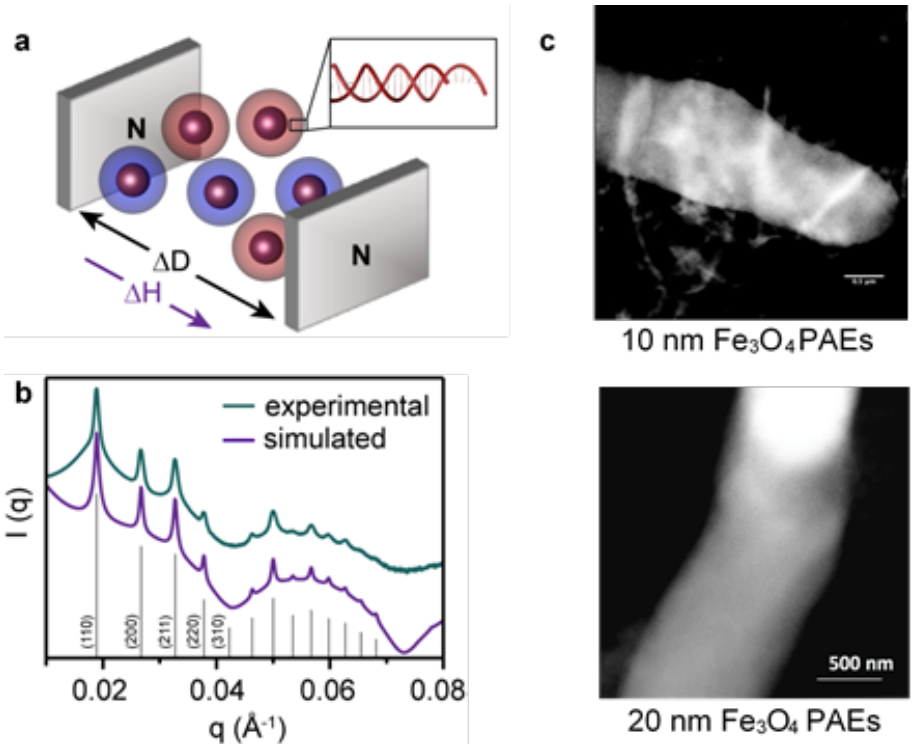


**Figure 12. DNA- and field-mediated assembly of magnetic iron oxide nanoparticles**. (a) Schematic of the experimental set-up. (b) Comparison of experimental and simulated SAXS data confirming assembly into a BCC superlattice. (C) TEM images of aligned rods assembled from (top) 10-nm and (bottom) 20-nm iron oxide PAEs.

**Stabilization of colloidal crystals engineered with DNA**

To realize the potential of DNA-mediated colloidal crystal engineering, it is imperative to develop techniques to increase the stability of DNA-interconnected colloidal crystals. From recent studies, it has been shown that the thermal stability of duplexed oligonucleotides can be increased by the insertion of $Ag^+$ ions in between the nucleobases. Specifically, $Ag^+$ ions replace the hydrogen bonds between the base pairs and form coordinate covalent bonds between $Ag^+$ ions and heterocyclic N atoms. In contrast with other metal ions, which form one specific metallo base pair (e.g., G-$Au^{3+}$-C and T-$Hg^{2+}$-T), $Ag^+$ is less specific and results in a variety of metallo base pairs such as C-$Ag^+$-C, C-$Ag^+$-T, C-$Ag^+$-A, G-$Ag^+$-G, G-$Ag^+$-C, and T-$Ag^+$-T and is, therefore, a candidate to fully metallize DNA duplex strands.

To test our hypothesis, colloidal single crystals of PAEs with body-centered cubic (bcc) structures were synthesized. Rhombic dodecahedra (RDs) were dispersed in 0.5 m $AgNO_3$ solution, where excess $Ag^+$ ions compared to the DNA base pairs were present (**Figure 13a**). At this stage, the effect of $Ag^+$-stabilization can be observed with the naked eye, since the dark suspension of RDs immediately becomes less opaque upon redispersion. This change is caused by the contraction of the DNA particle interconnections, resulting in a reduction of the visible light scattering cross-section of the crystals. Small-angle X-ray scattering (SAXS) confirms this contraction with peak-shifts to higher $q$, a consequence of the decrease in lattice parameter. This contraction occurs due to a shortening of the metallo-DNA duplex, compared to the metal-free form, which has been crystallographically characterized.

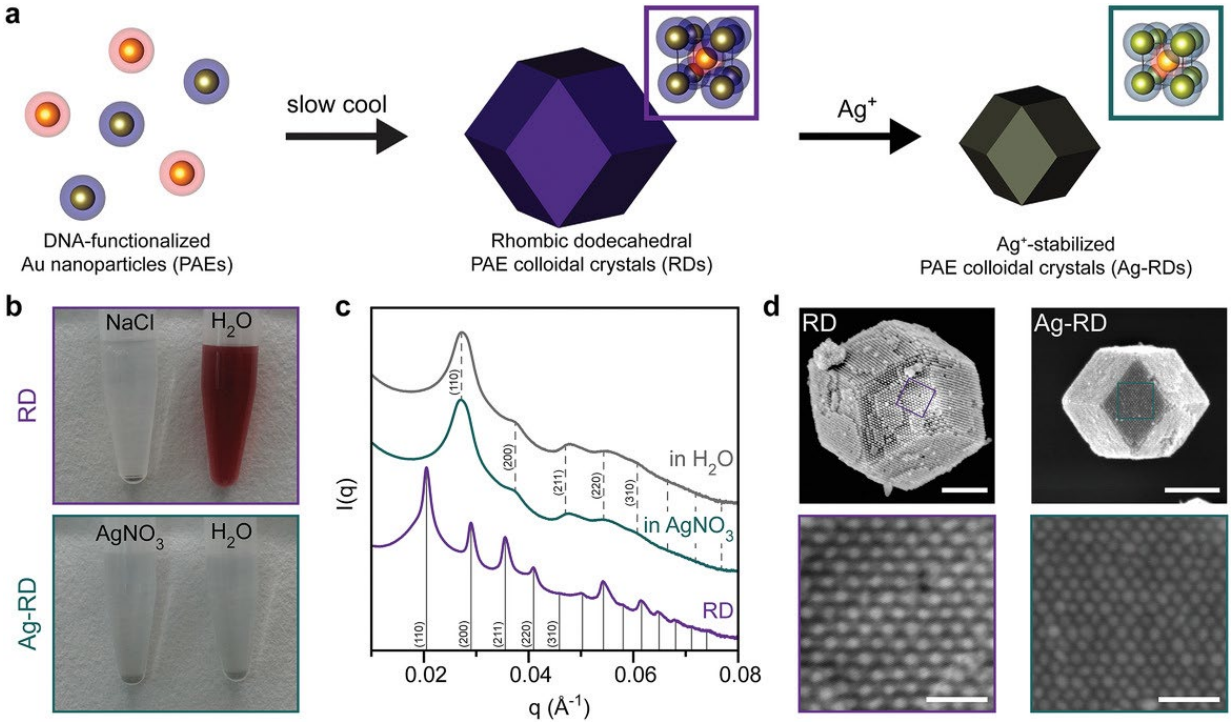


**Figure 13. Stabilization of colloidal crystals with $Ag^+$.** (a) Schematic illustrating the synthesis of $Ag^+$-stabilized PAE crystals (Ag-RDs). (b) In contrast to unmodified PAE crystals (RDs), which are stable in 0.5 M NaCl but dissociate upon resuspension in pure water, Ag-RDs are stable in water. (c) Radially averaged 1D SAXS patterns show lattice contraction upon the transformation into Ag-RDs (green) by transferring RDs (purple) to 0.5 M $AgNO_3$. Ag-RDs are stable in unsalted water (grey). The first five peaks in each pattern were assigned to bcc lattices. (d) SEM images (bottom: high-resolution images of (110) facets from the corresponding squares) confirm the nondestructive contraction of RD to Ag-RD while maintaining crystallinity. Scale bars: (top) 500 nm and (bottom) 100 nm.

Scanning electron microscopy (SEM) also shows that the $Ag^+$-stabilized PAE crystals (Ag-RDs) retain their RD crystal habit and bcc lattice symmetry (**Figure 13d**). Importantly and remarkably, the Ag-RDs can be transferred to pure water without them disassembling, something not possible with untreated DNA-interconnected RDs, which disassemble into colloidal suspensions of particles (**Figure 13b**). Not only does $Ag^+$ stabilize PAE crystals in pure water, but it also prevents their thermal dissociation. $Ag^+$-coordinated base pairs are orders of magnitude stronger than canonical Watson–Crick base pairing. SAXS confirms that the Ag-RDs show no change in lattice structure in water at 90 °C (**Figure 13c**), whereas the bcc SAXS pattern for the

untreated RDs disappears at and above 50 °C. In addition, Ag-RDs maintain their Wulff shape after heat treatment at 90 °C in water for 1 h, and even in the solid state after being heated to 200 °C for 5 h.

Remarkably, the crystalline Ag-RDs were stable in aqueous media over the 5–11 pH range and in many organic solvents (acetone, ethanol, and isopropyl alcohol) as evidenced by SAXS. The robust nature and thermal stability of Ag-RDs in the solid-state will be important as these structures become the basis for device components, where they must be compatible with conventional lithographic procedures, including heat treatment and exposure to various types of photoresists (organic) and developers (typically, basic solutions).

In conclusion, we have developed a general method for stabilizing colloidal crystals made with DNA by integrating $Ag^+$ ions into their DNA bonds. Crystals treated in this manner can be studied and manipulated in media and at temperatures typically incompatible with such materials, and therefore, this technique will increase the scope of their utility, especially in the areas of optics, catalysis, electronics, and other applications where the pristine crystal habit and crystal symmetry are critical for device performance.

**A crosslinking approach for stabilizing stimuli-responsive colloidal crystals engineered with DNA**

To utilize DNA-engineered colloidal crystals as stimuli-responsive materials, methods for stabilizing them in ways that preserve the flexibility and integrity of their DNA linkages must be developed. Interstrand DNA crosslinking reagents covalently cross-link hybridized DNA strands and have been used successfully as drugs since they block DNA replication. We hypothesized that a similar DNA crosslinking strategy could be used to increase the chemical and thermal stability of colloidal crystals engineered with DNA, while maintaining their solvent-dependent responsiveness. To test this hypothesis, two carbon-based reagents, bis-chloroethylnitrosourea (BCNU) and 8-methoxypsoralen (8-MOP), were studied, due to their known abilities to crosslink DNA duplexes. Since these small molecules are comprised of low atomic number elements, we anticipated that they would not significantly affect the chemical composition of the DNA-engineered colloidal crystals, but would stabilize them without significantly affecting the flexibility of the DNA linkers (**Figure 14**).

To test our hypothesis, body-centered cubic (BCC)- and face-centered cubic (FCC)-type crystals were assembled according to literature methods and crosslinked with either BCNU or 8-MOP.

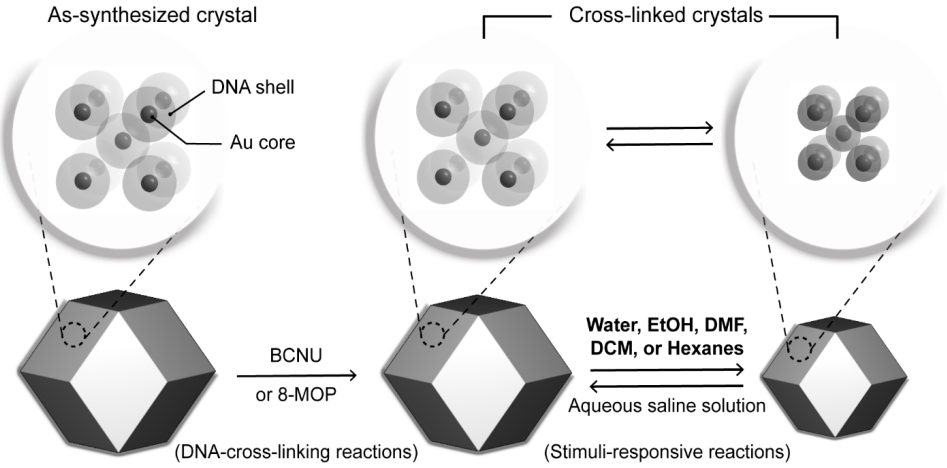


**Figure 14. DNA-crosslinking strategy for stimuli-responsive colloidal crystals**.

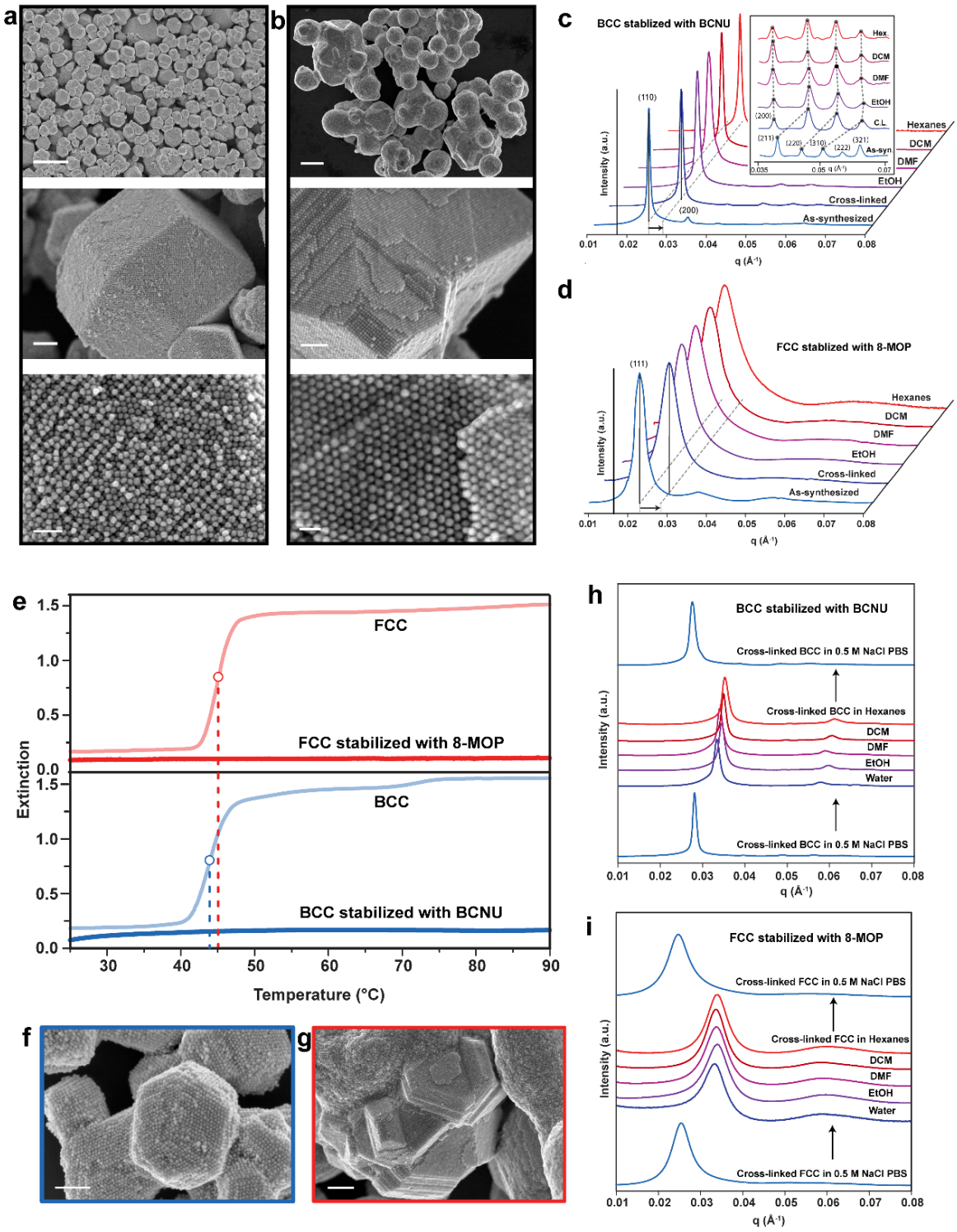


**Figure 15. Colloidal crystals stabilized by cross-linking reagents BCNU and 8-MOP**. (a) SEM images of BCC-type crystals stabilized with BCNU. Scale bars: from top to bottom, 3 μm, 300 nm, and 100 nm, respectively. (b) SEM images of FCC-type crystals stabilized with 8-MOP. Scale bars: from top to bottom, 1 μm, 200 nm, and 100 nm, respectively. (c and d) SAXS patterns of the stabilized crystals treated with various solvents. (e) Melting curves measured by variable-temperature UV–vis spectroscopy. (f and g) SEM images of the BCC- (f) and FCC-type (g) stabilized crystals after the melting experiment. Scale bars: 200 and 300 nm for (f) and (g), respectively. (h and i) Reversible lattice parameter changes of the stabilized crystals measured by SAXS.

Scanning electron microscopy (SEM) images and small-angle X-ray scattering (SAXS) data of the stabilized crystals are shown in **Figure 15a–d**. Remarkably, the surfaces of both BCC- and FCC-type crystals feature the long-range order of the PAEs, even after washing with deionized water and ethanol to remove salts and unreacted chemicals in the cross-linking solution (**Figure 15a and b**). This is in stark contrast to the crystals synthesized in the absence of the crosslinking reagents, which are not stable out of aqueous saline solution, and thus dissociate and lose long-range order after this procedure. These ordered features clearly demonstrate the successful crystal stabilization with the crosslinking reagents. SAXS was used to assess the stability of the cross-linked crystals out of aqueous saline solution and common solvents, such as ethanol (EtOH), *N*,*N*-dimethylformamide (DMF), dichloromethane (DCM), and hexanes, in which the crosslinking reagents are highly soluble (**Figure 15c and d**). The crystals soaked in the solvent were flushed several times with the solvent using a pipette, and each sample was placed on a shaker (at 300 rpm for 24 hours at 25 °C). All crystals retain their crystallinity after such treatment and have essentially identical lattice parameters with the initial stabilized crystals, suggesting they maintain their structural properties under conditions that normally destabilize DNA duplexes.

The thermal stability of the cross-linked crystals was evaluated by carrying out a melting temperature experiment (**Figure 15e**). While the as-synthesized BCC- and FCC-type crystals both display melting transitions at 44 and 45 °C, respectively, as indicated by a sharp increase in absorbance, the stabilized crystals do not melt, even when the temperature is raised to 90 °C, the instrument temperature limit. The stabilized crystals collected after the melting experiments still show long-range order under SEM, as indicated by their sharp edges and the ordering of PAEs on the surfaces (**Figure 15f and g**).

Finally, this crosslinking strategy allows one to study the stimuli-responsive structural characteristics of the colloidal crystals in environments other than PBS. Specifically, the flexibility of the stabilized crystals was studied in various chemical environments using SAXS. Both BCC- and FCC-type crystals show reversible lattice parameter changes when the chemical environment is cycled between PBS solution and pure water (**Figure 15h and i**). Under these conditions, the lattice parameters alternated between 31.5 (PBS) and 26.7 nm (water) for the BCC-type crystals and between 43.3 and 32.5 nm for the FCC-type structures. These changes correspond to a 56.8% (from 7.27 to 3.14 nm) and 72.2% (from 10.63 to 2.96 nm) reduction in the initial DNA length between nearest neighbor particles, respectively. This behavior is fully reversible since the initial lattice parameters are recovered when the crystals are redispersed in the initial PBS solution. The chemical environment of the crosslinked crystals can also be cycled with EtOH, DMF, DCM, and hexanes with similar results (**Figure 15h and i**).

The crystals stabilized using DNA-cross-linking reagents can sustain conditions that would otherwise destabilize colloidal crystals. In addition, they preserve the flexibility of the DNA linkers found within the lattice and their responsiveness to cues in their environment. These findings will facilitate the design and synthesis of stimuli-responsive DNA colloidal crystals, with tunable optical and electronic properties for applications such as laser cavities, nonlinear waveguides, and light emitting diodes.

**Assembly of reconfigurable, sophisticated, and functional superlattices on surfaces**

Under this objective, we report progress on the surface assembly of nanoparticles through the use DNA ligands. In Section D1, we describe a generalizable facet-selective strategy for anchoring PAEs to surfaces and how this strategy enables the fabrication of a dynamically tunable optical metamaterial. In Section D2, we show that the plasmonic arrays assembled from nanocube PAEs

can be used to tune the fluorescence properties of a dye placed in the plasmonic hotspots. Section D3 reveals that the arrangement of surface-bound PAEs can be controlled by modulating the DNA-patterns and densities on the substrate as well as the temperatures.

**3. Precise in-plane arrangement of anisotropic nanocrystals**

Recently, DNA-mediated assembly has been combined with top-down lithography to generate dynamically responsive surface-bound colloidal nanoparticle superlattices. Specifically, it was determined that in order to maintain a satisfactory yield (>95%) of the multi-layered structures,

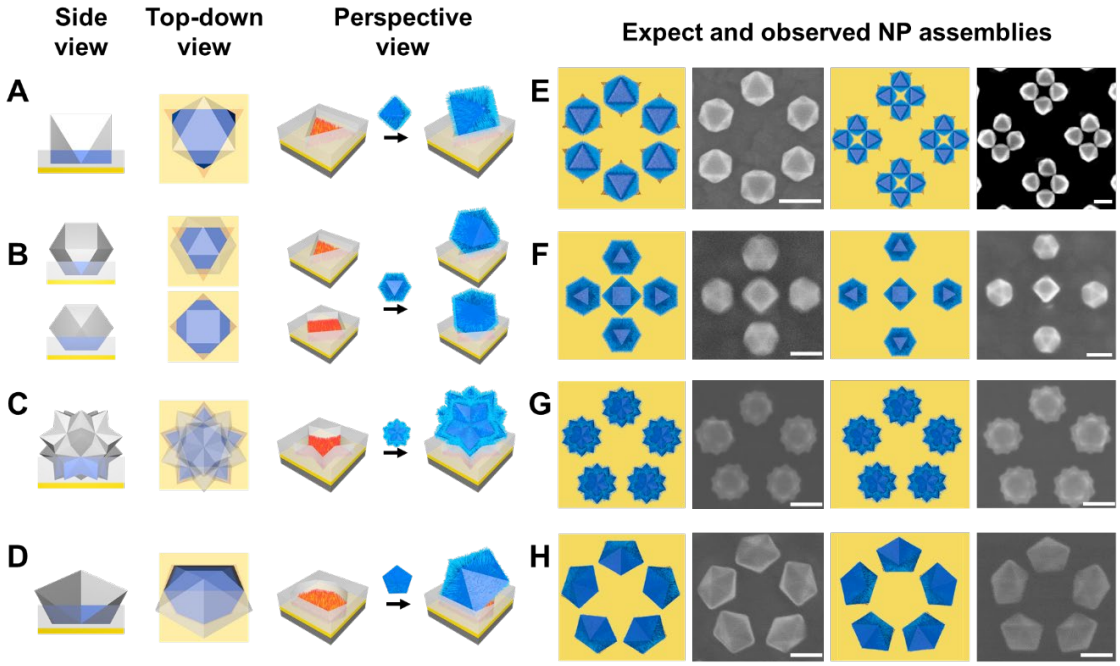


**Figure 16. Template-directed assembly of anisotropic nanoparticles on a surface.** (A–D) Pores in the template layer can be designed to enable specific orientations of nanoparticles via precise facet registration. (E–H) Assembled structures exhibit high fidelity to the nanoparticle arrangement designed via programmed shape and size of pores.

the width of the pores must be ~1.4 times the hydrodynamic diameter (i.e., diameter of the nanoparticle + twice the thickness of the DNA shell), d, of the nanoparticles. For example, two cubes with 80 nm edge lengths could not be placed with an average gap of ~110 nm between them, a limitation that poses a major impediment to the design of optically active metamaterials. To tackle this synthetic challenge, we have developed a novel shallow template strategy where DNA-modified colloidal nanocrystals of almost any shape can be precisely arranged onto a substrate, with control over position, symmetry, orientation, as well as the facet of the nanoparticle interacting with the surface (**Figure 16**). Importantly, this technique can be used to place nanoparticles within 100 nm on one another, enabling one to deliberately adjust the optical coupling between the particles.

With the newly developed shallow pore-based trapping strategy, where the template thickness is less than the dimension of the nanoparticles, we have achieved precise control over the in-plane position and orientation of anisotropic nanoparticles with virtually any shapes. We note that due to lithographic limitations, only pores with prismatic shapes can be fabricated by electron beam lithography (EBL). Therefore, it is nearly impossible to control the orientation of non-prismatic nanoparticles, such as the ones used in this study with deep pores. The newly developed shallow-template strategy, on the other hand, enables partial trapping of the nanoparticles, which results in

previously unobtainable control over particle position and orientation. Importantly, this strategy provides the opportunity to arbitrarily construct surface-bound architectures using nanoparticles as building blocks with sub-10-nm precision in the *x*, *y*, and *z* directions. In addition, the oligonucleotide bonds between the nanoparticles and the substrate can be reversibly expanded and contracted, providing dynamic control over the position of the nanoparticles along the *z* direction.

We designed a proof-of-concept metasurface based on finite-difference time-domain (FDTD)

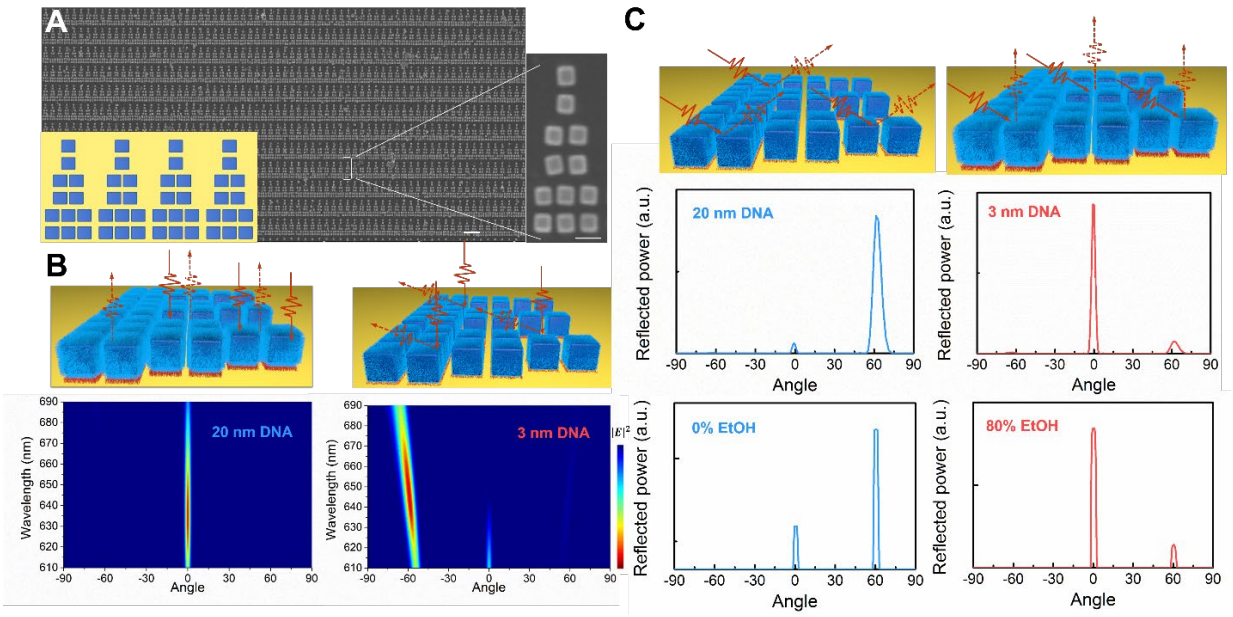


**Figure 17. Optical response dictated by distance between nanoparticles and substrate.** (A) SEM images of nanocubes assembled via the template pore strategy. (B) FDTD simulations of reflection of incoming light as a function of DNA length. (C) Experimental realization of anomalous reflection achieved by varying DNA length using solvent mixtures of ethanol and water.

simulations. The metasurface was composed of 12 cubes arranged into a triangular formation and repeated across the entire substrate. The size of the cubes was chosen to be 80 nm, in part due to optical activity and ease of synthesis. The periods (center of triangle to center of neighboring triangles) in the *x* and *y* directions were 320 and 750 nm, respectively. The distance between the individual cubes in both directions was 30 nm. Such arrangement of nanoparticles leads to a metasurface that forms a spatial phase gradient that can reflect light in an anomalous direction. In **Figure 17a**, we show a scanning electron microscope (SEM) image of the synthesized metasurface demonstrating a high yield (>90 %) and uniformity over a 700 µm × 700 µm area.

We next proceeded to determine if the predicted optical behavior can be realized experimentally. However, from an experimental standpoint, it is challenging to detect the reflected power along the direction of the incident light. Based on the law of reciprocity, we reasoned that if incident 670 nm wavelength light was set at the angle of anomalous reflection (62°), the normal power would be guided to the other side with the same angle of reflection (the law of reflection), while the anomalous power would be guided to ~0°. We confirmed these expectations through another set of FDTD simulations (**Figure 17b**). We then built an angle-resolved measurement setup that allows collimated light to illuminate a sample and measured the power of the reflected light at different collection angles using a rotational arm. The incident wavelength (670 nm) was chosen from the broadband light source with a bandpass filter. After passing through the focus and collimation lenses, the incident light was polarized perpendicular to the *y* direction of the structure.

The sample was placed in the imaging chamber so that the distance between the nanoparticles and the substrate could be dynamically modulated by controlling the DNA bond length using various concentrations of EtOH. We measured the reflected power around the anomalous (~0°) and normal (62°) angles of reflection for both 0% EtOH (20-nm DNA length) and 80% EtOH (3-nm DNA length) (**Figure 17c**). As predicted, changing the EtOH concentration dramatically switched the metamaterial from a mirror-like reflector to an anomalous reflector.

**Tunable fluorescence from dye-modified DNA-assembled plasmonic nanocube arrays**

Colloidal crystal engineering with DNA is emerging as a robust method for controlling crystal composition, lattice parameter, and habit. In addition to being useful for preparing three-dimensional assemblies, the technique can be combined with top-down lithography (e.g., electron beam lithography, EBL) to position nanoparticles on substrates, which allows one to synthesize two-dimensional structures not attainable through conventional lithographic techniques. For example, arrays of single crystalline nanocubes that display strong coupling between plasmonic gap modes and photonic lattice modes have been assembled on gold-coated silicon substrates. Here, we explore how such structures, combined with DNA structural sensitivity to solvent, can be used to modify the emission properties of dyes strategically placed into the gap hotspots of the

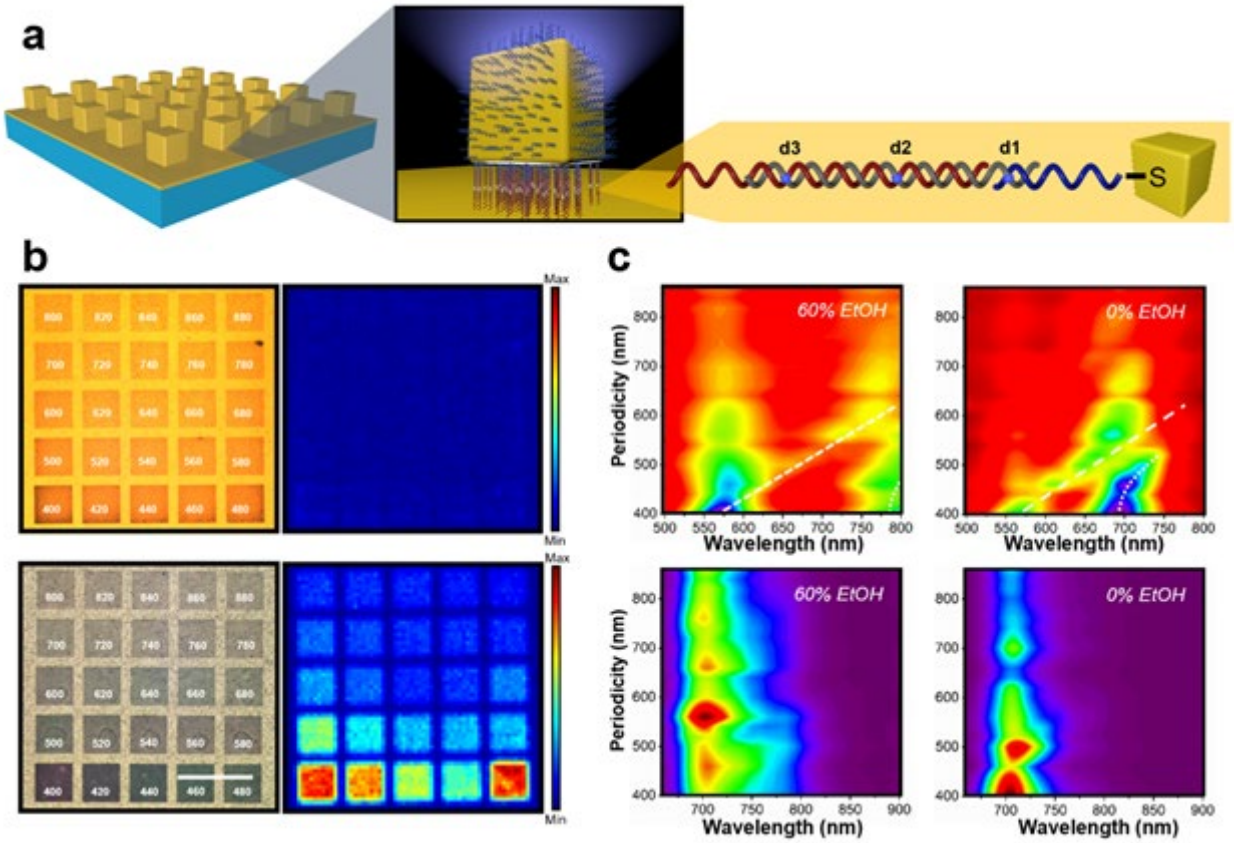


**Figure 18. Photoluminescence (PL) of plasmonic nanocube arrays**. (a) Assembly scheme. Dyes are attached to a specific base on the DNA, which holds the nanocubes to the substrate. Nanocubes are then arranged in a periodic lattice through EBL design. (b) PL maps of nanocube arrays at different periodicities (bottom) compared to a control sample (dye-labeled linker without nanocubes, top). (c) Reflection and PL spectra of assemblies at 60% (left) and 0% (right) ethanol as a function of periodicity.

particle array structure (**Figure 18a**). These studies reveal four novel and attractive characteristics of such assemblies, which enable precise control over structural parameters that affect the

plasmonic resonances, coupling strength, and emission enhancement. First, the emission of the dye can be controlled through lattice spacing, which controls the lattice mode resonance. Second, the gap mode resonance, tunable through DNA length and solvent, can be used to control dye emission. This is important because it allows one to do so without irreversibly changing lattice structure. Third, the position of the dye, which can be controlled through chemical attachment to specific bases, can be fine-tuned with sub-nm precision and used to influence and optimize emission. Finally, using multiple different dyes, emission of each can be regulated through an understanding of these effects and coupling to specific structures.

To experimentally characterize these assemblies, dye-labeled nanocube arrays of periodicities from 400 to 880 nm were assembled onto the same substrate. PL maps of these assemblies were taken at 700 nm (**Figure 18b**). PL intensity was then examined as a function of lattice periodicity and ethanol concentration (**Figure 18c**). At 60% ethanol, the dye emission and laser excitation only overlap with lattice modes, which depend on periodicity. The PL maximum occurs at a periodicity of 560 nm, where the strong enhancement is attributed to coupling between the dye emission and lattice mode around 700 nm. A smaller PL peak occurs for a periodicity of 460 nm and, in this case, is due to coupling between the laser and the lattice mode around 630 nm. These peaks occur at periodicities for which the lattice mode overlaps with either the incident laser or dye emission wavelengths and are known as excitation and emission enhancement, respectively. At 0% ethanol, PL maxima occur for 400 and 500 nm periodicities. In both cases, emission enhancements are observed, but this time, in the presence of the gap mode occurring near 700 nm. Only a gap mode exists for 400 nm periodicity, but for 500 nm periodicity the dye emission is in the regime of lattice-gap coupling and could be interacting with both modes simultaneously. The ability for two spectrally separate, yet spatially overlapping, tunable modes, to interact with the dye could be used to simultaneously produce excitation and emission enhancements.

To explore the potential for such lattices in tunable optics, 400 nm period array samples with two dyes under the nanocubes were prepared. These assemblies contained two dyes physically in the same proximity to the cubes but randomly mixed within the plane (**Figure 19**, top). Emission was recorded after excitation of the sample with a green laser (**Figure 19**, bottom). One can clearly see that ethanol can contract the DNA and shorten the gap distance, which in turn diminishes the ATTO 680 emission with little effect on that of ATTO Rho101. Indeed, at 0% ethanol, the gap mode is spectrally matched with the emission maximum of ATTO 680, causing enhanced emission near 700 nm, while at 60% ethanol, the gap mode moves away from the dye emission, resulting in little fluorescence. In contrast, the emission of ATTO Rho101 is relatively unaffected by ethanol since it is spectrally mismatched with the gap mode at all ethanol concentrations. It has a large peak near 609 nm, at all ethanol concentrations, because of its inherently high quantum yield coupled to off-resonant enhancement.

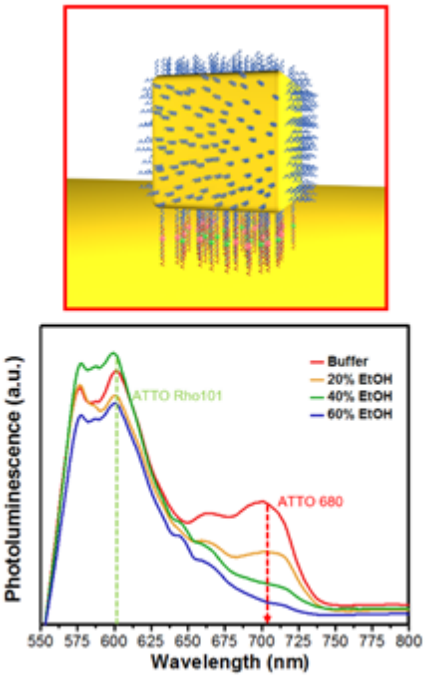


**Figure 19. Nanocubes functionalized with two dyes**. (Top) Schematic illustration of nanocube labeled with two dyes, ATTO Rho 101 (green) and ATTO 680 (red). (Bottom) PL spectra of the sample upon excitation with a green laser.

Therefore, by changing the concentration of ethanol, the intensity ratio of the two dyes can be tuned, yielding a tunable light source.

**Temperature-dependent configurations in 2D nanoparticle arrays**

The 2D assembly of nanoparticles on DNA-functionalized landing sites has been demonstrated by lithographically defined trenches or islands. We previously reported on the use of the electron beam irradiation of DNA monolayers to drive size-selective assembly and, more recently, the directed assembly of DNA-functionalized nanorods with control over position and orientation. The primary innovation in this technique is that it allows for in-plane reorganization of the nanoparticle arrays since there is no physical template. The resulting arrays are stimuli-responsive and represent a critical step toward reconfigurable two-dimensional nanoparticle assemblies. Here, we develop at new technique that combines these two approaches. We first use high-resolution DNA patterning on suspended silicon nitride membranes to allow nanometer-scale patterning and then couple that with assembly from a bimodal suspension of small (30 nm) and large (80 nm) spherical nanoparticles.

The assembly behavior of the mixed suspension is probed by patterning arrays of circular patterns with a range of sizes, array spacings, and electron beam dose (which results in different

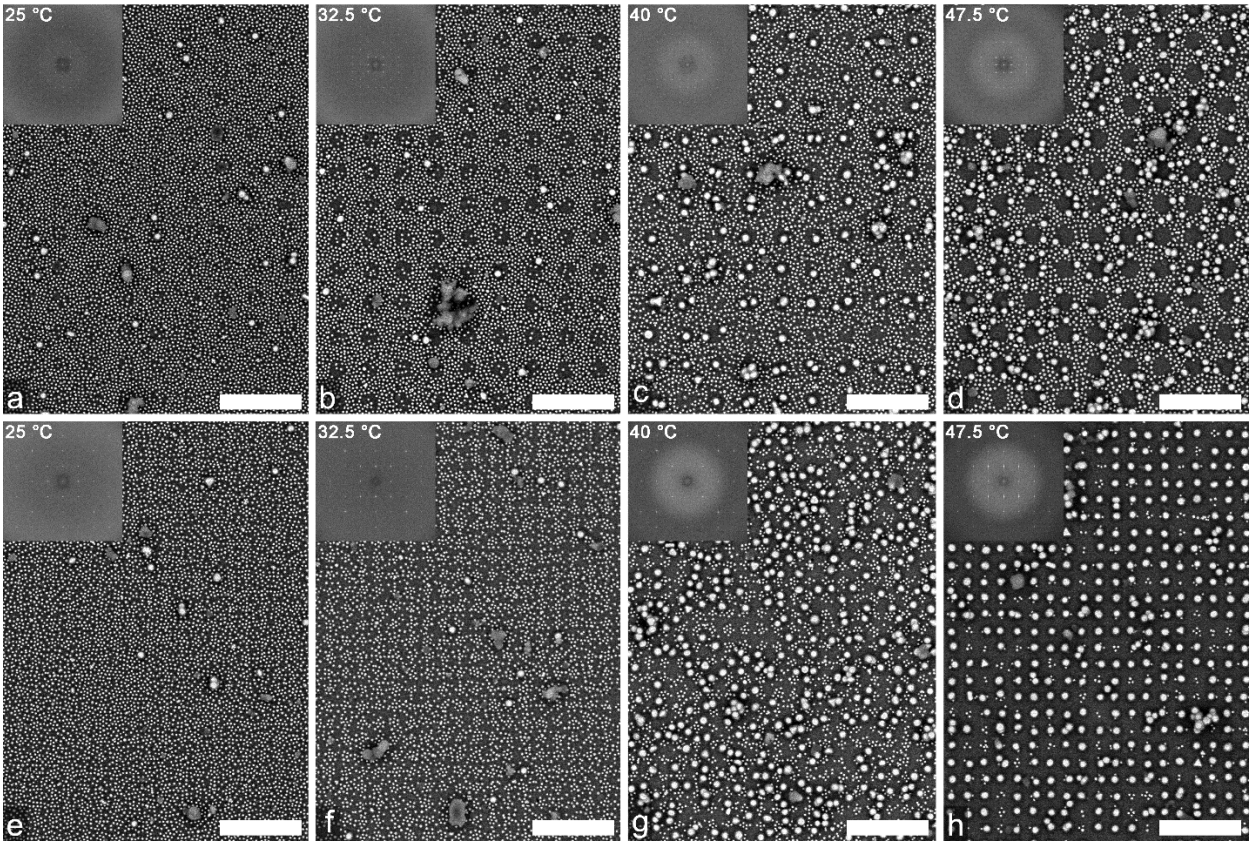


**Figure 20. Circle array patterns with nanoparticles.** Arrays were assembled from (a-d) a bimodal suspension with 220 nm diameter, x/y pitch of 400 nm, and 900 μC $cm^{-2}$ electron dose and (e-h) a bimodal suspension of spherical nanoparticles on a circle array pattern with 200 nm circle diameter, x/y pitch of 200 nm, and 1000 μC $cm^{-2}$ electron dose. Scale bars are 1 μm.

DNA densities). Nanoparticles from the mixed suspension were then assembled on these substrates under different assembly temperatures, locked in place by silica embedding and analyzed by SEM

to understand the interaction between the pattern geometry, DNA density, and nanoparticle size. Two examples of the emergent behavior are shown, where the primary differences are the circle diameter and the array spacing. From the previous size-selective assembly behavior, we expected that large particles would predominate at higher temperatures due to the larger surface area for interaction with the substrate and small particles would predominate at low temperature due to the overall higher surface coverage. However, given the geometric confinement resulting from patterning, a more interesting set of transitions is observed.

The first example (**Figure 20a-d**) shows an array of 220-nm circles and a x/y pitch of 400 nm, and the second (**Figure 20e-h**) shows an array of 200-nm circles and a x/y pitch of 200 nm. At low temperature, these samples start as a relatively disordered film dominated by small particles, but transition to very different architectures at higher temperature. In the first example, the large particles are segregated to the lower density regions at intermediate temperature (**Figure 20c**) and, in the second example, the large particles are segregated to the interstitial regions at high temperature (**Figure 20h**). The parameter space for these experiments is quite large, but we expect a range of interesting reconfigurable architectures can be achieved by coupling different pattern geometries with nanoparticle of different sizes and shapes. Such structures are expected to exhibit concomitant changes in optical properties for application as reconfigurable metasurfaces.

**CHANGES IN RESEARCH OBJECTIVES, if any:**

None

**SUPPORTED PERSONNEL**

The Mirkin Group

Chad Mirkin, PI
Anindita Das, postdoctoral fellow
Seungkyu Lee, postdoctoral fellow
Sarah Park, postdoctoral fellow, (IIN fellowship)
Devleena Samanta, postdoctoral fellow
Heather Calcaterra, graduate student, (CBES fellowship)
Christine Laramy, graduate student
Yuanwei Li, graduate student
Taegon Oh, graduate student
Lin Sun, graduate student
Zachary Urbach, graduate student, (NDSEG fellowship)
Shunzhi Wang, graduate student
Cindy Zheng, graduate student
Wenjie Zhou, graduate student
Jinghan Zhu, graduate student

The Aydin Group

Koray Aydin, Co-PI
Wisnu Hadibrata, graduate student
Edgar Palacios, graduate student

The Dravid Group

Vinayak Dravid, Co-PI
Chamille Lescott, graduate student
Jingshan Du, graduate student
Will Kellogg, graduate student
Kelly Parker, graduate student, (NSF-GRF)
Roberto dos Reis, Dravid Group Scientific Officer, (unfunded)

**COLLABORATIONS**

1. Advanced imaging was performed with individuals associated with the NU*ANCE* Center at Northwestern University, including Eric Roth, Dr. Ben Myers, Dr. Xiaobing Hu, and Dr. Paul Smeets, and AFRL researchers, including Dr. Larry Drummy and Dr. Cheri Hampton
2. Simulations of DNA-mediated crystallization behavior were conducted with Prof. Monica Olvera de la Cruz (Northwestern University)
3. Grazing incidence small angle x-ray scattering (GISAXS) experiments were conducted in collaboration with Dr. Byeongdu Lee (Argonne National Laboratory)
4. DFT calculations of polyelemental nanoparticles were performed with Prof. Chris Wolverton (Northwestern University)
5. Metal-organic framework (MOF) experiments: Prof. Fraser Stoddart (Northwestern

University) and Prof. Omar Farha (Northwestern University)
6. Structural biology work with Jonathan Remis (Structural Biology Facility, Northwestern University)

**PUBLICATIONS**

1. Zhou, W.; Lin, Q.-Y.; Mason, J. A.; Dravid, V. P.; Mirkin, C. A. "Design Rules for Template-Confined DNA-Mediated Nanoparticle Assembly," *Small*, **2018**, *14*, 1802742, doi: 10.1002/smll.201802742.
2. Seo, S. E.; Girard, M.; Olvera de la Cruz, O.: Mirkin C. A. "Non-Equilibrium Anisotropic Colloidal Single Crystal Growth With DNA," *Nat. Comm*. **2019**, *9*, 4558, doi: 10.1038/s41467-018-06982-9
3. Laramy, C. R.; O'Brien, M. N.; Mirkin, C. A. "Crystal Engineering with DNA," *Nat. Rev. Mater.*, **2019**, *4*, 201-224, https://doi.org/10.1038/s41578-019-0087-2.
4. Seo, S.; Girard, M.; Olvera de la Cruz, M.; Mirkin, C. A. "The Importance of Salt-Enhanced Electrostatic Repulsion in Colloidal Crystal Engineering with DNA," *ACS Cent. Sci.*, **2019**, *5*, 186–191, doi: 10.1021/acscentsci.8b00826
5. Oh. T.; Park, S. S.; Mirkin, C. A. "Stabilization of Colloidal Crystals Engineered with DNA," *Adv. Mat.*, **2019**, 31, 1805480, doi: 10.1002/adma.201805480.
6. Laramy, C. R.; Lopez-Rios, H.; O'Brien, M. N.; Girard, M.; Stawicki, R. J.; Lee, B.; Olvera de la Cruz, M.; Mirkin, C. A. "Controlled Symmetry Breaking in Colloidal Crystal Engineering with DNA," *ACS Nano*, **2019**, *13*, 1412–1420, doi: 10.1021/acsnano.8b07027.
7. Chen, P.-C.; Liu, M.; Du, J. S.; Meckes, B.; Wang, Shunzhi; Lin, H.; Dravid, V. P.; Wolverton, C.; Mirkin, C. A. "Interface and Heterostructure Design in Polyelemental Nanoparticles," *Science*, **2019**, *363*, 959-964. doi: 10.1126/science.aav4302.
8. McMillan, J. R., Hayes, O. G.; Winegar, P. H.; Mirkin, C. A. "Protein Materials Engineering with DNA," *Acc. Chem. Res.*, **2019**, doi: 10.1021/acs.accounts.9b00165.
9. Girard, M.; Wang, Shunzhi; Du, J. S.; Das, A.; Huang, Z.; Dravid, V. P.; Lee, B.; Mirkin, C. A.; Olvera de la Cruz, M. "Particle Analogs of Electrons in Colloidal Crystals," *Science*, **2019**, *364*, 1174-1178, doi: 10.1126/science.aaw8237.
10. Lee, S.; Zheng, C. Y.; Bujold, K. E.; Mirkin, C. A. "A Crosslinking Approach to Stabilizing Stimuli-Responsive Colloidal Crystals Engineered with DNA," *J. Am. Chem. Soc.*, **2019**, doi: 10.1021/jacs.9b06106.
11. Myers, B. D.; Palacios, E.; Myers, D. I.; Butun, S.; Aydin, K.; Dravid, V. P.; "Stimuli-Responsive DNA-Linked Nanoparticle Arrays as Programmable Surfaces," *Nano Letters*, **2019**, *19*, 4535-4542, doi: 10.1021/acs.nanolett.9b01340
12. Hanson, E. D.; Lilley, L. M.; Cain, J. D.; Shiqiang, H.; Palacios, E.; Aydin, K.; Wolverton, C.; Meade, T.; Dravid, V. P.; "Phase engineering and optical properties of 2D MoSe2: Promise and pitfalls" *Materials Chemistry and Physic*s, **2019**, 225, 219-226, doi:10.1016/j.matchemphys.2018.11.069
13. Parker, K. A.; Bobbala, S.; Drachuk, I. V.; Mirau, P. A.; Chavez, J. L.; Drummy, L. F.; Scott, E. A.; Dravid, V. P. "Soft Microscopy Of Macromolecules: Correlative Imaging and Enhancing Contrast," *Proceedings of Microscopy and Microanalysis 2018"*, in press.
14. Zheng, C. Y.; Palacios, E.; Zhou, W.; Hadibrata, W.; Sun, L.; Huang, Z.; Schatz, G. C.; Aydin, K.; Mirkin, C. A. "Tunable Fluorescence from Dye-Modified DNA-Assembled Plasmonic Nanocube Arrays," *Adv. Mat*., **2019**, in press.

15. Nam, K. W.; Park, S. S.; dos Reis, R.; Dravid, V. P.; Mirkin, C. A.; Stoddart, J. F. "Conductive 2D Metal-Organic Framework for High-Performance Cathodes in Aqueous Rechargeable Zinc Batteries," *Nat. Energy*, **2019**, submitted.
16. Wang, Shunzhi; Park, S. S.; Lin, H.; Chen, P.-C.; Roth, E. W. Mirkin, C. A. "Colloidal Crystal Engineering with Metal-Organic Framework Nanoparticles and DNA," *Nature Mater.,* **2019**, submitted.

**PRESENTATIONS**

1. Chad A. Mirkin, Metals in Medicine Gordon Research Conference, Andover, NH, "Ushering in the Digital Drug Design Revolution with Spherical Nucleic Acid Nanoparticle Conjugates" (2018).
2. Chad A. Mirkin, 13th Sino-US Forum on Nanoscale Science and Technology, Chengdu, China, "MegaLibraries: Changing the Pace of Materials Discovery" (2018).
3. Chad A. Mirkin, MITRE Nanomedicine Workshop, McLean, VA, "The Convergence of Nanoscience and Nanomedicine: New Approaches for Tracking and Treating Disease" (2018).
4. Chad A. Mirkin, Fall 2018 ACS Meeting, Boston, MA, "Structure-function relationships in the development of immunotherapeutic agents" (2018).
5. Chad A. Mirkin, Fall 2018 ACS Meeting, Boston, MA, "Controlling Cellular Architecture and Fate with Nanopatterned Substrates" (2018).
6. Chad A. Mirkin, Fall 2018 ACS Meeting, Boston, MA, "Colloidal crystal engineering with high information content polymers" (2018).
7. Chad A. Mirkin, Fall 2018 ACS Meeting, Boston, MA, "Combinatorial nanoscience: Expanding the materials genome" (2018).
8. Chad A. Mirkin, Sanofi Scientific Symposium, Boston, MA, "Rational Vaccinology: In Pursuit of the Perfect Vaccine" (2018).
9. Chad A. Mirkin, Aggarwal Lecture in Polymer Science, Cornell University, Ithaca, NY, "Crystal Engineering with DNA" (2018).
10. Chad A. Mirkin, Air Force Research Laboratory Award Banquet Keynote, Dayton, OH (2018).
11. Chad A. Mirkin, Remsen Award, Baltimore, MD, "Colloidal Crystal Engineering with DNA" (2018).
12. Chad A. Mirkin, BUnano Symposium, Boston University, Boston, MA, "Rational Vaccinology: In Pursuit of the Perfect Vaccine" (2018).
13. Chad A. Mirkin, Materials Research Society Fall Conference, Boston, MA, "Colloidal Crystal Engineering with DNA—Creating a Genetic Code for Materials Design" (2018).
14. Chad A. Mirkin, Materials Research Society Fall Conference, Boston, MA, "Megalibraries—Changing the Pace of Materials Discovery" (2018).
15. Chad A. Mirkin, **AFOSR Natural Materials, Systems & Extremophiles Program Review, Niceville, FL "Reconfigurable Matter from Programmable Atom Equivalents" (2018).**
16. Chad A. Mirkin, **AFOSR Natural Materials, Systems & Extremophiles Program Review, Niceville, FL "A 4D Nanoprinter for Making and Manipulating Macroscopic Material" (2018).**
17. Chad A. Mirkin, **Pennsylvania University CT3N Symposium, Philadelphia, PA, "**Rational Vaccinology: In Pursuit of the Perfect Vaccine" (2018).

18. Chad A. Mirkin, 3M Lectureship, Minneapolis, MN, “MegaLibraries: Changing the Pace of Materials Discovery” (2018).
19. Chad A. Mirkin, University of Miami, Coral Gables, FL, “Crystal Engineering with DNA” (2018).
20. Chad A. Mirkin, W. Allan Powell Lecture, University of Richmond, Richmond, VA, “Rational Vaccinology: In Pursuit of the Perfect Vaccine” (2019).
21. Chad A. Mirkin, Theodore William Richards Award and Medal Award Ceremony and Lecture, Boston, MA, “Rational Vaccinology: In Pursuit of the Perfect Vaccine” (2019).
22. Chad A. Mirkin, Pittcon 2019, Philadelphia, PA, “Rational Vaccinology: In Pursuit of the Perfect Vaccine” (2019).
23. Chad A. Mirkin, Pittcon 2019, Philadelphia, PA, “Peering into Cells with Nanotechnology” (2019).
24. Chad A. Mirkin, Spring 2019 ACS Meeting, Orlando, FL, “Rational vaccinology: In Pursuit of the Perfect Vaccine” (2019)
25. Chad A. Mirkin, Spring 2019 ACS Meeting, Orlando, FL, “High-index Facet Particle Shape Regulation by Dealloying” (2019)
26. Chad A. Mirkin, Spring 2019 ACS Meeting, Orlando, FL, “Rational Metamaterial Design Through Colloidal Crystal Engineering” (2019)
27. Chad A. Mirkin, Bioengineering Colloqui, Ecole Polytechnique Federale de Lausanne, Lausanne, Switzerland, “Rational Vaccinology: In Pursuit of the Perfect Vaccine” (2019)
28. Chad A. Mirkin, Sanders Tri-Institutional Chemical Biology Seminar Series, New York, NY, “Rational Vaccinology: In Pursuit of the Perfect Vaccine” (2019).
29. Chad A. Mirkin, Bigeleisen Lecture, SUNY Stony Brook, “Colloidal Crystal Engineering with DNA” (2019).
30. Chad A. Mirkin, Eli Ruckenstein Lecture, University of Buffalo, Buffalo, NY, “Rational Vaccinology: In Pursuit of the Perfect Vaccine” (2019).
31. Chad A. Mirkin, Spring 2019 MRS Meeting, Phoenix, AZ, “Polymer Nanoreactors—Vehicles to Control and Observe Nanoparticle Formation” (2019).
32. Chad A. Mirkin, Spring 2019 MRS Meeting, Phoenix, AZ, “Exploring the Materials Genome Through Nanomaterial Megalibraries” (2019).
33. Chad A. Mirkin, University of Rochester, Rochester, NY, “Colloidal Crystal Engineering with DNA" (2019).
34. Chad A. Mirkin, Harrison Howe Award Lecture, University of Rochester, Rochester, NY, “Megalibraries: Discovering New Materials and Cellular Functions" (2019).
35. Chad A. Mirkin, National University of Singapore Seminar, Singapore, “Megalibraries: New Tools for Studying the Materials Genome and Cellular Function” (2019).
36. Chad A. Mirkin, Technical Institute of Physics and Chemistry, Chinese Academy of Sciences, Beijing, China “Exploring the Materials Genome with MegaLibraries” (2019).
37. Chad A. Mirkin, A 4D Nanoprinter MURI Site Visit Program Review, Evanston, IL “Printing Multifunctional 3D Structures of Hard and Soft Materials” (2019).
38. Chad A. Mirkin, Midwest-China Symposium & the 12th Annual Yao Yuan Biotech-Pharma Symposium, University of Chicago, Chicago, IL “Four Technologies that Will Change the World” (2019).
39. Chad A. Mirkin Polymers Gordon Research Conference, South Hadley, MA, “Tip- and Polymer-directed Synthesis of Nanoclusters” (2019).

40. Chad A. Mirkin Midwest Ideas Forum of Private Institutions, Evanston, IL, “Startups in an innovative field” (2019).
41. Koray Aydin. PQE Physics of Quantum Electronics, Snowbird, UT, “Programmable and Reconfigurable Metamaterials and Metasurfaces based on DNA-mediated nanoparticle assembly” (2019).
42. Koray Aydin, 2019 MRS Spring Meeting, Phoenix, AZ, “Anisotropic 2D Layered Materials: Photonic, Plasmonic and Phononic Properties from Visible to IR” (2019).
43. Vinayak P. Dravid. International Conference on Materials for Advanced Technologies, Singapore, “Experimental Materials Genome at the Nanoscale” (2019).
44. Vinayak P. Dravid. Microscopy and Microanalysis, Portland, OR, “Hybrid” Microscopy: Multimodal, Correlative and Dynamic Characterization of Soft and Hybrid Structures” (2019).
45. Vinayak P. Dravid. Chevron, San Ramon, CA, “Nanocombinatorics: Multicomponent Multicomponent Multiplexed and Multifunctional Nanostructures” (2019).
46. Vinayak P. Dravid, Reliance Industries, India, “Research Facilities as an Innovation Ecosystem” (2019).
47. Vinayak P. Dravid, ChemPhysMat, India,“Inspiration from Professor CNR Rao: Experimental Materials Genome at the Nanoscale,” (2019).
48. Vinayak P. Dravid. Southern University of Science and Technology, Shenzhen, China. “Multiplexed Nanopatterning of Multifunctional Materials” (2019).
49. Vinayak P. Dravid. International Workshop on Materials Genomics, Materials Genome Institute, Shanghai University, Shanghai, China, “Teaching ‘Old’ Material ‘New’ Tricks: Nanopatterning and Microscopy of Multifunctional Materials” (2018).
50. Vinayak P. Dravid, Center for Hierarchical Materials Design Materials Microscopy Data Workshopm Northwestern University, “Welcome to NUANCE, SHyNE, and the VPD Group!” (2018).
51. Cindy Zheng, Edgar Palacios, Wenjie Zhou, Wisnu Hadibrata, George Schatz, Koray Aydin, Chad Mirkin. Gordon Research Conference: Crystal Growth and Assembly, Manchester, NH, “Tunable Fluorescence from Dye-Modified DNA-Assembled Plasmonic Nanocube Arrays” (2019).
52. Wenjie Zhou. Chad A. Mirkin. ACS Spring 2019 Meeting, “Template-Confined DNA-Mediated Nanoparticle Assembly on Surfaces” (2019)
53. Wenjie Zhou, Zizhuo Liu, Qingyuan Lin, Ziyin Huang, Haixin Lin, Koray Aydin, Chad A. Mirkin. Gordon Research Conference: Crystal Growth and Assembly, Manchester, NH, “DNA-Mediated, Single Particle Control of Colloidal Nanocrystals within Superlattices on Surfaces” (2019) poster.
54. Shunzhi Wang. Martin Girard, Jingshan S. Du, Anindita Das, Byeongdu Lee, Chad A. Mirkin, Monica Olvera de la Cruz, Gordon Research Conference: Crystal Growth and Assembly, Manchester, NH, “Colloidal Crystal Metallicity” (2019) poster.
55. Taegon Oh, Sarah S. Park, Chad A. Mirkin. MRS Spring Meeting & Exhibit, Phoenix, AZ “Matrix-Free Stabilization of DNA-Engineered Colloidal Crystals with Silver Ions.”, USA, (2019), poster.
56. Taegon Oh, Jessie C. Ku, Jae-Hyeok Lee, Mark C. Hersam, Chad A. Mirkin. MRS Spring Meeting & Exhibit, Phoenix, AZ, “Control over Colloidal Supercrystal Formation with Density Layers” (2019), poster.

57. Taegon Oh. SPIE-MRSEC Student Seminar Series, Evanston, IL, "Advanced Production Processes for Colloidal Crystals Engineered with DNA" (2018).
58. Jinghan Zhu, Youngeun Kim, Haixin Lin, Shunzhi Wang, Chad A. Mirkin. MRS Fall Conference, Boston, MA, "Reconfigurable Nanoparticle Superlattices with Tunable DNA Bonds" (2018).
59. Jingshan S. Du. 43rd International Precious Metals Institute Annual Conference, Reno, NV, "Accelerating Complex Nanomaterial Discovery Using A Combinatorial Library Approach" (2019).
60. Jingshan S. Du, 36th John E. Hilliard Symposium, Northwestern University, Evanston, IL, "Classical Electron Equivalent Nanoparticles in Metal-like Colloidal Crystals" (2019).
61. Jingshan S. Du, Vinayak P. Dravid, Chad A. Mirkin. Gordon Research Conference & Seminar: Crystal Growth and Assembly, Manchester, NH, "Polymer Nanoreactor Approach for Combinatorial Investigation of Complex Nanoparticles" (2019).
62. Jingshan S. Du, Vinayak P. Dravid, Chad A. Mirkin. 257th American Chemical Society National Meeting, Orlando, FL, "Attoliter Polymer Reactors as Combinatorial Tools for Understanding Alloy Nanocrystal Structure−Function Relationship" (2019).
63. Kelly A. Parker. Society of Women Engineers Annual Conference (WE18), Minneapolis, MN, "Seeing the Invisible: Targeted Staining for Improved Contrast of Macromolecules in Electron Microscopy" (2018).
64. Kelly A. Parker. Microscopy & Microanalysis, Portland, OR, "Soft Microscopy of Macromolecules: Enhancing Contrast" (2019).
65. William R. Kellogg. Microscopy & Microanalysis, Baltimore, MD, "Investigation of Electron Beam Deposition Parameters within a Scanning Electron Microscope" (2018).

**AWARDS**

Chad A. Mirkin. Friendship Award (2019).
Chad A. Mirkin. Theodore William Richards Medal (Northeastern Section of the ACS) (2018).
Chad A. Mirkin. Netherlands Award for Supramolecular Chemistry (2019).
Chad A. Mirkin. SCI Perkin Medal (2019).
Vinayak Dravid. Fellow, Micoanalysis Society, Inaugural Class of 2019.
Jingshan S. Du. IPMI Sabin Metal Ron Bleggi Award, International Precious Metals Institute (2019).
Jingshan S. Du. Perkin Scholar, Society of Chemical Industry America (2019).
Christine Laramy. 2018 IIN Outstanding Researcher Award, International Institute of Nanotechnology (2018)
Chamille Lescott. Ryan Fellowship, International Institute of Nanotechnology (2019).
Sarah Park. 2018 IIN Outstanding Researcher Award, International Institute of Nanotechnology (2018)
Kelly Parker. Ryan Fellowship, International Institute of Nanotechnology (2019).
Kelly Parker. National Science Foundation Graduate Research Fellowship (2018).
Devleena Samanta. HHMI Hannah Gray Fellow Finalist (2019)
Edgar Palacios. 2018 IIN Outstanding Researcher Award, International Institute of Nanotechnology (2018)
Shunzhi Wang. 2018 IIN Outstanding Researcher Award, International Institute of Nanotechnology (2018)

**INTERACTIONS/TRANSITIONS**

**Patent Applications**

1. "Photonic Crystal Built with Nanoparticles and Spacer Groups" Chad A. Mirkin, George C. Schatz, Haixin Lin, Lin Sun, PCT/US2019/015965, Jan. 1, 2019.
2. "A Crosslinking Approach to Stabilizing Stimuli-Responsive" Katherine Bujold, Seungkyu Lee, Chad Mirkin, Cindy Zheng, Provisional, 62/851,697, May 23, 2019.

**YEAR 3**
**Cover Page**
**To:** Dr. Aura Gimm, jung-hwa.gimm.1@us.af.mil
**Subject:** Annual Report
**Contract/Grant Title:** Reconfigurable Matter from Programmable Atom Equivalents
**Contract/Grant #:** FA9550-17-1-0348
**Reporting Period:** August 15, 2019-August 14, 2020

**ABSTRACT**

DNA-functionalized colloidal nanoparticles, called programmable atom equivalents or PAEs, can be assembled into sophisticated architectures through their surface DNA ligands. The central theme of our ongoing work under this grant is to design, assemble, and study reconfigurable colloidal crystals composed of a diverse set of functional PAE building blocks.

In Year 3, we have made significant advances toward the aims of this grant, and these were reported to the scientific community through publications in high-impact journals and presentations around the world. In particular, we have developed a strategy to synthesize high-index-faceted single- and multi-metallic nanoparticles through the underpotential deposition of trace amounts of shape-regulating metals. We have also created a universal strategy to perform secondary growth on anisotropic gold nanoparticles with controlled growth on the corners, edges, or facets of the seed nanoparticles, thus creating a library of designer nanoparticles. Toward our goal of reconfigurable nanoparticle superlattices, we have developed a supramolecular DNA dendron-based system that can switch between PAEs and electron equivalents through hierarchical assembly, utilizing toehold displacements to assemble and disassemble the supramolecular dendrimer construct. Furthermore, we have made progress in our goal to rigorously characterize our nanoparticle superlattices, particularly in cases where the size of the colloidal crystals has limited the characterization techniques available. Here, by employing a substantially decreased cooling rate during superlattice formation, we were able to grow crystals greater than 100 μm in size, such that we can now study individual crystals using optical microscopy and X-ray diffraction. Additionally, we found that cubic $Fe_3O_4$ PAEs assembled in the presence of a strong external magnetic field form aligned, micron-scale rods comprised of multiple domains, the orientation and alignment of which depend on the nanoparticle size and field strength.

Towards our ultimate goal of making functional PAE-based devices, we have investigated the organization of anisotropic PAEs into dense structures and studied their optical response. For example, we found that high-volume fraction (>70%) superlattices comprised of Au nanocubes can be used to create Mie-resonant 3D metamaterials with unusual and novel optical properties. Using patterned substrates in conjunction with DNA-mediated colloidal crystallization, we were able to control the position, orientation, and shape of superlattices assembled on a substrate. Finally, we explored the surface assembly of anisotropic nanoparticles into 2D monolayers and studied the optical properties that arise from these metasurfaces.

The progress made during Year 3 represents a significant advance over the previous year in the development of structurally sophisticated and functional superlattices, due in large part to the development of new anisotropic building blocks and their incorporation into nanoparticle superlattices.

**OBJECTIVES**

**Year 1**

Objective 1: Develop a new feedstock of functional PAE building blocks

- *Synthesis of three-dimensional anisotropic plasmonic nanoparticles*
- *Synthesis of MOF nanoparticles with control over their physical properties*

Objective 2. Synthesize and investigate dynamically reconfigurable superlattices

- *Transmutable nanoparticle superlattices.*
- *High resolution and contrast imaging of soft materials by electron microscopy.*

Objective 3. Synthesize and investigate structurally sophisticated and functional superlattices.

- *Superlattices with controlled crystal habit.*
- *Explore emergent optical phenomena in nanoparticle superlattices.*

Objective 4. Assemble reconfigurable, sophisticated, and functional superlattices on surfaces

- *Fabricate surface templates with well-defined DNA binding sites.*

**Year 2**

Objective 1. Develop a new feedstock of functional PAE building blocks

- *Synthesis of two-dimensional anisotropic plasmonic nanoparticles.*
- *Algorithmic characterization of nanoparticle yield and dispersion.*
- *Synthesis of MOFs nanoparticles with control over their physical properties*

Objective 2. Synthesize and investigate dynamically reconfigurable superlattices

- *Transmutable nanoparticle superlattices.*
- *Sparse imaging for soft materials characterization.*
- *High resolution and contrast imaging of soft materials by electron microscopy.*

Objective 3. Synthesize and investigate structurally sophisticated and functional superlattices.

- *Co-crystallization of multiple building blocks with chemically, physically, and structurally distinct properties.*
- *Superlattices with controlled crystal habit.*
- *Explore emergent optical phenomena in nanoparticle superlattices.*

Objective 4. Assemble reconfigurable, sophisticated, and functional superlattices on surfaces

- *Layer-by-layer growth of single-crystal superlattices with defined crystal shape and size.*

**Year 3**

Objective 1. Develop a new feedstock of functional PAE building blocks

- *Synthesis of two-dimensional anisotropic plasmonic nanoparticles.*
- *High-throughput screening of anisotropic nanoparticle synthesis conditions*

Objective 2. Synthesize and investigate dynamically reconfigurable superlattices

- *Transmutable nanoparticle superlattices.*
- *In situ characterization of reconfigurable superlattices via fluidic-cell S/TEM.*

Objective 3. Synthesize and investigate structurally sophisticated and functional superlattices.

- *Co-crystallization of multiple building blocks with chemically, physically, and structurally distinct properties.*
- *Unique low-symmetry and quasicrystalline structures.*
- *Explore emergent optical phenomena in nanoparticle superlattices.*

Objective 4. Assemble reconfigurable, sophisticated, and functional superlattices on surfaces

- *Layer-by-layer growth of single-crystal superlattices with defined crystal shape and size.*

**Year 4**

Objective 1. Develop a new feedstock of functional PAE building blocks

- *High-throughput screening of anisotropic nanoparticle synthesis conditions*

Objective 2. Synthesize and investigate dynamically reconfigurable superlattices

- *Transmutable nanoparticle superlattices.*
- *In situ characterization of reconfigurable superlattices via fluidic-cell S/TEM.*

Objective 3. Synthesize and investigate structurally sophisticated and functional superlattices.

- *Co-crystallization of multiple building blocks with chemically, physically, and structurally distinct properties.*
- *Unique low-symmetry and quasicrystalline structures.*

- *Explore emergent optical phenomena in nanoparticle superlattices.*

Objective 4. Assemble reconfigurable, sophisticated, and functional superlattices on surfaces

- *Superlattice assembly on flexible and porous supports.*
- *Emergent properties of surface-bound superlattices.*

**Year 5**

Objective 1. Develop a new feedstock of functional PAE building blocks

- *High-throughput screening of anisotropic nanoparticle synthesis conditions*

Objective 2. Synthesize and investigate dynamically reconfigurable superlattices

- *Synthesis of dynamically responsive superlattices from MOF building blocks.*
- *Develop new strategies for transferring DNA-assembled superlattices to the solid state.*

Objective 3. Synthesize and investigate structurally sophisticated and functional superlattices.

- *Unique low-symmetry and quasicrystalline structures.*
- *Explore emergent optical phenomena in nanoparticle superlattices.*

Objective 4. Assemble reconfigurable, sophisticated, and functional superlattices on surfaces

- *Emergent properties of surface-bound superlattices.*

**FINDINGS**

**Development of a New Feedstock of Functional PAE Building Blocks**

Under this objective, we pushed the lower limits of nanoparticle (NP) size and increased the geometric complexity of accessible NP building blocks. By using trace amounts of shape-regulating metals during underpotential deposition, we can generate multimetallic NPs terminated by high-index crystal planes (Section A1). Additionally, by changing the polymer used as the nanoreactors to synthesize polyelemental NPs, we were able to precisely control the absolute amount of metal precursors in the nanoreactors, allowing us to produce particles of a much smaller size than previously possible (Section A2). Furthermore, we developed a general strategy for the controlled overgrowth of metals on anisotropic NP seeds, substantially increasing the complexity of nanoparticle architecture available.

**Multimetallic High-Index Faceted, Heterostructured Nanoparticles**

Three of the most common ways to improve the catalytic efficiency of NPs are the incorporation of high-index facets; alloying two or more metals; and introducing interfaces into the catalysts. Thermolysis of solid-state precursors, a method widely used in industry to produce noble metal nanoparticles at scale, typically yields thermodynamically favored NPs with flat, low-index facets that have much lower catalytic activity than those with high-index facets with low coordination metal sites. There are limited methods that can produce ligand-free NPs with high-index facets, and most of these are relatively low throughput electrochemical methods. Higher throughput solution-phase methods to control particle shape typically rely on stabilizing ligands that are often difficult to remove and can adversely affect catalytic activity by blocking active sites.

Inspired by the observation that underpotential deposition of trace amounts of shape-regulating metal elements can be used to synthesize nanoparticles with high-index facets, we hypothesized that solid-phase syntheses could similarly be used to control anisotropic growth of NPs consisting of catalytically-relevant metals. We heated metal precursors of interest in a tube furnace with a foreign metal (Sb, Bi, Pb, and Te) atmosphere to influence NP growth (**Figure 1A**). Foreign metals were chosen based on their low evaporation temperatures and known ability to promote catalytic reactions. Indeed, we show that this strategy can be used to prepare tetrahexahedral (THH)–shaped Pt, Pd, Rh, Ni, Co, and multimetallic NPs (**Figure 1B-D**), irrespective of the foreign metal, after

appropriate thermal treatment. Importantly, this strategy can be used for bulk-scale synthesis and provides control over nanoparticle size uniformity.

According to the design rules discovered in Year 2 for engineering the interfaces between metals, NPs that consist of immiscible metals thermodynamically form heterostructures upon thermal annealing. We therefore hypothesized that multimetallic, heterostructured NPs enclosed by high-index facets can be synthesized by treating irregularly shaped NPs containing immiscible metal elements with shape-regulation metals. However, the method above provides limited control over the amount of each component in the multimetallic NPs due to phase separation-induced self-nucleation, especially for immiscible metals. To overcome this limitation, we explored how scanning probe block copolymer lithography (SPBCL), a high-throughput, site-specific multimetallic NP synthesis method, can be used in combination with foreign metal modification to achieve composition and size-controlled synthesis of heterostructured THH NPs. In a typical experiment, the patterning ink was prepared by mixing a block copolymer (PEO-b-P2VP) solution with metal precursors of interest (e.g., $H_2PtCl_6$ and $HAuCl_4$), followed by dip-coating onto AFM tips. The tips were brought into contact with a silicon wafer to pattern arrays of hemispherical polymeric features, which behave as nanoreactors for NP synthesis. The patterned substrate was transferred into a tube furnace for thermal treatment with Bi powder to produce uniform THH NPs (**Figure 2A**). Confining the

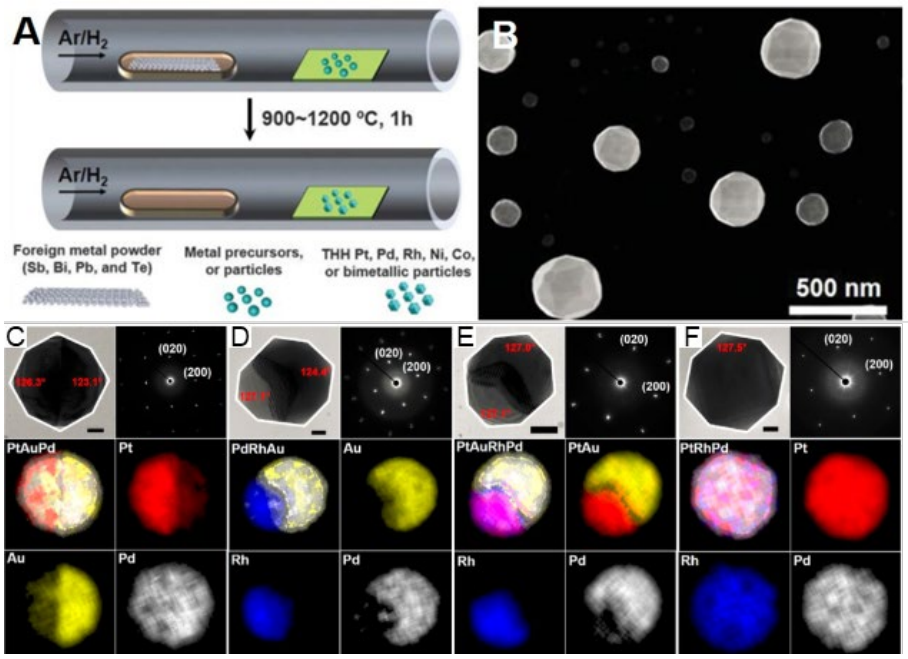


**Figure 1. Synthesis of THH NPs through trace foreign metal-assisted thermoregulation in the solid phase**. (A) Schematic for synthesizing THH NPs with a chemical vapor deposition setup. (B) SEM image of synthesized Pt THH NPs. TEM images, corresponding diffraction patterns, and EDS elemental maps of (C) PtAuPd, (D) PdRhAu, (E) PtAuRhPd, and (F) PtRhPd THH NPs. Scale bars: 20 nm.

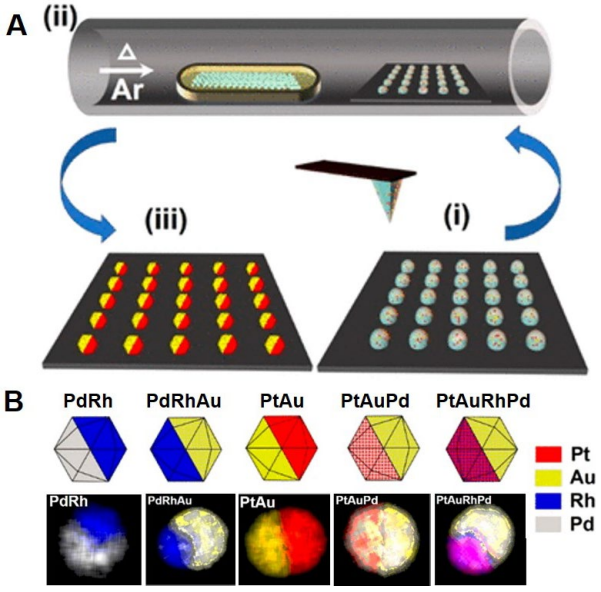


**Figure 2. Synthesis of heterostructured multimetallic THH NPs through a combination of trace foreign metal-assisted thermo-regulation and SPBCL**. (A) Scheme depicting the synthesis of multimetallic THH NPs via a combination of SPBCL and Bi modification. (B) EDS elemental maps of heterostructured multimetallic THH NPs and corresponding models.

metal precursors inside isolated, individual polymer nanoreactors resulted in precise composition and size control of the resulting NPs. A library of heterostructured, multimetallic (Pt, Pd, Rh, and Au) THH NPs was synthesized (**Figure 2B**).

Taken together, these results highlight the effectiveness of this novel solid-state shape regulation strategy for synthesizing multimetallic high-index facet NPs with uniform composition, size, and phase structure. This represents a synthetic advance toward a higher level of control in NP synthesis and likely provides opportunities for designing multifunctional catalysts.

**Nanoreactor Approach for Synthesizing Ultrafine Particles**

Uniform metallic NPs can be prepared via colloidal synthesis with sizes ranging from a few nm to tens or hundreds of nm. While gold, silver, and other compositions have been used as the cores for generating PAEs, these NPs are typically larger than 10 nm. Although we discovered in Years 1 and 2 that NPs as small as ~1.4 nm in diameter can function as electron equivalents (EEs), the synthesis of uniform NPs with such small sizes and controlled compositions is still challenging.

Here, we developed a new way of synthesizing sub-2 nm particles in a site-isolated manner using a polymer nanoreactor approach (**Figure 3A**). We first synthesized metalloporphyrin-terminated poly(ethylene oxide) (MTPP-PEO5k) as a quantitative carrier polymer for metal precursor ions. Each porphyrin can specifically bind to one metal atom, such as Pt, Cu, or Ni. By patterning this metal-loaded polymer ink to a substrate, uniform polymer nanoreactor arrays are synthesized (**Figure 3B**). After heat treatment in a hydrogen atmosphere, metal ions within each

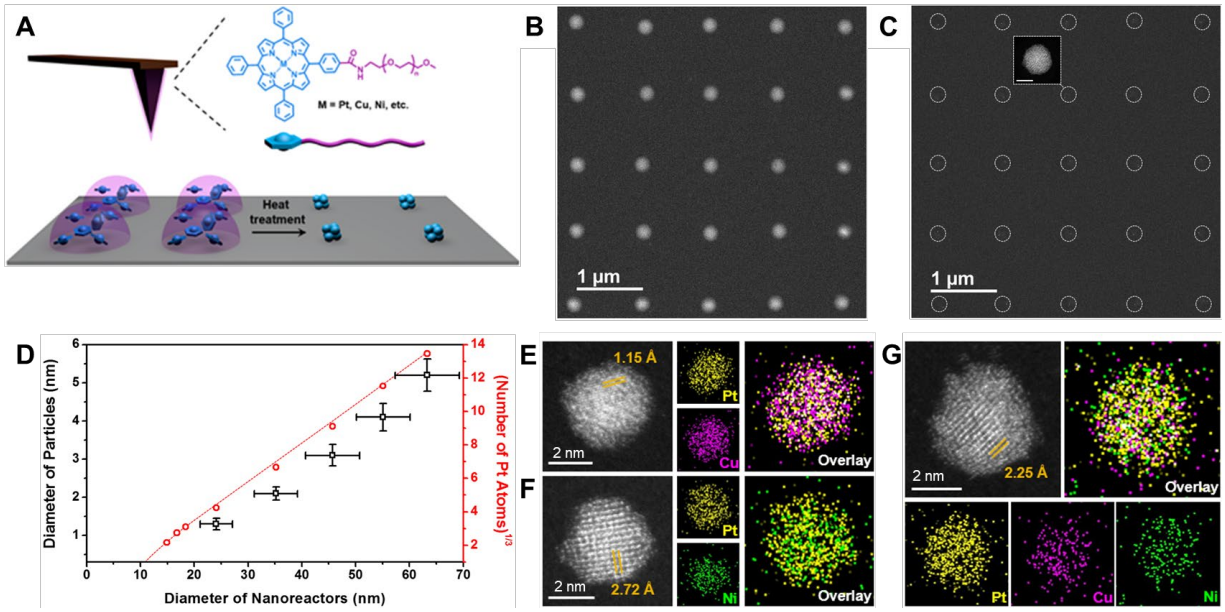


**Figure 3. Synthesis of ultrafine NPs using polymer nanoreactors.** (A) Schematic illustration of the synthetic approach. (B) HAADF-STEM image of a nanoreactor array. (C) HAADF-STEM image of a Pt NP array after heat treatment. Scale bar in inset: 3 nm. (D) Comparison between the size of the deposited nanoreactors, the size of the resulting Pt NPs, and the theoretical number of metal atoms in each nanoreactor, estimated based on nanoreactor volume. (E–G) HAADF-STEM images and EDS elemental maps of Pt-Cu (E), Pt-Ni (F), and Pt-Cu-Ni (G) alloy NPs synthesized from mixtures of metalloporphyrin-terminated PEO polymers.

nanoreactor are reduced to the elemental metal and converge into a single NP (**Figure 3C**).

The NP size is controlled by the size (volume) of the nanoreactors. This is achieved by fixing the number of metal atoms per polymer chain, as defined by the porphyrin-metal interaction. To study the correlation between nanoreactor and NP size in the products, we synthesized size-

gradient samples and quantified the nanoreactor size with AFM and the NP size using electron microscopy (**Figure 3D**). Indeed, a strong linear correlation is observed. When we decrease the nanoreactor size to ~25 nm, uniform Pt NPs as small as ~1.3 nm can be obtained.

This approach can be generalized to the synthesis of alloy NPs by mixing polymers that are coordinated to different metal species. As a proof-of-concept, ultrafine binary Pt-Cu and Pt-Ni NPs were synthesized and characterized using high angle annular dark field (HAADF)-scanning transmission electron microscopy (STEM) imaging and energy dispersive spectroscopy (EDS) elemental mapping (**Figure 3E**,**F**). The complexity of these NPs can be further increased by adding more metal species to the polymer ink. Indeed, ternary Pt-Cu-Ni NPs were synthesized with all three elements uniformly distributed in these sub-5 nm NPs (**Figure 3G**).This study illustrates that the careful design of polymers provides an important way to control NP composition and size, increasing the library of possibilities available through nanoreactor-mediated synthesis. Such nanostructures may have important applications in catalysis, magnetics, optics, and other fields.

**Corner-, Edge-, and Facet-Controlled Growth of Nanoparticles**

Seed-mediated strategies have proven effective for preparing a wide variety of NP structures, but a poor understanding of how to selectively grow corners, edges, and facets has limited the development of a general strategy to control structure evolution. Here, we report a universal synthetic strategy for directing the site-specific growth of anisotropic seeds to prepare a library of designer nanostructures, where many architectural elements, including shape and composition, can be programmed deliberately and independently.

Site-specific growth of NPs is challenging because NP seeds have no inherent energy barrier ($E$) to growth, such that in a growth solution, deposition occurs at all positions on the seed. The use of an appropriate ligand (i.e., mPEG6 disulfide) introduces significant $E$ differences on different sites of the seeds. Once capped by this ligand, the nucleation $E$ profiles of the NPs are dictated by the curvature and facet-dependent energy differences within the seeds. The growth position can therefore be controlled by adjusting the supersaturation in the growth solution ($\Delta\mu$) relative to $E$, with growth occurring only when $\Delta\mu$ can overcome $E$ at that site (i.e., $\Delta\mu > E$). Three elementary design rules were developed to guide site-

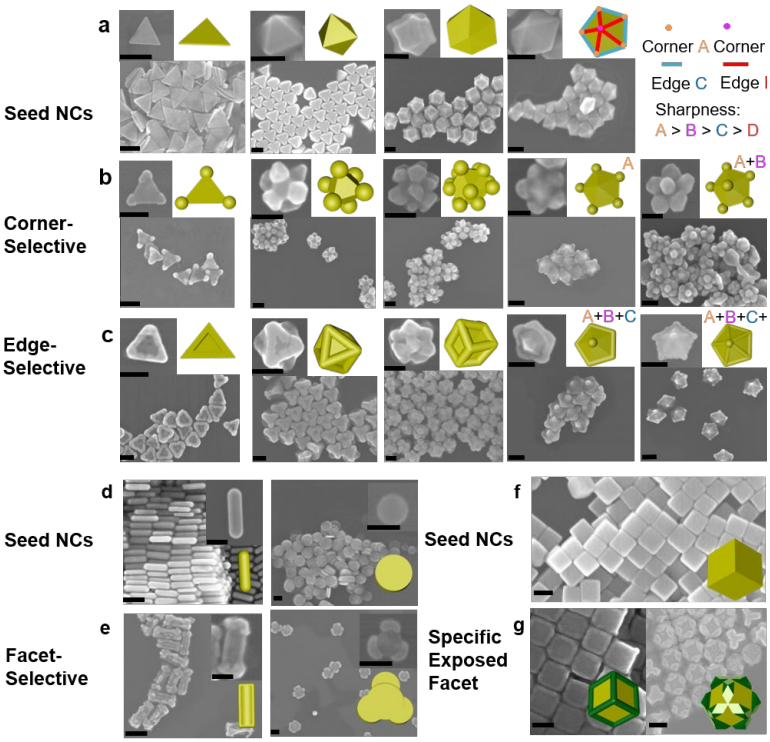


**Figure 4. Design rules for site-selective NP growth.** (a–c) SEM images and (inset) models of curvature-selective nucleation on seed NPs. (a, left to right) Nanoprism, octahedral, concave rhombic dodecahedral, and decahedral seed NPs. (b) Corner- and (c) edge-selective nucleation on the seed NP shown in (a). (d, e) SEM images and models of facet-selective nucleation. (d) Nanorod and nanodisk seed NPs. (e) Facet-selective growth on nanorods and nanodisks. (f, g) Tuning the chemical potential of the growth solution controls where growth occurs. SEM image and model of (f) cubic seed NPs and (g) nanocubes after edge-selective growth with specific facets exposed. Scale bars: 100 nm.

specific growth: (1) curvature-selective design rule (**Figure 4a–c**): sites with larger curvature grow at smaller $\Delta\mu$; (2) facet-selective design rule (**Figure 4d,e**): facets with higher surface energy grow at smaller $\Delta\mu$; (3) specific exposed-facet design rule (**Figure 4f,g**): facets with higher surface energy are exposed at higher $\Delta\mu$ without affecting the selectivity of nucleation. Through this methodology, we have synthesized over 10 previously unreported gold NP architectures. In principle, many others are possible with different seeds.

To highlight the versatility of this strategy, the site-specific growth of bimetallic structures was investigated. Au seeds of different shapes, including nanoprisms, octahedra, and concave rhombic dodecahedra, were grown in solutions of Ag or Pd to give corner- or edge-selective growth (**Figure 5**). Elemental mapping confirms the spatial arrangement of the NPs. Importantly, this strategy is generalizable and more sophisticated architectures can likely be synthesized thus substantially increasing the library of accessible PAEs to include greater structural complexity, specificity, and compositional diversity. Such structures will positively impact a broad range of disciplines, spanning catalysis, plasmonics, magnetics, and electronics.

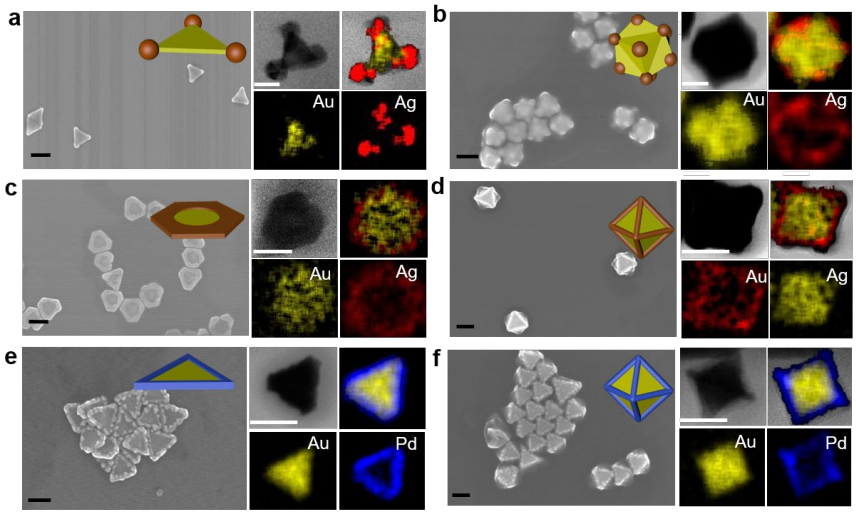


**Figure 5. Site-specific growth of multicomponent NPs.** SEM images and corresponding elemental maps of (a, b) corner- and (c, d) edge-selective growth of Ag on Au (a, c) nanoprisms, (b) concave rhombic dodecahedra, and (d) octahedra. SEM images and elemental maps showing edge-selective growth of Pd on Au (e) nanoprisms and (f) octahedra. Scale bars: 100 nm.

**Synthesis and investigation of dynamically reconfigurable superlattices**

This year we continued to design and explore dynamically reconfigurable superlattices. First, we report the use of multivalent cations as a method to actuate the DNA bond length in a nanoparticle superlattice (Section B1). We show that high valent metals like Ni can contract the DNA bond by as much as 80% as well as increase the melting temperature of the superlattice by >60 °C. We then designed a reconfigurable superlattice that utilizes a DNA dendron that can switch between PAE and EE conformations through a toehold displacement reaction (Section B2). The dendron alone is capable of assembling as an EE, but supramolecular assembly of the dendron into a higher order structure results in a PAE structure. Finally, we developed a new superlattice assembly method that utilizes a substantially decreased cooling rate to create superlattices >100 μm, which enables investigation into their physical properties as they can be visualized with an optical microscope and resolved individually by diffraction methods (Section B3). We end this section by discussing an upgrade to our imaging techniques that allow for the structural characterization of soft materials in controlled environments (Section B4).

## 4. Multivalent Cation-Induced Actuation of Colloidal Superlattices

By controlling the NP size, shape, and composition as well as the DNA sequence, length, and density, a vast library of crystalline structures can be obtained from PAEs. In this work, we developed a strategy that allows the DNA bond length to be modified post-synthetically, allowing interparticle spacings to be altered dynamically, thus leading to a new class of tunable metamaterials.

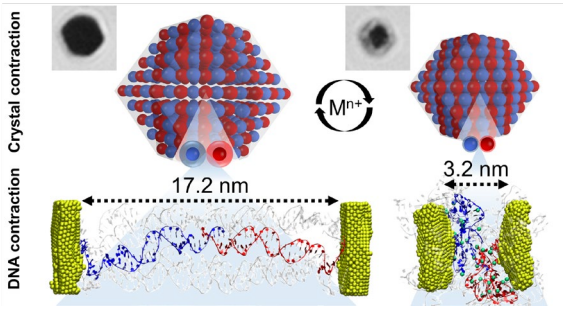


**Figure 6.** Reversible actuation of DNA-mediated colloidal crystals induced by multivalent cations ($M^{n+}$).

Inspired by histone proteins that condense DNA within the nuclei of cells due to the interactions of the negatively charged DNA backbone with the multiple positive surface residues on the proteins, we investigated the ability of 10 different cations ($Na^+$, $K^+$, $NH_4^+$, $Mg^{2+}$, $Ca^{2+}$, $Ni^{2+}$, $Co^{2+}$, $Mn^{2+}$, $Cu^{2+}$, and $[Co(NH_3)_6]^{3+}$) to actuate the DNA bonds in colloidal crystals (**Figure 6**). Our results show that cations with multiple charges alter DNA structure on the molecular scale, enabling the DNA bond length to be reversibly altered between 17 nm and 3 nm (**Figure 7A**), ultimately leading to changes in the overall dimensions of the original micron-sized superlattice at sub-second timescales (**Figure 7B**). The lattice symmetry and crystal structure are retained throughout the process (**Figure 7C–E**). The extent of actuation increases with increasing charge and concentration of the cation. However, two cations with identical charges may result in dramatic differences in actuation. For example, 2 M $Mg^{2+}$ induces ~30% contraction whereas 2 M $Ni^{2+}$ induces ~80% change in DNA length (**Figure 7A**). These differences can be attributed to the increased binding affinity of $Ni^{2+}$ to DNA compared to that of $Mg^{2+}$. The addition of multivalent cations is accompanied by an increase in the "bond strength" which increases the

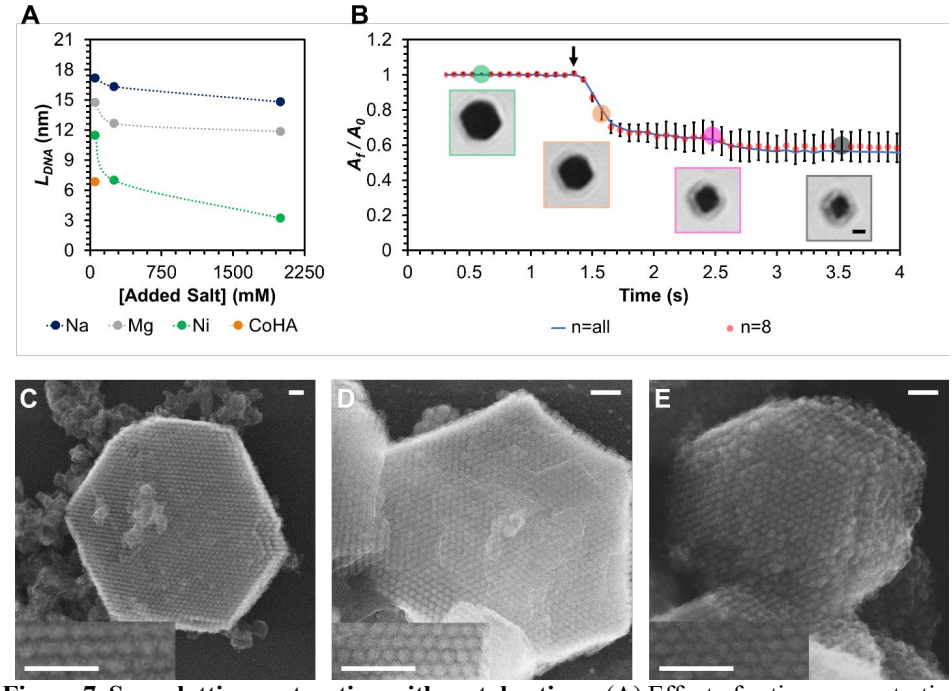


**Figure 7. Superlattice contraction with metal cations.** (A) Effect of cation concentration on DNA length within superlattices. (B) Timescale of superlattice contraction in the presence of excess $Ni^{2+}$. Blue dots correspond to the ratio of the final ($A_f$) and initial ($A_0$) areas occupied by all the crystals in the field of view at different points in time. Red dots designate the same for the average of 8 individual crystals. Error bars denote one standard deviation, arrow indicates the addition of $Ni^{2+}$, and all images showing the contracting crystal are brightfield. Scale bar: 1 μm. SEM images of superlattices with (C) no added multivalent cations, (D) 50 mM $[Co(NH_3)_6]^{3+}$, and (E) 2 M $Ni^{2+}$. Scale bars: 125 nm.

thermal stability of the superlattices by >60 °C.

To understand the conformational changes in the DNA structure associated with the actuation process, we performed molecular dynamics simulations. These studies show that cations that more effectively screen the negative charge on the DNA backbone cause greater crystal contraction. Taken together, the use of multivalent cations represents a powerful strategy to alter superlattice structure and stability, which can impact diverse applications through the dynamic control of material properties, including optical, magnetic, and mechanical properties.

**5. Programmable Colloidal Crystal Bonding Using Reconfigurable DNA Dendrimers**

AFOSR-funded research has led to the development of design rules for crystal structures composed of PAEs and the newly discovered EE. When superlattices are assembled from only PAEs, the large size and multivalency of the PAEs result in assemblies that mimic ionic bonding, whereby each PAE within an assembly occupies a discrete location in the lattice. As reported last year, assemblies of PAEs and EEs, 1.4-nm AuNPs with fewer than ten DNA strands on their surfaces, yield metallic-like bonding, as the EEs are mobile within the crystal structure. EEs and PAEs are typically synthesized by functionalizing NPs with DNA without valency or position control. Thus, a challenge and opportunity in colloidal crystal engineering is the absence of a general approach to achieve molecularly defined, modular PAE architectures. The lack of precise control over supramolecular architecture limits our understanding of, and ultimately, our control over the bonding, structure, and function of the resulting colloidal superlattice. We hypothesized that the templated assembly of oligonucleotide-based molecules would provide us with a modular approach to PAE architectures that not only possesses defined size and valency, but also introduces reconfigurability.

DNA dendron EEs were designed that comprise a stem attached to a branched DNA region where the DNA contains single-stranded sticky ends capable of engaging in multivalent base pairing with PAEs that have complementary sticky ends (**Figure 8**). The number of branches on the dendrons is precisely controlled by the structure of each branching unit and the number of generations. These dendron EEs can be hybridized to DNA templates to form DNA dendrimer PAEs. The DNA template is designed with an anchor region that recognizes the stem of the dendron, such that multiple copies of the dendron can duplex onto the template to form the desired DNA dendrimer PAE. The azide-containing DNA templates, with valencies from two to eight, were synthesized via a previously developed solid-phase click coupling strategy. We found that at stoichiometric ratios and in mild conditions, nearly all the anchor strands on the template hybridize with a DNA dendron resulting in high valent, high molecular weight DNA dendrimers.

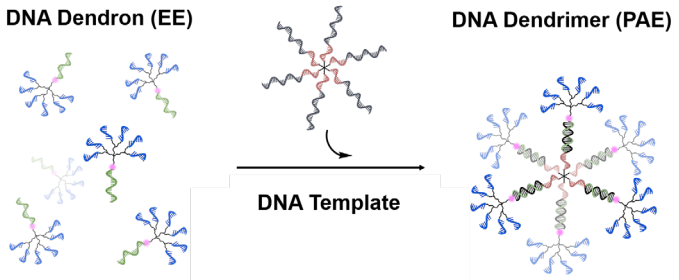


**Figure 8. Designing molecularly defined DNA architectures for colloidal crystal engineering.** Individual DNA dendrons, designed to serve as EEs, are hybridized to DNA templates to create high valency DNA dendrimer PAEs. The sticky ends (blue) can recognize and hybridize to the sticky ends on AuNP PAEs, thus enabling DNA-mediated programmable assembly.

We first investigated whether the architectures of dendrons and dendrimers dictate their bonding behavior. We assembled them with PAEs prepared from 5 nm and 10 nm AuNP PAEs (**Figure 9b**). Small angle X-ray scattering (SAXS) and STEM confirm that two different crystal structures are formed. Consistent with previous findings in this field, the DNA dendrimer PAEs

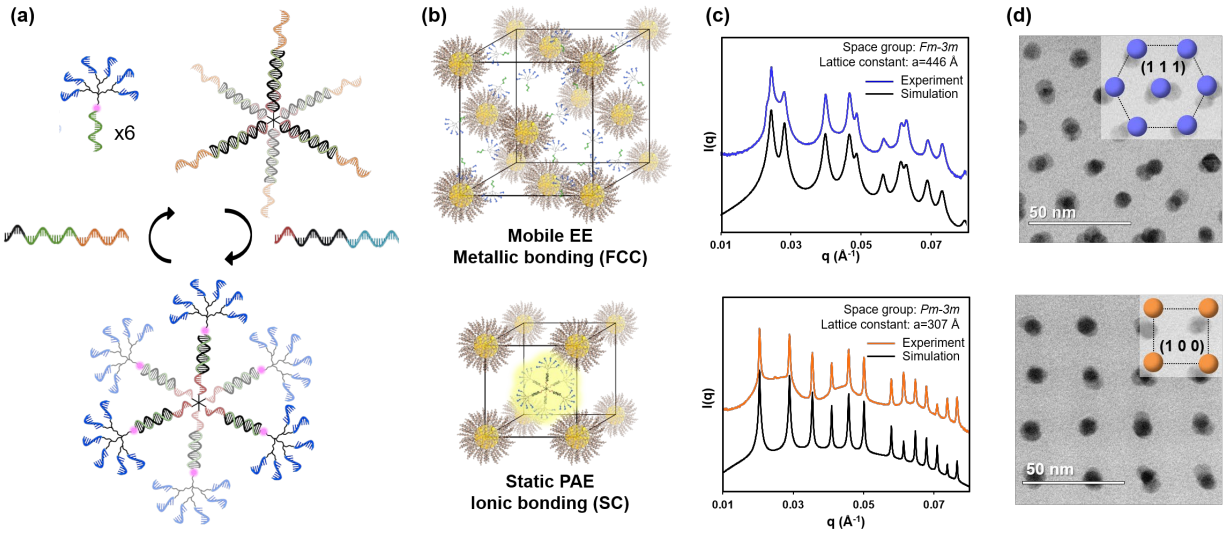


**Figure 9. The impact of DNA ligand architecture on bonding behavior.** (a) Reversible, fuel-strand mediated PAE and EE formation. Here, a fuel strand hybridizes to the toe-hold region on the template anchor strands resulting in dendron displacement. This process is reversible as upon the addition of a second fuel-strand the DNA dendrimer is reformed. (b) Dendron EEs and Dendrimers PAEs assemble with 10 nm AuNP-based PAEs to give face-centered cubic (FCC) and simple cubic (SC) phases, respectively. (c) Solution state characterization by SAXS. (d) STEM imaging of sectioned superlattices. Top: FCC phase. Bottom: SC phase.

produced a simple cubic crystal structure, while the DNA dendron EEs produced a face-centered cubic crystal (*fcc*) structure (**Figure 9b-d**). We further characterized the difference in EE and PAE behavior by studying the thermodynamic stability of the resultant assemblies and the diffusion of DNA dendrons and dendrimers within the assemblies. Melt experiments revealed that the DNA dendrons and dendrimers produce assemblies with vastly different melting temperatures, consistent with the observation that PAE-only assemblies have a greater thermodynamic stability than those consisting of EEs and PAEs (**Figure 10a**). Furthermore, a key characteristic of EE behavior is the ability to diffuse throughout a crystal structure. This was investigated by preparing assemblies with fluorescently tagged dendrons and introducing a non-tagged dendron into the

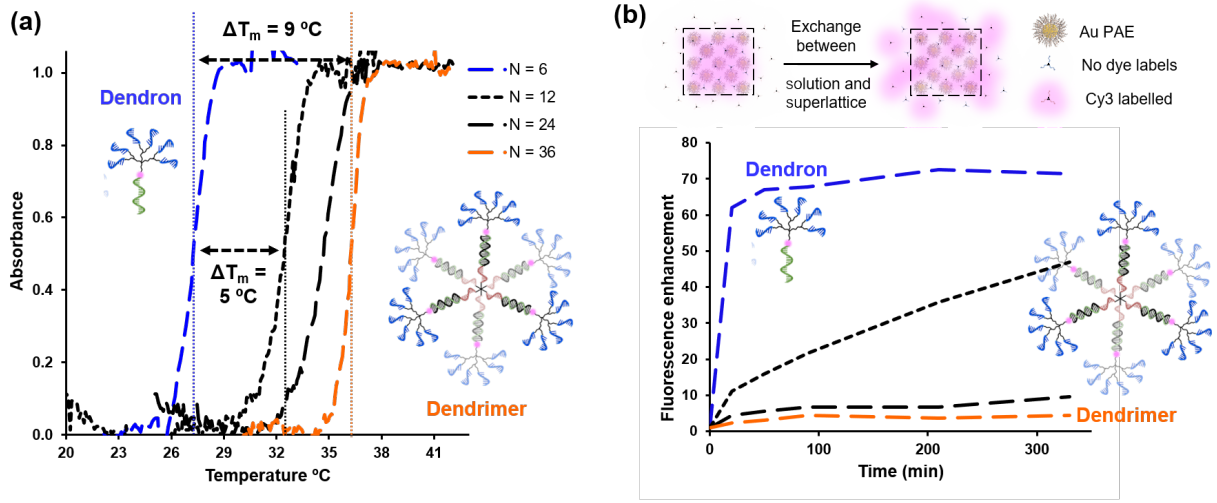


**Figure 10. Characterization of assembles with DNA dendrimer PAEs and dendron EEs**. (a) UV-Vis melt of colloidal crystals synthesized using DNA dendrons/dendrimers with different valencies. (b) Tracking the diffusion of dye-labelled DNA constructs across the solution-superlattice interface via supernatant fluorescence enhancement.

surrounding solution (**Figure 10b**). If the dendron/dendrimer is an EE, an increase in the fluorescent signal will be observed as the EE diffuses out of the superlattice and exchanges places with its non-fluorescent counterpart. We observed that only the DNA dendrons undergo rapid diffusion.

We have shown that by hybridizing DNA dendrons to DNA based templates, we can create EEs and PAEs that are molecularly defined, and tunable in valency, size, and geometry. Importantly, through judicious DNA design, we can efficiently switch between these two structures by employing DNA fuel strands (**Figure 9a**). Thus, these structures have enabled us to create a system in which we can reversibly switch the bonding character of assemblies. Furthermore, due to the programmability of these structures, we can use them to understand the impact of ligand valency and position on resultant crystal structure and bonding behavior. Looking ahead, as the first truly molecularly defined PAE and EE, DNA dendrimers can be used to access high quality crystalline structures. This platform increases not only our understanding of colloidal crystal engineering, but also our ability to create functional, reconfigurable NP assemblies that can be used to access unique catalytic, optical, and electronic properties.

### 6. Large Single-Crystalline Colloidal Crystals Engineered with DNA

Sufficiently large single crystals of soft materials are necessary for rigorous physical property characterization techniques, such as single-crystal X-ray diffraction and optical microscopy, as well as the measurement of conductivity, elastic modulus, and thermal resistance. All of these measurements are contingent on the size and grain boundary of the samples. Carrying out such experiments on large single crystals will significantly enhance the precision of the characterization and may allow for the discovery of new and unexpected properties. Therefore, large single crystals are highly sought after when new crystalline materials are invented.

However, growing large (>100 μm) DNA-engineered colloidal crystals has remained an outstanding challenge; the largest crystal reported is 23 μm in diameter, an outlier in a batch of crystals with an average size of 12 μm. DNA-engineered colloidal crystals are known to have relatively sharp melting and aggregation transitions due to the cooperative DNA duplex-to-duplex interactions on the surface of the PAEs. We surmised that during the crystallization process, the sharp aggregation transition of PAEs could inhibit the sufficiently slow nucleation and growth processes, which are essential to obtaining large single crystals. While the typical slow cooling rate is 0.1 °C/10 min, here we varied the cooling rate from 0.1 °C/5 min to 0.1 °C/120 min through the aggregation transition temperature range for both 10 and 5 nm PAEs that assemble into *bcc*-type colloidal crystals (**Figure 11**).

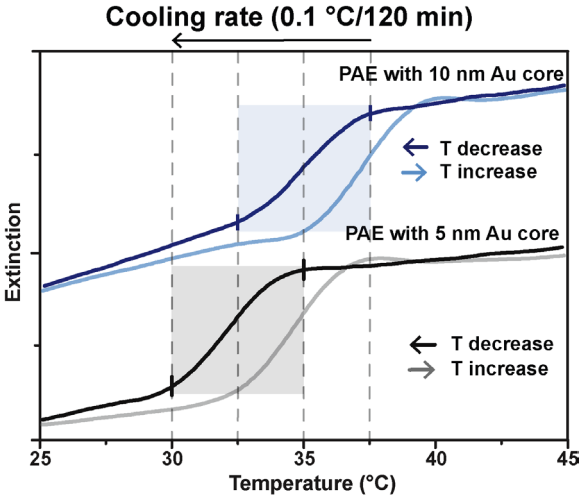


**Figure 11. Melting curves of the PAEs with 10 and 5 nm AuNPs.** Instead of applying the conventional slow-cooling rate of 0.1 ºC/10 min, a slower cooling rate of 0.1 ºC/120 min was applied during the crystallization over the temperature range (shaded region) that encompasses the aggregating transition.

Optical microscopy images of the crystals synthesized with a cooling rate of 0.1 °C/120 min (**Figure 12a, b**) show a well-faceted rhombic dodecahedron morphology, reflecting the internal point symmetry of the *bcc* structure. The average sizes of the crystals assembled from 10 and 5

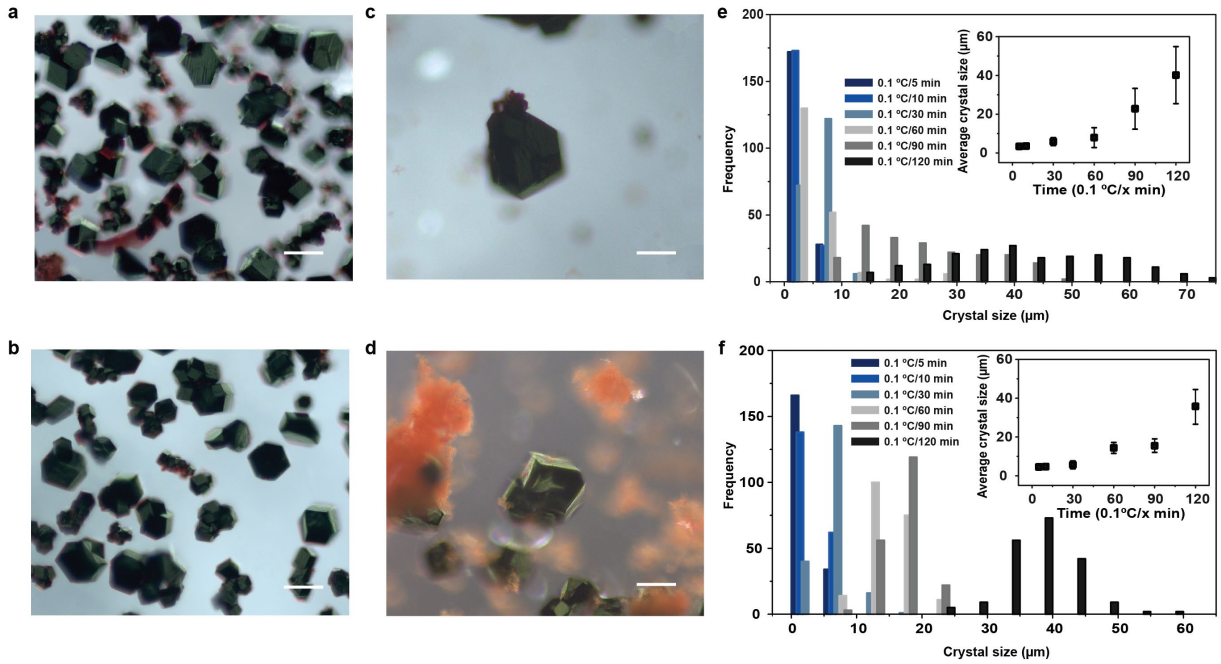


**Figure 12. Crystal size dependence on the cooling rate of the crystallization.** Optical microscope images of crystals assembled from 10 nm PAEs at (a) 50 nM and (c) 200 nM and 5 nm PAE at (b) 200 nM and (d) 600 nM concentrations with a cooling rate of 0.1°C/120. Scale bars: 50 μm. (e and f) Size histograms of crystals assembled from (e) 10 nm and (f) 5 nm PAEs as a function of cooling rate. Inset: plot of average crystal size vs cooling rate.

nm PAEs are 42 and 36 μm, respectively (the size of the individual crystals was measured by selecting the longest distance between vertexes in a single crystal). The largest crystals found in these experiments are 72 and 59 μm for the crystals prepared from 10 and 5 nm PAEs, respectively. Additionally, a clear dependence of the crystal size on the cooling rate is observed: the slower the cooling rate, the larger the crystals that assemble (**Figure 12e, f**). These results highlight that slowing down the rapid aggregation transition provides sufficient time for the error-correction process to occur.

Another variable that affects the crystallization process is particle concentration. Therefore, to further increase the crystal size, the concentration of the PAEs in the reaction solution was varied. Crystals larger than 100 μm were obtained by increasing the concentration of the 10 nm PAEs from 50 to 200 nM and the 5 nm PAEs from 200 to 600 nM (**Figure 12c, d**).

These results indicate that large DNA-engineered colloidal crystals can be synthesized, and the average size of crystals can be controlled over a wide range. This size control, combined with our density gradient method that increases the uniformity of the crystals size distribution, may lead to more comprehensive size control of the colloidal crystals engineered with DNA. The uniform synthesis of large colloidal crystals is essential for many applications, in particular optics, where each crystal operates as a single device.

### Atmospheric Control System for *in situ* Electron Microscopy of MOFs and Other Building Blocks in Gaseous Environments

When artificial crystals comprising metals, MOFs, and organic ligands (including DNA) are exposed to the environment, significant structural and chemical transitions can occur depending on the atmosphere and temperature. To understand the structural stability of these materials, it is essential to study the transition and degradation mechanisms of the NP building blocks and

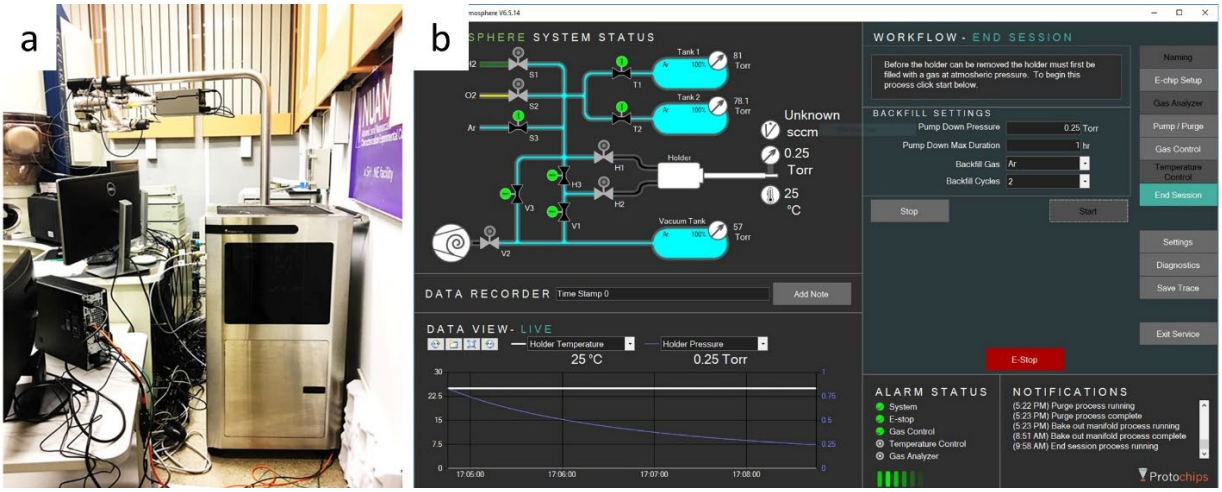


**Figure 13. Installed ProtoChips Atmosphere 210 gas control system.** (a) Atmosphere gas system connected to the aberration-corrected microscope. (b) Control software showing the ability to mix multiple gases with real-time control of temperature, gas content, and pressure.

superlattices in real time under controlled atmospheric environments. During this reporting period, a ProtoChips Atmosphere 210 gas system was installed and fully tested at Northwestern's NUANCE facility. This system, which is connected to an aberration-corrected STEM (JEOL ARM200), enables *in situ* gas delivery and heating to samples for atomic-resolution imaging (**Figure 13a**). Gas mixtures with customized gas contents and pressure can be created to reproduce complex gas/material operating environments (**Figure 13b**). Samples can be heated to 1000 ºC in a mono-component gas environment up to 1 atm pressure, therefore covering almost all possible conditions that building blocks and superlattices may encounter in actual applications. The gas system is integrated with a residual gas analyzer (RGA) which enables rapid gas detection during imaging. In addition to common dry gases, other less conventional vapor sources including water vapor, alcohol, and light alkanes can be introduced.

As proof-of-concept, we investigated the stability of MOF nanostructures in a reducing atmosphere at elevated temperatures. The NU-1000 MOF, which was developed as a candidate functional PAE building block in previous years, contains $Cu^{2+}$ ions that hold the organic framework together. Using the *in situ* gas system, we monitored Cu reduction in a $H_2$ environment at 150–200 ºC. Under these conditions, we found that metallic Cu NPs are generated from the MOF scaffold, and the volume of the MOF shrinks over time (**Figure 14a,b**). Importantly, even with the loss of Cu, the remaining MOF structure still possesses high crystallinity, as shown by the integrity of the atomic

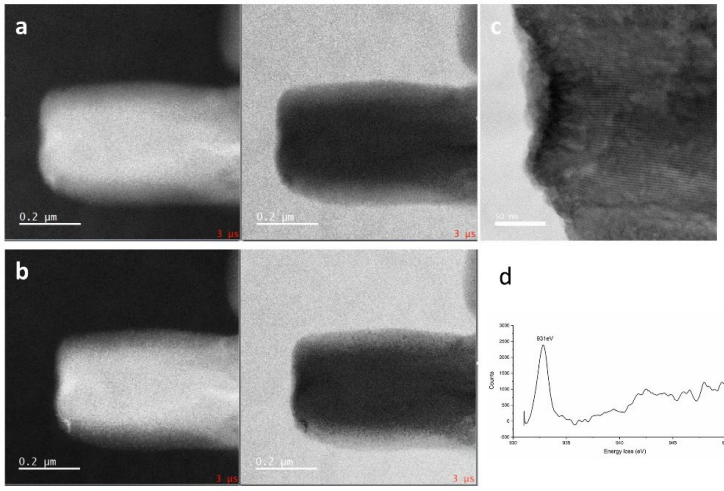


**Figure 14. *In situ* investigation of Cu reduction in NU-1000 MOF.** (a) The pristine MOF structure. (b) Reduced Cu NPs decorated on MOF after reduction in $H_2$ at 150 ºC. (c) Observation of atomic Cu lattice within MOF (2.8 nm spacing). (d) EELS spectrum of Cu after reduction.

lattice (**Figure 14c**).

The ability control the atmosphere during imaging is vital to preforming real-time and real-space observations of the assemblies, and thus this work is foundational to achieving the specific goals of this grant.

**Synthesis and investigation of structurally sophisticated and functional superlattices**

Under this objective, we report our progress on the development of structurally complex and functional superlattices. Several advances have been made toward greater structural sophistication in colloidal superlattices. First, we show a new class of colloidal crystal "alloys" that can be assembled using two different sizes of PAEs and EEs (Section C1). We also prepared several new densely packed superlattice structures employing anisotropic PAEs (Section C2). We then discuss how cubic $Fe_3O_4$ NPs assembled with DNA in the presence of external magnetic fields result in polycrystalline rods comprised of unaligned grains (Section C3). Towards the development of functional superlattices (Sections C4 and C5), we found that Mie-resonant 3D metacrystals possess unique optical properties due to their high-volume fraction and low interparticle distance. Finally, we show that gold pentabipyramids assembled into a rhombohedral superlattice have novel optical properties such as birefringence and dichroism.

**7. Metallurgic Engineering of Colloidal Crystal "Alloys"**

Last year, we reported the discovery of EEs and the assembly of "metallic" colloidal crystals. These "metallic" colloidal crystals have unique structural versality both in terms of the roaming nature of the EEs and the accessibility of new crystal structures. During the past year, we have increased structural complexity by mixing two different sizes of PAEs with EEs functionalized with complementary DNA (**Figure 15A**). Here, both types of PAEs are functionalized with the same type of DNA linkers, and their assembly is driven by the inclusion of EEs which carry complementary DNA linkers. This system resulted in a series of "alloy" structures and enabled the derivation of a new set of design principles inspired by the Hume-Rothery rules that govern macroscale metallic alloys. Specifically, SAXS and cross-sectional electron microscopy images show that as the hydrodynamic radius ratio of the two PAEs is decreased below 1, the resulting crystals possess a substitutional, then phase-separated, and then interstitial alloy structure (**Figure 15B–E**).

When the size difference between the two types of PAEs is large enough that smaller PAEs can fill the spaces within the lattice defined by the larger PAEs, an interstitial alloy forms. It is important to note that the formation of intermetallic crystals is different from binary colloidal crystals which are formed from complementary PAEs. When the size of the two types of PAEs is comparable, substitutional lattices form where the PAEs occupy lattice sites randomly. When the size ratio of the two PAE types is intermediate, phase separation occurs. In these alloys, the two types of PAEs do not chemically order due to the high strain penalty between neighboring building blocks. To overcome this strain penalty, the DNA shell was modified to include hexa(ethylene glycol) spacers which result in a compressible shell (**Figure 15F**). When 15 hexa(ethylene glycol) spacers were added to the DNA on 10 + 40 nm PAEs, a CsCl-type intermetallic structure formed as confirmed by both SAXS and cross-sectional electron microscopy images (**Figure 12G,H**).

To synthesize alloy structures with different microstructures (i.e., geometric configurations of different domains), we used a kinetically controlled procedure where we systematically varied the cooling rate during "alloy" annealing. This revealed that different types of microstructures, including amorphous structures, matrix/precipitates, separate crystals, and core-shell structures can be accessed by controlling the cooling rate (**Figure 15I–K**). Taken together, these results

create guidelines for preparing a range of alloy phases.

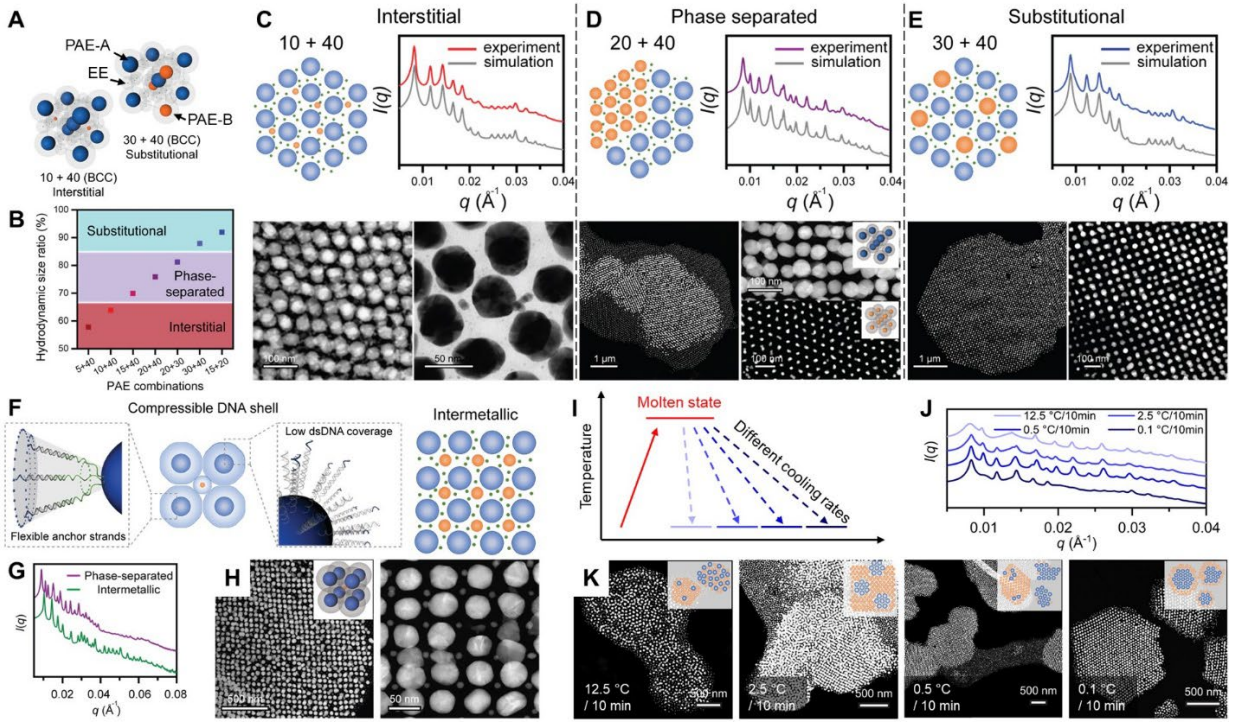


**Figure 15. Metallurgical engineering of "metallic alloy" colloidal crystals.** (A) 3D models of interstitial (10 + 40 nm) and substitutional (30 + 40 nm) alloys formed when 2 types of PAEs with different sizes were assembled with EEs. (B) Phase behavior plotted as a function of PAE hydrodynamic radius ratio. The phase structures were determined by SAXS. (C–E) Schematic, SAXS spectra (top), and cross-sectional images (LAADF or BF, bottom) of different alloys: interstitial (C), phase-separated (D), and substitutional (E). (F) Schematic showing that engineering the DNA with hexa(ethylene) glycol (PEG) spacer units (green lines) results in a compressible DNA shell which can accommodate local stress induced by lattice mismatch. The DNA shell on the PAEs and EEs are omitted in the cartoons for clarity. (G) SAXS reveals the formation of a CsCl-type intermetallic structure when 15 PEG spacers were inserted in the DNA on 10 + 40 nm PAEs, and phase-separated structures when 6 spacers were used. (H) Cross-sectional LAADF images of the intermetallic structure. (I) After heating to the molten state, the cooling rate controls the microstructure of the colloidal crystals. (J, K) Characterization of the kinetic products obtained by four different cooling rates via SAXS (J) and cross-sectional LAADF imaging (K). Inset schematics depict the four types of phase-separated colloidal crystal alloys formed by cooling at different rates.

## 8. Enthalpy-driven Dense Packing of Polyhedral Nanocrystals into Designer Superlattices

Led by studies on DNA-mediated crystal engineering, the past two decades have witnessed the rapid development of enthalpy-driven crystallization. This has resulted in the preparation of hundreds of colloidal crystals with dozens of crystal symmetries. One major differentiating feature of the enthalpy-driven packing of colloidal particles is the collective binding of their surface ligands, as seen by the facet-registration in assemblies of DNA-functionalized polyhedral NPs. The dense close packing of polyhedral NPs, however, remains a synthetic challenge because NPs functionalized with short DNA strands often do not assemble into extended, ordered structures. Specifically, large polyhedral NPs (>60 nm) only assemble into well-ordered structures when functionalized with double stranded (ds) DNA containing more than 70 bases (shell thickness: ~22 nm); efforts with shorter DNA have produced only small, malformed crystal domains (< 0.5 μm). Larger NPs such as trigonal bipyramids (edge length: ~200 nm) require significantly longer DNA (238 bases, shell thickness: ~69 nm) to assemble into long-range ordered structures. To study the

enthalpy-driven dense packing of polyhedral NPs, a new design of short DNA is critically needed.

The main causes that hinder the formation of larger colloidal crystals include: a) low degree of freedom at the sticky end; b) limited flexibility of the DNA strand; and c) high charge density induced by short and rigid dsDNA. We hypothesized that adding a short, flexible, and charge-neutral region next to the sticky end would provide a way to assemble larger colloidal crystals with dense NP packing. To test our hypothesis, we synthesized a series of linkers noted as d0, sp1, sp2, sp3, and sp5, containing increasing lengths of a PEG region next to the sticky end. Polyhedral AuNPs with different shapes and sizes were synthesized in high yield, functionalized with DNA, and assembled through a standard slow-cooling process (0.1 °C/10 min).

We started by assembling monodisperse NPs with the simplest space-filling shapes (**Figure 16**): cubes, rhombic dodecahedra (RD), truncated tetrahedra (TO), and truncated trigonal bipyramids (TTBP). These shapes were chosen because they can fill 3D space themselves, without gaps. In doing so, they generate lattice symmetries for which they represent the approximate Voronoi polyhedra: cubes fill space to form simple cubic (*sc*), RDs form face-centered-cubic (*fcc*), TOs form body-centered-cubic (*bcc*), and TTBPs form interlocked honeycomb (*ih*) lattices. To our surprise, single crystals with crystal domain sizes up to 50 μm and well-defined crystal habits were found when sp5 linkers were employed (**Figure 16**).

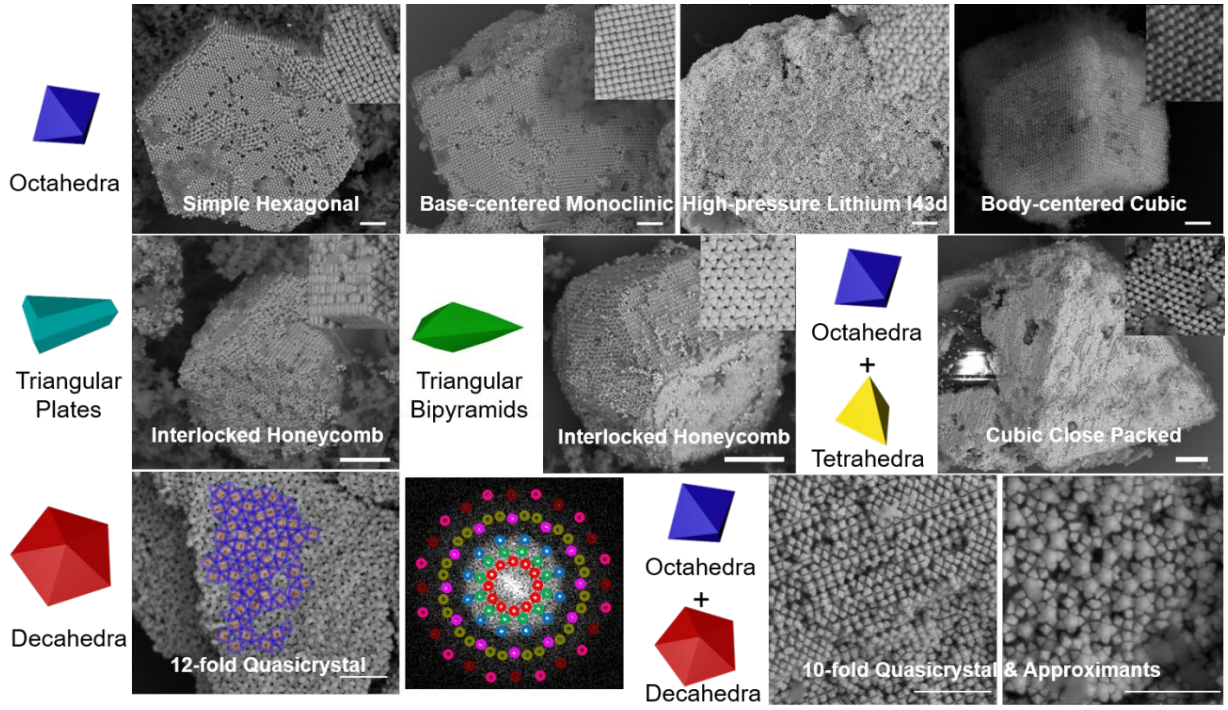


**Figure 16. New structures formed through DNA-mediated dense packing of polyhedral NPs.** Octahedral NPs show polymorphic behavior when packing into ordered structures, forming pure-phased single hexagonal, base-centered monoclinic, high pressure lithium, and body-centered cubic structures as NP size is reduced. Triangular plates and rounded triangular bipyramids pack into interlocked honeycomb structures. Co-assembly of octahedra and tetrahedra with matching edge lengths form a cubic close-packed structure. Decahedral NPs pack into a dodecagonal quasicrystal. Co-assembly of octahedra and decahedra with matching edge lengths form a decagonal quasicrystal as well as its crystalline approximants. Scale bars: 1 μm.

Interestingly, a polymorphic effect was observed when octahedral NPs with different sizes were assembled. When octahedra are large (edge length >85 nm), they assemble with a simple hexagonal packing (*sh*) in high yield, with hexagonal prism crystal habits. When smaller octahedra

(75–85 nm) are assembled, the same hexagonal planar structures are observed, yet a base-centered-monoclinic (*bcm*) packing is found when using sp1 linkers, with monoclinic crystal habits. The structural difference between *sh* and *bcm* is only their out-of-plane packing directions. Further decreasing octahedra size (60–75 nm) shifts the packing into an *I*43*d* lattice, a cubic lattice containing 16 octahedra within each unit cell, all with different orientations. Finally, *bcc* lattices with RD crystal habits are observed when octahedra sizes were decreased to 30 nm. This is the first time that polymorphic packing of octahedra has been elucidated, and can be controlled by the length of linker relative to the NP size.

In short, polyhedral nanocrystals with different sizes and shapes were densely assembled and co-assembled, bringing 10 new structures to the DNA-engineered colloidal crystal family. Through this research, we emphasize the design principles based on considerations of shape complementarities and the highly predictable binding nature of DNA. This advance opens the possibility for designing and making many more complex and sophisticated structures for material scientists to employ.

## 9. Orientation of Colloidal Crystals of Cubic $Fe_3O_4$ NPs with DNA and Magnetic Fields

Previously, we investigated the assembly of spherical $Fe_3O_4$ PAEs and discovered that they assemble in an elongated rod morphology, when a magnetic field is applied. These superlattices have a body centered cubic (*bcc*) symmetry, as dictated by the DNA design. To further explore the assembly behavior, during the past year, we investigated the assembly behavior of particles with lower symmetry.

Specifically, we studied how DNA surface ligands modify the assembly behavior of cubic $Fe_3O_4$ PAEs in the presence of magnetic fields. Here, cubic $Fe_3O_4$ oleate-coated NPs were synthesized through high-temperature thermal decomposition. Subsequently, a polymer functionalization route was employed to transfer the particles to the aqueous phase for DNA

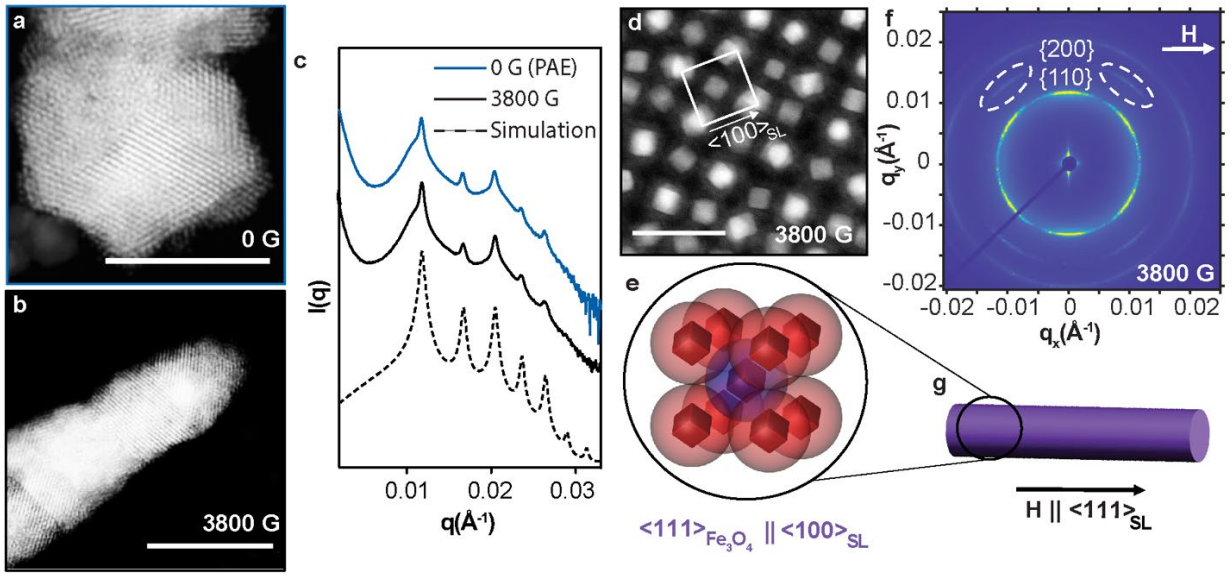


**Figure 17. Assembly of cubic $Fe_3O_4$ PAEs in a magnetic field.** Cubic $Fe_3O_4$ PAEs assembled (a) outside a magnetic field form rhombic dodecahedral superlattices and (b) in a magnetic field of 3800 G form elongated rods. (c) SAXS 1-D azimuthally-averaged patterns showing the *bcc* symmetry of the superlattices from (a, b). (d) TEM image of a cross-sectioned sample and (e) schematic depiction of the unit cell showing the orientation of cubes in the lattice. (f) 2-D SAXS pattern of a superlattice suspended in a magnetic field revealing orientation of the $<111>_{SL}$ along the field direction. (g) An elongated rod with the field direction and superlattice crystallographic orientation indicated.

functionalization. Once synthesized, the cubic $Fe_3O_4$ PAEs were assembled via slow cooling according to established DNA design rules in the presence of an externally applied magnetic field.

As the strength of the applied magnetic field increased, the habit of the superlattices evolves from rhombic dodachedra to eleongated rods as seen via STEM (**Figure 17a, b**). Importantly, as the binding is dictated by the DNA shell, the symmetry of particles is *bcc* irrespective of field strength (**Figure 17c**). Closer analysis of the SAXS patterns and cross-sectioned TEM images reveals an unexpected orientation of the cubes within the *bcc* unit cell for superlattices assembled under an applied field. Here, the <111> axis of the cube ($<111>_{Fe_3O_4}$) points along the <100> of the superlattice ($<100>_{SL}$) (**Figure 17d**). This alignment is hypothesized to stem from a maximization of facial interactions and minimization of repulsive magnetic dipole-dipole interactions. Additionally, the orientation of the cubes in the superlattices facilitates the alignment of the $<111>_{SL}$ along the field direction (**Figure 17g–i**). Wide-angle X-ray scattering (WAXS) further supported the orientation of the cubes within the unit cell as $<111>_{Fe_3O_4}||<100>_{SL}$. This orientation and crystal alignment occurs for different field strengths and cubic edge lengths, but the degree of alignment varies depending on magnetic coupling strength.

The aligned micron-size rods are comprised of unaligned domains similar to the nanoscale "grains" formed in polycrystals. To investigate how these domains vary depending on particle size and field strength, we turned to electron microscopy; however, traditional imaging is limited to a two-dimensional projection of a 3D object. Electron tomography allows for a 3D view of the structure by combining images across a wide range of tilt angles. In general, approximately 60 images were recorded of the same structure from -60° to +60° using HAADF STEM, and these images were compiled to form a tilt series that shows the shift in domain structure depending on the angle of the sample relative to the electron beam. This HAADF STEM tomography analysis was performed on a variety of superlattices assembled from different sizes (10 and 20 nm) of both cubic and spherical $Fe_3O_4$ particles under field strengths ranging from 140 to 3800 G. **Figure 18**

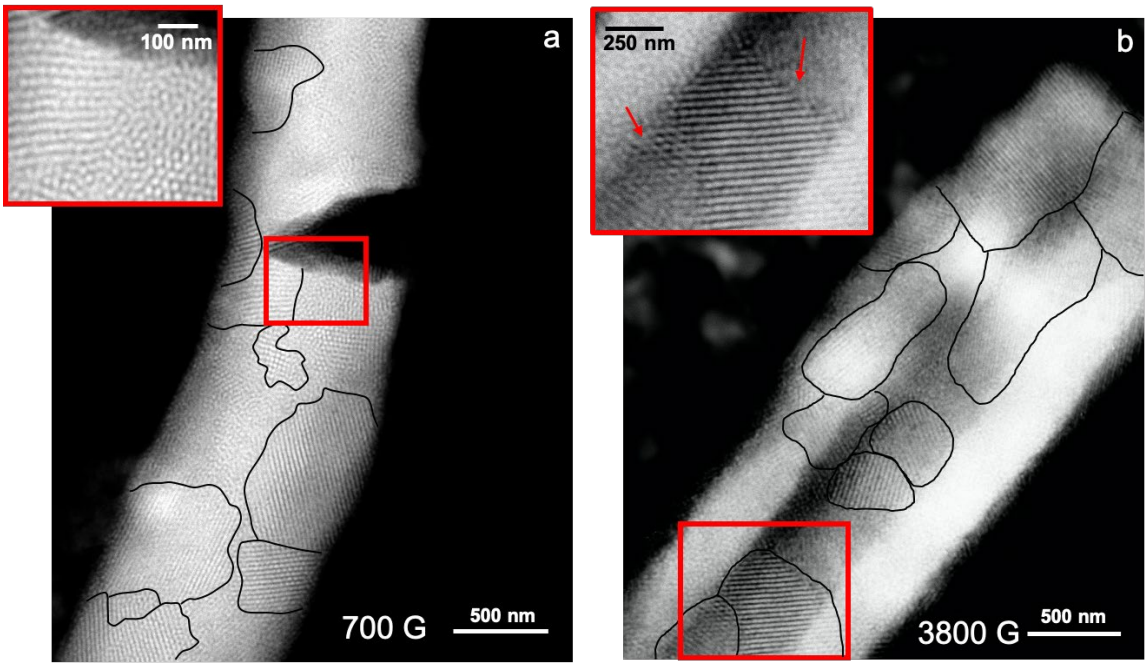


**Figure 18. HAADF STEM images of iron oxide superlattices.** Superlattices formed from 20 nm particles under field strength of (a) 700 G and (b) 3800 G. Aligned domains are roughly separated by black lines to illustrate the variation in domain size and shape. Insets show magnified regions with domain boundaries.

shows images at a single tilt angle for superlattices formed from 20 nm spherical particles at 700 and 3800 G. Some domains of aligned particles are highlighted, and insets show magnified views of domain boundaries between aligned regions. **Figure 18a** also shows a rod defect, which was common during imaging; this may be due to the embedment process before imaging or fragility after synthesis. Broken rods were more often detected when assembled under lower field strengths. After a rough quantitative analysis of domain size using multiple tilt angles per sample, larger domains of aligned particles were observed for smaller particles and higher field strength; this was expected from theoretical predictions. Superlattices formed from cubic particles also displayed larger domain areas than their spherical counterparts.

The results of these studies show how a combination of physical and chemical control can increase the scope of crystal engineering possibilities with DNA by enabling orientational control across multiple length scales. Additionally, this work lays the ground work for the structural characterization needed to investigate the crystallographic orientation of complex assemblies.

**10. Mie-Resonant Three-Dimensional Nanocrystals**

Optical metamaterials, comprised of resonant or non-resonant nanoparticle (NP) *meta-atoms*, are artificial structures engineered to have properties not found in nature. Previously, we have shown that bottom-up colloidal crystal engineering with DNA can yield 3D metamaterials that cannot be prepared by lithographic methods. Characterization of these 3D metamaterials has uncovered epsilon-near-zero properties, photonic band gaps, and unusual optical metallic scattering capabilities. In these studies, the meta-atom concentration was dilute, such that they did not interact with their neighbors. However, closely packed metacrystals, where the constituent meta-atoms strongly couple to each other, should have enhanced optical properties compared to their constituent materials. Here, we use DNA-mediated programmable assembly to prepare high-volume fraction (>70%) superlattices in which the individual plasmonic NPs exhibit strong coupling.

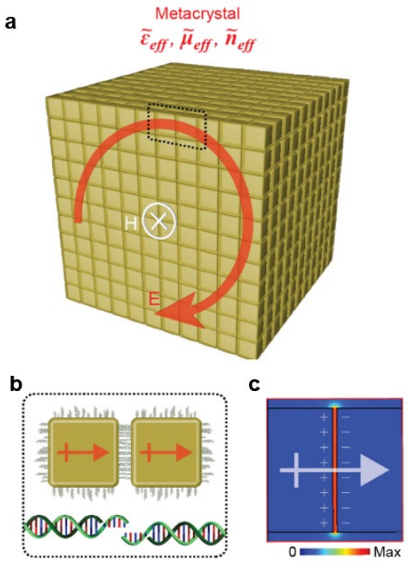


**Figure 19. Metacrystals engineered with DNA.** (a) Depiction of the working principle of a metacrystal. (b) Inset of the boxed region from (a) showing DNA programmable bonding of two polarized Au nanocubes. (c) Finite-element model showing a capacitively enhanced dipole moment in a small nanogap.

To explain the working principle underpinning these novel metacrystals, we compare them with atomic crystals. The two most common resonant modes in NPs are plasmonic and dielectric Mie resonances. In a plasmonic NP, an incoming electric field will displace the free carriers in a direction opposing the driving field, creating a linearly polarized dipole moment. In contrast, in a dielectric NP, each bound charge will be polarized by an electric (magnetic) field, producing a circular displacement current loop, which in turn induces a penetrating magnetic (electric) dipole. We hypothesized that a hybrid behavior would emerge from micron-sized, cube-shaped metacrystals comprised of Au nanocubes equally spaced in 3D arrays (**Figure 19a**). Here, each *plasmonic* nanocube meta-atom should be linearly polarized under an electric field (**Figure 19b**) leading to a collective electric displacement current loop and consequently a *dielectric* magnetic dipole Mie resonance (**Figure 19a**). This behavior arises because the highly polarizable metallic nanocubes are separated by gaps due to the insulating DNA duplex bonds (**Figure 19b**), analogous to the internal structure of dielectric materials. The optical properties of the metacrystal can thus be described by effective optical constants including

effective permittivity ($\tilde{\varepsilon}_{eff}$), permeability ($\tilde{\mu}_{eff}$), and refractive index ($\tilde{n}_{eff}$). Furthermore, the electric response of each meta-atom is enhanced when the interparticle distance is less than 10 nm as this increases the gap capacitance between neighboring nanocubes and induces stronger polarizability (**Figure 19c)**. We calculated the real and imaginary parts of the effective parameters as a function of gap distance (**Figure 20**). Both the permittivity and refractive index increase with decreasing gap distance, and this is attributed to the inverse dependence of gap capacitance on gap distance. At 2 nm, the smallest gap achievable through DNA-mediated assembly, the off-resonance permittivity and refractive index reach ~70 and ~8, respectively, much higher than those of the highest index materials in nature (Ge, GaAs, or SiC). Using the calculated effective parameters, we used finite-element modeling to obtain the scattering spectra of metacrystals as a function of gap distance (**Figure 20b**), which clearly show multiple Mie resonances in the mid-IR. The magnetic field patterns of the two lowest-order Mie modes (red arrows in Figure 18b) are shown in **Figure 20c,d**. These two modes are the magnetic and electric dipolar Mie resonances, respectively.

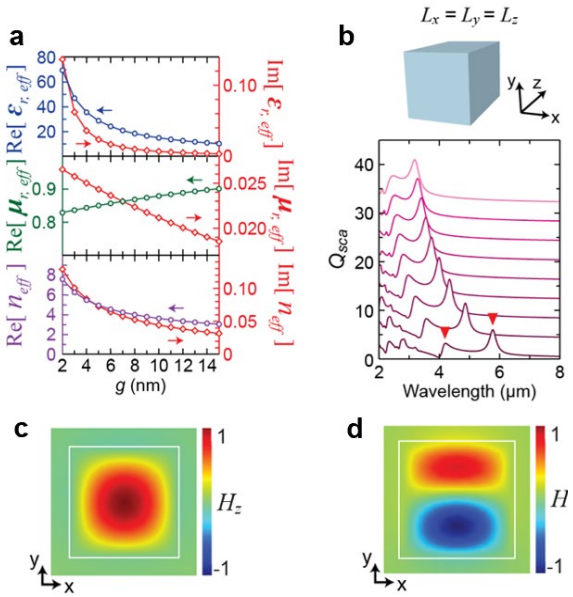


**Figure 20. Simulation of metacrystal properties.** (a) Effective parameters as a function of gap distance. (b) Schematic and calculated scattering spectra of effective medium metacrystals with differnt gap distances decreasing from top to bottom (10 - 2 nm)) (c, d) Magnetic field profiles of two lowest order modes in a metacrystal.

To experimentally realize these unusual metacrystals, we assembled Au nanocube superlattices via colloidal crystal engineering with DNA. To observe strong coupling between individual nanocubes, it is critical to assemble SLs from sufficiently large particles (> 60 nm) but with small interparticle spacings (< 10 nm). The assembly of such high volume-fraction SLs, previously elusive due to the formation of amorphous, kinetic structures, was enabled by the addition of flexible spacer units in both the anchor and linker sequences. We performed far-field Fourier-transform infrared (FTIR) extinction measurements using a synchrotron IR beamline to collect the scattering response from single metacrystals (**Figure 21a**). The experimental extinction spectrum for the metacrystal in **Figure 21b** shows two clear peaks at ~7.3 and ~5.7 μm, in good agreement with the calculated extinction spectra (**Figure 21d**). It is worth noting that

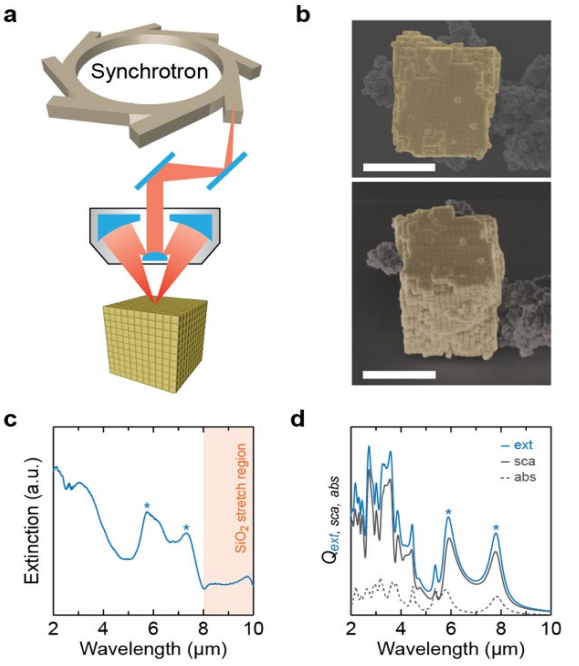


**Figure 21. Experimental characterization of metacrystals.** (a) Light path for the synchrotron measurements of single metacrystals. (b) SEM images of a representative metacrystal. Scale bar = 1 μm (c) Experimental and (d) simulated scattering spectra of the metacrystal in (b).

absorption contributions are substantially lower than scattering contributions (**Figure 21d**) because most of the electric field is concentrated inside the gap regions. This low-loss characteristic, analogous to that of metal-insulator-metal waveguides, distinguishes these metacrystals from infrared surface plasmon nanoantennas and should enable various technologies that have previously been limited by the high Ohmic losses of plasmons. Taken together, these results highlight that colloidal crystal engineering with DNA has potential as a platform for engineering devices with unnatural optical properties.

**11. Synthesis of Low Symmetry Colloidal Crystals with Unique Optical Properties**

Conventional low symmetry crystals have unique optical properties, such as birefringence and dichroism, because the refractive index in the crystals is direction-dependent. At a normal incidence to a crystal face, light will interact with the crystal in three different ways according to the orientation of the optical axis, which may lie perpendicular, parallel, or oblique to the face. Crystals with an oblique optical axis may have the most unique properties. For example, calcite, which has a rhombohedral lattice with an oblique optical axis, is a natural birefringent crystal and widely used in optical systems. However, natural crystals have a fixed refractive index, lattice symmetry, and working wavelength, which restricts their applications. We hypothesized that birefringence and dichroism can be endowed to any material if we can assembly them into low symmetry colloidal crystals. However, although colloidal crystals with dozens of symmetries have been engineered with DNA, most of them are high symmetry structures.

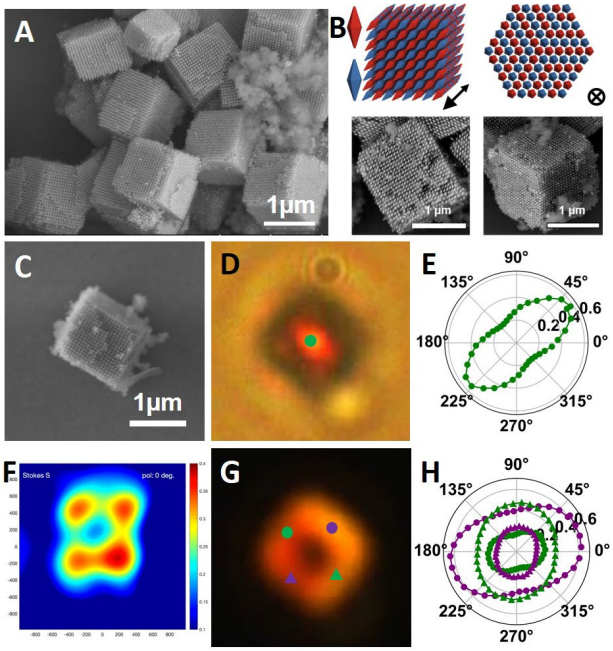


**Figure 22. DNA-engineered rhombohedral colloidal crystals with unique optical properties.** (A) SEM image of rhombohedral colloidal crystals assembled from Au pentabipyramid NPs. (B) 3D models of rhombohedral colloidal crystals viewed from the face and along the optical axis with corresponding SEM images. (C) SEM image of a single rhombohedral colloidal crystal. (D) Transmission optical image of the crystal in (C). (E) Polar plot showing the change in transmission intensity with polarization at the green spot in (D). (F) Simulated Stokes parameter, S, of transmitted light, which is non-zero and varies with polarization direction. (G) Dark-field image of the rhombohedral colloidal crystal in (C). (H) Polar plots of the change in scattering intensity with polarization for the four side faces in (G).

Here, two sets of Au pentabipyramid NPs modified with complementary DNA strands were assembled into rhombohedral colloidal crystals with rhombohedral crystal habits by slow cooling (**Figure 22A, B**). The crystal symmetry and habit are the same as calcite, and the optical axis is oblique to the crystal faces. To study their optical properties, the crystals were silica embedded and then dropcast on a glass slide. SEM was used to locate single crystals with upward crystal faces (**Figure 22C**) which were then studied in a home-built optical microscope. A polarizer converted the light source into linearly polarized light, and the polarization direction was controlled by rotating the polarizer. In transmission mode, the colloidal crystal shows a large transmittance ratio, which can be used as polarizer (**Figure 22D, E**). The Stokes S-parameter of transmission light was simulated to be non-zero, suggesting that this crystal

acts as a wave plate and can generate chiral light (**Figure 22F**). Additionally, dark-field experiments show abnormal asymmetric scattering behavior (**Figure 22G, H**). This property has never been observed in any material, including conventional birefringent materials and may result in the development of a new type of beam splitter.

Importantly, this work serves as a proof-of-concept highlighting that a new class of materials with unique and designable optical properties can be developed using colloidal crystal engineering of low-symmetry crystals. These structures are promising for optical applications including plasmonic devices, quantum computing, cloaking, micro-optical systems, and non-linear optics.

**Assembly of reconfigurable, sophisticated, and functional superlattices on surfaces**

Under this objective, we report our progress toward the assembly of superlattices of interest onto surfaces. First, we used patterned substrates to grow Wulff-shaped colloidal crystals with controlled shape, orientation, and position (Section D1). We then studied the reorganization of anisotropic PAEs into 2D films on a substrate (Section D2). Finally, in Section D3, we show that 2D films of close-packed gold nanocubes with low interparticle distance, assembled using DNA onto a surface, exhibit interesting optical properties as a metasurface, owing to the coupling between the Au nanocubes.

### 12. Position- and Orientation-Controlled Growth of Wulff-Shaped Colloidal Crystals Engineered with DNA

The ability to control symmetry and crystal habit has advanced crystal engineering with DNA towards a variety of unique applications, especially in nanophotonics. However, since crystal orientation, shape, and location (with respect to other structures) can significantly affect the optical light path, control over these parameters is needed to realize elaborate on-chip devices. Although there have been crude early examples of colloidal crystals engineered on substrates, full control over crystal orientation, shape, and location has not been achieved. Therefore, a synthetic approach needs to be developed that allows for such structural control. To this end, we drew inspiration from epitaxial growth strategies in atomic crystallization and prepared patterned substrates that when used in conjunction with DNA-mediated NP crystallization, provide control over Wulff-shaped crystal growth, location, and orientation. In addition, this approach allows one to control the patterned substrate/crystal lattice mismatch, something not yet realized for any epitaxy process.

Driven by the hypothesis that substrates encoded with nanoscale features resembling the lattice planes of NP crystals will direct epitaxial growth, we utilized lithography to design and generate patterns on Si wafers resembling the (001), (110), and (111) lattice planes of *bcc* NP crystals, which are composed of arrays of Au posts (**Figure 23**). On each post array-bearing substrate, a micrometer-sized strip was patterned with the same metal layers to serve as a control where no pattern is defined. The post arrays serve as "seeds" for epitaxial growth, which direct NP assembly in the orientation perpendicular to the lattice plane defined by the pattern; the micron-sized Au strips provide nucleation sites for crystal assembly. The substrates (posts and strips) were functionalized first with A DNA duplexes. These substrates were then immersed into a solution containing equal concentrations of 30-nm Au NPs functionalized with A and B DNA, respectively (designated A and B NPs, respectively). The seven-base single-stranded regions of the A and B DNA duplexes (i.e., the "sticky ends") are complementary to each other and hybridize to drive particle assembly. The solution was heated above the melting temperature of the duplex formed between the sticky ends on A and B NPs and then slowly cooled to room temperature. A temperature gradient was also incorporated to facilitate assembly on the substrate (**Figure 23**). After the reaction solution reached room temperature, both crystals grown in solution and the ones

grown on the substrate were embedded in silica for characterization.

SAXS and SEM were used to assign the lattice symmetry of the crystals that assembled in solution. These crystals adopt a *bcc* lattice symmetry and RD habit, which is the thermodynamically expected Wulff equilibrium shape given the NP and DNA design that were used. The RD-shaped crystals are enclosed by the lowest-energy, closest-packed (110) planes, and

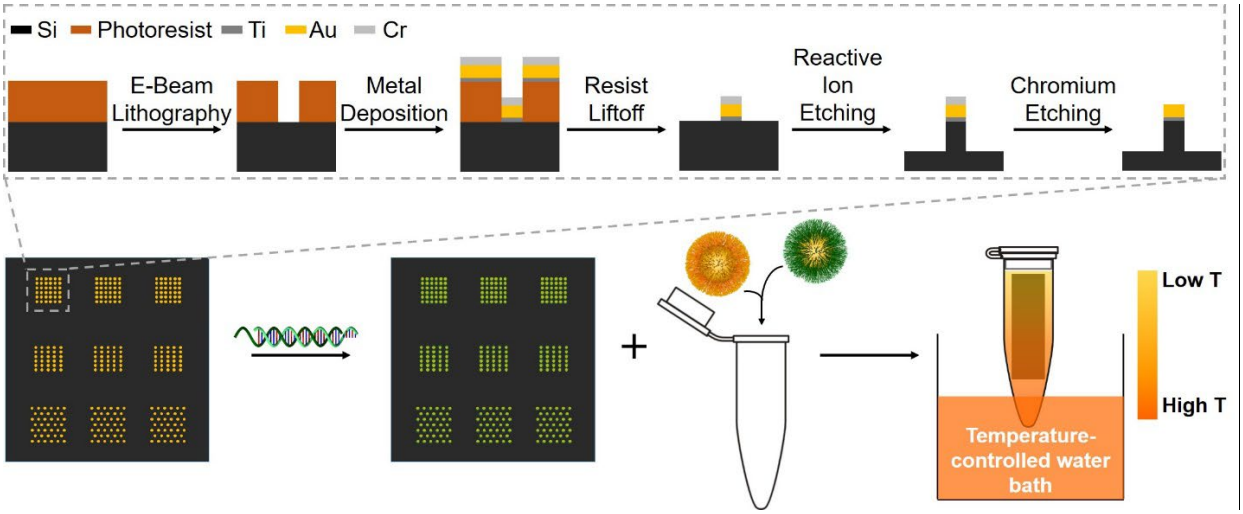


**Figure 23. Schematic representation of the experimental process and setup. S**ubstrates are fabricated through the sequence of lithographic processes shown in the dashed box at the top of the figure. The patterns are comprised of arrays of Au posts ~ 30 nm in both height and diameter, sitting on top of taller (height > 50 nm) Si nanopillars. This elevated-post design effectively prevents the substrate from sterically hindering the DNA shell of the NP directly attached to the posts. Patterned substrates are functionalized with a dense layer of A DNA duplex (green-colored DNA) and submerged into a solution of NPs coated with either A or B DNA duplex strands. The sample is then partially submerged in a temperature-controlled water bath to create a temperature gradient, and the water bath is slowly cooled. The higher temperature at the bottom of the reaction tube allows for the precipitated crystals to melt into individual NPs, replenishing the solution above; this setup effectively slows NP depletion through unproductive solution-based crystallization and enhances the rate and extent of substrate-driven crystal growth.

these crystals served as a guide for our substrate pattern design. When an unpatterned substrate (i.e., the micrometer-sized Au film) was used, the crystals selectively grew on the Au film (**Figure 24a**), but there was little control over position and orientation. In contrast, on the patterned substrate (i.e., the Au posts), arrays of crystals grew on locations defined by the pattern (**Figure 24b**). Moreover, crystals grown on the (001), (110), or (111) patterns (**Figure 24c–e**) had shapes that were orientation-specific for Wulff structures enclosed by (110) facets (**Figure 24f–h**). In other words, each post acted as a Au NP with a fixed position, coated with B DNA duplexes, and each pattern composed of these posts acted as a lattice plane of *bcc* crystals with a specific symmetry.

Crystals assembled epitaxially can be viewed as parts of a RD cut by the substrate lattice plane. Indeed, NPs assemble in the direction perpendicular to the lattice plane as defined by the crystal orientation of the patterned substrate (z-axis) (**Figure 24f–h**); the pattern also dictates the crystal orientation parallel to the substrate (x-y plane). Note that for the (111) pattern, there are two degenerate crystal orientations due to their symmetries in the *xy*-plane. Importantly, the overall square shape of the pattern does not dictate the crystal shape, i.e. it does not lead to square-shaped crystals (**Figure 24**), nor is the size of the crystal dictated by the size of the pattern. Rather, a large pattern can support multiple nucleation sites where the epitaxially grown crystals do not form one single Wulff-shaped crystal. Although the substrate patterns serve as nucleation sites for epitaxial assembly, the grown crystals are thermodynamic products with shapes and sizes dictated by the

growth conditions (e.g., NP type, DNA design).

Conceptually, this procedure can be applied to other systems comprised, for example, of different NP sizes, shapes, and compositions, or different DNA designs. Indeed, when 20-nm spherical NPs functionalized with the same A or B DNA duplexes are used, the expected crystal outcomes and specifically, orientations, are observed. Thus, this technique likely can be applied

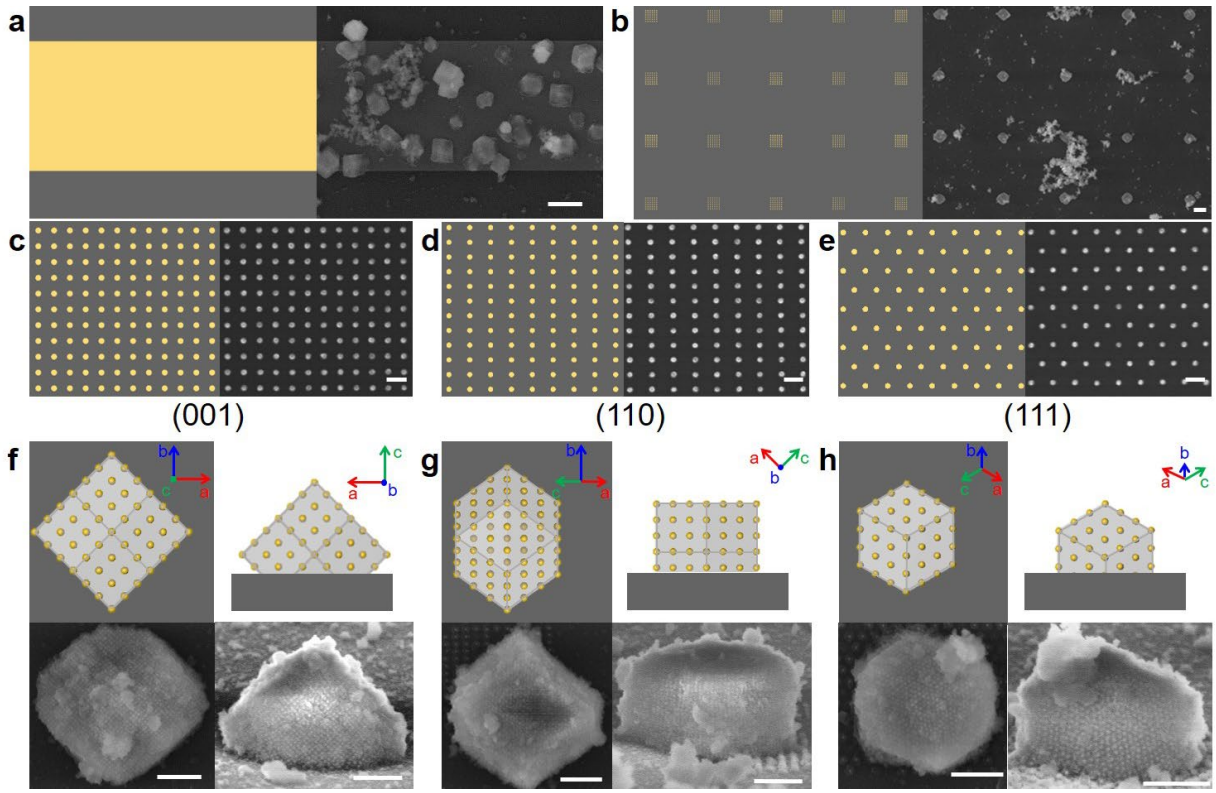


**Figure 24. Arrays of Wulff-shaped nanoparticle crystals with controlled orientation and location epitaxially grown on patterned substrates**. Crystals assemble on micron-sized gold strips at random (a), while the ones grown on patterned substrates have specified orientation, shape, and location (b). Schematics of the pattern design (left) and SEM images of assembled crystals (right) are shown. (c–e) Schematics (left) and SEM images (right) of the pattern design imitating the (001), (110), and (111) crystals planes, respectively. (f–h) Schematics (top row) and SEM images (bottom row) of the top-down (left) and side view (right) of epitaxially grown crystals along the [001], [110], and [111] orientations, respectively. The side views are tilted 75 ° from the top-down views in the schemes and SEM images. Scale bars: (a, b) 2 μm, (c–e) 100 nm, (f–h) 500 nm. The apparent imperfections in the crystals are in large part due to silica embedding and the residual silica.

generally to other lattice symmetries or NP shapes to control lattice orientation and attain symmetry-specific crystal shapes and provides a level of structural control that has not been previously reported in colloidal crystal engineering. Similar to conventional colloidal NP assembly processes, which have served as ideal models to inform atomic homogeneous crystallization, our system provides unique opportunities to understand and explore epitaxy due to the ability to tailor the lattice mismatch between the substrate and crystal. Specifically, this level of structural control is a significant step towards realizing complex, integrated devices with colloidal crystal components.

## 13. Anisotropic PAE Reorganization on Substrates

Controlling nanoparticle assembly into 2D films is critical for nanophotonics applications, where superlattice symmetry and interparticle distance largely dictate the optical response. Colloidal crystal engineering with DNA is an ideal platform for preparing and studying NP surface assemblies since it offers a large degree of control over such parameters. Previously, we assembled complementary spherical PAEs layer-by-layer on a DNA-functionalized substrate and found that upon annealing, the PAEs organize into the thermodynamically preferred *bcc* symmetry with an orientation that maximizes the number of favorable DNA interactions with the substrate. In contrast to spherical NPs, anisotropic PAEs have an inherent directionality imparted by the shape of the NP, which can give rise to new crystal symmetries. Additionally, anisotropic plasmonic NPs have enhanced optical properties compared to their spherical counterparts due to their flat facets, sharp corners, and non-unity aspect ratios. Here, we assembled three types of anisotropic PAEs - cubes, octahedra, and RD - on DNA-functionalized substrates and studied their thermally-induced reorganization into 2D crystalline

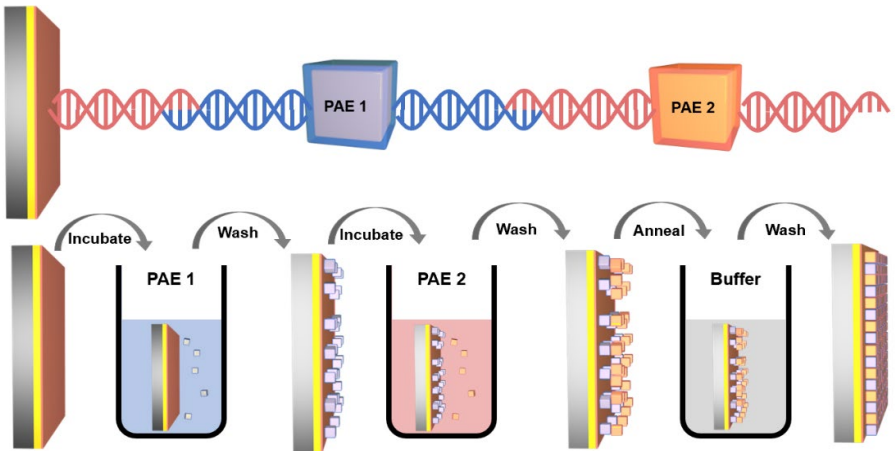


**Figure 25. Schematic of 2D PAE thin film assembly process.** (Top) Thin films containing two PAEs with complementary DNA strands (PAE 1 and PAE 2) are assembled onto a substrate functionalized with a single DNA strand (left). (Bottom) Thin film assembly is achieved via a layer-by-layer approach.

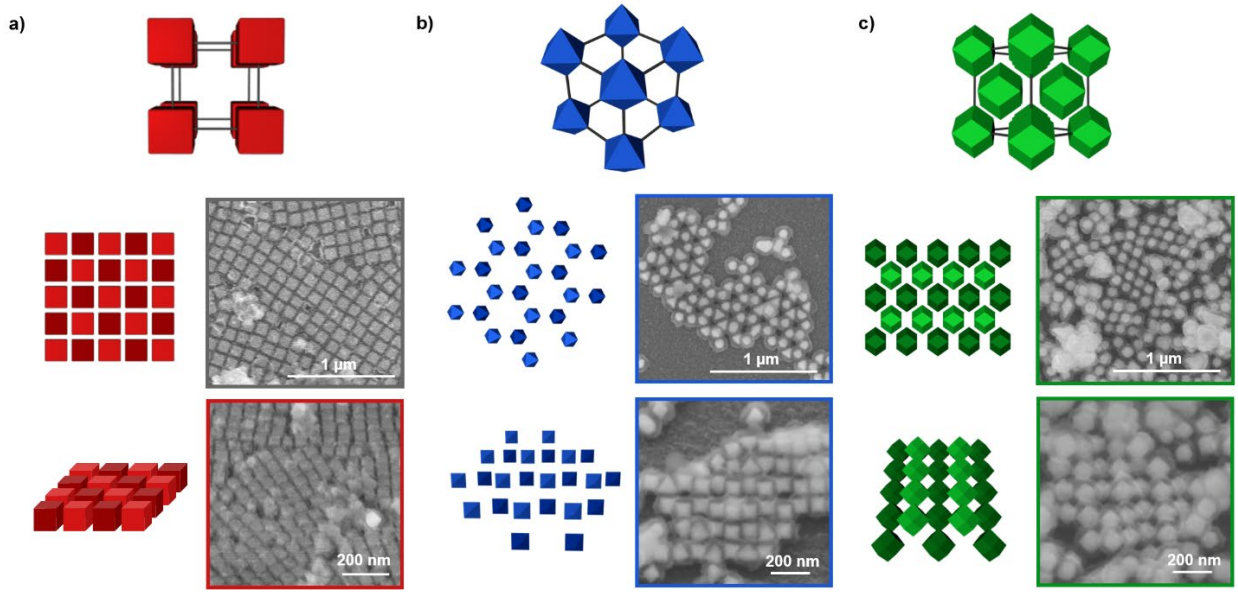


**Figure 26. Schematic and SEM images of surface-templated thin film colloidal assembly.** Models and SEM images of (a) cube, (b) octahedra, and (c) RD assembly. Tilted SEM images (bottom) show that NPs occupy different heights in the assemblies of octahedra and RDs.

lattices (**Figure 25**). We found that the governing driving force during reorganization is the retention of face-to-face DNA binding between complementary particles while maximizing favorable binding between the first layer of PAEs and the substrate (**Figure 26**). Interestingly, both the octahedra and RD assemblies result in relatively open 2D structures that are difficult to obtain by other NP assembly methods, which typically tend towards maximization of entropy. In particular, the octahedra assembly leads to a honeycomb lattice, an unusual but sought after structure in the optoelectronics community due to its similarity with graphene. Our results point to the use of colloidal crystal engineering with DNA as a method to prepare structures that cannot be prepared by conventional methods and may possess unique optical properties.

**14. IR-Resonant Colloidal Metasurfaces**

Previously, we have shown that colloidal Au nanocubes assembled with DNA onto a Au thin film exhibit a plasmonic gap mode in the volume between the cube and the film. The gap mode gives rise to extremely large electric and magnetic field enhancements due to the strong capacitive coupling between the parallel facets of the nanocube on the film. The spectral location of this gap mode is extremely sensitive to DNA length. Since the gap is created by the DNA ligands that attach nanocube to the Au film, its distance can be tuned *in situ* using stimuli that cause DNA to expand or contract. An alternative method to tune the optical response of colloidal metasurfaces is to exploit the coupling between individual NPs. When metallic NPs are placed within 20 nm of each other, strong coupling between them gives rise to a coupled electromagnetic response. Thus, in-plane coupling between meta-atoms is expected to provide an additional handle on the design of colloidal metasurfaces. Additionally, since the periodicities of the unit cells in these closely packed structures are subwavelength, the metamaterials can be treated as an effective medium with effective materials parameters.

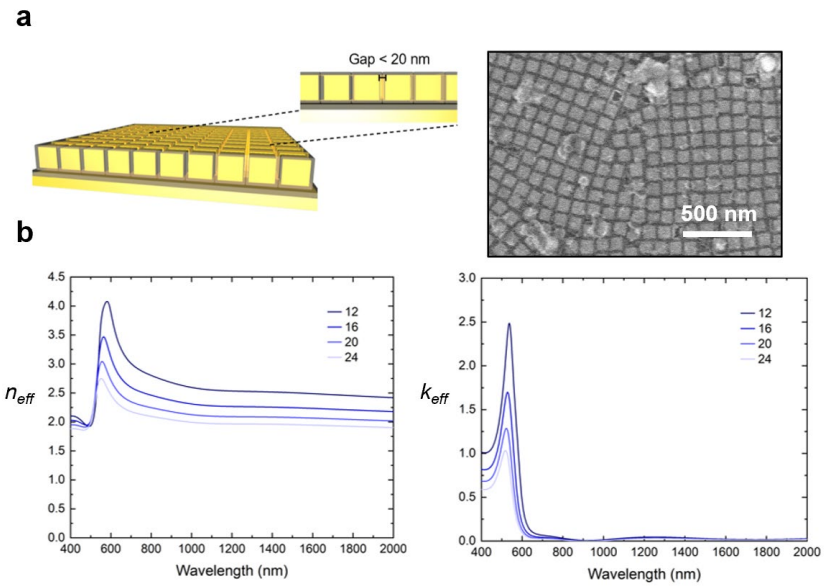


**Figure 27. IR-resonant colloidal metasurfaces.** (a) Schematic and SEM image of IR-resonant colloidal metasurfaces. (b) Real (left) and imaginary (right) parts of the effective refractive index of metasurfaces with varying gap distances.

Here, we assembled ordered monolayers of closely packed Au nanocubes on Au thin-films using DNA-mediated crystallization and studied their effective materials properties using finite-difference time-domain (FDTD) simulations and FTIR reflection measurements (**Figures 27 and 28**). Using the s-parameter retrieval method, we obtained the real and imaginary parts of the effective refractive index of the metasurface as a function of gap distance (**Figure 27b**). We observe that the nanocube monolayer behaves like an effective dielectric material in the near- and mid-IR with moderate refractive indices of above 2, which increase as the gap distance is

decreased, indicating their optical tunability. Additionally, the metasurfaces have low-to-negligible losses away from the resonance, pointing to their potential use in devices.

To better understand the optical response from typical metasurfaces, we simulated their reflection spectra and near-field profiles using FDTD (**Figure 28a,b**). The simulated reflection spectra reveal multiple resonances that can be understood as Fabry-Perot resonances of the metamaterial slab, with the fundamental resonance in the near-IR (**Figure 28a)**. These resonances shift towards the red as the gap distance decreases, which can be explained by the increase in effective refractive index. The experimental reflection spectra (**Figure 28c,d)** also exhibit multiple resonances, with the fundamental mode in the near-IR, in agreement with simulations. We used solvent polarity as a means of tuning the gap distance *in situ* and clearly measured the tunable reflection from a metasurface (**Figure 28d)**. From simulations of the electric and magnetic near-field profiles of the metasurface at its fundamental resonance (**Figure 28b)**, we see that the electric field is highly concentrated inside the in-plane gaps, while the magnetic field is delocalized across the collective out-of-plane gap. Diffusion of emitters into these highly concentrated fields should enable applications such as lasing and ultrafast emission through large plasmonic enhancements of excitation and emission rates. Our findings highlight the potential of colloidal metasurfaces to be used in tunable optical devices.

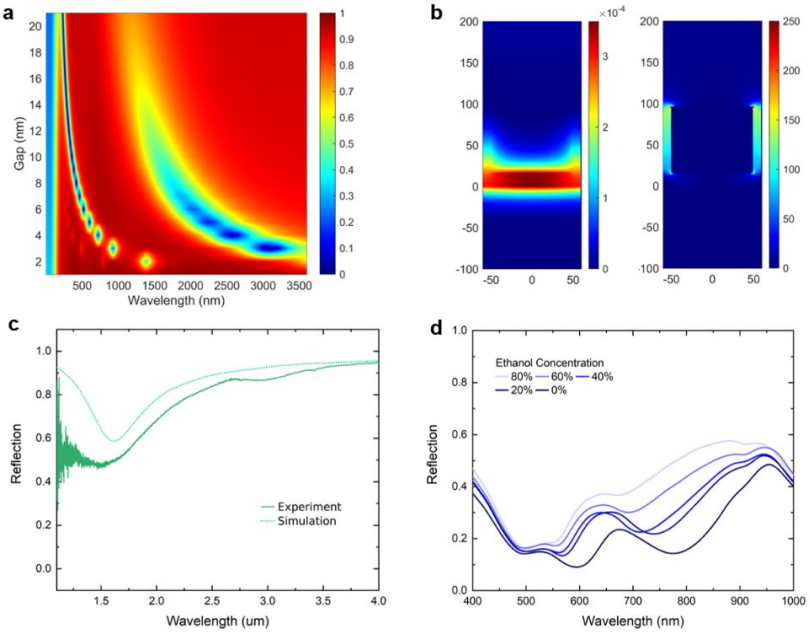


**Figure 28. Tuning metasurface properties by modulating gap distance.** (a) Simulated reflection spectra as a function of gap distance from 2 - 20 nm. (b) Magnetic (left) and electric (right) near-field profiles of a unit cell of the metasurface on resonance. (c) Experimental and simulated reflection spectra of a representative metasurface clearly showing the fundamental IR resonance. (d) Visible measurements with varying ethanol concentrations showing the tunability of the metasurfaces.

**CHANGES IN RESEARCH OBJECTIVES, if any:**

none

**SUPPORTED PERSONNEL**

The Mirkin Group

Chad Mirkin, PI
Anindta Das, postdoctoral fellow
Kyle Gibson, postdoctoral fellow
Yuwei Gu, postdoctoral fellow
Seungkyu Lee, postdoctoral fellow
Sarah Park, postdoctoral fellow, (IIN fellowship)
Devleena Samanta, postdoctoral fellow, (IIN fellowship)
Shunzhi Wang, postdoctoral fellow
Yueh Te Chu, graduate student
Kaitlin Landy, graduate student
Yuanwei Li, graduate student
Lin Sun, graduate student
Zachary Urbach, graduate student, (NDSEG fellowship)
Cindy Zheng, graduate student
Wenjie Zhou, graduate student
Jinghan Zhu, graduate student

The Aydin Group

Koray Aydin, Co-PI
Wisnu Hadibrata, graduate student
Edgar Palacios, graduate student

The Dravid Group

Vinayak Dravid, Co-PI
Jingshan Du, graduate student
Chamille Lescott, graduate student
Kelly Parker, graduate student, unfunded (NSF Fellowship)
Carolin Wahl, graduate student, unfunded
Roberto dos Reis, Scientific Officer, unfunded

**COLLABORATIONS**

Advanced imaging was performed with individual associated with the NU*ANC*E Center at Northwestern University including Eric Roth, Dr. Xiaobing Hu, Dr. Paul Smeets, and AFRL research including Dr. Larry Drummy and Dr. Cheri Hampton
DFT calculations of polyelemental nanoparticles were performed with Prof. Chris Wolverton (Northwestern University)
Metal-organic framework (MOF) experiments Prof. Fraser Stoddart (Northwestern University) and Prof. Omar Farha (Northwestern University)
Simulations of DNA-mediated crystallization behavior were conducted with Sharon Glotzer (University of Michigan) and George Schatz (Northwestern University)

Grazing incidence small angle x-ray scattering (GISAXS) experiments were conducted in collaboration with Dr. Byeongdu Lee (Argonne National Laboratory

**PUBLICATIONS**


1. Lee, S.; Zheng, C. Y.; Bujold, K. E.; Mirkin, C. A. "A Crosslinking Approach to Stabilizing Stimuli-Responsive Colloidal Crystals Engineered with DNA," *J. Am. Chem. Soc.*, **2019**, *141*, 11827-11831.
2. Zheng, C. Y.; Palacios, E.; Zhou, W.; Hadibrata, W.; Sun, L.; Huang, Z.; Schatz, G. C.; Aydin, K.; Mirkin, C. A. "Tunable Fluorescence from Dye-Modified DNA-Assembled Plasmonic Nanocube Arrays," *Adv. Mater.*, **2019**, *31*, 1904448.
3. Nam, K. W.; Park, S. S.; dos Reis, R.; Dravid, V. P.; Mirkin, C. A.; Stoddart, J. F. "Conductive 2D Metal-Organic Framework for High-Performance Cathodes in Aqueous Rechargeable Zinc Batteries," *Nat. Commun.*, **2019**, *10*, 4948.
4. Samanta, D.; Iscen, A.; Laramy, C. R.; Ebrahimi, S. B.; Bujold, K. E.; Schatz, G. C.; Mirkin, C. A. "Multivalent Cation-Induced Actuation of DNA-Mediated Colloidal Superlattices," *J. Am. Chem. Soc.*, **2019**, *141*, 19973-19977.
5. Park, S. S.; Urbach, Z. J.; Brisbois, C. A.; Parker, K. A.; Partridge, B. E.; Oh, T.; Dravid, V. P.; Olvera de la Cruz, M.; Mirkin C. A. "DNA- and Field-Mediated Assembly of Magnetic Nanoparticles into High-Aspect Ratio Crystals," *Adv. Mater.*, **2019**, *32*, 1906626.
6. Wang, Shunzhi; Du, J. S.; Diercks, N. J.; Zhou, W.; Roth, E. W.; Dravid, V. P.; Mirkin, C. A. "Colloidal Crystal 'Alloys'," *J. Am. Chem. Soc.*, **2019**, *141*, 20443-20450.
7. Lee, S.-H.; Oh, T.; Ryu, J.; Mirkin, C. A.; Jang, J.-W. "Understanding Optomagnetic Interactions in Fe Nanowire-Au Nanoring Hybrid Structures Synthesized Through Coaxial Lithography," *Chem. Mater.*, **2020**, *32*, 2843-2851.
8. Samanta, D.; Ebrahimi, S. B.; Mirkin, C. A. "Nucleic-Acid Structures as Intracellular Probes for Live Cells," *Adv. Mater.*, **2020**, *32,* 1901743.
9. Zhu, J.; Lin, H.; Kim, Y.; Yang, M.; Skakuj, K.; Du, J. S.; Lee, B.; Schatz, G. C.; Van Duyne, R. P.; Mirkin, C. A. "Light-Responsive Colloidal Crystals Engineered with DNA," *Adv. Mater.*, **2020**, *32*, 1906600.
10. Winegar, P. H.; Hayes, O. G.; McMillan, J. R.; Figg, C. A.; Focia, P. J.; Mirkin, C. A. "DNA-Directing Protein Packing within Single Crystals," *Chem*, **2020**, *6*, 1-11.
11. Figg, C. A.; Winegar, P. H.; Hayes, O. G.; Mirkin, C. A. "Controlling the DNA Hybridization Chain Reaction," *J. Am. Chem. Soc.*, **2020**, *142*, 8596-8601.
12. Huang, L.; Lin, H.; Zheng, C. Y.; Kluender, E. J.; Golnabi, R.; Shen, B.; Mirkin, C. A "Multimetallic High-Index Faceted, Heterostructured Nanoparticles," *J. Am. Chem. Soc.*, **2020**, *142*, 4570-4575.
13. Wang, Shunzhi; Park, S. S.; Lin, H.; Chen, P.-C.; Roth, E. W. Mirkin, C. A. "Colloidal Crystal Engineering with Metal-Organic Framework Nanoparticles," *Nature Commun.,* **2020**, *11*, 2495.
14. Chen, P.-C.; Liu, Y.; Du, J. S.; Meckes, B.; Dravid, V.; Mirkin, C. A "Chain-End Functionalized Polymers for the Controlled Synthesis of Sub-2nm Particles," *J. Am. Chem. Soc.*, **2020**, *142*, 7350-7355.
15. Huang, L.; Zheng, C. Y.; Shen, B.; Mirkin, C. A. "High-Index-Facet Metal-Alloy Nanoparticles as Fuel Cell Electrocatalysts," *Adv. Mater.*, **2020**, 2002849.

16. Ebrahimi, S. B.; Samanta, D.; Mirkin, C. A "DNA-Based Nanostructures for Live-Cell Analysis," *J. Am. Chem. Soc*., **2020**, *142*, 11343-11356.
17. DiStefano, J. G.; Murthy, A. A.; Lescott, C. J.; dos Reis, R.; Li, Y.; Dravid, V. P. "Au@$MoS_2$@$WS_2$ Core-Shell Architectures: Combining Vapor Phase and Solution-Based Approaches." *J. Phys. Chem. C,* **2020**, 124, 2627-2633
18. Parker, K. A.; Bobbala, S.; Drachuk, I. V.; Mirau. P. A.; Chavez, J. L.; Drummy, L. F.; Scott, E. A.; Dravid, V. P. "Soft Microscopy of Macromolecules: Correlative Imaging and Enhancing Contrast." Microscopy and Microanalysis, **2020**, *25* (S2) 496-497.
19. Wei, H.; Callewaert, F.; Hadibrata, W.; Velev, V.; Liu, Z.; Kumar, P.; Aydin, K.; Krishnaswamy, S. "Two-Photon Direct Laser Writing of Inverse-Designed Free-Form Near-Infrared Polarization Beamsplitter," *Adv. Opt. Mat.*, **2019**, *7*, 1900513.
20. Wei, C.; Dereshgi, S. A.; Song, X.; Murthy, A.; Dravid, V.P.; Cao, T.; Aydin, K. "Polarization Reflector/Color Filter at Visible Frequencies via Anisotropic α-$MoO_3$" *Adv. Opt. Mat.*, **2020**, *8*, 2000088.
21. Zhou, W.; Liu, Z.; Huang, Z.; Lin, H.; Samanta, D.; Lin, Q.-Y.; Aydin, K.; Mirkin, C. A "Device-Quality Reconfigurable Metamaterials from Shape-Directed Nanocrystal Assembly," *Proc. Natl. Acad. Sci. U. S. A*., **2020**, *accepted*
22. Du, J. S.; Shin, D.; Stanev, T. K.; Musumeci, C.; Zie, X.; Huang, Z.; Lai, M.; Sun, L.; Zhou, W.; Stern, N.; Dravid, V.; Mirkin, C. A. "Halide Perovskite Nanocrystal Arrays: Multiplexed Synthesis and Size-dependent Emission," *Sci. Advances*, **2020**, *accepted*.
23. Kim, S.; Zheng, C. Y.; Schatz, G. C.; Aydin, K.; Kim, K.-H.; Mirkin C. A. "Mie-Resonant Three-Dimensional Metacrystals," *Nano Lett.*, **2020**, *submitted*.
24. Sun, L.; Lin, H.; Li, Y.; Zhou, W.; Du, J. S.; Mirkin, C. A. "Position- and Orientation-Controlled Growth of Wulff-Shaped Colloidal Crystals Engineered with DNA," *Adv. Mat.*, **2020**, *submitted*.
25. Du, J.; Wang, S.; Dravid, V.; Mirkin, C. "Microscopy-Based Approaches to Characterizing Analogs of Classical Electrons in Colloidal Crystals Engineered with DNA," Microscopy and Microanalysis, 26(S2), 2016-2019. doi:10.1017/S1431927620020152

**PRESENTATIONS**

1. Chad A. Mirkin, International Conference on Molecular Systems Engineering, Radbound University, Nijmegen Netherlands "Mega-Libraries: Expanding and Exploring the Materials Genome Through High-throughput Cantilever-free Scanning Probe Lithography" (2019).
2. Chad A. Mirkin, International Conference on Molecular Systems Engineering, Radbound University, Nijmegen Netherlands "Colloidal Crystal Engineering with DNA" (2019).
3. Chad A. Mirkin, Nakamura Award, UCLA, Los Angeles, CA, "Megalibraries: Expanding and Exploring the Materials Genome" (2019).
4. Chad A. Mirkin, Fall 2019 ACS Meeting, San Diego, CA, "Exploration of the nanomedicine-design space with high-throughput screening and machine learning" (2019).
5. Chad A. Mirkin, Fall 2019 ACS Meeting, San Diego, CA, "Subcellular control over focal adhesion anisotropy, independent of cell morphology, dictates stem cell fate" (2019).
6. Chad A. Mirkin, Center for Integrated Nanotechnology User Conference, Santa Fe, NM, "Expanding and Exploring the Materials Genome Through Cantilever-Free Scanning Probe Lithography" (2019).

7. Chad A. Mirkin, Tsinghua University Global Vision Lecture Series, Beijing, China, "MegaLibraries: Tools for Exploring and Expanding the Materials Genome" (2019).
8. Chad A. Mirkin, O'Brien Kidney Center Symposium, Northwestern Feinberg, Chicago, IL, "Opening the Field of Digital Medicine through Spherical Nucleic Acids" (2019).
9. Chad A. Mirkin, Contemporary Crystal Engineering and Solid-State Chemistry Symposium, Rehovot, Israel, "Colloidal Crystal Engineering with DNA: Repurposing the Blueprint of Life" (2019).
10. Chad A. Mirkin, Gilbert Newton Lewis Memorial Lecture, Berkeley, CA, "Repurposing the Blue Print of Life for Materials Design" (2019).
11. Chad A. Mirkin, Kabiller Award Lecture, International Institute for Nanotechnology Symposium, Evanston, IL, "Opening the Field of Digital Medicine through Spherical Nucleic Acids" (2019).
12. Chad A. Mirkin, Materials Research Society Fall 2019 Conference, Boston, MA "Programmable Metamaterials through Colloidal Crystal Engineering with DNA" (2019).
13. Chad A. Mirkin, 15th US-Japan Symposium on Drug Delivery Systems, Maui, HI, "Opening the Fields of Digital Medicine and Rational Vaccinology through Spherical Nucleic Acids" (2019).
14. Chad A. Mirkin, KAUST Winter Enrichment Program, Jeddah, Saudia Arabia, via video conference, "Rational Vaccinology: In Pursuit of the Perfect Vaccine" (2020).
15. Chad A. Mirkin, ACS Silicon Valley Harry & Carol Mosher Award, San Francisco, CA, "Ushering in the Era of Digital Drug Design with Spherical Nucleic Acids" (2020).
16. Chad A. Mirkin, Pittcon 2020, Chicago, IL, "Rational Vaccinology: Unlocking the Power of Spherical Nucleic Acid (SNA) Therapeutics Through Structural Design" (2020).
17. Chad A. Mirkin, Pittcon 2020, Chicago, IL, "Forced Intercalation Aptamers" (2020).
18. Chad A. Mirkin, Frontiers in Molecular Science, Beijing, China, via video conference "Rational Vaccinology: In Pursuit of the Perfect Cancer Vaccine" (2020).
19. Chad A. Mirkin, ACS Fall, 2020 Virtual, "Spherical Nucleic Acids for Live-Cell Analysis" (2020).
20. Vinayak P. Dravid. Microscopy and Microanalysis Conference, Portland, USA "Hybrid" Microscopy: Multimodal, Correlative and Dynamic Characterization of Soft and Hybrid Structures." (2019)
21. Vinayak P. Dravid, ChemPhysMat, India, "Inspiration from Professor CNR Rao: Experimental Materials Genome at the Nanoscale," (2019).
22. Vinayak P. Dravid, Southern University of Science and Technology, Shenzhen, China. "Multiplexed Nanopatterning of Multifunctional Materials" (2019).
23. Koray Aydin. PQE Physics of Quantum Electronics, PQE 2020, Snowbird, UT, "Emerging Anisotropic 2D Layered Materials for Photonics, Plasmonics and Phononics" (2020).
24. Koray Aydin. MRS Fall Meeting 2019, Boston, MA, "Emerging Anisotropic 2D Layered Materials for Photonics, Plasmonics and Phononics" (2019).
25. J. G. DiStefano**,** V. P. Dravid. Materials Research Society Fall Meeting. "The Solution to the Solution—Colloidal Suspension of 3D Architectures of 2D Materials," Oral Presentation. (2019).
26. Jingshan S. Du, 36$^{th}$ John E. Hilliard Symposium, Northwestern University, Evanston, IL, "Classical Electron Equivalent Nanoparticles in Metal-like Colloidal Crystals" (2019).
27. Kelly A. Parker. Microscopy & Microanalysis, Portland, OR, "Soft Microscopy of Macromolecules: Enhancing Contrast" (2019).

28. Devleena Samanta. ACS Fall Meeting, Virtual Seminar, "NanoFlares for Detection and Diagnosis" (2020)
29. Devleena Samanta. Hebrew University of Jerusalem Department of Pharmacy Seminar, Jerusalem, Israel, May 2020 "DNA-Based Nanostructures for Live-Cell Analysis" (2020)
30. Devleena Samanta. SPIE-MRSEC Student Seminar Series at Northwestern University, Evanston, IL, "Nucleic Acid-Based Structures as Stimuli-Responsive Materials" (2020)
31. Devleena Samanta. International Symposium on Clusters and Nanomaterials, Richmond, VA, "Detecting Intracellular Analytes Using Nanoparticle-Based Platforms" (2019)
32. Devleena Samanta. Virginia Military Institute, Richmond, VA, "Nanomaterials for Biomedical Applications" (2019)
33. Devleena Samanta. 2019 AIChE Annual Meeting, "Engineering Nanomaterials for Biomedical Applications" (2019) poster
34. Wenjie Zhou. Contemporary Crystal Engineering and Solid-State Chemistry, Israel “DNA-Mediated, Single Particle Control of Colloidal Nanocrystals on Surfaces” (2019) poster
35. Seungkyu Lee. ACS Fall Meeting, Virtual Seminar, " Cross-linking approach to stabilizing stimuli-responsive colloidal crystals engineered with DNA" (2020)

**AWARDS**

Chad A. Mirkin. ACS Division of Colloid and Surface Science Award for Outstanding Achievement in Nanoscience (2020)
Chad A. Mirkin. AAAS Philip Hauge Abelson Award (2020)
Chad A. Mirkin. Nakamura Award, American Association for Advances in Functional Materials (AAAFM) (2019)
Chad A. Mirkin. Harry and Carol Mosher Award (Silicon Valley Section of the American Chemical Society) (2019)
Chad A. Mirkin. Kabiller Prize in Nanoscience and Nanomedicine (2019)
Chad A. Mirkin. Yao Yuan Innovation Award (2019)
Vinayak Dravid. Fellow, Microanalysis Society, Inaugural Class of 2019.
Koray Aydin. JCI Ten Young Outstanding Person (TOYP) Turkey Award (2019).
Koray Aydin. JCI Ten Young Outstanding Person (TOYP) Global Finalist (2019).
Jingshan Du. SPIE Optics and Photonics Education Scholarship, SPIE (2020).
Jingshan Du. Weertman Fellowship Runner Up, Northwestern University (2019).
Devleena Samanta. Outstanding Researcher Award, International Institute for Nanotechnology (IIN) (2019)
Devleena Samanta. AIChE Women in Science Travel Award (2019)
Taegon Oh Outstanding Researcher Award, International Institute for Nanotechnology (IIN) (2019)
Wenjie Zhou, IPMI Bright Futures Award, International Precious Metals Institute (2020)

**INTERACTIONS/TRANSITIONS**

**Patent Applications**

"Polymer-assisted synthesis of ultrasmall nanoparticles" C A Mirkin, P Chen, Y Liu, J S Du. 62/824,617. U.S. Patent Application, Provisional.

"Orientation determination and mapping by stage rocking electron channeling and imaging reconstruction" Vinayak P. Dravid, Benjamin Myers, Karl A. Hujsak. WO2019152585A3 U.S Patent (April 2020)

"High speed/low dose multi-objective autonomous scanning materials imaging" Karl A. Husjak, Vinayak P. Dravid WO2019152585A3 U.S. Patent (Jan, 2020)

"Photonic crystals comprising nanoparticles and space group" Haixin Lin, Chad Mirkin, George Schatz, Lin Sun, 16/959,395, U.S. Patent Application (June 2020)

"Stabilized colloidal crystals and methods of stabilizing colloidal crystals Katherine Bujold, Seungkyu Lee, Chad Mirkin, Cindy Zheng, 16/882,002 U.S. Patent Application (May 2020)

"Halide Perovskite Nanocrystal Array and Its Preparation" Vinayak Dravid, Jingshan Du, Chad Mirkin, Donghoon Shin, 62/944,734 U.S. Patent Application, provisional (Dec 2019)

"Fit-flares for detection of intracellular analytes in live cells" Sasha Brian Ebrahimi, Chad Mirkin, Devleena Samanta, PCT/US2020/042835 (July 2020)

"Methods for epitaxial growth of colloidal single crystals engineered with DNA" Haixin Lin, Chad Mirkin, Lin Sun, 63/038,501, U.S. Patent Application, provisional (June 2020)

"Conductive 2D Metal-Organic Framework for Aqueous Rechargeable Battery Cathodes" Chad Mirkin, KwanWoo Nam, Sarah Park, James Stoddart, PCT/US2020/041615, (July 20200

**YEAR 4**
**Cover Page**
**To:** Dr. Patrick Bradshaw, patrick.bradshaw.3@us.af.mil
**Subject:** Annual Report
**Contract/Grant Title:** Reconfigurable Matter from Programmable Atom Equivalents
**Contract/Grant #:** FA9550-17-1-0348
**Reporting Period:** August 15, 2020–August 14, 2021

**ABSTRACT**

In Year 4, we continued to significantly enhance our understanding of reconfigurable matter at the nanoscale and our ability to program sophisticated, functional structures using programmable atom equivalents (PAEs) as building blocks. New porous nanoparticles have been developed that assemble through a fundamentally new DNA-mediated edge-sharing regime to afford mesoscale porous superlattices with extended open channels (Objective 1). DNA dendrons have been advanced as highly tunable, dynamic PAEs that undergo multiple levels of hierarchical assembly and enable *in situ* reconfiguration of lattice symmetry at ambient temperatures (Objective 2). Furthermore, we have pushed past the constraints of periodic superlattices and have designed highly ordered quasicrystalline nanoparticle superlattices (Objective 3). In addition, 2D colloidal metasurfaces with exotic optical phenomena (such as negative refractive index) were identified by simulation and subsequently realized and experimentally characterized using DNA-mediated assembly (Objective 4). Together, the progress made in Year 4 substantially advances in our ability to design and realize structurally sophisticated, reconfigurable, and functional superlattices.

**OBJECTIVES for the funding period**

## Year 1

Objective 1: Develop a new feedstock of functional PAE building blocks

- *Synthesis of three-dimensional anisotropic plasmonic nanoparticles*
- *Synthesis of MOF nanoparticles with control over their physical properties*

Objective 2: Synthesize and investigate dynamically reconfigurable superlattices

- *Transmutable nanoparticle superlattices*
- *High resolution and contrast imaging of soft materials by electron microscopy*

Objective 3: Synthesize and investigate structurally sophisticated and functional superlattices.

- *Superlattices with controlled crystal habit*
- *Explore emergent optical phenomena in nanoparticle superlattices*

Objective 4: Assemble reconfigurable, sophisticated, and functional superlattices on surfaces

*Fabricate surface templates with well-defined DNA binding sites*

## Year 2

Objective 1: Develop a new feedstock of functional PAE building blocks

- *Synthesis of two-dimensional anisotropic plasmonic nanoparticles*
- *Algorithmic characterization of nanoparticle yield and dispersion.*
- *Synthesis of MOFs nanoparticles with control over their physical properties*

Objective 2: Synthesize and investigate dynamically reconfigurable superlattices

- *Transmutable nanoparticle superlattices*
- *Sparse imaging for soft materials characterization*
- *High resolution and contrast imaging of soft materials by electron microscopy*

Objective 3: Synthesize and investigate structurally sophisticated and functional superlattices

- *Co-crystallization of multiple building blocks with chemically, physically, and structurally distinct properties*
- *Superlattices with controlled crystal habit*
- *Explore emergent optical phenomena in nanoparticle superlattices*

Objective 4: Assemble reconfigurable, sophisticated, and functional superlattices on surfaces

- *Layer-by-layer growth of single-crystal superlattices with defined crystal shape and size*

**Year 3**

Objective 1: Develop a new feedstock of functional PAE building blocks

- *Synthesis of two-dimensional anisotropic plasmonic nanoparticles*
- *High-throughput screening of anisotropic nanoparticle synthesis conditions*

Objective 2: Synthesize and investigate dynamically reconfigurable superlattices

- *Transmutable nanoparticle superlattices*
- *In situ characterization of reconfigurable superlattices via fluidic-cell S/TEM*

Objective 3: Synthesize and investigate structurally sophisticated and functional superlattices

- *Co-crystallization of multiple building blocks with chemically, physically, and structurally distinct properties*
- *Unique low-symmetry and quasicrystalline structures*
- *Explore emergent optical phenomena in nanoparticle superlattices*

Objective 4: Assemble reconfigurable, sophisticated, and functional superlattices on surfaces

- *Layer-by-layer growth of single-crystal superlattices with defined crystal shape and size.*

**Year 4**

Objective 1: Develop a new feedstock of functional PAE building blocks

- *High-throughput screening of anisotropic nanoparticle synthesis conditions*

Objective 2: Synthesize and investigate dynamically reconfigurable superlattices

- *Transmutable nanoparticle superlattices*
- *In situ characterization of reconfigurable superlattices via fluidic-cell S/TEM*

Objective 3: Synthesize and investigate structurally sophisticated and functional superlattices

- *Co-crystallization of multiple building blocks with chemically, physically, and structurally distinct properties*
- *Unique low-symmetry and quasicrystalline structures*
- *Explore emergent optical phenomena in nanoparticle superlattices*

Objective 4: Assemble reconfigurable, sophisticated, and functional superlattices on surfaces

- *Superlattice assembly on flexible and porous supports*
- *Emergent properties of surface-bound superlattices*

**Year 5**

Objective 1: Develop a new feedstock of functional PAE building blocks

- *High-throughput screening of anisotropic nanoparticle synthesis conditions*

Objective 2: Synthesize and investigate dynamically reconfigurable superlattices

- *Synthesis of dynamically responsive superlattices from MOF building blocks*
- *Develop new strategies for transferring DNA-assembled superlattices to the solid state*

Objective 3: Synthesize and investigate structurally sophisticated and functional superlattices.

- *Unique low-symmetry and quasicrystalline structures*
- *Explore emergent optical phenomena in nanoparticle superlattices*

Objective 4: Assemble reconfigurable, sophisticated, and functional superlattices on surfaces

- *Emergent properties of surface-bound superlattices*

## FINDINGS

### Development of a new feedstock of functional PAE building blocks

Under this objective, we enhanced the library of anisotropic nanoparticles and used protein-based cores and dendrimeric DNA as components in functional programmable atom equivalents (PAEs). The use of sophisticated nanoframes and nanocages in conjunction with DNA has led to the synthesis of unique open channel superlattices for the first time (Section A1). We have developed a new strategy to impart functional transport properties upon PAEs using DNA dendrons and a DNA-gated hydrogel capable of selectively transporting cargo (Section A2). Finally, we have advanced polymer ink compositions for the synthesis of nanostructured alloy metal nanoparticles (Section A3).

### 1. Open Channel Superlattices

Porous crystals are a distinct class of materials with unique properties, including high surface area and low density; they are able to physically absorb and chemically interact with guest species. The combination of their ordered lattice spacings and porosity makes these materials attractive for many applications, including gas storage, separation, sensing, catalysis, and crystal structure determination. Crystals with continuous pores with sizes of 50–500 nm would open new opportunities in applications involving large organic, inorganic, and biological materials, supramolecular structures, and viscous solutions, but their synthesis largely remains an outstanding challenge until now. We have developed the synthesis for a broad class of porous nanoparticle (NP) building blocks, including nanoframes and nanocages (**Figure 1**), and show that through DNA-mediated assembly, these new porous NPs can be assembled into the first colloidal porous crystals with continuous voids; we term these crystals open channel superlattices.

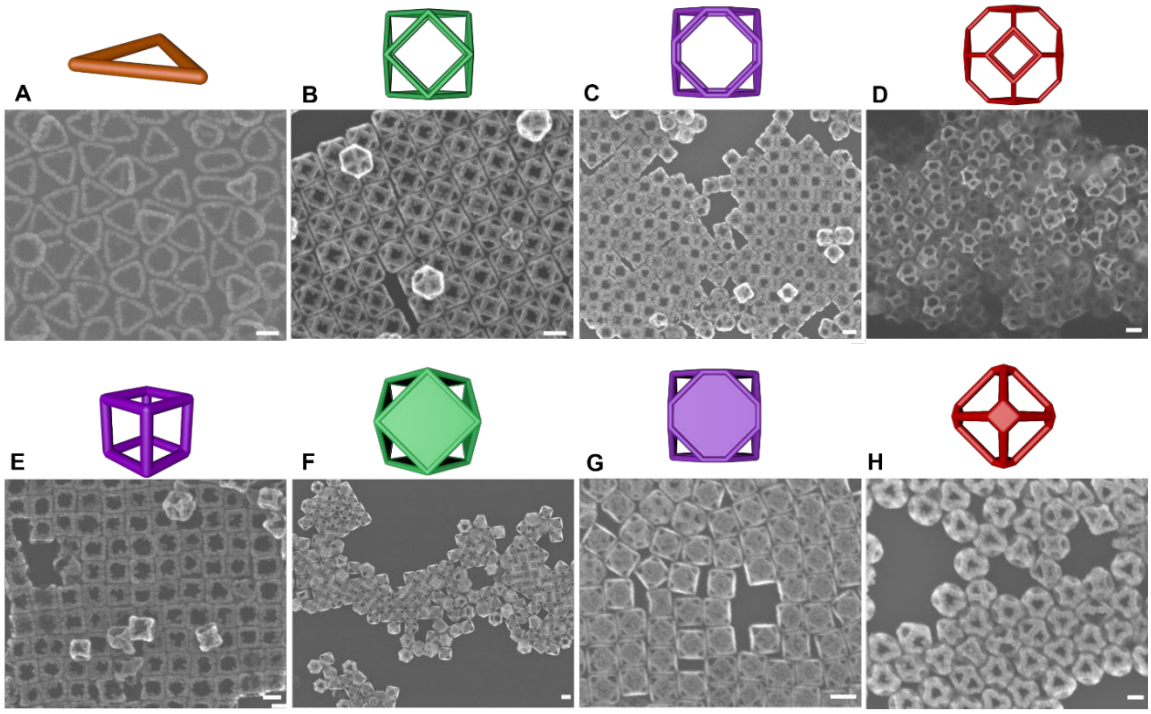


**Figure 1.** Porous nanoparticles (NPs) of different shapes. (A to H) Model and corresponding SEM images of porous NPs, including triangular prism nanoframes (NFs) (A), cuboctahedral NFs (B), truncated cubic NFs (C), truncated octahedral NFs (D), cubic NFs (E), cuboctahedral nanocages (NCs) (F), truncated cubic NCs (G), and slightly truncated octahedral NCs (H). Scale bars: 100 nm.

DNA-functionalized nanoframes and nanocages were synthesized so that they could be assembled through the complementary interactions between DNA surface ligands. Importantly, DNA interactions drive the formation of ordered superlattices in which interparticle registry is enforced by the maximization

of DNA hybridization between the edges of adjacent nanoframes. Notably, this edge-to-edge assembly (edge-tiling) is fundamentally distinct from the canonical face-to-face interactions (face-packing) that dictate the assembly outcomes of the solid NPs that have most commonly been utilized. Through DNA-mediated registry of porous NPs, we discovered 12 types of designer porous crystals with different symmetries, topologies, and porosities (**Figure 2**). The crystal symmetry, channel size, and porosity can be tuned via the geometry, outline size, and thickness of constituent nanoframes, as well as through the selective retention of specific faces to form nanocages. Importantly, we delineated four design rules that guide assembly in this new design space (edge-tiling of nanoframes). Furthermore, we show the capability of these porous superlattices to host large guest species by encapsulating colloidal gold nanospheres within them. In principle, other desired functional materials (such as quantum dots, proteins, and viruses) can be localized in the open channels. As such, this work addresses a challenge in the synthesis of crystalline materials with large, nanometer pore sizes. Importantly, it represents an exciting new direction in colloidal crystal engineering, which could enable previously inaccessible functionalities and impact a broad range of fields, spanning catalysis, plasmonics, electronics, biology, medicine, and many others.

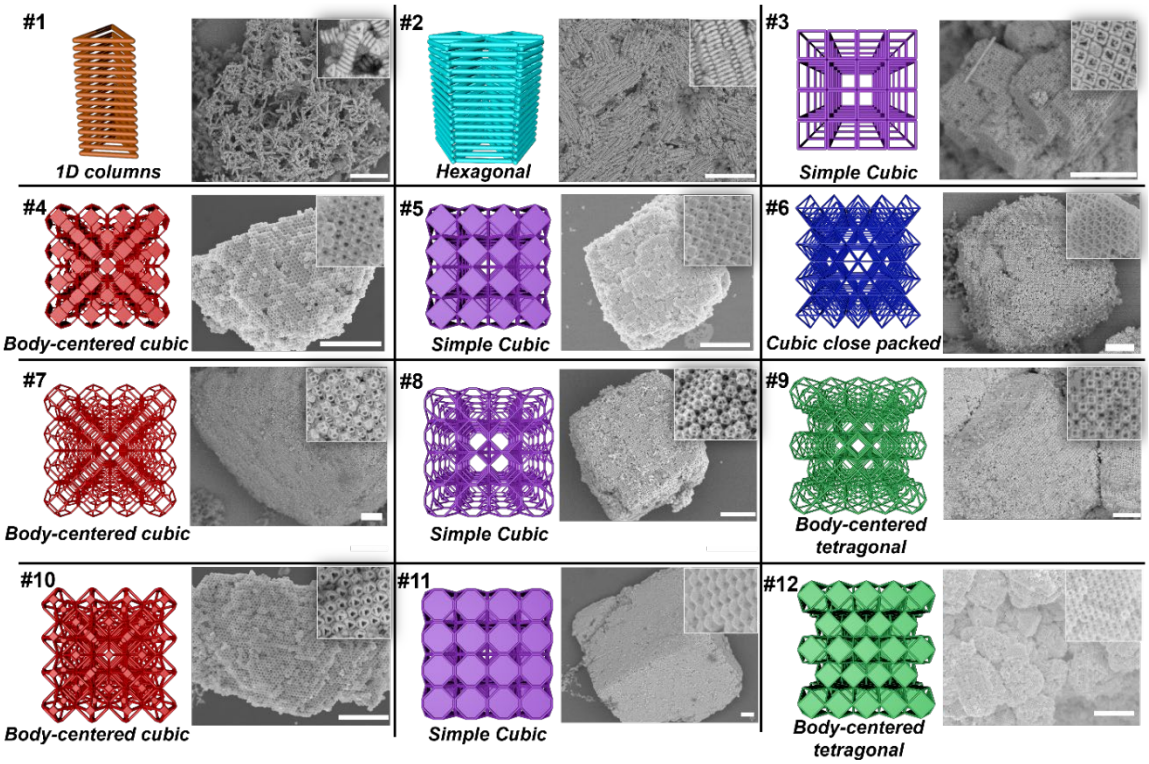


**Figure 2.** 12 types of designer porous crystals with different symmetries, topologies, and porosities. Scale bars: 2.5 μm.

## 2. DNA-gated Hydrogels for Selective Chemical Cargo Transport

The selective transport of molecular cargo is critical in many biological and chemical/materials processes and applications. Although nature has evolved highly efficient *in vivo* biological transport systems, man-made transport systems are often limited by the challenges associated with fine-tuning interactions between cargo and synthetic or natural transport barriers. Therefore, we designed and synthesized a molecular transport platform where the cargo-barrier interactions can be systemically modulated. By studying this platform as a model system, we learned how cargo-barrier interactions can fundamentally affect the transport process; the knowledge gained will ultimately lead to new selective transport systems with efficiencies that surpass that of existing ones.

In this work, we have elaborated deliberately designed DNA-DNA interactions as a new modality for selective DNA-modified cargo transport through DNA-grafted hydrogel supports. Specifically, a DNA-gated hydrogel was developed as the transport barrier, where DNA strands were covalently incorporated into hydrogel pores to mediate the diffusion of nanoscopic species, resulting in a "gating" mechanism based on volume exclusion; only cargo tagged with complementary DNA sequences may reversibly bind to these gating DNA strands and thus pass through the barrier (**Figure 3a**). We performed a theory-guided study to systematically examine how the DNA sequence and cargo valency (i.e., the number of DNA strands on the cargo) affected the transport processes, and we discovered a binding regime that leads to optimal transport selectivity.

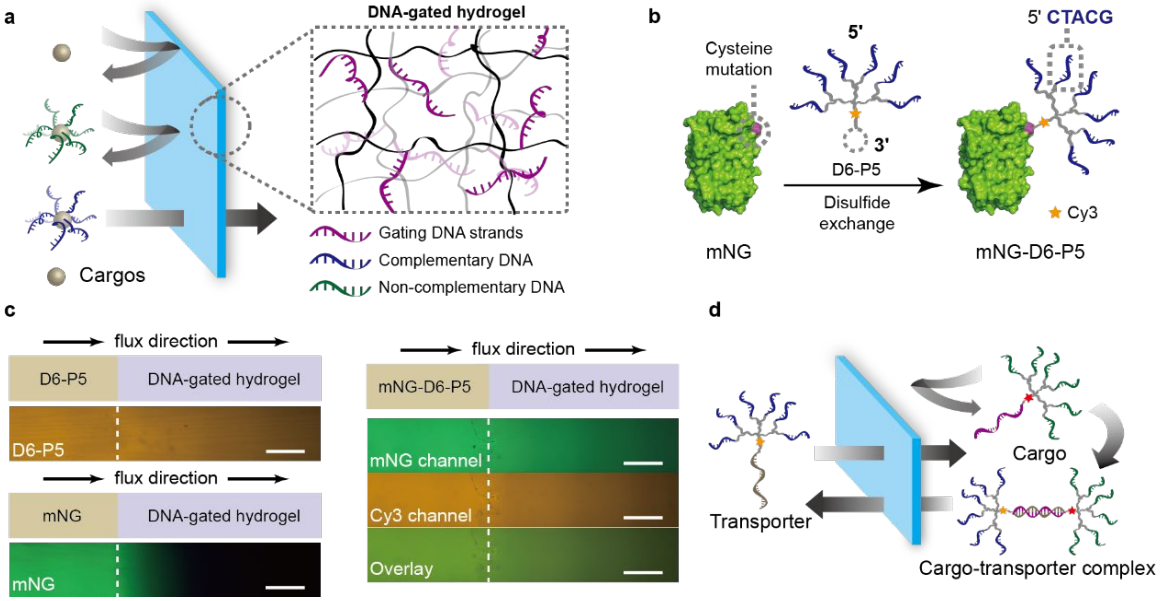


**Figure 3.** (a) Schematic representation of a selective transport process facilitated by transient DNA-DNA interactions. (b) A universal DNA-dendron transport tag was developed to functionalize complex biomacromolecules, such as mNeonGreen (mNG). (c) The DNA-dendron tagging strategy enabled the selective transport of mNG through the DNA-gated hydrogel (Scale bars: 500 μm). (d) Schematic representation of a biomimetic facilitated transport process enabled by the DNA-dendron transport tag.

These observations led to the design of a DNA-dendron transport tag, which can be used to universally modify macromolecular cargo so that the barrier can differentiate the specific species to be transported. We demonstrated that this tagging strategy enables selective transport of complex biomacromolecules (**Figure 3b, c**) and a biomimetic-facilitated transport process (**Figure 3d**) that has not been realized before in a synthetic macromolecular transport system.

Taken together, these results enhance our basic understanding of how cargo-barrier interactions dictate cargo transport and allowed us to present a modular approach that has the potential to meet the demands of various emerging applications involving selective macromolecular transport processes, where the level of complexity has exceeded what can be addressed by existing synthetic systems and thus requires fundamentally new solutions.

## 3. Exploring the Synthetic Conditions for Chemically Complex Alloy and Intermetallic Nanoparticles

Scanning probe block copolymer lithography (SPBCL) has become a vital tool for the synthesis of unique nanoparticles due to its ability to combine several immiscible elements into a single nanoparticle. Heterostructured particles consisting of multiple phases are highly anisotropic and can be selectively functionalized to support unique assemblies. Traditional SPBCL relies on water to transport the metal

precursor-containing ink from the scanning probe tip onto the substrate; however, there are many metals in the periodic table that are incompatible with this system because they react with water to form metal hydroxides, and thus cannot be used to form the desired NPs (**Figure 4A**). Thus, we developed a water-free SPBCL technique that relies on a non-volatile organic solvent, which prevents the formation of metal hydroxides. In this technique, polymer inks composed of poly(2-vinyl-pyridine) (P2VP) and metal precursor ions were coated onto atomic force microscopy (AFM) scanning probes. These inks were deposited onto a silicon nitride membrane in the form of dome-shaped nanoreactors. After a series of heat treatments in a hydrogen atmosphere, the metal precursor ions were reduced resulting in the formation of individual nanoparticles in each nanoreactor. (**Figure 4B**). By using polymers and metal precursors that are compatible with the organic solvent, we were able to synthesize metallic NPs composed of elements including nickel (Ni), Fe, and indium (In) (**Figure 4C–E**). With access to a greater number of elements, this water-free SPBCL platform can be used to increase the complexity of the resulting nanoparticles, and consequently the complexity of 3D-assemblies prepared using them.

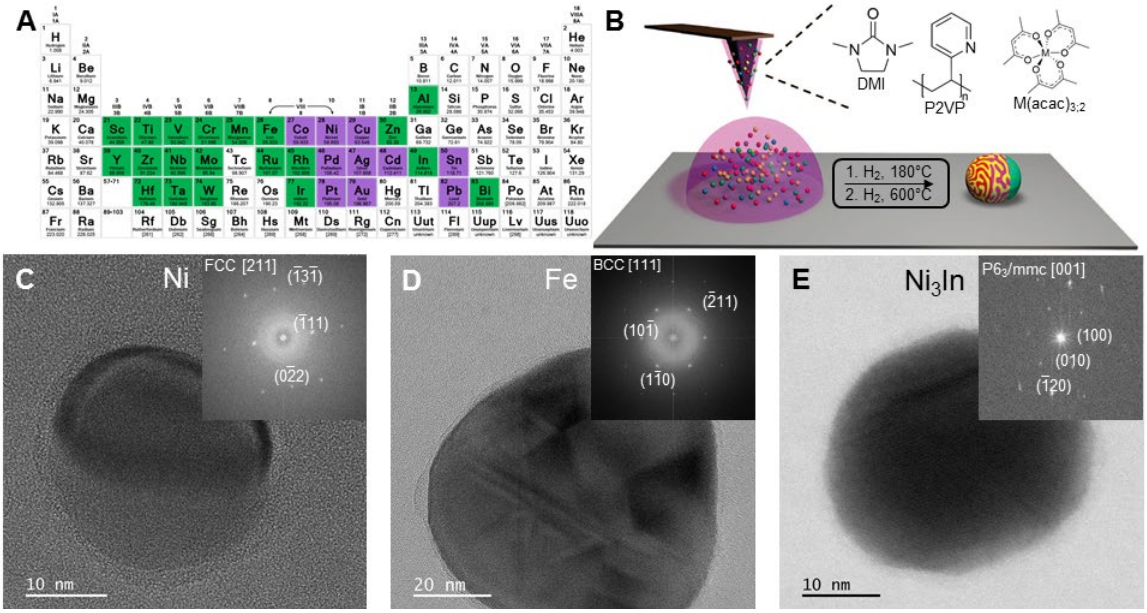


**Figure 4.** (A) Overview of the elements accessible via conventional SPBCL (purple) and target elements for the water-free approach (green). (B) Schematic illustrating the water-free SPBCL approach. (C–E) Electron microscope images of (C) Ni, (D) Fe, and (E) $Ni_3In$ nanoparticles synthesized via non-aqueous SPBCL. Insets: Fast Fourier transforms (FFTs) of the respective images highlighting the crystal structure of the resulting nanoparticles.

**Synthesis and investigation of dynamically reconfigurable superlattices**

Under this objective, we explored both physical and chemical reconfigurability in colloidal crystal superlattices. The use of large, single colloidal crystals capable of being viewed through an optical light microscope allows the monitoring of these crystals as they go through dehydration and rehydration steps in real-time (Section B1). DNA dendrons assembled with templates containing various degrees of valency have shown reconfigurability upon assembly using DNA strands capable of assembling and disassembling the template, as well as surfactant micelles that induce association of dendrimers into larger, supramolecular PAE structures (Section B2).

**1. Deformability in Large Single Colloidal Crystals**

The strength, length, and flexibility of the bonds within a crystal are crucial in determining their thermal, chemical, optical, and mechanically responsive behaviors. However, the allowable restorable deformations in synthetic organic and inorganic crystals still do not compare well with the large deformations possible with highly flexible synthetic polymers and biological organisms. In this work, we

have enabled polymer-like anisotropic but reversible mechanically responsive behavior in large (> 50 μm), single-crystalline colloidal crystals by utilizing long and flexible DNA bonds to connect building blocks. Upon dehydrating and rehydrating well-faceted and large rhombic dodecahedral (RD) crystals composed of either 5- or 10-nm gold nanoparticles, we observed that the crystals crumpled into irregular shapes with wrinkles and creases (generally considered permanent damage in the context of conventional crystals) and recovered their initial morphologies and nanoscale internal orders within a few seconds (**Figure 5a–f**). Through shape parameter analysis studies, we quantified the extent of deformation to the crystals' exteriors and their almost complete recovery (**Figure 5g, h**). To quantify the softness of the crystals composed of the 5- or 10-nm nanoparticles, we measured the reduced moduli of intact crystals (**Figure 5i**) using AFM and found the values to be closer to those of elastomers and polymers than most traditional crystalline materials.

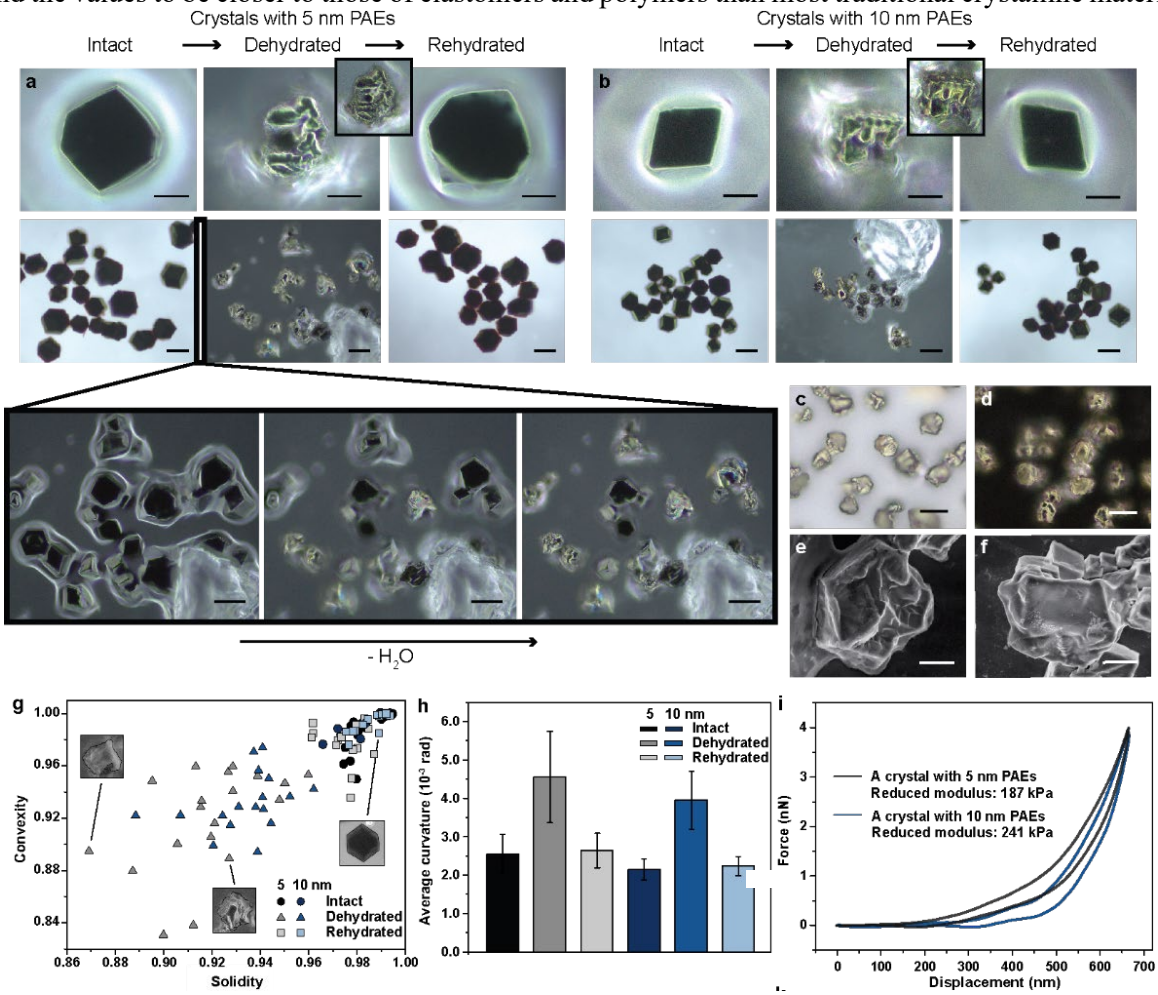


**Figure 5.** Deformation and recovery behavior of crystals during a dehydration-rehydration cycle. (a and b) Dark-field optical microscopy images of crystals assembled from (a) 5- and (b) 10-nm PAEs. From left to right, the three columns indicate intact, dehydrated, and rehydrated crystals. The inset images were collected with twice lower magnification to show clearer projection boundaries of the crystals. Scale bars: 20 and 50 μm for the top and bottom row, respectively. (c) Bright and (d) dark-field optical microscopy images of dehydrated crystals assembled from 5-nm PAEs. Scale bars: 20 μm. (e and f) Electron microscope images of the dehydrated crystals assembled from (e) 5- and (f) 10-nm PAEs. Scale bars: 5 μm. (g) A solidity-convexity diagram. (h) Average curvatures of the crystals. (i) Determination of the hardness and reduced modulus of the intact crystals assembled with 5-and 10-nm PAEs using atomic force microscopy nanoindentation measurements.

These findings have changed the notion of bonding in crystalline materials from being thought of as rigid and static to being thought of as flexible and dynamic. Since single-crystals are the basis for many

optical and electronic device components, the deformation behaviors of the large single crystals described herein, when combined with emerging methods to tailor crystal stability and DNA bond flexibility, may enable a new regime of stimuli-responsive structures important in chemical sensing, optics, and soft robotics.

## 2. Reconfigurable Colloidal Crystals Through Template-Encoded DNA Dendrimers

Biopolymers assemble into hierarchical structures through sequence-defined intra- and intermolecular interactions. Alternatively, many synthetic macromolecules can undergo shape- or topology-controlled packing. These synthetic structures can associate with one another through dynamic, supramolecular interactions to yield nanoscale domains with adaptable sizes and shapes, capable of forming hierarchical materials that have low-symmetry phases. Developing nanoscale building blocks that can form both dynamic associations and sequence-defined interactions could afford novel structure types and provide important insights into how hierarchical architectures arise in both natural and synthetic systems. Programmable atom equivalents (PAEs) have emerged as a powerful, sequence-defined approach to program nanoparticle assembly, with control over phase symmetries, lattice parameters, crystal habits, and thermostabilities. Nevertheless, PAEs are typically synthesized from nanoparticle cores that are structurally static. We hypothesized that by employing DNA-presenting supramolecules that can undergo dynamic structural reorganization, novel nanoparticle arrangements could be templated, and new lattice reconfiguration strategies could be enabled.

By hybridizing DNA-containing templates and DNA dendrons, each with programmable valences and sizes, we formed molecularly defined DNA dendrimers that can assemble with 10-nm AuNP PAEs to form extended, crystalline assemblies. Using this approach, five distinct crystal structures were obtained, one of which has never been reported before in the field of colloidal crystal engineering (**Figure 6a**). DNA dendrons alone (not hybridized to a template) always produced an FCC crystal structure when assembled with PAEs (**Figure 6b**) (commonly observed in systems containing electron equivalents (EEs)). Indeed, we experimentally confirmed that, like EEs, DNA dendrons are diffusive within colloidal crystals. For dendrimers composed of lower valency templates, a simple hexagonal (SH) crystal structure formed, which is commonly observed when one PAE (AuNP core) is significantly larger than the other (dendrimer) (**Figure 6c**). Finally, dendrimers containing high valency templates yielded a simple cubic (SC) crystal structure, which typically arises when both PAEs are approximately the same size (**Figure 6d**). However, according to the complementary contact model (CCM), the size ratio between building blocks dictates the structure of the resultant crystal, but when comparing the size ratios between the AuNP-core PAEs and the DNA dendrimers, we would expect an SH crystal structure to form, not an SC one. To understand this seeming departure from the CCM, we investigated the stoichiometric make-up of the SC crystals. Typically, one would expect to measure a 1:1 ratio of dendrimer to PAE in a SC crystal; however, we observed that this stoichiometric ratio is actually approximately 2:1 dendrimer to PAE (**Figure 6g**). These findings indicate that there is another level of dendrimer association that we had not yet accounted for. Due to the high concentration of hydrophobic moieties at the core of the DNA dendrimers, we hypothesized that hydrophobic interactions, facilitated by the presence of sodium dodecyl sulfate (SDS) in the assembly buffer, led to dendrimer-dendrimer associations, forming larger, higher valency dendrimers that can template crystal structures such as SC.

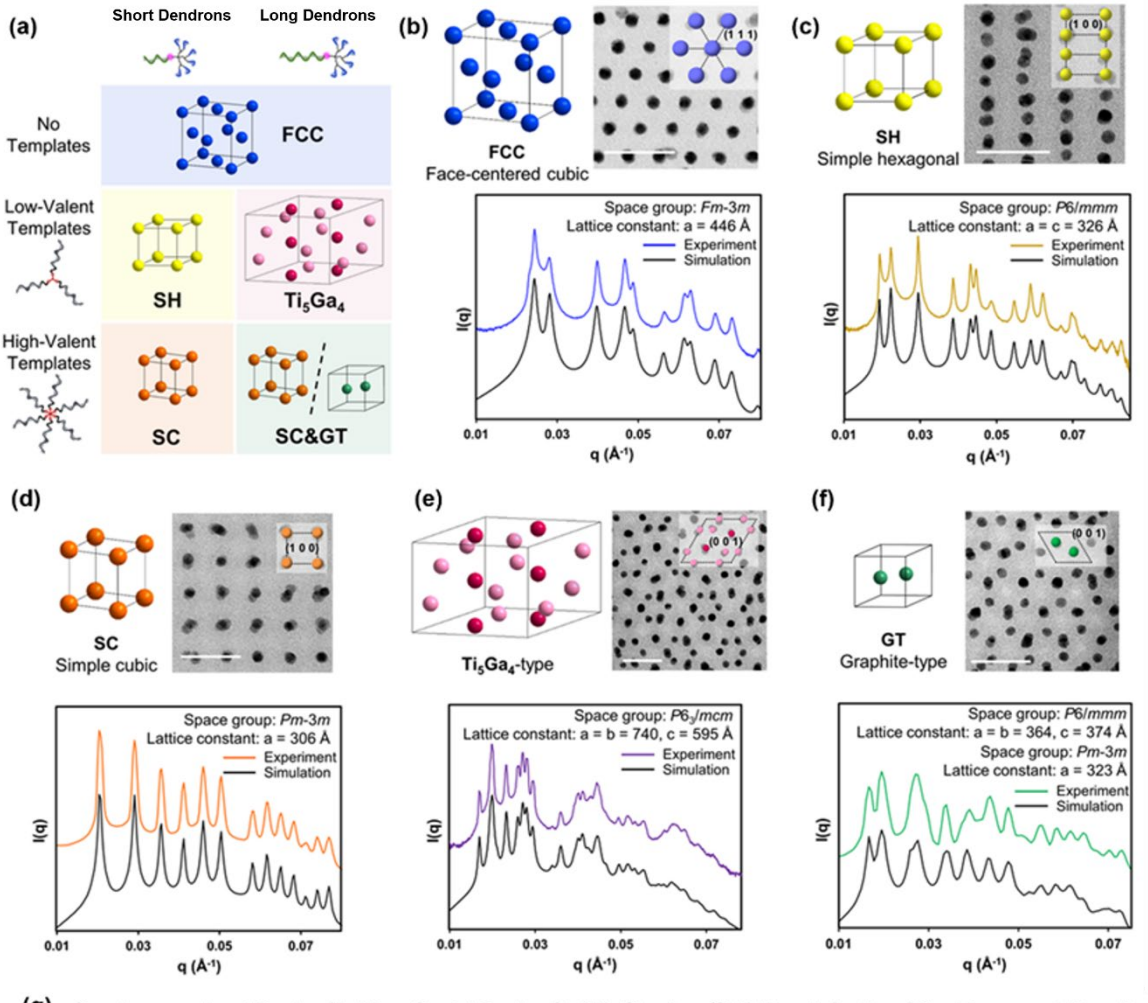


(g)

| Sample | Input Dendron/AuNP | Crystal Dendron/AuNP | Structure (Stoichiometry) | No. of Dendrimers per lattice site |
|---|---|---|---|---|
| T3 + 6Dn | 16 | 12.20 ± 1.09 | SH ($AB_2$) | 2.03 ± 0.18 |
| T6 + 6Dn | 16 | 14.13 ± 2.34 | SC (AB) | 2.35 ± 0.39 |
| T8 + 6Dn | 16 | 14.64 ± 0.99 | SC (AB) | 1.83 ± 0.12 |

**Figure 6.** (a) A depiction of the phase space: crystal structures depend on the presence and the identity of the DNA-containing templates, as well as the stem length of the DNA dendrons (e.g., compared to 6Dn, 6Dn-L1 has an additional eight-base, non-hybridized region between the core and the branching region, while 6Dn-L2 and 6Dn-L3 have additional 12-base non-hybridized regions). (b–f) All structures were screened and characterized in the solution-state via small angle x-ray scattering (SAXS). Colored traces are experimental data, and black traces are simulated spectra. Representative samples were imaged via scanning transmission electron microscopy (STEM) after stabilization in the solid state. (b) Face-centered cubic (FCC). (c) Simple hexagonal (SH). (d) Simple cubic (SC). (e) $Ti_5Ga_4$-type. (f) A mixture of graphite-type (GT) and SC. Scale bars: 50 nm. (g) A table showing the composition of colloidal crystals, quantified by the ratio of dendron per gold nanoparticles. Each entry represents the average and standard deviation of three replicates. The number of dendrimers per lattice site is calculated by dividing the dendron to AuNP ratio by the template valency.

Under typical assembly conditions, SDS should form micelles, leading to the following hypothesized pathway for dendrimer-dendrimer association (**Figure 7a**). Just above the CMC of SDS (~0.01% at 0.5 M NaCl), a small number of micelles form, and the hydrophobic moieties that define the dendritic core can insert into these micelles, mediating the association of two or more DNA dendrimers. Far above the CMC of SDS, the dendrimers are divided among many micelles, disfavoring dendrimer-dendrimer association. To test this hypothesis, we combined DNA dendrimers (6Dn and T6) with 10-nm AuNP-core PAEs and

added an increasing amount of SDS (0, 0.005, 0.01, 0.02, and 0.04%). *In situ* SAXS revealed that, at 0 and 0.005 % SDS (**Figure 7b**), SH phases were formed, because there were not dendrimer-dendrimer associations in the absence of micelles. At 0.01 % SDS, the SC phase formed exclusively, suggesting that micelle-dendrimers assemble near the CMC of SDS. At higher SDS concentrations, the SH phase reappears, consistent with our hypothesis that dendrimer-dendrimer association is disfavored when there are more micelles. We also demonstrated that DNA dendrons can be designed to place the bulky branches further from the dendrimer core, allowing more dendrimers to be inserted into a micelle without prohibitive repulsion. This setup enables the formation of the $Ti_5Ga_4$-type phase, which has not yet been reported in colloidal crystal engineering. Together, these experiments show that assembly can be guided along different pathways by controlling the degree of dendrimer-dendrimer association *via* 1) surfactant concentration and 2) DNA structure design.

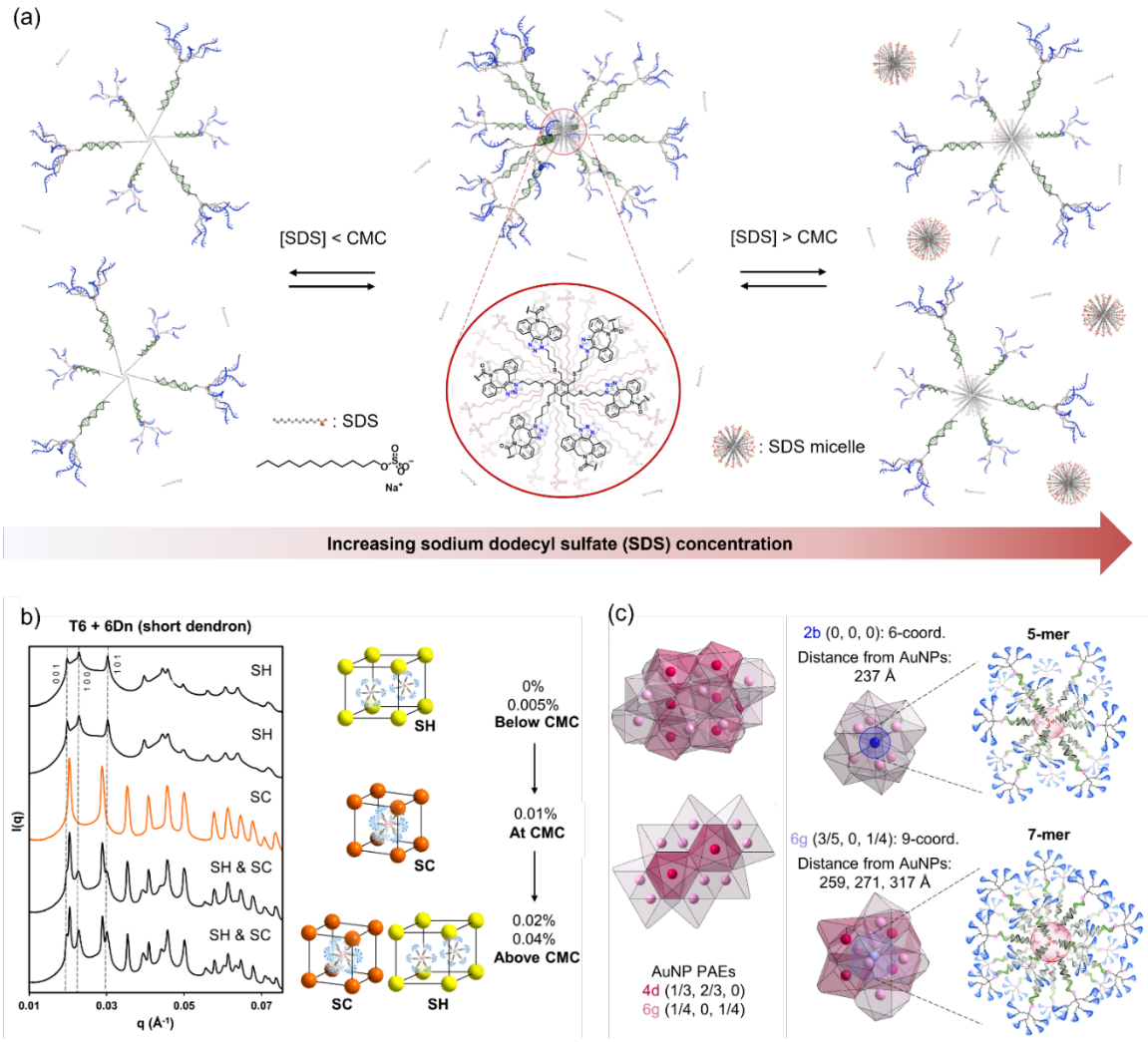


**Figure 7.** (a) Proposed pathway for dendrimer-dendrimer association. Surfactant sodium dodecyl sulfate (SDS) forms micelles at concentrations equal to or higher than the critical micelle concentration (CMC). These micelles encapsulate the hydrophobic cores of the templates, leading to dendrimer-dendrimer association at and slightly above the CMC. (b) SAXS data collected at 0, 0.005, 0.01, 0.02, and 0.04 % SDS. Observed crystal structures are represented by unit cells that depict DNA dendrimer and micelle-dendrimer locations. (c) Voronoi polyhedra decomposition of AuNP sublattice identifies and locates two types of DNA micelle-dendrimers in the unit cell, at Wyckoff positions 2b and 6g, respectively.

To understand the emergence of the $Ti_5Ga_4$-type phase, we constructed Voronoi polyhedra around the AuNP locations (**Figure 7c**). The polyhedra vertices meet at Wyckoff positions 2b (0, 0, 0) and 6g (3/5, 0, 1/4); these locations have the highest equidistant connectivity to the AuNPs and pinpoint the most energetically favorable sites for the micelle-dendrimers. Micelle-dendrimers at Wyckoff position 2b are coordinated by six AuNPs at shorter distances, while those at Wyckoff position 6g are coordinated by nine AuNPs at longer distances (**Figure 7c**). The significant difference in coordination environments can only be explained by the presence of micelle-dendrimers with distinct sizes, specifically a 5-mer in 2b and a 7-mer in 6g. Overall, the emergence of the $Ti_5Ga_4$-type phase is predicated on supramolecules undergoing further association into micellar architectures with non-degenerate sizes. This type of symmetry-breaking mechanism has been observed in soft matter but is new to systems involving inorganic nanoparticles.

In summary, this work illustrates how sequence-defined recognition and dynamic association can be combined to yield complex hierarchical materials. Reorganizable supramolecular templates offer new routes for accessing novel structure types in nanoparticle assembly, setting the stage for the design of metamaterials with unconventional crystal structures.

**Synthesis and investigation of structurally sophisticated and functional superlattices**

Under this objective, we enhanced our ability to synthesize and characterize unique and sophisticated colloidal crystals. We showed that the assembly of DNA-functionalized decahedral nanoparticles, with their 5-fold symmetry, forms densely packed dodecagonal quasicrystalline superlattices (Section C1). Molecularly defined electron equivalent (EE) cores containing discrete numbers of DNA strands allowed the study of the relationship between valency and structural outcome when they were assembled with PAEs (Section C2). Precise matching of PAE size through the careful engineering of DNA has enabled the synthesis of randomly substituted crystal alloys, enabling colloidal crystals with any ratio of nanoparticle cores, regardless of crystal symmetry, for the first time (Section C3). Furthermore, we continue to pioneer new techniques that provide unrivalled capabilities for imaging both hard, inorganic (Section C4) and soft, organic (Section C5) materials.

**1. Colloidal Quasicrystals Engineered with DNA**

Since their first experimental identification in 1984, quasicrystals have garnered intense interest due to their exotic structure and lack of long-range translational order. Experimental efforts in pursuit of such materials span from atomic quasicrystals to colloidal quasicrystalline superlattices in recent years. Whether it is possible to synthetically achieve colloidal quasicrystals using a single and uniformly functionalized constituent building block remains undetermined. Polyhedral NCs, with their unique geometries, were theoretically predicted to form densely packed quasicrystalline structures, a new category of quasicrystals. A variety of polyhedral NC shapes can be synthesized in high quality, providing an opportunity for the experimental realization of exotic, densely packed superlattices. Among the synthetically available polyhedral NCs, the decahedron (Johnson solid *J13*) is of particular interest due to its 5-fold symmetry, which is one type of forbidden symmetry in the context of periodic tiling, and, therefore, less likely to form periodic structures. We hypothesized that the 5-fold symmetry of the decahedron would result in multiple local packing environments that slightly deviate from a 5-fold symmetric cluster, leading to the formation of unusual, aperiodic structures. Indeed, computational investigation into the packing phase of decahedra revealed that a dodecagonal quasicrystal (DDQC) can arise as a *metastable* phase in a hard particle simulation when considering entropy only, in addition to the previously reported stable rhombohedral phase.

To experimentally evaluate our hypothesis, highly monodisperse decahedral gold NCs (edge length = 80 nm) were functionalized with short, double stranded DNA (dsDNA) with self-complementary sticky ends (33 bases, ~11.2 nm, **Figure 8A–C**). Since decahedra cannot fill space, flexible surface ligands are needed to stabilize the gaps. To address this need, and therefore enable the growth of extended, defect-free colloidal crystals, a short oligoethylene glycol (OEG) region (i.e., 6 units) was added to the dsDNA design (**Figure 8D**). The decahedral building blocks were then slowly cooled down, starting at a temperature that

ensured a stable colloidal suspension of NCs (i.e., higher than the melting temperature of the NC aggregates). After slow cooling, the resulting aggregates were collected for small-angle X-ray scattering (SAXS) analysis, and then transferred to the solid state through a silica-embedding procedure for scanning electron microscopy (SEM) and scanning transmission electron microscopy (STEM) characterization. Remarkably, a dense and highly ordered structure was found to be the primary assembly product (**Figure 8E**).

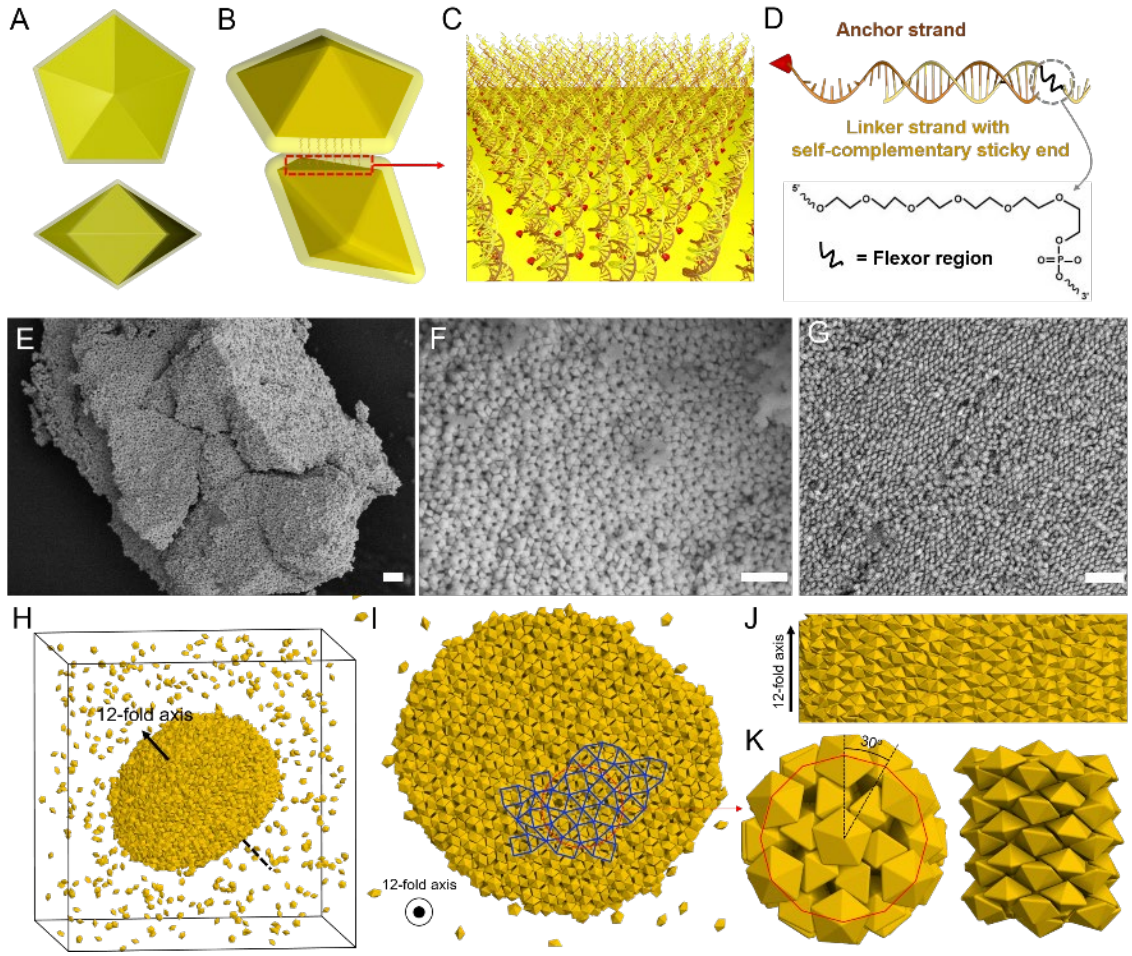


**Figure 8.** Schematic illustrations of experimental and simulated dodecagonal quasicrystals (DDQCs) from DNA-functionalized decahedral NCs (edge length = 82 nm). (a) Front and side view of decahedral NCs. (B, C, D) Schematic illustrations of decahedral NCs functionalized with short, flexible DNA strands. (E, F, G) SEM images of DDQCs assembled from DNA-functionalized decahedral NCs. Scale bars: 500 nm. (F, G) Zoomed in images along and perpendicular to the 12-fold axis, respectively. (H, I, J, K) MD simulation results of DDQCs assembled from decahedral particles with DEM. Zoomed-in images along the 12-fold axis (I, K), and perpendicular to the 12-fold axis (J, K).

Analysis of both the surface and cross-section (SEM, **Figure 8F**) of silica-embedded superlattices revealed a singular 12-fold axis in each crystal domain. When viewed along the main axis, the structures show a high degree of rotational order (**Figure 8F**); perpendicular to this axis, the structures appear in a 1D quasi-periodic fashion (**Figure 8G**). These data underscore the conclusion that these crystals possess a high degree of internal and external order post-assembly. The DNA-mediated assembly of decahedra into an ordered structure was further confirmed by molecular dynamics (MD) simulations using the discrete element method (DEM), in which DNA hybridization is modeled by an effective pair potential between patches on the surface of decahedra. The system initialized as a random fluid that was subsequently cooled

down to a temperature slightly lower than the melting temperature ($T^*/T_m^*$~0.9) to induce spontaneous ordering. The particles initially formed an aggregate and later underwent a phase transition into an ordered phase. Crystallization occurred for a range of potential parameters, indicating the robustness of the assembly. To obtain a large single domain of the crystal, we conducted a seed-assisted growth simulation and stabilized it (**Figure 8H**). Cross-sections of the crystal cluster viewed along (**Figure 8I**) and perpendicular to the 12-fold axis (**Figure 8J**) show local order that agrees well with the experimental observations. The crystal structure can be mapped as square-triangle tiles, a well-known DDQC model, by connecting nearest decahedra whose polar tips are oriented along the 12-fold symmetry axis (**Figure 8I**). To obtain a clear view of the 12-fold order, we extracted a columnar structure with 12-fold symmetry (Figure **8K**) where a hexagonal inner structure is surrounded by a dodecagon of 12 decahedra.

## 2. Valency Control through Molecular Electron Equivalents

Recent studies have shown that a novel phenomenon, colloidal crystal metallicity, emerges when there is a large size disparity (e.g., 1.4 nm vs. 10 nm) between NPs functionalized with complementary DNA. Here, the smaller NPs behave as electron equivalents (EEs) and can roam through and stabilize the sublattice defined by the larger PAEs. However, studying how DNA architecture (e.g., EE valency) affects the properties of colloidal crystals has been challenging because there is inherent polydispersity in the number of DNA strands on these NPs.

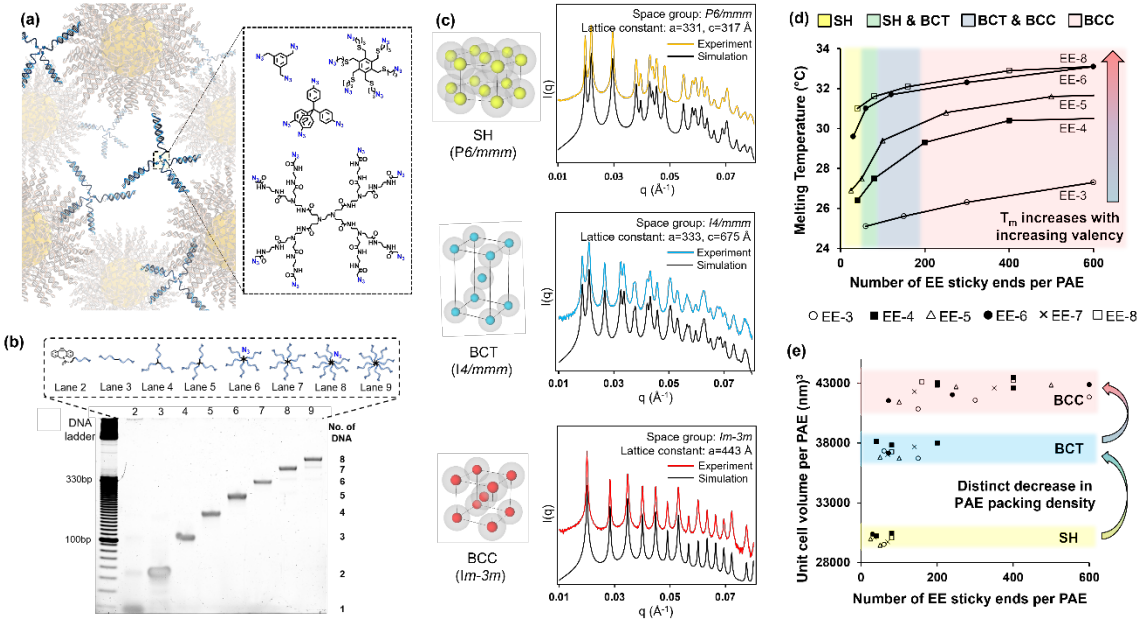


**Figure 9.** (a) Molecular EEs, with a precise number of DNA strands, can engage in transient base-pairing interactions with AuNP-based PAEs. (b) Denaturing polyacrylamide gel electrophoresis (5 %) of molecule-DNA conjugates. Lane 2: DBCO (dibenzocyclooctyne)-functionalized DNA. Lanes 3−9: molecule-DNA conjugates with 2 to 8 DNA strands, respectively. (c) SAXS characterization of the three "metallic" phases observed in molecular EE-PAE superlattices. (d) EE-PAE assembly phase diagram overlaid on a plot of melting temperature ($T_m$) versus the number of EE sticky ends per PAE. (e) A plot of the unit cell volume per PAE versus the number of EE sticky ends per PAE.

To tackle this challenge, we developed a strategy for synthesizing colloidal crystals where the EEs are templated by well-defined molecular entities (**Figure 9a**), instead of NPs, and functionalized with a precise number of DNA strands, which define their valency (**Figure 9b**). When molecular EEs were assembled with complementary AuNP-based PAEs, small angle X-ray scattering (SAXS) and scanning transmission electron microscopy (STEM) revealed the formation of three distinct "metallic" phases (**Figure 9c**)—simple hexagonal (SH), body-centered tetragonal (BCT), and body-centered cubic (BCC). Through

systematic studies, we discovered that the thermal stability of these colloidal crystals, as reflected by their melting temperatures ($T_m$), is influenced by both EE valency and the number of EE DNA bonds (**Figure 9d**). On the other hand, their phase symmetry is dictated by packing and is only controlled by the total number of EE DNA bonds (**Figure 9e**). We also showed that the polydispersity in EE-type building blocks does not affect the crystallinity and phase symmetry of the resulting superlattices, a non-trivial finding made possible via the use of well-defined, multivalent DNA architectures.

Taken together, this work introduced the notion that, unlike conventional electrons, EEs that are molecular in nature can possess a defined valency that can be harnessed to template the formation of colloidal crystals made up of DNA-functionalized nanoparticles, with specific "metallic" phases and thermal properties. This work opens the avenue for using molecularly defined, multivalent macromolecules as a tailorable building block in the broader field of colloidal crystal engineering.

### 3. Programming "Atomic Substitution" in Colloidal Crystals

Multicomponent or "alloy" colloidal crystals containing different classes of nanoparticles are desirable to realize new and tunable properties not found in single-component colloidal crystals. Although examples of colloidal crystal analogues to metal alloys were reported in Year 3, general synthetic routes for preparing 3D analogues to random substitutional alloys have not yet been established. Here, we use DNA length and sequence to precisely match the sizes of nanoparticle core components, define a parent lattice symmetry and substitutional order, and achieve faceted, three-dimensional crystal habits in substitutional alloy colloidal crystals.

We hypothesized that the ability to independently tune the PAE core composition and DNA shell could be used to encode both ordered and random substitutional arrangements. Au and $Fe_3O_4$ nanoparticles were used as the two PAE core components with a complementary DNA design known to form a BCC lattice and rhombic dodecahedron crystal habit. Total PAE sizes were matched by tuning DNA length, and DNA loading density was similar for both cores. Ordered substitutional alloy crystals were assembled by combining an equal ratio of Au PAEs with A-type DNA and $Fe_3O_4$ PAEs with B-type DNA (**Figure 10**). Random alloy crystals were assembled by combining equal amounts of both A and B-type Au and $Fe_3O_4$ PAEs. Alloy colloidal crystals were characterized across multiple length scales to confirm the lattice symmetry, component ratio, and local order.

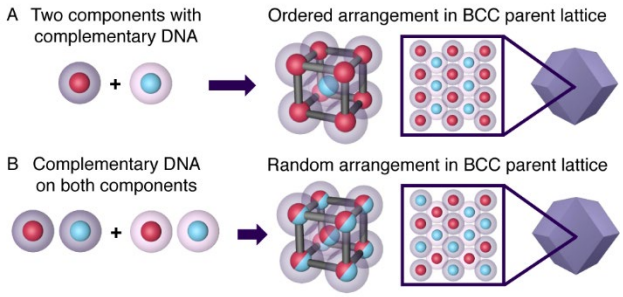


**Figure 10.** Substitutional alloy colloidal crystal design. (A) An ordered arrangement of two components with complementary DNA into a CsCl lattice and (B) a random alloy colloidal crystal, both with the same BCC parent lattice and rhombic dodecahedron habit.

The expected CsCl lattice symmetry was observed via SAXS for ordered substitutional alloy crystals, while the experimental SAXS pattern of the random alloy crystals is in strong agreement with a simulated SAXS pattern for a BCC structure with a 50 % site occupancy ratio of each core in both the A and B lattice sites (**Figure 11**). Both ordered and random alloy crystals retained the same faceted rhombic dodecahedron crystal habit as the BCC parent lattice (**Figure 11a–d**). Random alloy crystals with different input ratios of Au:$Fe_3O_4$ PAEs showed that the input ratio can be used to control the average particle ratio in crystal products as measured via energy dispersive x-ray spectroscopy (EDS) (**Figure 11e**). EDS mapping of thin crystal sections further confirms the expected ordered arrangement in a CsCl crystal cut along the (100) direction (**Figure 11f**). In contrast, a random alloy crystal cut along the (111) direction (**Figure 11g**) did not show signs of ordering or clustering. Finally, to demonstrate the importance of core composition, we assembled crystals with the same component ratio and parent lattice (but different types of DNA chemistry-enabled substitution) in a magnetic field and found that substitution impacts the final morphology of crystals

that contain magnetic nanoparticles. Specifically, these studies show that ordered substitution leads to rod-like crystals while random substitution leads to core-shell structures.

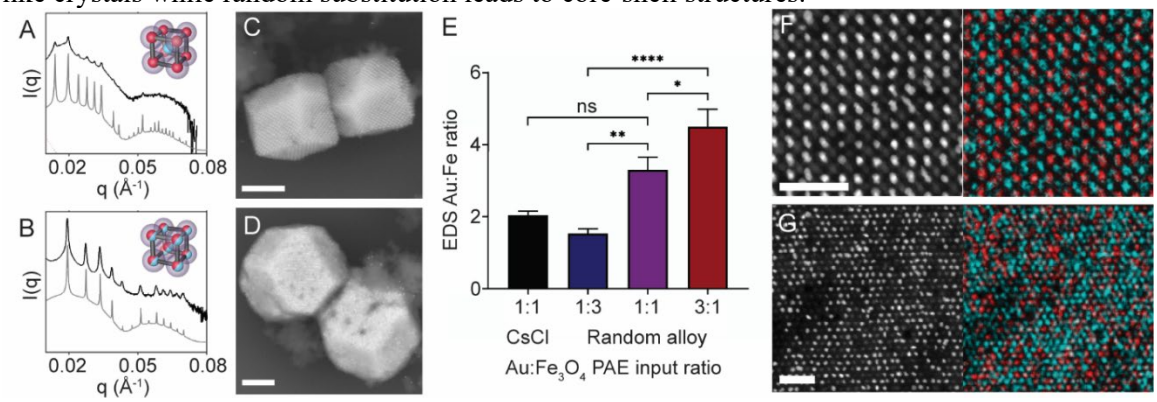


**Figure 11.** Characterization of substitutional alloy colloidal crystals. SAXS characterization (black) compared to simulated patterns (gray) for (A) ordered substitutional alloy crystals with CsCl symmetry and (B) random alloy crystals. SEM characterization showing defined crystal habits for (C) ordered substitutional alloy crystals and (D) random alloy crystals. Scale bars: 500 nm. (E) Plot showing the average Au:Fe ratio calculated from EDS spectra of individual crystals with different input Au:$Fe_3O_4$ PAE ratios. Error bars reflect standard error of the mean, significance between random alloy conditions is indicated (* $p < 0.05$, ** $p < 0.01$, **** $p < 0.0001$, ns = not significant). STEM image of crystal sections and EDS maps for (F) a CsCl crystal section showing the (100) plane and (G) a random alloy crystal section showing the (111) plane. Scale bars: 250 nm.

Taken together, these results constitute a general synthetic strategy for programming substitutional order within colloidal crystals. The ability to program substitutional order independently from lattice symmetry and crystal habit enables the design of colloidal crystals with structures, functions, and properties that can be tuned by the deliberate substitution of components.

## 4. Tomography of Iron Oxide Superlattices

Scanning transmission electron microscopy (STEM) with high angle annular dark field (HAADF) detection is a useful imaging technique for metal nanoparticle superlattices because the contrast is dominated by high-atomic number elements. In combination with other techniques, STEM can help analyze the crystallinity and nature of aligned nanoparticle domains. This is particularly true when evaluated in more than one two-dimensional projection. Electron tilt tomography is a three-dimensional imaging technique that uses a series of images across a range of tilt angles to evaluate a 3D structure based on 2D projections. Sixty images were acquired using high angle annular dark field (HAADF) scanning transmission electron microscopy (STEM) at intervals of 2°, and these were then aligned and reconstructed into a continuous series. In addition to providing three-dimensional morphology, this tilt series can be used to analyze individual snapshots more thoroughly at interesting tilt angles. **Figure 12** shows two images pulled from the series at a 32° tilt and –36° tilt. While this synthesis condition yielded a low degree of crystallinity, patterns or potential short-range order can be observed at certain orientations. When other assemblies with higher degrees of crystallinity are identified, electron tilt tomography will be used to analyze the extent of the aligned domains, the nature of defects, and the orientations of domains relative to one another.

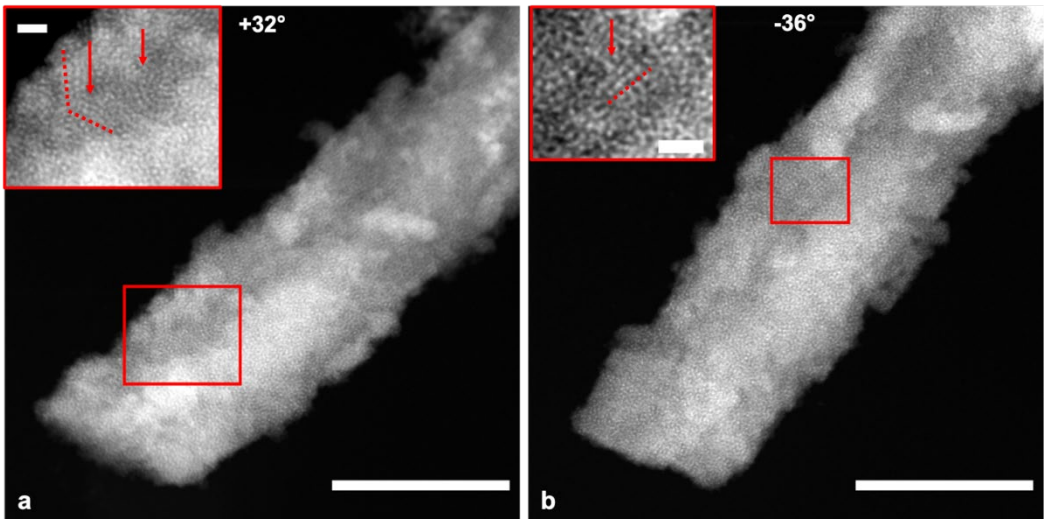


**Figure 12.** High angle annular dark field (HAADF) scanning transmission electron microscopy (STEM) of iron oxide superlattices at a) a 32° tilt angle and b) a -36° tilt angle. Brighter amorphous regions are silica used for embedment. Insets show interesting patterns observed at these tilt angles. Scale bars: 1 μm and 100 nm (inset).

## 5. Imaging of Soft and Hybrid Structures using STEM-in-SEM

The low inherent contrast of soft systems necessitates contrast enhancement by either sample preparation or imaging methodologies not often employed during hard material imaging. For small biological molecules, such as proteins or DNA, this improved contrast is commonly achieved either through negative heavy metal staining or cryo-electron microscopy with class averaging.

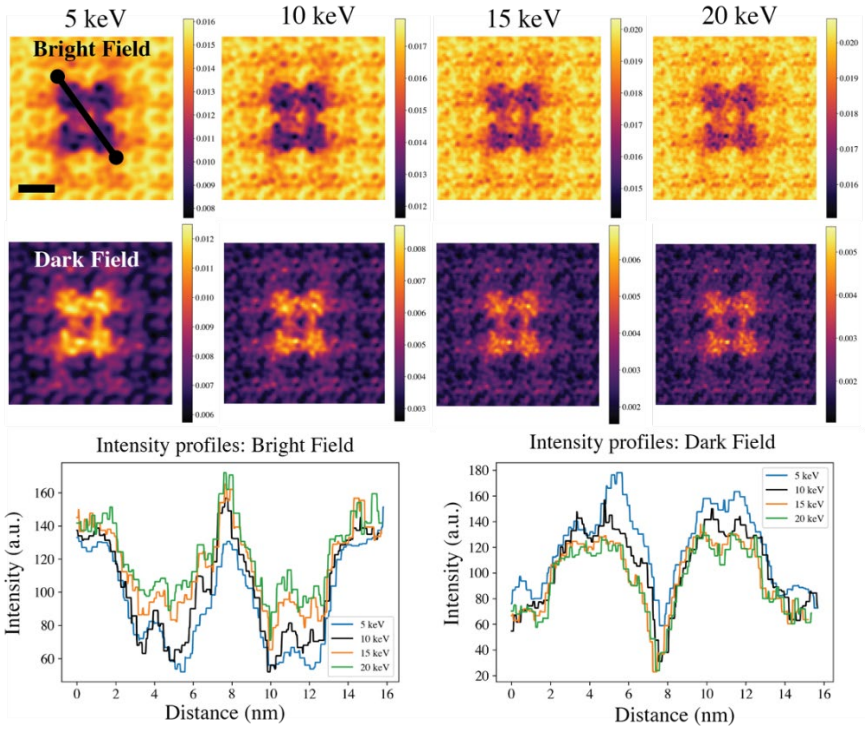


**Figure 13. (**Top) Bright field and (middle) high angle annular dark field multi-slice STEM simulations of tetracutinase on amorphous carbon from 5-20 keV. Color bar represents intensity normalized by total electron dose. Scale bar: 5 nm. (Bottom) intensity profiles comparing contrast along tetracutinase diagonal for all four beam voltages.

We have used a number of these methods to enhance contrast, but we also aim to extract the contrast inherent in soft systems by manipulating microscope conditions. Low-voltage electron microscopy enables contrast enhancement by increasing the electron scattering cross-section, with the trade-off of slight resolution degradation due to increased chromatic aberration. This allows for the imaging of soft or hybrid materials with improved contrast (**Figures 13 and 14**). We have developed this technique using precisely defined protein constructs, which are synthesized from fusion protein building blocks into macromolecular assemblies. One such protein assembly, tetracutinase, is formed from four cutinase proteins joined by a four-armed linker (schematic in **Figure 14a** (inset)). Three-dimensional reconstruction methods are then possible to observe the spatial arrangement of individual proteins within the larger construct.

Commercial transmission electron microscopes (TEMs) typically operate at 100–300 kV, or as low as 40 kV in certain instruments. To achieve lower beam energies under 30 keV, we use a scanning electron microscope (SEM) with a STEM detector under the sample stage. This allows for transmission detection, but in an SEM instrument. Using STEM image simulations of tetracutinase on an amorphous carbon film for bright field (BF) and high angle annular dark field (HAADF) detection (**Figure 13**), the contrast is theoretically improved at 5 kV compared to 20 kV. These simulations are normalized by total electron dose.

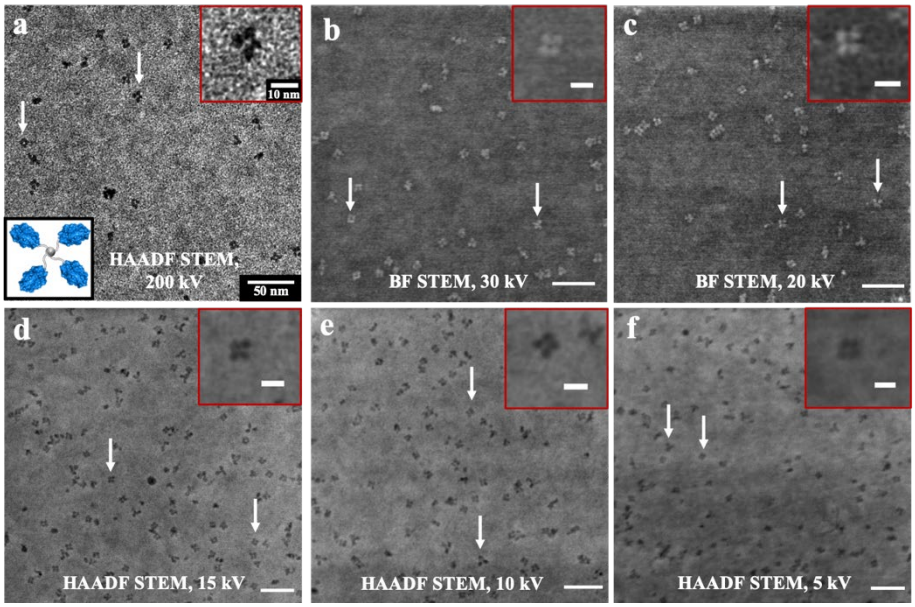


**Figure 14.** Images of UF-stained tetracutinase (schematic in inset) using a) HAADF STEM at 200 kV, b, c) BF STEM at 30 and 20 kV and d–f) HAADF STEM from 15-kV. Insets show representative examples of four-lobed structure.

Protein assemblies were negatively stained with uranyl formate (UF) and imaged using STEM-in-SEM (**Figure 14**). A comparison with conventional HAADF STEM at 200 kV is shown in **Figure 14a**, **Figure 14b, c** show bright field STEM images at 30 and 20 kV, and **Figures 14d-f** show HAADF STEM images from 5–15 kV in a different instrument. The four protein lobes of tetracutinase are resolvable at all voltages, but the effect of chromatic aberration and practical limitations resulting from low signal are apparent at 5 kV. Though these images show stained structures, our eventual goal is to image unstained structures using the contrast enhancement from lower voltage. Protein assemblies are used as a model system, but this method can easily be adapted to more complex structures. It is particularly useful for hybrid systems, such as those consisting of many different types of PAEs because it can improve contrast in the soft component while maintaining high contrast for the hard component. The different STEM modes and capabilities in SEMs, including backscattered electron imaging and spectroscopy, can also aid in the multimodal analysis of soft and hybrid structures. In addition to the improved contrast and the availability of additional detection modes, STEM imaging in SEM is very high-throughput and allows for the rapid screening of many structures.

**Assembly of Reconfigurable, Sophisticated, and Functional Superlattices on Surfaces**

Under this objective, we continued to explore how surface-bound assembly can generate sophisticated structures that are inaccessible in solution and functional structures with relevance for device applications. Building on work achieved in Year 3, we elucidated how the interaction of anisotropic nanoparticles with a surface can lead to low-density 2D superlattices with a high proportion of exposed surface area (Section D1). Furthermore, we explored the properties of 2D colloidal metasurfaces and discovered that tuning the gap distance within densely packed 2D superlattices enables the toggling of optical properties, including refractive index and effective permittivity (Section D2).

## 1. Low Density 2D Superlattices Assembled via Directional Bonding of Anisotropic NPs

The ability to assemble nanoparticle (NP) superlattices with predictable symmetry and spacing is important for controlling their unique optical, electrical, and magnetic properties. Programmable atom equivalents (PAEs) have been shown to enable the fabrication of a wide variety of different superlattice symmetries. This is due to the specific base-pair interactions with DNA, which results in reliable and tunable nanoparticle interactions. In addition to colloidal crystals formed free in solution, PAEs can also be assembled as a thin-film, using a flat substrate as a template, which allows for better characterization of optical and mechanical properties and makes it more practical for further integration into devices. Previously, only spherical PAEs have been investigated in this context, showing the ability to direct the crystal orientation of the thin-film by using different proportions of DNA on the substrate surface. This type of thin-film assemblies has not been studied for anisotropic nanoparticles.

Here, we investigated the thin-film PAE assembles of three anisotropic NPs (**Figure 15**): cubes, octahedra, and rhombic dodecahedra (RD). Like spherical PAEs, these anisotropic PAEs were functionalized with a binary DNA system, where DNA A and B contain complementary sticky ends. This allows for the thin-film to be assembled in a layer-by-layer fashion. We assembled a two-layer amorphous film by first functionalizing a Au-coated Si wafer with A-type DNA, then incubating the substrate in a solution of B-type PAEs, followed by a solution of A-type PAEs. Next, the film was annealed by heating the substrates to just a temperature below the melting temperature of the PAE assemblies. This allows for the rearrangement of PAEs on the substrate without causing them to completely detach from the surface.

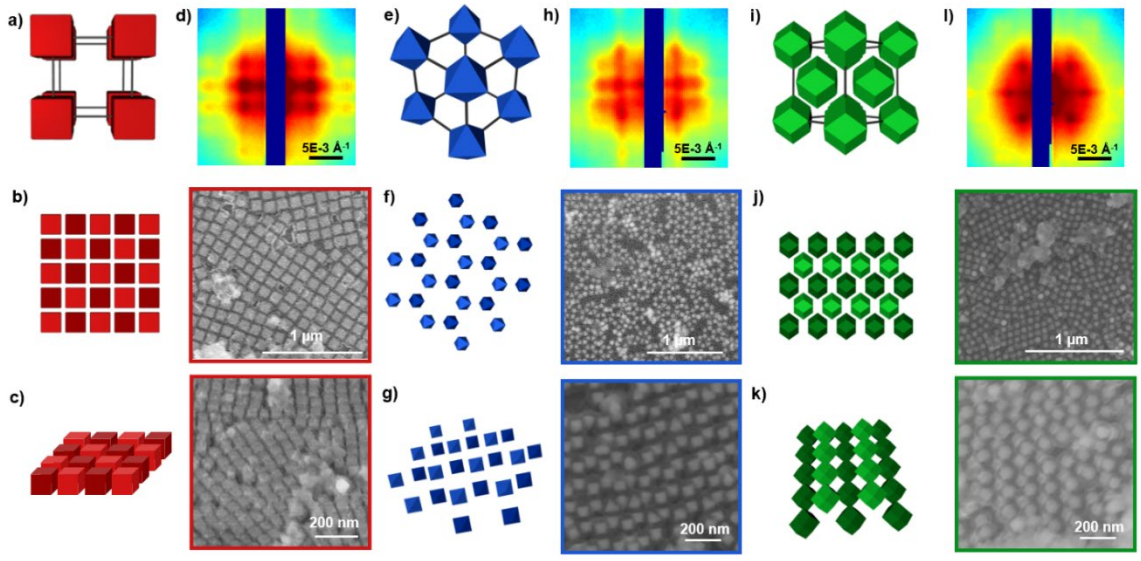


**Figure 15.** NP films. a,e,i) Schematics of the unit cells of cubic, octahedral, and RD PAE SLs rotated to match the orientation of the resulting 2D films. b,f,j) Schematics and corresponding SEM images of the resulting 2D films. Square, honeycomb, and rhombic symmetries were observed in films consisting of cubic, octahedral, and RD PAEs, respectively. c,g,k) Schematics and corresponding SEM images taken at a 30º tilt angle showing the height difference

between A and B-type PAEs in each structure. d,h,l) GISAXS scattering patterns from the samples in b, f, and j, respectively.

Cube PAEs formed into a simple square packing consistent with the {100} planes of a simple cubic (SC) lattice. Octahedra PAEs formed into a buckled honeycomb structure consistent with the {111} planes of a body-centered-cubic (BCC) lattice. RD PAEs formed into a rhombic lattice consistent with the {110} planes of a face-centered-cubic (FCC) lattice. One trend that is consistent across all three types of PAEs is that the individual particles are all oriented such that one flat facet is in full contact with the substrate. This is because the DNA interaction between the full facet of a nanoparticle and a flat surface is highly favorable. When these NP-substrate interactions are combined with NP-NP interactions, the results are unique thin-film structures that are difficult to controllably obtain in other systems. Specifically, the octahedra and RD assemblies resulted in structures that are non-close-packed compared to their in-solution counterparts. To lower their surface energy, colloidal crystals tend to minimize the amount of exposed unbound DNA to the surface. These surfaces are also usually the most close-packed planes of their respective crystal symmetries. However, for the octahedra and RD systems, the added interaction with the substrate forces them to expose more open facets. The graphene-like structure resulting from octahedra is the first that has been prepared with nanoparticles in the ~100 nm size range.

These assemblies allow for a better understanding of the interactions between substrates and nanoparticles. In contrast to spherical PAEs, anisotropic PAEs form directional bonds that maximize both the NP-NP and NP-substrate interactions. These results show that the choice of particle shape has a major influence on how they assemble on substrates, and the careful selection of particle shape and DNA design can provide an added level of control over the formation of structures with desirable properties.

## 2. Colloidal Metasurfaces with Broadly Tunable Optical Properties

We previously showed that colloidal Au nanocubes assembled into a 2D metasurface exhibits unnaturally dielectric-like high effective refractive index. The enhanced gap mode between neighboring Au NP due to the small gap distance gives rise to increased capacitive coupling, which results in an increased effective permittivity. We further observed that when the 2D Au superlattice is placed atop of thin Au layer, the effective permittivity is altered significantly. The metasurface behaves similarly to a dielectric below its resonance wavelength in the near infrared, while it behaves like a metal at longer wavelengths. We calculated the effective optical parameters using the S-parameters retrieval method (**Figure 16**). These calculations reveal that, at lower wavelengths, the real part of the refractive index ($n_{\text{eff}}$, **Figure 16a**) stays relatively high then rapidly decreases closer to zero. At the same time, the imaginary part of the refractive index ($k_{\text{eff}}$, **Figure 16b**) rapidly increases from zero to a very high number at longer wavelengths, showing metal-like behavior.

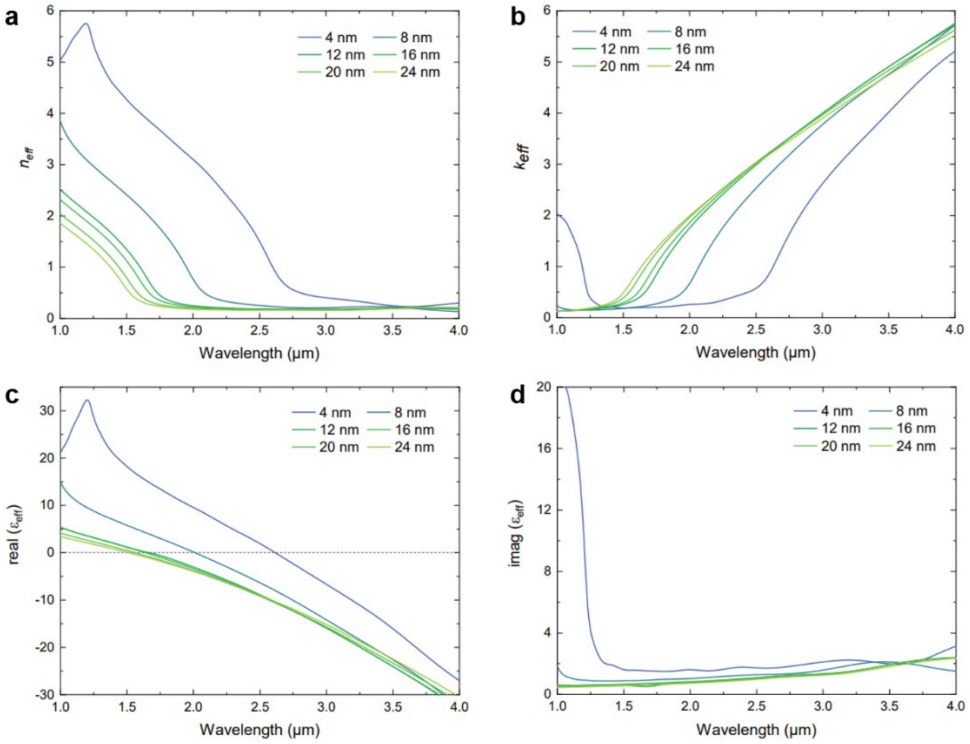


**Figure 16.** Calculated effective parameters of nanocube metasurfaces with DNA length varying from 4 to 24 nm, above a gold film 8 nm thick. (a) $n_{eff}$. (b) $k_{eff}$. (c) real($\varepsilon_{eff}$). (d) imag($\varepsilon_{eff}$).

The effective permittivity was also calculated and found to depend substantially on gap distance. The real part of the permittivity (real($\varepsilon_{eff}$), **Figure 16c**) is positive below the resonance wavelength and decreases with increasing wavelength, eventually becoming negative. The wavelength at which the real part of the permittivity crosses zero is known as the epsilon-near-zero condition (ENZ). ENZ materials, such as highly doped semiconductors like indium tin oxide (ITO), exhibit large optical nonlinearities and therefore are promising for applications ranging from all-optical data processing to microscopy. Since the gap is created by the DNA ligands that attach the nanocube to the Au film, its distance can be tuned *in situ* using stimuli that cause DNA to expand or contract. Our calculation shows that the ENZ condition can be tuned over a relatively large window from 1.5 μm to 2.6 μm, for 80-nm Au NPs on top of 8-nm Au layer. The ENZ condition can further be tuned by changing the thickness of the underlying Au layer.

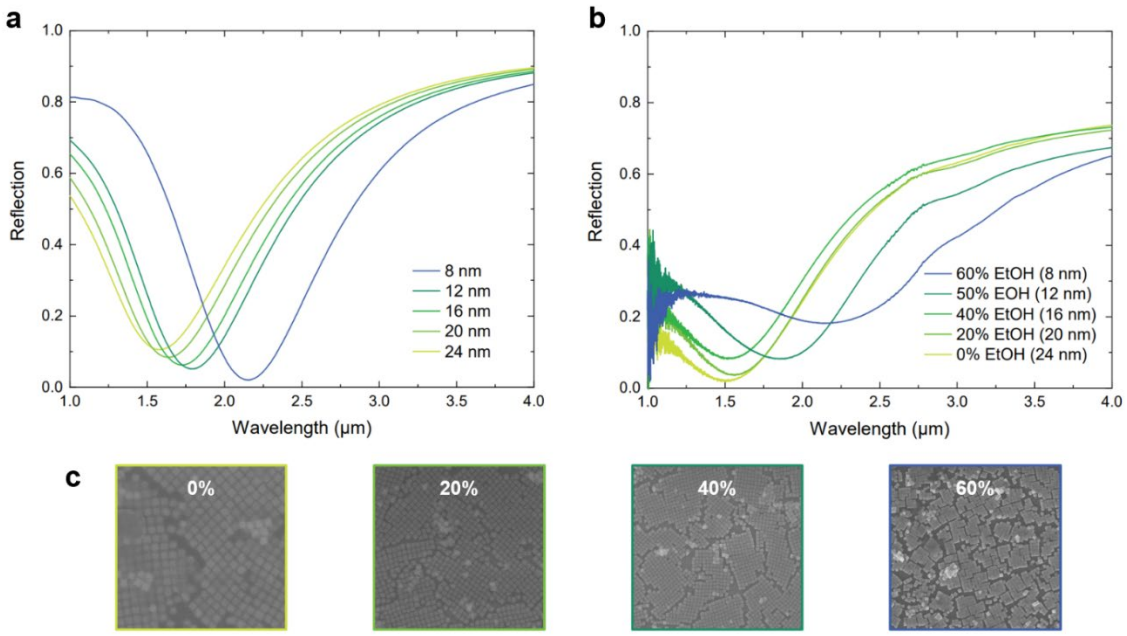


**Figure 17**. a) Simulated reflection spectra for metasurfaces with varying interparticle spacings. b) Experimental spectra for metasurfaces prepared with varying ethanol concentrations. c) SEM images of the metasurfaces measured in b).

We measured the reflectance spectra of the metasurfaces using an FTIR setup. The calculated reflection spectra for metasurfaces with varying gap spacings are shown (**Figure 17a**). The spectra exhibit large minima in reflection at the resonance wavelength and near unity reflection at other wavelengths. The measured reflectance spectra of the metasurfaces with varying gap distances show excellent agreement between the simulation and the experimental results (**Figure 17b**). The minima in the reflection spectra coincide with the location of the ENZ condition (**Figure 16c**) because the highly localized E-field between the neighboring AuNPs causes the appearance of the ENZ mode, or so-called Berreman mode. The diffusion of emitters into these highly concentrated fields should enable applications such as lasing and ultrafast emission through large plasmonic enhancements of excitation and emission rates. Our findings highlight the potential of colloidal metasurfaces to be used in tunable optical devices.

**CHANGES IN RESEARCH OBJECTIVES, if any:**

None

**EXTENSIONS GRANTED OR MILESTONES SLIPPED, if any:**

None

**SUPPORTED PERSONNEL**

**The Mirkin Group**

Chad Mirkin, PI
Kyle Gibson, Postdoc
Yuwei Gu, Postdoc
Seungkyu Lee, Postdoc
Devleena Samanta, Postdoc
Nikhil Chellam, Graduate Student, NSF Graduate Research Fellowship

Yueh Te (Ricky) Chu, Graduate Student
Max Distler, Graduate Student
Kaitlin Landy, Graduate Student
Zachary Urbach, Graduate Student
Alexa Mauying Wong, Graduate Student, NSF Graduate Research Fellowship
Yuanwei Li, Graduate Student
Cindy Zheng, Graduate Student
Wenjie Zhou, Graduate Student

**The Dravid Group**
Vinayak P. Dravid, co-PI
Jingshan Du, Graduate Student
Chamille Lescott, Graduate Student
Carolin Wahl, Graduate Student

**The Aydin Group**
Koray Aydin, co-PI
Wisnu Hadibrata, Graduate Student
Ibrahim Tanriover, Graduate Student, ONR YIP

## COLLABORATIONS

Programmable atom equivalents were explored in DoD-related applications in biomedicine with Dr. Arabela A. Grigorescu, Dr. Jorge L. Chávez, and Dr. Peter A. Mirau (Air Force Research Lab)
Advanced imaging was performed with individuals associated with the NU*ANCE* Center at Northwestern University, including Eric Roth and Dr. Reiner Bleher
Theoretical/modeling work was conducted with Profs. Sharon Glotzer (University of Michigan), George Schatz (Northwestern University), Nathan Stern (Northwestern University), Monical Olvera de la Cruz (Northwestern University), and Chris Wolverton (Northwestern University), Dr. Charles Cerqui (Northwestern University), and Dr. Larry Drummy (Air Force Research Lab)
X-ray characterization experiments were conducted in collaboration with Dr. Byeongdu Lee, Steve Weigand, and James Rix (Argonne National Laboratory)
Work related to nanochemistry education was carried out with Dr. Riki Drout (Northwestern University)
Optical and FTIR experiments were conducted with Prof. Joshua Caldwell (Vanderbilt) and Dr. Thomas Folland (Vanderbilt)
Optical work was carried out with Prof. Wei Chen (Northwestern University) and Prof. Sridhar Krishnaswamy (Northwestern University)
The Aydin group engaged in additional collaborations with Prof. Maria Cristina Larciprete (Sapienza University of Rome), Prof. Shachar Richter (Tel Aviv University), Prof. Koby Scheuer (Tel Aviv University), and Prof. Ekmel Ozbay (Bilkent University)
The Dravid group interacted with the technical group/Protochips, Inc. pertaining to the gas-cell *in situ* electron microscopy holder and gas delivery system

## PUBLICATIONS


1. Zhou, W.; Liu, Z.; Huang, Z.; Lin, H.; Samanta, D.; Lin, Q.-Y.; Aydin, K.; Mirkin, C. A "Device-Quality Reconfigurable Metamaterials from Shape-Directed Nanocrystal Assembly," *Proc. Natl. Acad. Sci. USA*, **2020**, *117*, 21052-21057.
2. Du, J. S.; Shin, D.; Stanev, T. K.; Musumeci, C.; Zie, X.; Huang, Z.; Lai, M.; Sun, L.; Zhou, W.; Stern, N. P.; Dravid, V. P.; Mirkin, C. A. "Halide Perovskite Nanocrystal Arrays: Multiplexed Synthesis and Size-dependent Emission," *Sci. Adv.*, **2020**, *6*, eabc4959.

3. Kim, S.; Zheng, C. Y.; Schatz, G. C.; Aydin, K.; Kim, K.-H.; Mirkin C. A. "Mie-Resonant Three-Dimensional Metacrystals," *Nano Lett.*, **2020**, *11*, 8096-8101.
4. Sun, L.; Lin, H.; Li, Y.; Zhou, W.; Du, J. S.; Mirkin, C. A. "Position- and Orientation-Controlled Growth of Wulff-Shaped Colloidal Crystals Engineered with DNA," *Adv. Mater.*, **2020**, *32*, 2005316.
5. Li, Y.; Lin, H.; Zhou, W.; Sun, L.; Samanta, D.; Mirkin, C. A. "Corner-, Edge-, and Facet-Controlled Growth of Nanocrystals," *Sci. Adv.*, **2021**, *7*, eabf1410.
6. Urbach, Z. J.; Park. S. S.; Weigand, S. L.; Rix, J. E.; Lee, B.; Mirkin, C. A. "Probing the Consequences of Cubic Particle Shape and Applied Field on Colloidal Crystal Engineering with DNA," *Angew. Chem. Intl. Ed.*, **2021**, *60*, 4065.
7. Cheng, H. F.; Wang, Shunzhi; Mirkin, C. A. "Electron-Equivalent Valency Through Molecularly Well-Defined Multivalent DNA," *J. Am. Chem. Soc.*, **2021**, *143*, 1752-1757.
8. Du, J. S.; Zhou, W.; Rupich, S. M.; Mirkin, C. A. "Twin Pathways: Discerning the Origins of Multiply Twinned Colloidal Nanoparticles," *Angew. Chem. Int. Ed.*, **2021**, *133*, 6934-6939.
9. Ebrahimi, S. B.; Samanta, D.; Partridge, B. E.; Kusmierz, C. D.; Cheng, H. F.; Grigorescu, A. A.; Chavez, J. L.; Mirau, P. A.; Mirkin, C. A. "Programming Fluorogenic DNA Probes for Rapid Detection of Steroids," *Angewandte Chemie*, **2021**, *60*, 15260-15265.
10. Shen, B.; Huang, L.; Shen, J.; He, K.; Zheng, C. Y.; Dravid, V. P.; Wolverton, C.; Mirkin, C. A. "Crystal Structure Engineering in Multimetallic High-index Facet Nanocatalysts," *Proc. Natl. Acad. Sci. USA*, **2021**, *118*, e2105722118.
11. Miao, Z.; Zheng, C. Y.; Schatz, G. C.; Lee, B.; Mirkin, C. A. "Low Density 2D Superlattices Assembled via Directional DNA Bonding," *Angew. Chem. Int. Ed.*, **2021**, doi:10.1002/anie.202105796.
12. Du, J. S.; He, K.; Xu, Y.; Wahl, C. B.; Xu, D. D.; Dravid, V. P.; Mirkin, C. A "Galvanic Transformation Dynamics in Heterostructured Nanoparticles," *Adv. Funct. Mater.*, **2021**, doi:10.1002/adfm.202105866.
13. Distler, M. E.; Teplensky, M. H.; Bujold, K. E.; Kusmierz, C. D.; Mirkin, C. A "DNA Dendrons as Universal Agents for Intracellular Delivery," *J. Am. Chem. Soc.*, **2021**, accepted.
14. Wang, Shunzhi; Lee, S.; Du, J. S.; Partridge, B. E.; Cheng, H. F.; Zhou, W.; Dravid, V. P.; Lee, B.; Glotzer, S. C.; Mirkin, C. A. "Valency control in colloidal crystals through electron equivalents," **2021**, submitted.
15. Zhou, W.; Li, Y.; Lin, H.; Partridge, B. E.; Huang, Z.; Mirkin, C. A. "Colloidal Crystal Dense Packing Through Polyhedra Complementarity" **2021**, submitted.
16. Petrosko, S. H.; Coleman, B. D.; Drout, R. J.; Mirkin, C. A. "Spherical Nucleic Acids (SNAs): Integrating Nanotechnology Concepts into General Chemistry Curricula," ***2021***, submitted.
17. Li, Y.; Zhou, W.; Partridge, B. E.; Lin, H.; Mirkin, C. A. "Open Channel Colloidal Superlattices," **2021**, submitted.
18. Ebrahimi, S. B.; Samanta, D., Kusmierz, C. D.; Mirkin, C. A. "Protein Transfection Via Spherical Nucleic Acids," **2021**, submitted.
19. Landy, K. M.; Gibson, K. J.; Urbach, Z. J.; Park, S. S.; Roth, E. W.; Weigand, S.; Mirkin, C. A. "Programming "atomic substitution" in colloidal crystals using DNA," **2021**, submitted.
20. Cheng, H. F.; Distler, M. E.; Lee, B.; Zhou, W.; Weigand, S.; Mirkin, C. A. "Nanoparticle Superlattices Through Template-Encoded DNA Dendrimers," **2021**, submitted.
21. Gu, Y.; Distler, M.; Cheng, H. F.; Huang, C.; Mirkin, C. A. "A general DNA-gated hydrogel strategy for effecting selective chemical cargo transport," **2021**, submitted.
22. Ribet, S.; Murthy, A.; Roth, E.; Hu, X.; Reis, R.; Dravid, V. "Emerging Opportunities in STEM to Characterize Soft-Hard Interfaces," *Microscopy and Microanalysis*, **2021**, *27(S1)*, 616-618.
23. Lescott, C.; Reis, R.; Modak, M.; Scott, E.; & Dravid, V. "Soft Microscopy of Negative Stained Soft Materials: Balancing Dose Rate and Sample Damage," *Microscopy and Microanalysis*, **2021**, *27(S1)*, 1408-1411.
24. DiStephano, J. G.; Murthy, A. A.; Jung, H. J.; dos Reis, R.; Dravid, V. P. "Structural defects in transition metal dichalcogenide core-shell architectures," *Appl. Phys. Lett.* **2021**, *118*, 223103.

25. Ribet, S. M.; Murthy, A. A.; Roth, E. W.; dos Reis, R.; Dravid, V. P. "Making the most of your electrons: Challenges and opportunities in characterizing hybrid interfaces with STEM," *Materials Today*, **2021**, doi: 10.1016/j.mattod.2021.05.006.
26. Tanriover, I.; Hadibrata, W.; Aydin, K. "Physics-based approach for neural networks enabled design of all-dielectric metasurfaces," *ACS Photonics*, **2020**, *7*, 1957.
27. Dereshgi, S. A.; Folland, T. G.; Murthy, A. A.; Song, X.; Tanriover, I.; Dravid, V. P.; Caldwell, J. D.; Aydin, K. "Lithography-free IR polarization converters via orthogonal in-plane phonons in $MoO_3$ flakes," *Nature Communications*, **2020**, *11*, 5771.
28. Hadibrata, W.; Wei, H.; Krishnaswamy, S.; Aydin, K. "Inverse-design and 3D printing of a metalens on an optical fiber tip for direct laser writing," *Nano Lett.* **2021**, *21*, 2422.
29. Hadibrata, W.; Noh, H.; Wei, H.; Krishnaswamy, S.; Aydin, K. "Compact, high-resolution inverse-designed on-chip spectrometer based on tailored disorder modes," *Laser Photonic Reviews*, **2021**, doi: 10.1002/lpor.202000556.

**PRESENTATIONS**

1. Chad A. Mirkin. Fall 2020 ACS Meeting (Virtual), "Spherical nucleic acids for live-cell analysis" (2020).
2. Chad A. Mirkin. Molecular Optoelectronic Sciences Seminar, Tianjin University (Virtual), "Mapping the Materials Genome with Megalibraries" (2020).
3. Chad A. Mirkin. First International Virtual Workshop on High Entropy Alloy and Complex Solid Solution Nanoparticles for Electrocatalysis, Ruhr University, Bochum, Germany, "Accelerating Materials Discovery Through Nanoparticle Megalibraries" (2020).
4. Chad A. Mirkin. Graham Lecture, University of Virginia (Virtual), "Repurposing the Blue Print of Life for Materials Design" (2020).
5. Chad A. Mirkin. ACS Materials Letters Global Webinar (Virtual), "Accelerating Materials Discovery through Nanoparticle Megalibraries" (2020).
6. Chad A. Mirkin. 20 years of National Nanotechnology Initiative (Virtual), "The Nanomedicine Frontier" (2020).
7. Chad A. Mirkin. Guest lecture in Kellogg Commercializing Innovations Class (Virtual) "20 Years of Cutting-edge Science, Innovation and Commercialization in Nanotechnology" (2021).
8. Chad A. Mirkin. National Nanotechnology Initiative Strategic Planning Stakeholder Workshop Keynote (Virtual), "20 Years of Cutting-edge Science, Innovation and Commercialization in Nanotechnology" (2021).
9. Chad A. Mirkin. Forum Club of Southwest Florida (Virtual), Nanotechnology overview (2021).
10. Chad A. Mirkin. Pittcon 2021 (Virtual), "Protein Spherical Nucleic Acids as Next-Generation Live-Cell Probes" (2021).
11. Chad A. Mirkin. GRC Connects (Virtual), "Nanomedicine: Why scale and chemical structure make a difference" (2021).
12. Chad A. Mirkin. Spring 2021 ACS Meeting (Virtual), "Megalibraries: Tools for exploring and expanding the materials genome" (2021).
13. Chad A. Mirkin. Spring 2021 ACS Meeting (Virtual), "Rapid, large-volume, thermally controlled 3D printing using a mobile liquid interface" (2021).
14. Chad A. Mirkin. 2021 RNA Biology Symposium (Virtual), "The Convergence of Nanoscience and Nucleic Acid Medicines: New Approaches for Tracking and Treating Disease" (2021).
15. Chad A. Mirkin. 2021 G. M. Kosolapoff Award, Auburn University (Virtual), "Rational Vaccinology: In Pursuit of the Perfect Vaccine" (2021).
16. Chad A. Mirkin. 2021 G. M. Kosolapoff Award, Auburn University (Virtual), "Colloidal Crystal Engineering with DNA - Repurposing the Blueprint for Life" (2021).

17. Chad A. Mirkin. Yonsei Center for Multi-dimensional Materials and Department of Materials Science and Engineering Colloquium (Virtual), "Colloidal Crystal Engineering with DNA - Repurposing the Blueprint for Life" (2021).
18. Chad A. Mirkin. Northwestern University and WWU Münster Workshop, Pioneers in Cell Dynamics and Imaging (Virtual), "The Convergence of Nanoscience and Nanomedicine: New Approaches for Tracking and Treating Disease" (2021).
19. Wenjie Zhou. 2021 MRS Spring Meeting (Virtual), "Shape-Driven, DNA-Mediated Engineering of Colloidal Superlattices" (2021).
20. Koray Aydin. SPIE Optics and Photonics 2021, San Diego, CA, "Anisotropic 2D layered materials for infrared photonics and polaritonics" (2021).
21. Koray Aydin. TMS 2021 Annual Meeting, Orlando, FL, "Emerging anisotropic 2D layered materials for plasmonics and polaritonics" (2021).
22. Wenjie Zhou. 2021 MRS Spring Meeting (Virtual), "Colloidal Quasicrystals Engineered with DNA" (2021).
23. Devleena Samanta. International Webinar on Chemistry at the Bio-Chemical Interface, St. Paul's Cathedral Mission College, Kolkata, India "DNA as a Stimuli-Responsive Material" (2020).
24. Devleena Samanta. ACS National Meeting Fall 2020, "NanoFlares for Detection and Diagnosis" (2020).
25. Devleena Samanta. 2020 Virtual AIChE Annual Meeting, "A Cation-Driven Bioinspired Approach to Actuate DNA Bonds in Colloidal Crystals" (2020).
26. Devleena Samanta. 2020 Virtual AIChE Annual Meeting, "Spherical Nucleic Acids as Live-Cell Probes and Stimuli-Responsive Synthons" (2020).
27. Devleena Samanta. ACS National Meeting Spring 2021, "Colloidal Protein Spherical Nucleic Acids for Live-Cell Chemical Analysis" (2020).
28. Devleena Samanta. National ChemE Seminar Series, "DNA-Based Nanostructures for Biology and Beyond" (2021).
29. Devleena Samanta. Proof School, San Francisco, USA, "DNA-Based Nanostructures" (2021).
30. Jingshan S. Du. 2021 MRS Spring Meeting, Online Virtual Meeting, "Multiplexed Nanocrystal Arrays of Halide Perovskites" (2021).
31. Jingshan S. Du. 2021 MRS Spring Meeting, Online Virtual Meeting, "Elucidating the Plasmonic Modes in Metal Nanojunctions with Nanoparticle Libraries" (2021).
32. Carolin B. Wahl. Microscopy & Microanalysis 2021 Virtual Meeting, "Precision Mapping of Structures and Interfaces in Heterostructured Nanoparticles Using 4DSTEM" (2021).

**AWARDS**

Chad A. Mirkin. Acta Biomaterialia Gold Medal (2022).
Chad A. Mirkin. Royal Society of Chemistry de Gennes Prize (2021).
Chad A. Mirkin. G. M. Kosolapoff Award, Auburn University and the Auburn Section of the ACS (2021).
Chad A. Mirkin. University of Virginia Graham Lecture (2020).
Vinayak Dravid. Clarivate Highest Cited Researcher list (2020-2021).
Alexa M. Wong. NSF Graduate Research Fellowship (2021).
Yuanwei Li. Fellowship in Leadership, Northwestern University (2020).
Wenjie Zhou. International Institute for Nanotechnology Outstanding Researcher Award (2020).
Wenjie Zhou. SPIE Optics and Photonics Scholarship (2021).
Seungkyu Lee. International Institute for Nanotechnology Outstanding Researcher Award (2020).
Nikhil S. Chellam. National Science Foundation Graduate Research Fellowship (2020).
Devleena Samanta, International Institute for Nanotechnology Outstanding Research Mentor Award (2020).
Jingshan S. Du, International Institute for Nanotechnology Outstanding Researcher Award (2020).

Jingshan S. Du, Materials Research Society Graduate Student Award (2021).
Cindy Y. Zheng. International Precious Metals Institute Student Award (2021).
Ibrahim Tanriover. Northwestern University PSED Fellowship (2021).

**INTERACTIONS/TRANSITIONS**

**Patent Applications**

1. Stabilization of Colloidal Crystals Engineered with Nucleic Acid, 62/736,260 United States, 9/25/2018, Converted, Chad Mirkin, Taegon Oh, Sarah Park
2. Stabilization of Colloidal Crystals Engineered with Nucleic Acid, PCT/US2019/052836, WO (WIPO - PCT App), 9/25/2019, Converted, Chad Mirkin, Taegon Oh, Sarah Park
3. Stabilization of Colloidal Crystals Engineered with Nucleic Acid, 17/272,139 United States, 2/26/2021, Filed, Chad Mirkin, Taegon Oh, Sarah Park
4. Halide Perovskite Nanocrystal Array and Its Preparation, 63/080,450 United States, 9/18/2020, Filed, Vinayak Dravid, Jingshan Du, Chad Mirkin, Donghoon Shin
5. Halide Perovskite Nanocrystal Array and Methods of Making the Same, PCT/US2020/063324, WO (WIPO - PCT App) 12/4/2020, Filed, Vinayak Dravid, Jingshan Du, Chad Mirkin, Donghoon Shin
6. Method for Controlled Growth of Nanocrystals, 62/706,796 United States, 9/10/2020, Filed, Yuanwei Li, Haixin Lin, Chad Mirkin, Wenjie Zhou
7. Antiviral Vaccines Using Spherical Nucleic Acids, 63/160,600 United States, 3/12/2021, Filed, Cassandra Callmann, Max Distler, Caroline Kusmierz, Chad Mirkin, Michelle Teplensky
8. CRISPR-Mediated Cleavage of Oligonucleotide-Detectable Marker Conjugates for Detection of Target Analytes, 63/165,483 United States, 3/24/2021, Filed, Sasha B. Ebrahimi, Chad Mirkin, Devleena Samanta
9. Open Channel Superlattices, 63/209,208 United States, 6/10/2021, Filed, Yuanwei Li, Chad Mirkin, Wenjie Zhou

**YEAR 5**
**To**: Dr. Bennett Ibey, bennett.ibey@us.af.mil
**Contract/Grant Title**: Reconfigurable Matter from Programmable Atom Equivalents
**Contract/Grant #**: FA9550-17-1-0348
**Reporting Period**: 8/15/2021-8/14/2022

**ABSTRACT:**

In Year 5, we continued to enhance our understanding of reconfigurable matter using programmable atom equivalents (PAEs) as building blocks. For example, nanoparticles from earth-abundant metals, such as aluminum, have been explored as highly plasmonic PAE feedstocks, and noncentrosymmetric Au bipyramids were introduced as feedstocks (Objective 1). PAE superlattices have been advanced to demonstrate a property known as hypereleasticity, where the crystals contain a shape memory capable of restoring their shape upon dehydration and rehydration (Objective 2). Superlattices with narrow size distributions have been synthesized by separating nucleation and growth during crystallization through the use of designed base mismatches in the DNA sticky ends (Objective 3). Finally, hollow nanoframe particles have been shown to be excellent broadband absorbers when ultrathin monolayers are dried on a substrate (Objective 4). Together, the progress made in Year 5 has substantially improved our ability to realize structurally sophisticated and complex programmable and reconfigurable superlattices and has enabled our exploration of their emergent functional properties.

**OBJECTIVES for the funding period**

**Year 1**

Objective 1: Develop a new feedstock of functional PAE building blocks

- *Synthesis of three-dimensional anisotropic plasmonic nanoparticles*
- *Synthesis of MOF nanoparticles with control over their physical properties*

Objective 2: Synthesize and investigate dynamically reconfigurable superlattices

- *Transmutable nanoparticle superlattices*
- *High resolution and contrast imaging of soft materials by electron microscopy*

Objective 3: Synthesize and investigate structurally sophisticated and functional superlattices.

- *Superlattices with controlled crystal habit*
- *Explore emergent optical phenomena in nanoparticle superlattices*

Objective 4: Assemble reconfigurable, sophisticated, and functional superlattices on surfaces

- *Fabricate surface templates with well-defined DNA binding sites*

**Year 2**

Objective 1: Develop a new feedstock of functional PAE building blocks

- *Synthesis of two-dimensional anisotropic plasmonic nanoparticles*
- *Algorithmic characterization of nanoparticle yield and dispersion.*
- *Synthesis of MOFs nanoparticles with control over their physical properties*

Objective 2: Synthesize and investigate dynamically reconfigurable superlattices

- *Transmutable nanoparticle superlattices*
- *Sparse imaging for soft materials characterization*
- *High resolution and contrast imaging of soft materials by electron microscopy*

Objective 3: Synthesize and investigate structurally sophisticated and functional superlattices

- *Co-crystallization of multiple building blocks with chemically, physically, and structurally distinct properties*
- *Superlattices with controlled crystal habit*
- *Explore emergent optical phenomena in nanoparticle superlattices*

Objective 4: Assemble reconfigurable, sophisticated, and functional superlattices on surfaces

- *Layer-by-layer growth of single-crystal superlattices with defined crystal shape and size*

**Year 3**

Objective 1: Develop a new feedstock of functional PAE building blocks

- *Synthesis of two-dimensional anisotropic plasmonic nanoparticles*
- *High-throughput screening of anisotropic nanoparticle synthesis conditions*

Objective 2: Synthesize and investigate dynamically reconfigurable superlattices

- *Transmutable nanoparticle superlattices*
- *In situ characterization of reconfigurable superlattices via fluidic-cell S/TEM*

Objective 3: Synthesize and investigate structurally sophisticated and functional superlattices

- *Co-crystallization of multiple building blocks with chemically, physically, and structurally distinct properties*
- *Unique low-symmetry and quasicrystalline structures*
- *Explore emergent optical phenomena in nanoparticle superlattices*

Objective 4: Assemble reconfigurable, sophisticated, and functional superlattices on surfaces

- *Layer-by-layer growth of single-crystal superlattices with defined crystal shape and size.*

**Year 4**

Objective 1: Develop a new feedstock of functional PAE building blocks

- *High-throughput screening of anisotropic nanoparticle synthesis conditions*

Objective 2: Synthesize and investigate dynamically reconfigurable superlattices

- *Transmutable nanoparticle superlattices*
- *In situ characterization of reconfigurable superlattices via fluidic-cell S/TEM*

Objective 3: Synthesize and investigate structurally sophisticated and functional superlattices

- *Co-crystallization of multiple building blocks with chemically, physically, and structurally distinct properties*
- *Unique low-symmetry and quasicrystalline structures*
- *Explore emergent optical phenomena in nanoparticle superlattices*

Objective 4: Assemble reconfigurable, sophisticated, and functional superlattices on surfaces

- *Superlattice assembly on flexible and porous supports*
- *Emergent properties of surface-bound superlattices*

**Year 5**

Objective 1: Develop a new feedstock of functional PAE building blocks

- *High-throughput screening of anisotropic nanoparticle synthesis conditions*

Objective 2: Synthesize and investigate dynamically reconfigurable superlattices

- *Synthesis of dynamically responsive superlattices from MOF building blocks*
- *Develop new strategies for transferring DNA-assembled superlattices to the solid state*

Objective 3: Synthesize and investigate structurally sophisticated and functional superlattices.

- *Unique low-symmetry and quasicrystalline structures*
- *Explore emergent optical phenomena in nanoparticle superlattices*

Objective 4: Assemble reconfigurable, sophisticated, and functional superlattices on surfaces

- *Emergent properties of surface-bound superlattices*

**FINDINGS**

**Develop a new feedstock of functional PAE building blocks**

Under this objective, we enhanced the library of plasmonic nanoparticles that can be used as PAE cores beyond gold and silver compositions. Aluminum (Al) is a particularly attractive material because Al nanoparticles have plasmon resonances tunable over a broader range of the spectrum, particularly in the UV range, and the element itself is considerably more Earth-abundant (Section 1A). We have also introduced another noncentrosymmetric gold (Au) bipyramidal PAEs for the first time (Section 1B). Finally, we show that using scanning probe block copolymer lithography we can synthesize structurally complex gold-copper (Au-Cu) alloy nanoparticles (Section 1C).

**1. A Perfluoroalkyl-Based Strategy to Functionalizing Moisture-Sensitive Nanoparticles with DNA**

Nanoparticles with collective oscillations of conduction band electrons, known as localized surface plasmons (LSPs), can be utilized to harness light with optical cross-sections greater than their physical cross sections. Historically, research utilizing plasmonic nanoparticle properties and engineering their collective responses (e.g., via DNA-directed assembly) have involved Au and Ag due to their optical response in the visible region of the electromagnetic spectrum, their ease of synthesis, and relative chemical inertness. Aluminum and other *sp*-block metals have emerged as Earth-abundant alternatives to Au and Ag, in part due to their ability to sustain LSPs ranging from the deep-UV to the near-IR. Furthermore, Al can sustain higher-order resonance modes at smaller sizes and at higher symmetries, a property unachievable in their coinage metal counterparts, thereby enabling small-molecule detection for a wide variety of substrates and the emergence of exotic optical properties when assembled into strongly coupled nanostructures.

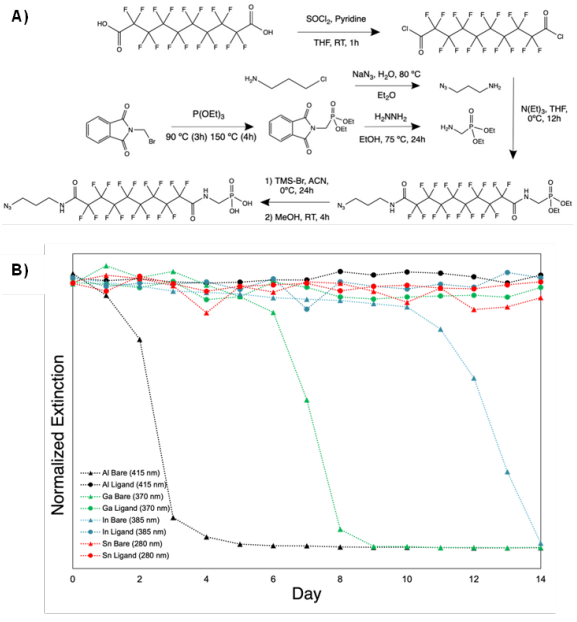


**Figure 1.** A) Synthetic scheme for ligand synthesis. The synthesis involves an amidation of a perfluorinated dicarboxylic acid via conversion to a diacyl chloride intermediate. B) Extinction intensity for bare and passivated Al, Ga, In and Sn nanoparticles. Samples were incubated in phosphate-buffered saline and the extinction was monitored at the dipolar LSPR for each system at room temperature.

Many biomolecules and organic molecules of interest have excitation wavelengths within the UV region, necessitating these nanoparticles' operability under aqueous, physiological environments. Al and other *sp*-block metals form a self-limiting passivating oxide layer around 2-5 nm thick, rendering them extremely air stable. However, this oxide shell is often amorphous and contains an abundance of surface defects, promoting the diffusion of water into this shell and

subsequent dissolution of the metallic core into various oxyhydroxides under aqueous or humid conditions. Herein, we present a single-molecule strategy to limit oxidation to avoid reducing the enhanced near-field of the nanoparticle LSP. This surface ligand consists of a phosphonic acid anchor, known to bind to Lewis acidic metals through strong coordination of its phosphoryl oxygen in a tridentate fashion, which can passivate surface defects in the oxide layer and inhibit water diffusion into these reactive surface sites. As an additional protective measure, the body of the ligand consists of a perfluorinated aliphatic chain linked via hydrolytically stable amide bonds: perfluorocarbons are effectively unpolarizable, rendering them resistant to dispersion interactions induced by water or other polar molecules. Finally, the head group of the ligand contains an azide group, thereby enabling subsequent functionalization of molecules of interest (e.g., DNA, dyes) via bio-orthogonal interactions (i.e., azide-alkyne cycloaddition).

The synthetic scheme for this ligand alongside a proof-of-concept demonstration of its versatility is shown in **Figure 1A**. To demonstrate the utility of these ligands, we synthesized and incubated coated and uncoated Al, Ga, In and Sn nanoparticles in a phosphate buffer saline (PBS) and monitored the LSPs for each material via UV visible spectroscopy. In **Figure 1B** we observe that all coated nanoparticle types retain their LSP properties over the course of 2 weeks in solution. In contrast, the bare (or uncoated) counterparts, degrade after ~3, 8 and 13 days for Al, Ga, and In respectively. Interestingly, Sn retains its LSP over the course of this time period, which is subject to further investigation. Taken together, the enhanced aqueous stability of these nanocrystals allows for their use in a variety of applications compatible with aqueous environments, paving the way for Earth-abundant nanoplasmonics for fieldable nanosensing applications.

## 2. Synthesis of Au bipyramid PAE building blocks

This year we expanded our PAE building blocks to include Au bipyramidal nanoparticles, which are pentatwinned nanocrystals that have an anisotropic shape and defined exposed facets, making them unique candidates for anisotropic colloidal crystal assembly.[1-3]Here we prepared pentatwinned Au nanocrystals by thermally inducing crystal twinning in seed particles which initiates the growth of Au bipyramids with the same crystal structures.[4] It has been found that the addition of $Ag^+$ (i.e., from a silver salt) can be used to control the size and aspect ratio of the Au bipyramids in the presence of a surfactant (i.e., cetyltrimethylammonium bromide (CTAB)). Further, in other reports of metal nanoparticle synthesis it has been postulated that the reduction and deposition kinetics of seeded growth can be controlled to prepare nanostructures with different shapes.[5-6] Therefore, we hypothesized that by using a similar approach we could control colloidal nanoparticles with reduced symmetry that can be used as functional PAE building blocks. [7] To this end, we chose cetylpyridinium chloride (CPC) to replace the CTAB. This substitution of the counterion from bromide to chloride is expected to increase the reduction kinetics and change reaction pathway to favor kinetic states rather than thermodynamic equilibrium.

Using these parameters, we synthesized Au bipyramids under varying conditions of $AgNO_3$ salt concentrations to the reaction mixtures. The resulting particles were analyzed using UV-vis spectrometer and the extinction spectra of these nanostructures are shown in **Figure 2a**. Here we see a gradual redshifted longitudinal peak position as $Ag^+$ concentration increases in the growth solution. The nanoparticle solutions show corresponding color changes from purple to red, green, and light red. These observations imply that the presence of $Ag^+$ slows the lateral growth while promoting the deposition of reduced Au atoms along the longitudinal direction, which is responsible for the elongated growth of the pentatwinned seeds into Au bipyramids. In the HAADF-STEM images in **Figures 2b** and **2c** we show that the pentagonal crystal domains and domain boundaries are preserved during growth. Finally, to investigate the structure of these nanoparticles further, we performed electron tomography and three-dimensional volume

reconstruction on one type of Au bipyramid. A STEM image in **Figure 2d** shows that the transverse symmetry is broken if 10-µL $AgNO_3$ is added in the seeded growth, leading to different projections of Au bipyramids. Further electron tomography demonstrates a C2 symmetry of the Au bipyramids, which indicates the presence of a rotation axis as indicated by the red dots in **Figure 2d**. Further, we also showed that by varying the $Ag^+$ concentration in the synthesis solution, we can access Au nanostructures of diverse shapes and a range of exposed nanocrystalline facets (ranging from 10 – 30 facets) and anisotropic bipyramids with reduced symmetries (**Figure 2e**). We propose that under the presence of CPC capping ligands, the C5 symmetry of the Au decahedrons is broken, leading to the formation of Au bipyramids with C2 symmetry. Further, the addition of more $Ag^+$ initiates the following shape transformation to Cs symmetry, where the Au bipyramids lose their two-fold rotation symmetry but feature one mirror plane. An illustration depicting these shape changes during synthesis is depicted in **Figure 2f**.

Importantly, these results imply that regulating the reduction kinetics during seeded growth is an effective approach to controlling colloidal nanocrystal syntheses with noncentrosymmetric shapes and symmetries. These new nanostructures can serve as functional PAE building blocks and can be used to assemble emerging colloidal crystals through DNA hybridization.

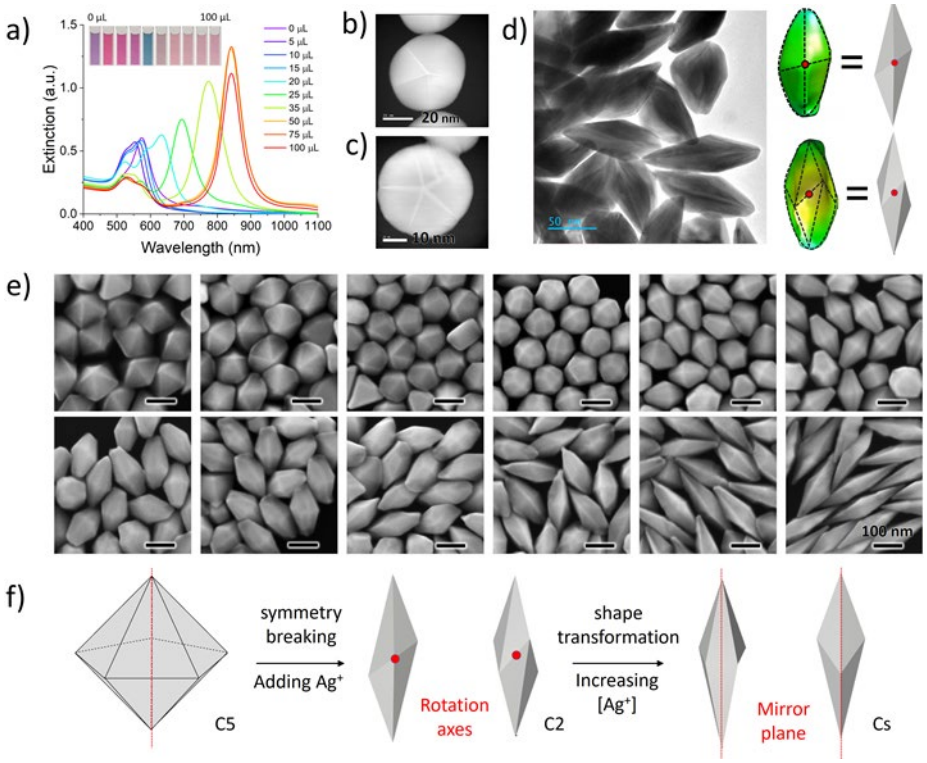


**Figure 2.** Shape-controlled growth of Au nanostructures with reduced symmetry. **a)** Extinction spectra of Au bipyramid nanoparticles prepared by adding different volumes of $AgNO_3$. Inset shows the images of the bipyramid solutions. High-angle annular dark field scanning transmission electron microscopy (HAADF-STEM) images of Au bipyramids prepared by adding **b)** 1-µL and **c)** 3.5-µL $AgNO_3$ solution. **d)** Scanning transmission electron microscopy (STEM) image (left) and three-dimensional reconstruction by electron tomography (right) of Au bipyramids prepared by adding 10-µL $AgNO_3$. **e)** Scanning electron microscopy (SEM) images of Au nanostructures prepared under different $Ag^+$ concentrations. **f) Schematic** illustration of the shape and symmetry changes in the synthesis.

## 3. Synthesis of Chemically and Structurally Complex Alloy Nanoparticles

In another activity, we developed a library of compositionally and structurally well-defined Au-Cu alloy nanocrystals via scanning probe block copolymer lithography (SPBCL). SPBCL is a synthetic platform that can be highly parallelized to make libraries of unique nanoparticles on a chip. Due to its ability to combine several immiscible elements into a single nanoparticle, we can access chemically and structurally complex nanomaterials that have yet to be explored. These libraries not only allow one to map compositional and structure space but also the conditions (e.g., cooling rate) required to access specific structures. This approach enabled the realization of a previously unobserved architecture, an intermetallic nanoprism, that is a consequence of hierarchical atom stacking (**Figure 3**). These structures exhibit distinctive diffraction patterns characterized by non-integer-index, forbidden spots, which serve as a diagnostic indicator of such structures. Inspection of the library's pseudospherical particles reveals a high-strain cubic–tetragonal interfacial configuration in the outer regions of the intermetallic nanocrystals. Since it is costly and time-consuming to explore the nanomaterials phase space via conventional wet-chemistry, this parallel kinetic-control approach, which relies on substrate- and positionally-isolated particles, may lead to the rapid discovery of complex nanocrystals that may prove useful in applications spanning catalysis and plasmonic sensing.

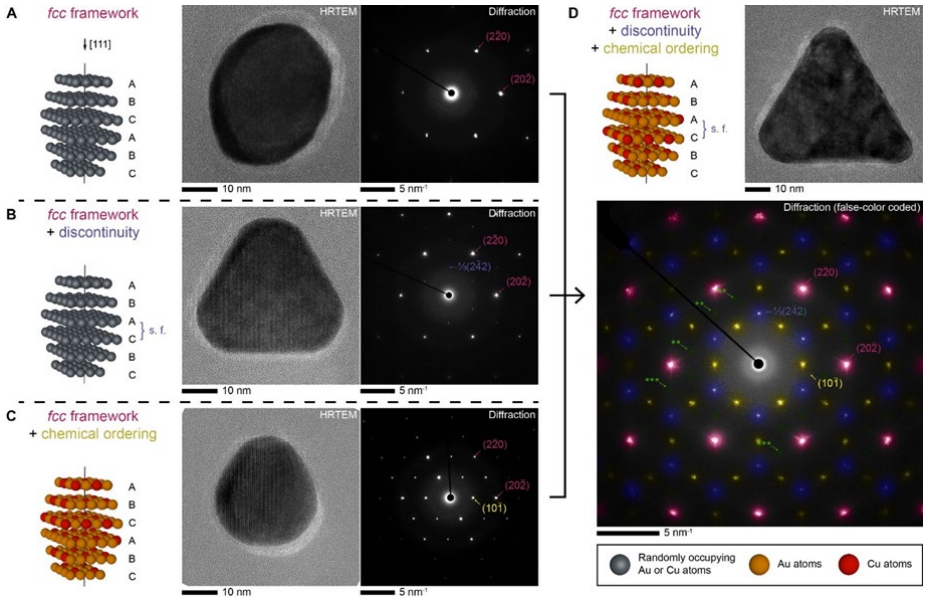


**Figure 3.** Atom stacking hierarchy along the [111] zone axis in cubic Au-Cu phases. Atomic ratio Au:Cu ≈ 3:1. (A) A chemically disordered single-crystalline nanocrystal. (B) A chemically disordered nanoprism. (C) A chemically ordered (L12) single-crystalline nanocrystal. (D) A chemically ordered (L12) nanoprism. In the atom stacking structures, layers perpendicular to the [111] axis (black line) are separated for clarity. s. f.: stacking fault. In (D), a false-colored diffraction pattern shows a combination of spots from the fcc framework (red), stacking discontinuity (blue), chemical ordering (yellow), and their interaction (green). The HRTEM images and electron diffraction patterns have been rotated to ensure that a pair of (20$\bar{2}$) reflections orient horizontally. Interaction spots: ⅓{$\bar{5}$ 41} (**) and ⅓{$\bar{7}$ 52} (***).

**Synthesize and investigate dynamically reconfigurable superlattices**

Under this objective, we investigated reconfigurability in large, single-crystalline assemblies. Methods to synthesize large (>100 μm) crystals have enabled in-situ measurements of crystal shape during dehydration and rehydration, enabling the discovery of unique shape memory properties following extreme shape deformation (Section B1).

## 1. Shape Memory in Self-Adaptive Colloidal Crystals

The ability to design crystalline materials that can dynamically and reversibly change shape would enable enormous advances essential to the development of flexible electronics, artificial muscles, and various dynamic components in soft robotics. However, the crystalline phase of a material tends to be brittle, especially in crystals composed of atomic building blocks, which to

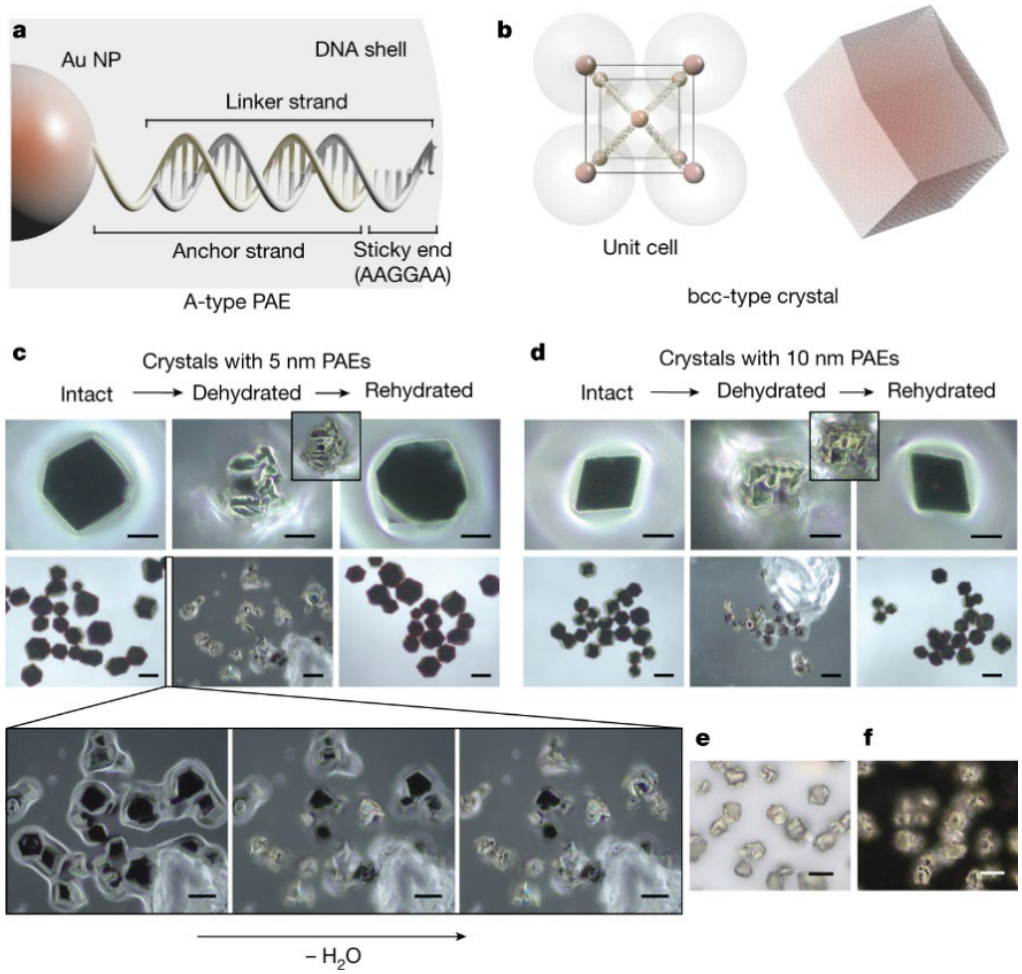


**Figure 4. a**, Schematic of an A-type PAE structure. Note, B-type PAEs have the same structure, but the complementary sticky end sequence is TTCCTT. **b**, A- and B-type PAEs are designed to interact with each other through DNA hybridization and assemble into non-close-packed bcc-type structures. **c**,**d**, Optical microscope images of crystals assembled from (**c**) 5 and (**d**) 10 nm PAEs. From left to right, the three columns indicate intact, dehydrated and rehydrated crystals. The inset images were collected with two times lower magnification to show the clear projection boundaries of the crystals. Scale bars, 20 and 50 μm for the top and bottom row, respectively. **e**,**f**, Bright (**e**) and dark-field (**f**) optical microscopy images of typical dehydrated crystals assembled from 5 nm PAEs. Scale bars, 20 μm.

date have only exhibited a limited range of mechanically responsive behaviors. PAEs, which utilize nanoscale particles as their building blocks and oligonucleotides as their underlying "bonds", have been shown to assemble into a complex variety of structures with tunable interparticle spacings and symmetries. We have previously shown that PAEs can assemble into small crystals that show promise in creating dynamic crystalline structures. However, due to the small size of existing crystals, typically on the order of microns in diameter, it has remained difficult to study their *in situ* behaviors.

Here, we investigated the shape memory properties of single crystals composed of spherical PAEs, shown in **Figure 4**. Large (>100 μm) single-crystals were first synthesized by changing the thermodynamic and kinetic properties of the solution by decreasing the rate of slow cooling. The mechanically responsive behaviors of these crystals were then studied by observing them via optical and dark-field microscopy.

Crystals were first fully dehydrated on a glass slide, upon which they completely lost their initial shape. They deformed into highly irregular shapes with wrinkles and creases, which is a type of deformation typically considered irrecoverable for single crystalline materials. However, upon re-addition of the solvent, we observed that the crystals were able to recover to their initial morphology. The crystals could be exposed to this dehydration and rehydration process > 6 times and still recover their initial faceting and morphology. The large size of these crystals also enabled unprecedented study of their internal structure and their resulting state-switchable properties. Taken together, this work elucidated the ability of single crystals composed of DNA to act as shape memory materials and recover from extreme deformation types, a behavior unique amongst other single crystalline materials. Critically, this work was enabled by solving the challenge of growing the first large single crystals composed of PAEs. By growing large PAE crystals of other symmetries, DNA lengths, and particle cores, we expect that we can unveil further novel properties and isolate behaviors only possible with large single crystals.

**Synthesize and investigate structurally sophisticated and functional nanoparticle superlattices**

Under this objective, we established new methods to synthesize sophisticated colloidal crystal architectures and investigated the properties that emerge from these unique structures. We demonstrated a library of new open channel superlattices using edge-to-edge assembly of three-dimensional metallic hollow nanoparticle building blocks (Section C1). Programming separate nucleation and growth steps in colloidal crystallization using multiple DNA interaction strengths resulted in improved crystal size uniformity on the mesoscale (Section C2). DNA dendrons with DNA junctions were to design new symmetry-breaking synthons to program unique intermetallic structures (Section C3). Finally, we show that low-voltage imaging improves contrast for the organic or low atomic number component of hybrid materials in scanning transmission electron microscopy in a scanning electron microscope (Section C4).

## 1. Open Channel Metal Particle Superlattices

Porous crystals are a class of materials with extraordinary properties, including high surface areas and low densities, that can be engineered to physically absorb and chemically interact with guest species of known size, shape, and chemical functionality. Although reticular chemical synthesis based upon metal ions and bridging ligand building blocks has led to significant advances in the realization of porous materials (pore apertures < 10 nm), and design rules now exist for the construction of such materials at the molecular scale, it is still remarkably difficult to prepare

porous crystals with customized pore topologies and pore sizes in the range between 10 nm and 1 μm.

We hypothesized that three-dimensional (3D) metallic hollow nanoparticles (NPs) (nanoframes (NFs) and nanocages (NCs)) could be assembled into open channel superlattices using colloidal crystal engineering with DNA, an approach that thus far yields access to over 70 different crystal symmetries via well-established design rules based upon the complementary contact model (CCM, the notion that DNA-modified building blocks will arrange themselves in space to maximize complementary interactions). Indeed, consistent with the CCM, we determined that the attractive DNA hybridization interactions between the edges of adjacent NFs lead to the formation of ordered superlattices. Notably, this registry-driven edge-to-edge assembly mode (edge-bonding) is distinct from the canonical face-to-face interactions (face-packing) that typically govern the assembly outcomes of solid anisotropic NPs. It should be noted that an approach that relies on the crystallization of DNA origami subunits has been developed, and although this method enables access to certain crystal structures through vertex-to-vertex bonding, it yields structures that are limited in pore dimensions (typical unit size < 50 nm).

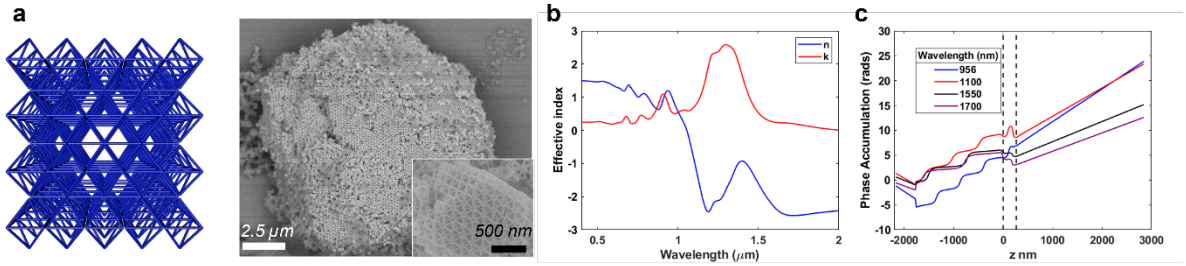


**Figure 5.** Negative effective index simulation of the porous ccp crystal assembled from Au-Pt octahedral NFs. **a,** Model and the corresponding SEM images of the simulated crystal. **b,** Calculated effective refractive index (n, blue line) and extinction coefficient (k, red line) of a porous Au- Pt ccp crystal. **c,** Electric field phase accumulated throughout the Au-Pt ccp crystal at wavelengths corresponding to positive (blue line), near-zero (red line), and negative index (black and purple line) regions.

The controllable and tunable pore topologies and periodicities of open channel superlattices make them promising candidates to realize unnatural optical properties, such as negative refractive index, which is desirable for different applications including super-resolution imaging and cloaking. Negative index phenomena have been theoretically predicted and, more recently, realized with the advent of metamaterials. Initial demonstrations of negative index metamaterials were realized in microwave electromagnetic frequencies (e.g., 300 GHz - 300 MHz). However, it has remained challenging to achieve negative refractive index materials over the visible and near-infrared ranges.

Open channel superlattices consist of subwavelength unit cells; therefore, they behave as an optical metamaterial with an effective permittivity ($\varepsilon_{eff}$) and an effective permeability ($\mu_{eff}$). The unit cell of open channel superlattices can be described using an RLC (resistor, inductor, capacitor) circuit. With building blocks of proper sizes and periodic arrangements, such an RLC circuit provides simultaneously negative $\varepsilon_{eff}$ and $\mu_{eff}$, which is the required conditions for negative refractive index. We performed full field electromagnetic simulations to calculate effective optical parameters of Au-Pt *ccp* open channel superlattices embedded into $SiO_2$. The effective refractive indices are calculated using the S-parameter retrieval method. The numerical calculations suggested negative effective index in the near-infrared range (**Figure 5a**). The calculated effective index is further confirmed by simulating the phase accumulation as light travels through the

medium at different wavelengths corresponding to positive, near-zero and negative effective indices (**Figure 5b**).

Importantly, we introduced two new design rules that summarize this edge-bonding construction strategy through which new open channel superlattices are synthesized. These structures have symmetries, pore geometries, and topologies that can be deliberately tuned through the choice of hollow NP and DNA. These open channel metallic superlattices not only have the potential to exhibit unnatural optical properties that make them attractive as optical metamaterials but also can be useful for localizing large guests for a variety of applications, including biomolecular absorption and storage, separation, chemical sensing, and catalysis.

## 2. Programming Nucleation and Growth in Colloidal Crystals Using DNA

Precise control over colloidal size, shape, and uniformity are required in order for colloidal crystals to be implemented into devices. For example, mesoscale size is known to be a key parameter in tuning the optical properties of colloidal crystals. Typically, DNA-mediated colloidal crystallization is carried out via slow cooling, where nucleation and growth occur simultaneously throughout the process, and results in limited uniformity and control over mesoscale sizes. Therefore, synthetic methods are needed to control nucleation and growth in colloidal crystals to improve control over size and uniformity.

Here, we explored how DNA sequence design can be used to deliberately separate nucleation and growth in colloidal crystallization. We hypothesized that a system with fully complementary "seed" PAEs and single-base mismatched "growth" PAEs would allow for initial nucleation of the "seeds" followed by heterogenous "growth", all occurring in a one-pot fashion. We designed four DNA strands, where the sticky ends of A and B were fully complementary and A* and B* included a single-base mismatch. 15 or 20 nm gold spheres were functionalized with one of the four sequences, and each PAE could interact with either the fully complementary sticky end or the mismatched sticky end (**Figure 6**). The assembly process was characterized by UV-vis spectroscopy and while cooling the PAE solution, and the uniformity of crystal products was visualized via scanning electron microscopy (SEM).

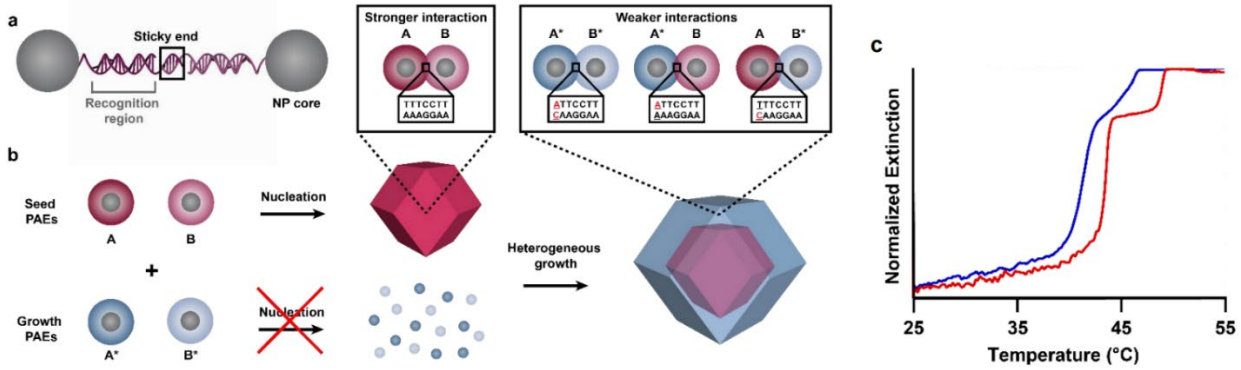


**Figure 6.** a) Schematic showing complementary PAEs with the sticky end region indicated. b) Growth PAEs and seed PAEs are combined in one solution, where the seed PAEs containing a stronger sticky end interaction nucleate first followed by heterogenous growth of the of the remaining PAEs through weaker sticky end interactions. c) UV-vis melting temperature characterization of a mixture of seed and growth PAEs at a 1:2 ratio showing two distinct transitions detected at 520 nm. Red: heating, blue: cooling.

UV-vis melting temperature characterization (**Figure 6c**) clearly showed a two-step process when seed and growth PAEs were combined. Crystal size distributions measured from SEM images showed improved uniformity of crystal sizes compared to a control with only one type of

DNA. Overall, this seed-mediated approach is a one-pot synthesis method that provides improved control over nucleation and growth of colloidal crystals. Introducing multiple interaction strengths through DNA base mismatches is a generalizable approach that could be applied to other DNA designs and nanoparticle building blocks for assembly moving forward.

## 3. Symmetry-Breaking Dendrimer Synthons in Colloidal Crystal Engineering with DNA

In previous work, we have shown that DNA dendrons can behave as electron equivalents (EEs) in colloidal crystal engineering with DNA. In addition, these DNA dendrons can be combined using molecular templates to create 3- and 6-branched dendron structures, for example, furthering understanding of how valency and size impact the transition between EE and PAE-like assembly. One disadvantage of using molecular templates, however, is that incorporation of multiple DNA sequences in an anisotropic manner is synthetically challenging. Using multiple distinct DNA sequences in a single construct is therefore desirable to program multicomponent assemblies with new and defined intermetallic structures.

We hypothesized that DNA junctions could template the assembly of DNA dendrons in a modular and anisotropic manner (**Figure 7**). Two- and three- way DNA junctions were designed as the cores, where each strand in the junction contained an 18-base pair (bp) overhang complementary to the stem region of a DNA dendron. The sequence and length of each overhang can be independently designed, enabling identical or orthogonal DNA dendrons within one structure. In addition, the length of double stranded DNA can be tuned as well, allowing one to program DNA junction length in a particular direction. Initial dynamic light scattering, and gel electrophoresis characterization confirmed the formation of the DNA junction cores, and UV-vis melting temperature characterization of the hybridized junction dendrimers with complementary PAEs showed an increase in melting temperature when the DNA junction core was present compared to controls with dendrons only. A library of crystal structures was then established for junction dendrimers with identical sticky ends but different junction numbers (two- or three-way), particle sizes, and DNA junction core bp length. This library includes a new, low symmetry $Si_2Sr$ structure never before reported in the field of colloidal crystal engineering (**Figure 7c**).

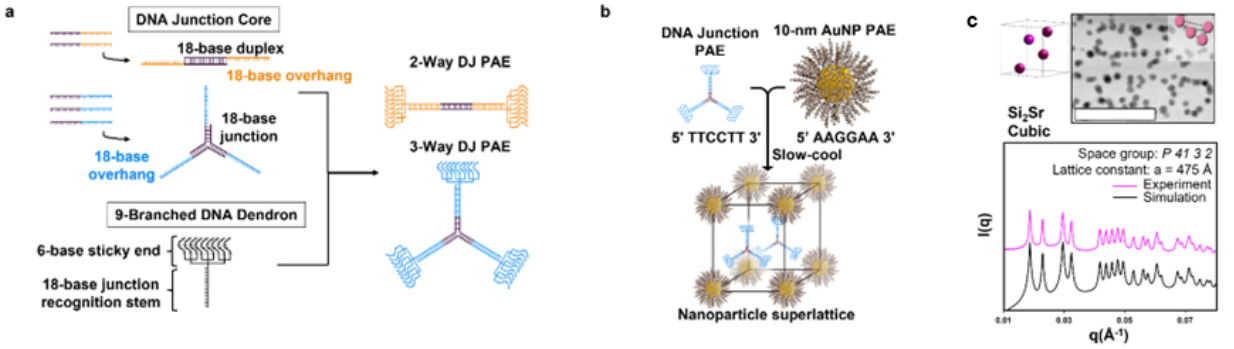


**Figure 7.** Bottom-up assembly of junction dendrimers. (a) Junction dendrimers consist of a DNA junction core and a 9-branched DNA dendron that can be assembled into the full structure by annealing the components together. (b) Junction dendrimers are coassembled with Au PAEs to produce colloidal crystals. (c) 5 nm Au PAEs form a $Si_2Sr$ lattice when assembled with 54-bp three-way junction dendrimers, as characterized by SAXS and STEM. Scale bars: 50 nm.

These symmetry-breaking synthons provide a unique opportunity to encode anisotropic DNA lengths and sequences, something that is not possible with traditional spherical PAEs or EEs templated with molecular cores. As an initial demonstration of this concept, we designed a two-

way junction with orthogonal sequences on the two overhangs as well as three bp lengths. Crystals using this symmetry-breaking synthon with two Au PAEs formed a simple hexagonal structure with increasing lattice parameter in the c direction as the bp length was increased, demonstrating controlled expansion along a single crystallographic direction. Taken together, this work introduces a new type of DNA-based building block that can be used to break the symmetry in colloidal crystal engineering. Future studies will use junction dendrimers with orthogonal sticky ends that correspond to different particle compositions towards complex multicomponent architectures.

## 4. Imaging of Soft and Hybrid Structures using STEM-in-SEM

Significant progress was made this year in the imaging of hybrid nanomaterials with low-voltage electron microscopy (EM) and tomography for three-dimensional characterization. Low-voltage imaging improves contrast for the organic or low atomic number component of hybrid materials by increasing the occurrence of electron scattering events. Scanning transmission electron microscopy in a scanning electron microscope (STEM-in-SEM) is a highly underutilized technique for soft material imaging; in addition to improving contrast for the soft components, SEM is high-throughput and cost-effective when compared with TEM or dedicated STEM.[8]

STEM-in-SEM was used to characterize a variety of hybrid materials, including protein-based nanoparticles and polymer vesicles infused with iron oxide nanoparticles. As shown in **Figure 8**, contrast is highly improved for the polymer component compared to the nanoparticle component using 30 kV STEM-in-SEM over conventional 200 kV STEM.

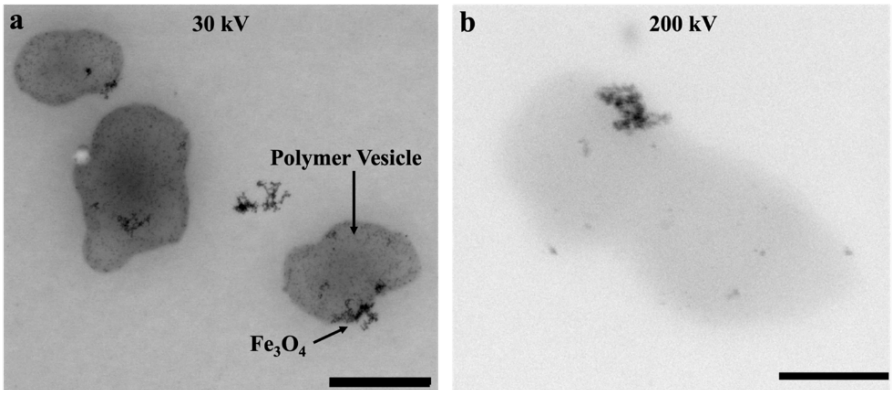


**Figure 8.** a) STEM-in-SEM at 30 kV of unstained polymer vesicle infused with iron oxide magnetic nanostructures. Scale bar 500 nm. b) Conventional high angle annular dark field (HAADF) STEM at 200 kV of same unstained polymer vesicle. Contrast is reversed for comparison. Scale bar 200 nm.

**Assemble reconfigurable, sophisticated, and functional nanoparticle superlattices on surfaces**

Under this objective, we continued to investigate the templated assembly of superlattices on surfaces and their emergent properties. Specifically, we looked at how crystallization proceeds under confinement in the context of colloidal crystallization with DNA and established methods to template assembly with position control of superlattices on a surface (Section D1). Furthermore, we investigated how plasmonic nanoframes can function as large area, broadband metasurface absorbers (Section D2).

## 1. Arrays of colloidal single crystals engineered with DNA in lithographically defined microwells

Crystallization in confined spaces is often found in nature and engineered systems. Because a confined volume can modify crystallization kinetics, confinement often leads to improved control over crystal features, in addition to control over both position and orientation in space. As such, in the context of colloidal crystal engineering, confinement has been used to program crystal position and orientation, parameters important for constructing optoelectronic devices and metasurfaces. In colloidal crystal engineering with DNA, PAEs have been used to achieve impressive control over parameters such as crystal symmetry, lattice parameter (sub-nm precision), and habit. Importantly, the optical properties of these colloidal crystals can be tuned via the aforementioned parameters, presenting PAE superlattices (SLs) as promising candidates for photonic- and plasmonic-applications.

In this effort, we fabricated lithographically defined microwells to confine the growth of AuNP SLs. The exposed gold surface at the bottom of each well was modified with a defined DNA sequence (sequence A or B, depending on experiment). Two sets of complementary PAEs were prepared, one from DNA sequence A and the other from DNA sequence B. DNA A and DNA B are complementary and designed to hybridize at room temperature, creating DNA bonds between the PAEs, which results in larger assemblies. Next, each patterned, DNA-functionalized substrate was submerged in solution containing the two types of PAEs, yielding SLs with thermodynamically preferred BCC symmetry upon slow cooling. DNA (sequence A or B, depending on experiment).

With this methodology we were able to realize two major advances in colloidal crystal engineering. First, we show that we are able to synthesize SLs with very narrow size distributions (AVG: 0.85 μm ± 0.050 μm, relative standard deviation of 5.9%) (**Figure 9a,b**). Second, this approach can be used to control the position and orientation of each SL in an ensemble array in designed shapes sizes, and orientations **(Figure 9c**). In sum, this effort demonstrates that PAE programmability can be used to design, synthesize, and manipulate plasmonically- and

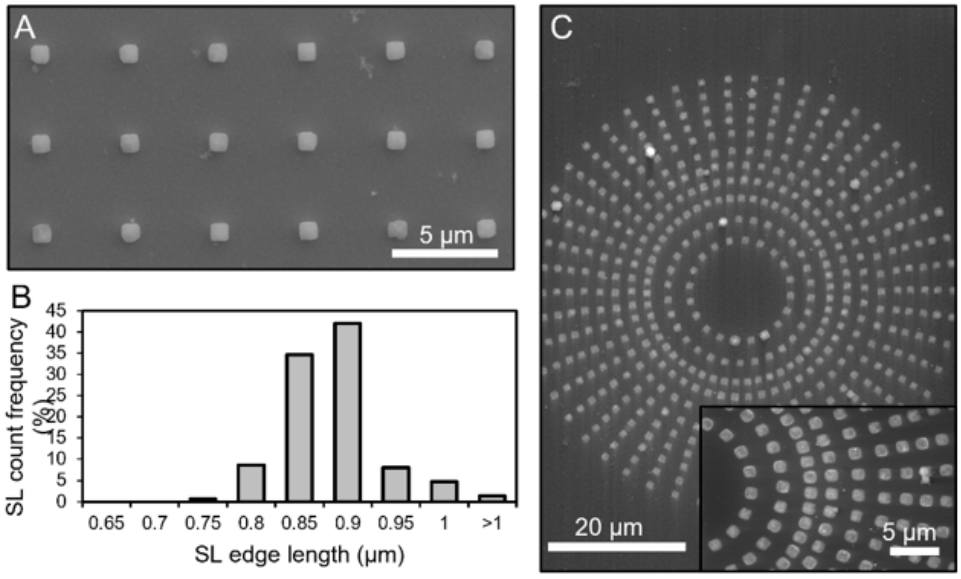


**Figure 9** (**A**) SEM image of SLs in lithographically defined microwells on a chip. (**B**) Edge length distribution analysis of superlattices (n=150). (**C**) Circular array of SLs demonstrating arbitrary positional control.

photonically-active SLs as building blocks to construct hierarchical materials for any substrate, or 'on-chip', application of interest.

## 2. Plasmonic Nanoframes as Large-Area, Broadband Metasurface Absorbers

Synthesizing broadband ultrathin absorbers in a scalable and straightforward manner remains technically challenging. We hypothesized that ultrathin, broadband metasurface absorbers could be synthesized by assembling plasmonic nanoframes (NFs) on a surface, taking advantage of their tendency to assemble on surfaces and strong light-absorbing properties.

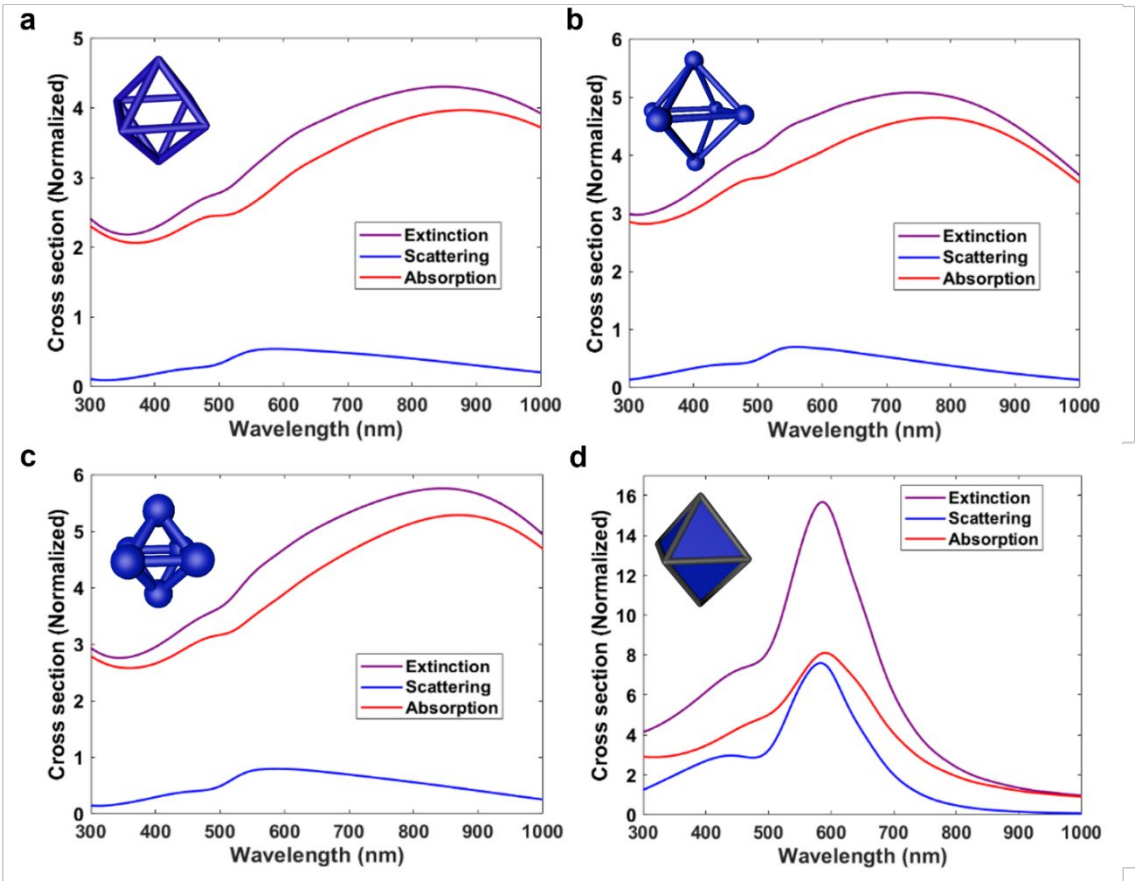


**Figure 10.** Extinction, scattering, and absorption cross-sections of the (**a**), (**b**), (**c**) different varieties of octahedral NFs, and (**d**) nanoparticles. The cross-sections were normalized with respect to the geometrical cross-sections of the volume defined by the unit structures, where the intra-particle voids were omitted for the NFs.

Plasmonic NFs composed of high-loss materials (for example, Pt-Au NFs) are good candidates for preparing such surfaces. Moreover, the structural complexity of plasmonic NFs permits them to support multiple plasmonic resonances and engage in increased light-matter interactions, and their porous nature results in enhanced field confinement. Due to their synthetic tunability (i.e., the ability to precisely control shape, edge length, and pore size), Pt-Au core-shell octahedral NFs are excellent model building blocks for broadband metasurface absorbers. Thus, Pt-Au octahedral NFs with ~ 130 nm edge lengths were assembled into a macroscopic ordered monolayer simply by drop-casting and air drying at room temperature. Their propensity to assemble into monolayer superlattices induces strong optical coupling between the NF building blocks. The versatility of this platform was investigated by assembling three different varieties of octahedral NFs, each of

which yields a discrete lattice with distinct symmetry. We investigated the optical properties of octahedral Pt-Au core-shell octahedral NFs in comparison to solid nanoparticles of the same geometry. As shown in **Figure 10**, single-particle NFs exhibited enhanced light-matter interactions and scattering suppression compared to solid nanoparticles. Taken together, these optical characteristics and the nanoscale size of these NFs make them ideal candidates for broadband absorbers that can be easily incorporated into thin and lightweight devices for applications spanning ultraviolet protection, energy harvesting, sensing, and thermal imaging.

## REFERENCES


1. Chow, T. H.; Li, N.; Bai, X.; Zhuo, X.; Shao, L.; Wang, J., Gold nanobipyramids: An emerging and versatile type of plasmonic nanoparticles. *Accounts of Chemical Research* **2019**, 52 (8), 2136-2146.
2. Sánchez-Iglesias, A.; Winckelmans, N.; Altantzis, T.; Bals, S.; Grzelczak, M.; Liz-Marzán, L. M., High-yield seeded growth of monodisperse pentatwinned gold nanoparticles through thermally induced seed twinning. *Journal of the American Chemical Society* **2017**, *139 (I)*, 107-110.
3. Liu, M.; Guyot-Sionnest, P., Mechanism of silver (I)-assisted growth of gold nanorods and bipyramids. T*he Journal of Physical Chemistry B* **2005**, *109 (47)*, 22192-22200.
4. Lee, J.-H.; Gibson, K. J.; Chen, G.; Weizmann, Y., Bipyramid-templated synthesis of monodisperse anisotropic gold nanocrystals. *Nature Communications* **2015**, *6 (1)*, 1-9.
5. Xia, X.; Xia, Y., Symmetry breaking during seeded growth of nanocrystals. *Nano Letters* **2012**, *12 (11)*, 6038-6042.
6. Yang, T. H.; Shi, Y.; Janssen, A.; Xia, Y., Surface capping agents and their roles in shape‐controlled synthesis of colloidal metal nanocrystals. *Angewandte Chemie International Edition* **2020**, 59 (36), 15378-15401.
7. Kou, X.; Ni, W.; Tsung, C. K.; Chan, K.; Lin, H. Q.; Stucky, G. D.; Wang, J., Growth of Gold Bipyramids with Improved Yield and Their Curvature‐Directed Oxidation. *Small* **2007,** *3* (12), 2103-2113.
8. Parker, K.; Singh, A.; and Dravid, V.P.; "Multi-Signal Characterization of Biological Structures at Low-Voltage Using STEM-in-SEM". *Microscopy and Microanalysis*, **2022** *28*, 1108 – 1110.


## CHANGES IN RESEARCH OBJECTIVES, if any:

Nothing to report.

## SUPPORTED PERSONNEL

Chad A. Mirkin, PI
Jenny K. Orbeck, Research Associate
Kyle Gibson (postdoctoral fellow)
Yuwei Gu (postdoctoral fellow)
Zhiwei Li (postdoctoral fellow)
Benjamin Partridge (postdoctoral fellow)
Ye Zhang (postdoctoral fellow)

John Cavaliere (graduate student)
Ho Fung (Edward) Cheng (graduate student)
Max Distler (graduate student)
Zhenyu (Henry) Han (graduate student)
Yuanwei Li (graduate student)
Kaitlin Landy (graduate student)
Yinglun Ma (graduate student)
Kent Miao (graduate student)
Namrata Ramani (graduate student)
Wenjie Zhou (graduate student)
Heather Calcaterra (unfunded, NSF Fellowship, graduate student)
Nikhil Chellam (unfunded, NSF Fellowship, graduate student)
Alexa Wong (unfunded, NSF Fellowship, graduate student)

Koray Aydin, co-PI
Ibrahim Tanriover (graduate student)
Wisnu Hadibrata (graduate student)
Sina Abedini Dereshgi (graduate student)

Vinayak Dravid, co-PI
Chamille Lescott (graduate student)
Yea-Shine Lee (graduate student)
Jingshan Du (graduate student)
Liban Jibril (unfunded, NU Fellowship, graduate student)
Carolin Wahl (unfunded, NU Fellowship, graduate student)

**COLLABORATIONS**

Milan Mrksich (Northwestern University)
Michael Jewett (Northwestern University)
Vadim Backman (Northwestern University)
Gerasimos Konstantatos (ICFO, Spain)
Maria Cristina Larciprete (Sapienza University of Rome, Italy)
Jacob Scheuer (Tel Aviv University, Israel)
Monical Olvera de la Cruz (Northwestern University)
Sharon Glotzer (University of Michigan)
A. Murthy (Fermi Labs)

**PUBLICATIONS during reporting period:**

1. Du, J. S.; He, K.; Xu, Y.; Wahl, C. B.; Xu, D. D.; Dravid, V. P.; Mirkin, C. A "Galvanic Transformation Dynamics in Heterostructured Nanoparticles," *Advanced Functional Materials*, **2021**, 2105866 doi: 10.1002/adfm.202105866.

2. Petrosko, S. H.; Coleman, B. D.; Drout, R. J.; Schultz, J. D.; Mirkin, C. A. "Spherical Nucleic Acids: Integrating Nanotechnology Concepts into General Chemistry Curricula," *Journal of Chemical Education*, **2021**, *98*, 3090-3099, doi: 10.1021/acs.jchemed.1c00441.
3. Miao, Z.; Zheng, C. Y.; Schatz, G. C.; Lee, B.; Mirkin, C. A. "Low Density 2D Superlattices Assembled via Directional DNA Bonding," *Angewandte Chemie*, **2021**, *60*, 19035-19040, doi: 10.1002/anie.202105796.
4. Distler, M. E.; Teplensky, M. H.; Bujold, K. E.; Kusmierz, C. D.; Evangelopoulos, M.; Mirkin, C. A "DNA Dendrons as Agents for Intracellular Delivery," *Journal of the American Chemical Society*, **2021**, *143*, 13513-13518, doi:10.1021/jacs.1c07240, PMCID: PMC8582297.
5. Ebrahimi, S. B.; Samanta, D., Kusmierz, C. D.; Mirkin, C. A. "Protein Transfection Via Spherical Nucleic Acids," *Nature Protocols*, **2022**, *17*, 327–357, doi: 10.1038/s41596-021-00642-x.
6. Landy, K. M.; Gibson, K. J.; Urbach, Z. J.; Park, S. S.; Roth, E. W.; Weigand, S.; Mirkin, C. A. "Programming "atomic substitution" in alloy colloidal crystals using DNA," *Nano Lett.,* **2022**, *22*, 280-285, doi.org/10.1021/acs.nanolett.1c03742.
7. Cheng, H. F.; Distler, M. E.; Lee, B.; Zhou, W.; Weigand, S.; Mirkin, C. A. "Nanoparticle Superlattices Through Template-Encoded DNA Dendrimers," *Journal of the American Chemical Society*, **2021**, *143*, 17170-17179, doi: 10.1021/jacs.1c07858.
8. Gu, Y.; Distler, M. E.; Cheng, H. F.; Huang, C.; Mirkin, C. A. "A General DNA-Gated Hydrogel Strategy for Selective Transport of Chemical and Biological Cargos," *Journal of the American Chemical Society*, **2021**, *143*, 17200-17208, doi: 10.1021/jacs.1c08114.
9. Zheng, C. Y.; Hadibrata, W.; Kim, S.; Schatz, G. C.; Aydin, K.; Mirkin, C. A. "Large-area, highly crystalline DNA-assembled metasurfaces exhibiting widely tunable epsilon-near-zero behavior," *ACS Nano*, **2021**, *15*, 18289–18296, doi: 10.1021/acsnano.1c07496.
10. Teplensky, M. H.; Distler, M. E.; Kusmierz, C. D.; Evangelopoulos, M.; Gula, H.; Elli, D.; Tomatsidou, A.; Nicoleascu, V.; Gelarden, I.; Yeldandi, A.; Batlle, D.; Missiakas, D.; Mirkin, C. A. "Spherical Nucleic Acids as an Infectious Disease Vaccine Platform," *Proc. Natl. Acad. Sci. USA*, **2022**, *119*, e2119093119. doi: 10.1073/pnas.2119093119.
11. Samanta, D.; Zhou, W.; Ebrahimi, S. B.; Petrosko, S. H.; Mirkin, C. A. "Programmable Matter: The Nanoparticle Atom and DNA Bond," *Adv. Mater.,* **2022**, *34*, 2107875, doi: 10.1002/adma.202107875.
12. Huang, L.; Shen, B.; Lin, H.; Shen, J.; Jibril, L.; Zheng, C. Y.; Wolverton, C.; Mirkin, C. A. "Regioselective Deposition of Metals on Seeds within a Polymer Matrix," *J. Am. Chem. Soc.,* **2022**, *144*, 4792-4798. doi: 10.1021/jacs.1c11118.
13. Zheng, C. Y.; Yao, Y.; Deng, J.; Seifert, S.; Wong, A. M.; Lee, B.; Mirkin, C. A. "Confined Growth of DNA-Assembled Superlattice Films," *ACS Nano*, **2022**, *16*, 4813-4822, doi: 10.1021/acsnano.2c00161.
14. Li, Y.; Tanriover, I.; Zhou, W.; Hadibrata, W.; Dereshgi, S. A.; Samanta, D.; Aydin, K.; Mirkin, C. A. "Monolayer Plasmonic Nanoframes as Large-Area, Broadband Metasurface Absorbers," *Small*, **2022**, *18*, 2201171, doi.org/10.1002/smll.202201171.
15. Jibril, L.; Cheng, M.; Wahl, C. B.; Dravid, V. P.; Mirkin, C. A. "Polymer-Mediated Particle Coarsening within Hollow Silica Shell Nanoreactors," *Chem. Mater.,* **2022**, *34*, 5094–5102. doi: 10.1021/acs.chemmater.2c00510.

16. Abedini, D.S.; Larciprete, M.C.; Centini, M.; Murthy, A.; Tang, K.; Wu, J.; Dravid, V.P.; Aydin, K. "Tuning of Optical Phonons in α MoO3–VO2 Multilayers," *ACS applied Materials & Interfaces*, **2021**,13 (41),48981-48987 doi:10.1021/acsami.1c12320
17. Parker, K.; Singh, A.; and Dravid, V.P.; "Multi-Signal Characterization of Biological Structures at Low-Voltage Using STEM-in-SEM". Microscopy and Microanalysis, **2022** 28, S1, pp. 1108 – 1110 doi:10.1017/S1431927622004688
18. Hinamoto, T.; Lee Y-S.; Dereshgi, S.A.; DiStefano, J. G.; dos reis, R.; Sugimoto, H; Aydin K.; Fujii, M.; Dravid, V.P. "Resonance Couplings in Si@$MoS_2$ Core–Shell Architectures". *Small*, **2022** 18, 17 2200413. doi:10.1002/smll.202200413
19. Ribet, S.; Murthy, A.A. Roth, E.W.; dos Reis, R.; Dravid, V.P. "Making the most of your electrons: Challenges and opportunities in characterizing hybrid interfaces with STEM". *Materials Today*, *Elsevier Ltd* **2021** 50, 100-115. doi:10.1016/j.mattod.2021.05.006

**PRESENTATIONS during reporting period**

1. Chad A. Mirkin. EFRC Blue Team Presentation (virtual), "DNA-engineered Hierarchical Structures," (2021).
2. Chad A. Mirkin. Fall 2021 ACS Meeting (virtual), "Megalibraries: Tools for Exploring and Expanding the Materials Genome with big Data and AI," (2021).
3. Chad A. Mirkin. Fall 2021 ACS Meeting (virtual), "Valency Control through Electron Equivalents: The VSEPR Equivalent for Colloidal Crystals," (2021).
4. Chad A. Mirkin. Oligonucleotide Therapeutics Society, Bob Letsinger – 100 Years of History Sympoisum, (virtual), "Business with Bob: Navigating the Start-up World with an Oligonucleotide Giant," (2021).
5. Chad A. Mirkin. The Kavli Nanoscience Institute Distinguished Lecture, Caltech, Pasadena, CA, "Colloidal Crystal Engineering with DNA: Repurpsoing the Blueprint for Life," (2021).
6. Chad A. Mirkin. Glen Research Webinar (virtual), "Rational Vaccinology and Precision Medicine Through Spherical Nucleic Acids," (2021).
7. Chad A. Mirkin. 2021 AFOSR Natural Materials and Systems Annual Program Review (virtual), "Reconfigurable Matter from Programmable Atom Equivalents," (2021).
8. Chad A. Mirkin. iCANx (virtual), "Exploring the Matterverse with Nanomaterial Megalibraries," (2022). https://www.youtube.com/watch?v=-BaUtaIW3JI.
9. Chad A. Mirkin. VP Guest Speaker Series - Kinder Morgan, San Francisco, CA, "Providing the Path to a Sustainable Future: Stoicheia Enabling Pathways for the Energy Transition Through Big Data and AI," (2022).
10. Chad A. Mirkin. Spring 2022 ACS National Meeting, San Diego, CA, "Repurposing the Blueprint of Life for Materials Design and Synthesis," (2022).
11. Chad A. Mirkin. University of Texas, Austin, McKetta Department of Chemical Engineering Seminar, Austin, TX, "Colloidal Crystal Engineering with DNA: Repurposing the Blueprint for Life," (2022).
12. Chad A. Mirkin. Society for Biomaterials 2022 Annual Meeting, Acta Biomaterialia Gold Medal Plenary, Baltimore, MD, "Nanostructures with Transformative Implications in Biology and Medicine," (2022).
13. Chad A. Mirkin. Expand Your Horizon Dinner Series, Evanston, IL, "Nanostructures with Transformative Implications in Biology and Medicine," (2022).
14. Chad A. Mirkin. ICMES 2022: Satellite Meeting: Materials for a Sustainable Future, Saïdia, Morocco, "Nanomaterials in Healthcare," (2022).

15. Chad A. Mirkin. NANO KOREA 2022: The 20th International Nanotech Symposium, virtual, “MegaLibraries: Defining and Mining the Materials Genome with Big Data and AI,” (2022).
16. Koray Aydin. EOSAM 2021, Rome, Italy, “Anisotropic 2D Materials for Infrared Phononics and Polaritonics” (2021).
17. Koray Aydin. SPIE Optics and Photonics, San Diego, CA. “Emerging Anisotropic 2D Layered Materials” (2021).
18. Vinayak P. Dravid. 2022-STC Learning Synthesis Science Workshop w/ Northwestern-Berkley-MIT (2022).
19. Vinayak P. Dravid. IWAM UAE - “Teaching “Old” Materials “New” Tricks: Waste Sponges and Foams for Energy, Environment and Sustainability” (2022)
20. Vinayak P. Dravid. Northwestern University, “NW Engineering Students and Industry Specialists,” NU engineering and AAEIO collaboration and Q&A panel member.
21. Vinayak P. Dravid. Northwestern University, TEDx Talk, "Teaching an 'Old' Dog 'New' Tricks" (2022)
22. Vinayak P. Dravid. WBEZ interview, Shedd Aquarium (2022)
23. Vinayak P. Dravid. NASEM Workshop Convergent Manufacturing A Future of Additive, Subtractive, and Transformative Manufacturing, “Heterogeneous Materials Design” (2021).
24. Vinayak P. Dravid. EES Seminar Series, “Using “Waste” to “Clean” Waste: Multifunctional Sponges and Membranes for Environmental Remediation” (2021).
25. Vinayak P. Dravid. Nanocombinatorics Workshops, “High-Throughput Characterization (Structural),” (2021).
26. Wenjie Zhou. 45th IPMI Conference, Reno, NV, USA, "Designer Previous Metal Nano-Architectures" (2021)
27. Wenjie Zhou. 2021 EFRC-Hub-CMS-CCS PI Meeting, Virtual, "Shape-Driven, DNA-Mediated Engineering of Colloidal Superlattices" (2021)
28. Wenjie Zhou. 2021 International Chemical Congress of Pacific Basin Societies, Virtual, "Colloidal Crystal Dense packing Through Polyhedra Complementarity" (2021)
29. Wenjie Zhou. 2022 MRS Spring Meeting, Honolulu, HI, USA, "Establishing the Rules for the Organization of Colloidal Anisotropic Nanoparticles" (2022)
30. Wenjie Zhou. GRS/GRC: Noble Metal Nanoparticles, South Hadley, MA, USA, "Colloidal Superlattices Engineering with DNA" (2022)
31. Benjamin E. Partridge. RSC Macrocyclic and Supramolecular Chemistry Young Scientist Series, Virtual, “Redefining Protein Interfaces within Protein Single Crystals with DNA” (2022).
32. Benjamin E. Partridge. Gordon Research Conference on Bioinspired Materials, Les Diablerets, Switzerland, “Protein-Based Materials Engineering with DNA” (2022).
33. Benjamin E. Partridge. Gordon Research Symposium on Bioinspired Materials, Les Diablerets, Switzerland, “Encoding Hierarchical Assembly Pathways of Proteins with DNA” (2022).
34. Benjamin E. Partridge. International Chemical Congress of Pacific Basin Societies (Pacifichem), Virtual, “Encoding Hierarchical Assembly Pathways of Proteins with DNA” (2021).
35. Benjamin E. Partridge. Wesleyan University, Middletown, CT, United States, “Protein-Based Materials Engineering with DNA” (2021).

36. Yuanwei Li. GRC&GRS: Noble Metal Nanoparticles, South Hadley, MA, United States, "Poster: Designing and Synthesizing Topologically Diverse Porous Colloidal Superlattices" (June 2022).
37. Yuanwei Li. MRS Spring Meeting, Honolulu, Hawai'i, United States, "Poster: Metallic Open Channel Colloidal Superlattices" (May 2022).
38. Yuanwei Li. Pacifichem Conference, Virtual, "Talk: Open Channel Superlattices" and "Poster: Edge-, Corner-, and Facet-Controlled Growth of Nanocrystals" (December 2021).

**AWARDS during reporting period**

Chad. A. Mirkin. MRS Medal (2022).
Chad A. Mirkin. Faraday Medal (IET) (2022).
Chad A. Mirkin. STEM Leadership Award for Outstanding Entrepreneurial Innovation (CME) (2022).
Chad A. Mirkin. John P. McGovern Science and Society Award (Sigma Xi) (2022).
Chad A. Mirkin. International Precious Metals Institute (IPMI) Jun-ichiro Tanaka Distinguished Achievement Award (2022).
Chad A. Mirkin. Acta Biomaterialia Gold Medal (2022).
Chad A. Mirkin. Royal Society of Chemistry de Gennes Prize (2021).
Chad A. Mirkin. UNESCO-Equatorial Guinea International Prize for Research in Life Sciences (2021).
Chad A. Mirkin. G. M. Kosolapoff Award, Auburn University and the Auburn Section of the ACS (2021).
Wenjie Zhou. MRS Graduate Student Gold Award (2022).
Wenjie Zhou. Chinese Government Award for Outstanding Self-Financed Students Abroad (2022).
Benjamin E. Partridge. International Institute for Nanotechnology Outstanding Researcher Award (2021).
Jingshan Du ASM Carl Samans Excellence Award (2021).
Yuanwei Li, Winner of 2021 Pacifichem Congress Student Research Competition (2021).
Yuanwei Li, Ludo Frevel Crystallography Scholarship (2022).
Yuanwei Li, SPIE Optics and Photonics Education Scholarship (2022)

**INTERACTIONS/TRANSITIONS**

**Patent Applications**

1. “Method for Controlled Growth of Nanocrystals” Y. Li, H. Lin, C.A. Mirkin, W. Zhou, PCT/US2021/049443, September 8, 2021.
2. “Antiviral Vaccines Using Spherical Nucleic Acids” C. Callmann, C. Kusmierz, C. A. Mirkin, M. Teplensky, European Patent Office, PCT/US2022/018384, March 1, 2022.
3. “Antiviral Vaccines Using Spherical Nucleic Acids” C. Callmann, C. Kusmierz, C. A. Mirkin, M. Teplensky, US Patent Application, 17/684,269, March 1, 2022.
4. “CRISPR-Mediated Cleavage of Oligonucleotide-Detectable Marker Conjugates for Detection of Target Analytes” C. A. Mirkin, S.B. Ebrahimi, D. Samanta, PCT/US2022/021786, March 24, 2022.
5. “Oligonucleotide Dendrimers for Dynamic Colloidal Crystal Engineering” H.F. Cheng, M. Distler, K. Gibson, C. A. Mirkin, US Patent Application, 63/286,524, December 6, 2021.

6. “Polymer Mediated Particle Coarsening Within Hollow Silica Shell Nanoreactors” V.P. Dravid, L. Jibril, C.A. Mirkin, US Patent Application, 63/317,734, March 8, 2022.
7. “Methods of Forming Stable Conductive Surfaces” V.P. Dravid, C.A. Mirkin, C. Wahl, US Patent Application, 63/354,100, June 21, 2022.
8. “Stepwise Synthesis of Colloidal Crystals” K. Gibson, K. Landy, C.A. Mirkin, US Patent Application, 63/391,554, July 22, 2022.
9. “Oligonucleotide Dendron Molecular Vaccines” J. Cavaliere, M. Distler, M. Evangelopoulos, C.A. Mirkin, M. Teplensky, US Patent Application, 63/373,315, August 23, 2022.
10. “Conductive 2D Metal-Organic Framework for Aqueous Rechargeable Battery Cathodes” C.A. Mirkin K. Nam, S. Park. J. Stoddart, US Patent Application, 17/597,507, January 10, 2022.
11. “Halide Perovskite Nanocrystal Array and Methods of Making the Same” V.P. Dravid, J. Du, C.A. Mirkin, D. Shin, US Patent Application, 17/782,613, June 3, 2022.

**Invention Disclosures**

1. “DNA Dendrimers for Dynamic and Functional Colloidal Crystal Engineering” November 24, 2021.
2. “Synthesis of Individual Nanoparticles within Hollow Silica Shells Facilitated by Polymer Incorporation” February 10, 2022.
3. “Methods of Forming Stable Conductive Surfaces” April 1, 2022.
4. “Stepwise Synthesis of Colloidal Crystals” June 17, 2022.
5. “DNA Dendrons as Molecular Therapeutics and Diagnostics” August 18, 2022.